NORTH ATLANTIC TREATY ORGANISATION

RESEARCH AND TECHNOLOGY ORGANISATION

AC/323(AVT-136)TP/388

www.rto.nato.int

RTO TECHNICAL REPORT **TR-AVT-136**

Assessment of Aerothermodynamic Flight Prediction Tools through Ground and Flight Experimentation

(Evaluation des outils aérothermodynamiques de prédiction de vol par l'expérimentation au sol et en vol)

This Report Documents the Efforts of Task Group AVT-136.

Published November 2011

NORTH ATLANTIC TREATY ORGANISATION

RESEARCH AND TECHNOLOGY ORGANISATION

AC/323(AVT-136)TP/388

www.rto.nato.int

RTO TECHNICAL REPORT **TR-AVT-136**

Assessment of Aerothermodynamic Flight Prediction Tools through Ground and Flight Experimentation

(Evaluation des outils aérothermodynamiques de prédiction de vol par l'expérimentation au sol et en vol)

This Report Documents the Efforts of Task Group AVT-136.

The Research and Technology Organisation (RTO) of NATO

RTO is the single focus in NATO for Defence Research and Technology activities. Its mission is to conduct and promote co-operative research and information exchange. The objective is to support the development and effective use of national defence research and technology and to meet the military needs of the Alliance, to maintain a technological lead, and to provide advice to NATO and national decision makers. The RTO performs its mission with the support of an extensive network of national experts. It also ensures effective co-ordination with other NATO bodies involved in R&T activities.

RTO reports both to the Military Committee of NATO and to the Conference of National Armament Directors. It comprises a Research and Technology Board (RTB) as the highest level of national representation and the Research and Technology Agency (RTA), a dedicated staff with its headquarters in Neuilly, near Paris, France. In order to facilitate contacts with the military users and other NATO activities, a small part of the RTA staff is located in NATO Headquarters in Brussels. The Brussels staff also co-ordinates RTO's co-operation with nations in Middle and Eastern Europe, to which RTO attaches particular importance especially as working together in the field of research is one of the more promising areas of co-operation.

The total spectrum of R&T activities is covered by the following 7 bodies:

- AVT Applied Vehicle Technology Panel
- HFM Human Factors and Medicine Panel
- IST Information Systems Technology Panel
- NMSG NATO Modelling and Simulation Group
- SAS System Analysis and Studies Panel
- SCI Systems Concepts and Integration Panel
- SET Sensors and Electronics Technology Panel

These bodies are made up of national representatives as well as generally recognised 'world class' scientists. They also provide a communication link to military users and other NATO bodies. RTO's scientific and technological work is carried out by Technical Teams, created for specific activities and with a specific duration. Such Technical Teams can organise workshops, symposia, field trials, lecture series and training courses. An important function of these Technical Teams is to ensure the continuity of the expert networks.

RTO builds upon earlier co-operation in defence research and technology as set-up under the Advisory Group for Aerospace Research and Development (AGARD) and the Defence Research Group (DRG). AGARD and the DRG share common roots in that they were both established at the initiative of Dr Theodore von Kármán, a leading aerospace scientist, who early on recognised the importance of scientific support for the Allied Armed Forces. RTO is capitalising on these common roots in order to provide the Alliance and the NATO nations with a strong scientific and technological basis that will guarantee a solid base for the future.

Published November 2011

ISBN 978-92-837-0142-2

Table of Contents

List of Figures

List of Tables

Programme Committee

Co-Chairs

Dr. W.F. Jones
Office of Naval Research
875 North Randolph Street, Suite 1445
Arlington, VA 22203-1995
UNITED STATES
Email: walter.f.jones@navy.mil

Dr. J.M. Muylaert
VKI
Chaussée de Waterloo, 72
B-1640 Rhode-St-Genèse
BELGIUM
Email: jean.muylaert@vki.ac.be

Dr. P. Erbland
AFRL/VAA
2130 8th Street, Room 290
WPAFB, OH 45433
UNITED STATES
Email: peter.erbland@wpafb.af.mil

Dr. J. Schmisseur
Air Force Office of Scientific Research
875 North Randolf Street, Suite 325, Room 3112
Arlington, VA 22203
UNITED STATES
Email: john.schmisseur@afosr.af.mil

Members

GERMANY

Dr. G. Herdrich
Institute of Space Systems (IRS)
University of Stuttgart
Pfaffenaldring 31
70550 Stuttgart
Email: herdrich@irs.uni-stuttgart.de

Dr. J. Longo
DLR
Institute of Aerodynamics and Flow Technology
Lilienthalplatz 7
38108 Braunschweig
Email: jose.long@dlr.de

GREECE

Dr. A. Panaras
National Technical University of Athens
Mechanical Engineering Department
Agias Elenis 63
15772 Athens
Email: a.panaras@gmail.com

ITALY

Prof. S. Borelli
CIRA
Aerothermodynamics Section
Via Maiorise
81043 Capua (CE)
Email: s.borelli@cira.it

UNITED STATES

Prof. D.G. Fletcher
University of Vermont
Mechanical Engineering, 201 Votey Hall
33 Colchester Avenue
Burlington, VT 05405
Email: douglas.fletcher@uvm.edu

Dr. J. Kelley
NASA ARC
Mountain View, CA
Email: jdanielkelley@sbcglobal.net

Contributors

GERMANY

Dr. K. Hannemann
German Aerospace Centre
Institute of Aerodynamics and Flow
Technology, Spacecraft
Bunsenstr.10
37073 Göttingen
Email: Klaus.Hannemann@dlr.de

NETHERLANDS

Dr. J. Walpot
AOES Group-B.V.
Haagse Schouwweg 6G
2332 KG Leiden
Email: lwalpot@aoes.com

UNITED STATES

Dr. D. Gaitonde
AFRL/VAC
Building 146, Room 225
2210 8th Street
WPAFB, OH 45433
Email: data.gaitonde@wpafb.af.mil

Dr. M. Holden
CUBRC, Aerothermal/Aero-Optic Evaluation Center
4455 Genesee Street
Buffalo, NY 14221
Email: holden@cubrc.org

Dr. B. Hollis
NASA Langley Research Center
MS 408A, Bldg 1251A, Room 208
16 Victory Street
Hampton, VA 23681-21999
Email: brian.r.hollis@nasa.gov

Dr. R. Kimmel
AFRL/RBAA
Building 45, Room 256, 2130 8th Street
WPAFB, OH 45433-7542
Email: roger.kimmel@wpafb.af.mil

Prof. D. Knight
Rutgers University
Dept. Mechanical and Aerospace Engineering
98 Brett Road
Piscataway, NJ 08854
Email: doyleknight@gmail.com

Dr. J. Marschall
SRI International
333 Ravenswood Avenue
Menlo Park, CA 94025-3493
Email: jochen.marschall@sri.com

Dr. J.N. Moss
NASA Langley Research Center
MS 408A
Hampton, VA 23681-2199
Email: j.n.moss@larc.nasa.gov

Dr. J. Olejniczak
NASA Ames Research Center
M/S 230-2
Moffett Field, CA 94035
Email: joseph.olejniczak@nasa.gov

Prof. S. Schneider
Purdue University
Aerospace Sciences Laboratory
1375 Aviation Drive
West Lafayette, IN 47907-2015
Email: steves@ecn.purdue.edu

Dr. M.J. Wright
NASA Ames Research Center
M/S 230-2, Building 230
Moffett Field, CA 94035
Email: mjwright@mail.arc.nasa.gov

Panel Mentor

Prof. Dr. C.C. Rossow
Institute of Aerodynamics and Flow Technology (DLR)
Lilienplatz 7, 38108 Braunschweig
GERMANY
Email: cord.rossow@dlr.de

Assessment of Aerothermodynamic Flight Prediction Tools through Ground and Flight Experimentation

(RTO-TR-AVT-136)

Executive Summary

In the upcoming decades military capabilities based on hypersonic flight systems will become increasingly important to NATO members as the need for time-critical responses evolves. Fast strike capabilities with conventional munitions and responsive, efficient space access are two examples. While a broad spectrum of technology development is required to realize such planned capabilities, the development of essential hypersonic systems will be paced by the ability to accurately predict the extreme aerothermodynamic environment.

In 2005 the RTO Applied Vehicle Technology Panel approved the organization of Task Group AVT-136, *Assessment of Aerothermodynamic Flight Prediction Tools through Ground and Flight Experimentation.*

The objective of the Task Group is to *assess and improve the understanding and prediction of aerothermodynamic phenomena and aerothermal loads for space transportation and earth/planetary entry systems through ground and flight experimentation*.

To achieve the above, AVT-136 organized its efforts around six scientific topic areas broadly relevant to the development of planned hypersonic capabilities:

1) Nose and Leading Edges;
2) Shock Interactions and Control Surfaces;
3) Shock Layers and Radiation;
4) Boundary Layer Transition;
5) Gas-Surface Interactions; and
6) Base and Afterbody Flows.

Although it was recognized from the onset of AVT-136 activities that reliance on flight research data yet to be collected posed significant risk to the achievement of Task Group objectives, the group concluded the significant benefit to be derived from comparison of computational simulations with flight data warranted pursuit of such a program of work. Unfortunately, program delays and failures in the flight programs contributing to the AVT-136 effort prevented access to flight research data.

Despite the unavailability of flight research data, most of the scientific topic areas developed by the Task Group made significant progress in the assessment of current capabilities. The chapters of this report document the program of work and contributions of most of the topic areas. Additionally, the activities of AVT-136 generated substantial interest within the international scientific research community and the work of the Task Group was prominently featured in a total of six invited sessions dedicated to AVT-136 in the Sixth European Symposium on Aerothermodynamics for Space Vehicles and the 48th (2010) AIAA Aerospace Sciences Meeting.

AVT-136 enjoyed enthusiastic support from the research communities and organizations of the participating countries during the four-year duration of the Task Group and it is clear that international interest and

support for collaborative efforts in hypersonics remains strong. Thus, the members of AVT-136 strongly recommend the continuation of international collaborative efforts in aerothermodynamics under the auspices of the Applied Vehicle Technology Panel.

Evaluation des outils aérothermodynamiques de prédiction de vol par l'expérimentation au sol et en vol

(RTO-TR-AVT-136)

Synthèse

Dans les prochaines décennies, les capacités militaires reposant sur les systèmes de vol hypersoniques vont devenir de plus en plus importantes pour les membres de l'OTAN au fur et à mesure que le besoin d'une plus grande réactivité évoluera. Les capacités de frappe rapide avec des munitions conventionnelles et l'accès réactif et efficace à l'espace en sont deux exemples. Alors qu'un large spectre de développements technologiques sera nécessaire pour réaliser les capacités ainsi envisagées, le développement des systèmes hypersoniques indispensables va être conditionné par la capacité à prédire avec précision le très sévère environnement aérothermodynamique.

En 2005, la commission Technologie Appliquée aux Véhicules (AVT) de la RTO a approuvé l'organisation du groupe de travail AVT-136, *Evaluation des outils aérothermodynamiques de prédiction de vol par l'expérimentation au sol et en vol.*

L'objectif du groupe de travail est *d'évaluer et d'améliorer, par l'expérimentation au sol et en vol, la compréhension et la prédiction des phénomènes aérothermodynamiques et des charges aérothermiques pour le transport spatial et les systèmes d'entrée terrestre/planétaire*.

Pour réaliser cet objectif, AVT-136 a organisé ses activités autour de six domaines scientifiques se rapportant très largement au développement des capacités hypersoniques envisagées :

1) Pointe avant et bords d'attaque ;
2) Interaction de chocs et gouvernes ;
3) Couches de chocs et rayonnements ;
4) Transition de couche limite ;
5) Interactions gaz-surface ; et
6) Ecoulements sur la partie inférieure et l'arrière.

Bien qu'il ait été reconnu dès le début des activités d'AVT-136 que le fait de se reposer sur des données de recherches en vol qui restent encore à obtenir n'était pas sans risques pour la réalisation des objectifs du groupe de travail, le groupe a conclu que les bénéfices significatifs à retirer de la comparaison des simulations calculées avec les données de vol devaient garantir la poursuite d'un tel programme de travail. Malheureusement, les retards et les défaillances des programmes de vol participant à l'activité de l'AVT-136 ont rendu impossible l'accès aux données des recherches en vol.

Malgré l'indisponibilité des données issues des recherches en vol, presque tous les domaines scientifiques développés par le groupe de travail ont produit des progrès significatifs dans l'évaluation des capacités actuelles. Les chapitres de ce rapport décrivent le programme de travail et les contributions apportées dans la plupart des domaines. De plus, les activités d'AVT-136 ont généré un intérêt significatif au sein de la

communauté internationale de la recherche scientifique et le travail du groupe a été souligné par les six sessions invitées dédiées à AVT-136 lors du Sixième Symposium Européen sur l'Aérothermodynamique pour les véhicules spatiaux et lors de la 48° réunion AIAA des Sciences aérospatiales.

AVT-136 s'est réjoui du soutien enthousiaste apporté par les communautés de la recherche et les organisations des nations participantes pendant ses quatre ans d'activité. Il est clairement apparu que l'intérêt et le soutien internationaux pour l'hypersonique restent forts. Ainsi, les membres d'AVT-136 ont fortement recommandé de poursuivre les travaux de coopération internationale dans l'aérothermodynamique sous les auspices de la commission Technologie Appliquée aux Véhicules.

Chapter 1 – SUMMARY OF TASK GROUP ACTIVITIES AND ACCOMPLISHMENTS

John D. Schmisseur
United States Air Force Office of Scientific Research
USA

1.1 SCIENTIFIC CHALLENGES IN AEROTHERMODYNAMIC PREDICTION AND THE NEED FOR FLIGHT RESEARCH

In the upcoming decades military capabilities based on hypersonic flight systems will become increasingly important to NATO members as the need for time-critical responses evolves. Fast strike capabilities with conventional munitions on both tactical and global scales will facilitate the engagement of time-critical and mobile targets while minimizing the threat to associated launch assets. Responsive, efficient space access will ensure both the rapid sustainment and replacement of critical space systems and the time-critical deployment of Intelligence, Surveillance and Reconnaissance (ISR) capabilities. While a broad spectrum of technology development is required to realize such planned capabilities, the development of essential hypersonic systems will be paced by the ability to accurately predict the extreme aerothermodynamic environment.

One of the primary technological challenges to the development of hypersonic capabilities is the management of the substantial thermal loads associated with the aerothermodynamic environment. Conservative approaches to thermal protection systems increase vehicle weight at the expense of performance, while aggressive, low-weight designs increase the potential risk for structural failure. At the heart of this problem lies the current inability to accurately predict the complex fluid dynamic, thermodynamic and chemical phenomena associated with hypersonic flows.

Unsteady and non-equilibrium aerothermodynamic phenomena are the source of the dominant acoustic and thermal loads experienced by hypersonic systems, effecting changes in the environment both locally and over large regions of the vehicle surface. A few examples of the broad spectrum of such phenomena include laminar-turbulent transition in the boundary layer, shock wave / boundary layer interactions, and catalytic heating resulting from non-equilibrium gas-surface interactions. Laminar-turbulent transition in the boundary layer increases surface heat transfer by almost an order of magnitude, making accurate estimation of the onset of transition a critical need for the design of efficient thermal protection systems. Local flow separation resulting from shock wave / boundary layer interactions generates extreme heat transfer rates in the region where the separated flow is reattaching and can be the source of significant acoustic loads if the interaction is unsteady. Finally, non-equilibrium thermodynamic processes and chemical reactions in the flowfield and at the system surface can substantially impact surface heat transfer by determining the availability of energy transferred to the vehicle from the flowfield through catalytic surface heating. Through the rigorous exploration, modelling and exploitation of these and other physical phenomena, the research community is attempting to develop accurate methods for the prediction and mitigation of the extreme aerothermodynamic environment.

High-fidelity numerical methods, large-scale computational simulations and advanced laser-based time- and space-resolved diagnostics are providing unprecedented insight into the fundamental phenomena associated with hypersonic flows. Despite this advantage, progress in modelling and exploiting critical phenomena is limited due to the inability of ground test facilities to duplicate the entire flight environment and the complex interactions that contribute to critical aerothermodynamic phenomena (for example, the influence of non-equilibrium thermophysics on laminar-turbulent transition). Ground test facilities typically excel in reproducing one aspect of the hypersonic environment at the expense of another

parameter, as illustrated by the following examples. Shock tunnels generate high-enthalpy flows but at the expense of potential non-equilibrium of the facility freestream. Arc-heated facilities used for thermal protection system material testing can provide very high heat flux into the material, but typically do so at subsonic or low supersonic conditions which do not reproduce the strong shock waves and high shear rates associated with hypersonic flows. Finally, a class of low-disturbance “quiet” wind tunnels has been developed for the exploration of boundary layer transition. Such facilities provide flight-like disturbance environments in the test sections by delaying the onset of transition in the nozzle but only in low-enthalpy flows at low Reynolds numbers. While computations have no such physical limitations, the utilization of high-fidelity, unsteady numerical simulation for the analysis of turbulent flows is currently limited to relatively low Reynolds numbers due to the excessive computational demands of such computations. Additionally, as with any numerical model, verification and validation of the solution accuracy is dependent on detailed comparison with well-characterized and resolved “real” experimental data. Unfortunately, the extraordinary expense and complexity associated with flight experiments in the hypersonic environment precludes the option of utilizing such an approach as the primary source of new insight into fundamental physical phenomena.

Given the challenges described above, there is significant need for reliable approaches to the extrapolation of numerical simulations validated at ground test conditions to application at actual flight conditions. One philosophical approach to the problem recently employed by a number of research organizations is the “Triangle” model illustrated in Figure 1-1. In this model, ground test, numerical simulation and flight research are all utilized in concert to provide an integrated approach to the identification and modelling of critical phenomena. As indicated in Figure 1-1, ground test and numerical simulation form the strong base of the triangle, a reflection of the fact that the bulk of the new insight required to develop essential knowledge will be acquired through these disciplines. Flight research, at the vertex of the triangle, provides a focus to the integrated research efforts and the opportunity to feed back critical “real world” observations to the foundational efforts of ground test and computation. The HIFiRE – Hypersonic International Flight Research Experiment – program jointly executed by the United States Air Force Research Laboratory and the Australia Defence Science and Technology Organisation was developed based on the triangle model and characteristics of such an approach are clearly evident in a number of other international flight research programs [1], most notably the DLR SHEFEX and ESA EXPERT efforts.

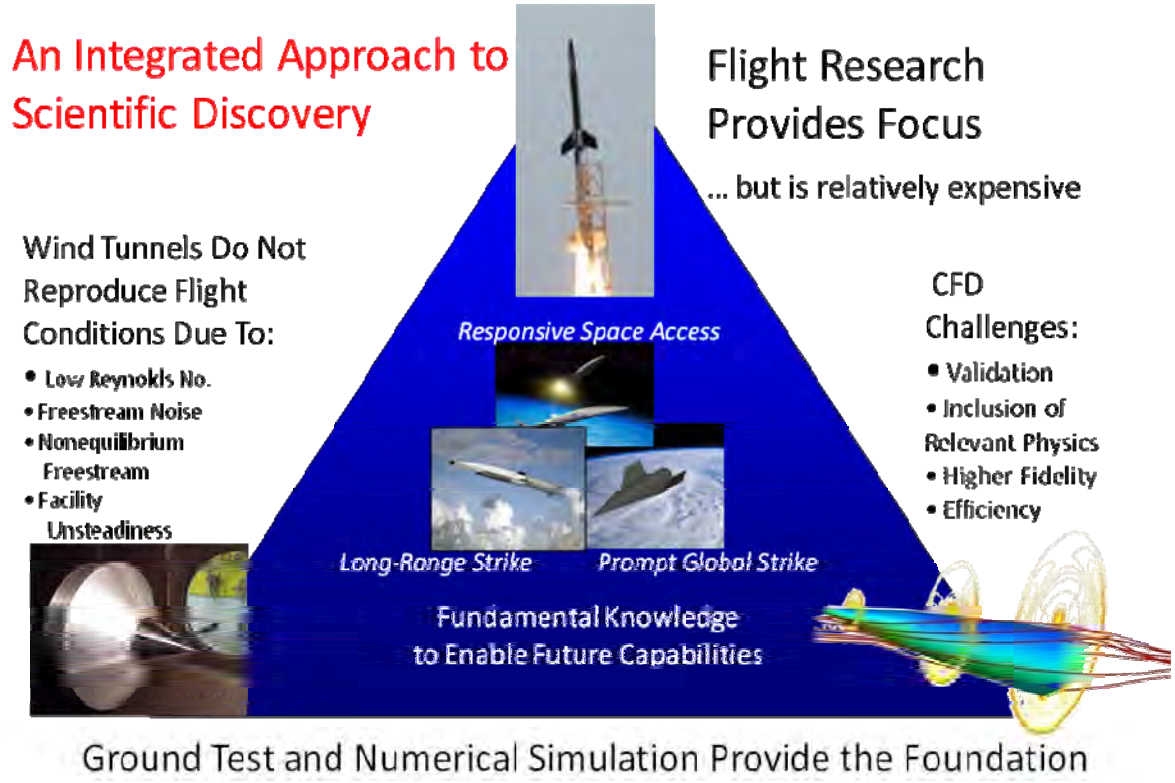

Figure 1-1: The "Triangle" Model for Scientific Discovery Integrating Ground Test, Numerical Simulation and Flight Research.

There have been several notable prior attempts by RTO to address the issue of critical aerothermodynamic phenomena. AGARD/FDP WG18 [2] explored a number of critical phenomena including laminar-turbulent transition, shock wave / boundary layer interactions, rarefied flows, real gas flows and extrapolation from ground test data to flight conditions based on the space shuttle. More recently, RTO-AVT-WG10, *Technologies for Propelled Hypersonic Flight*, [3] addressed the areas of plug nozzles, scramjet combustion and CFD validation for hypersonic flight. These prior efforts led to significant improvements in predictive capabilities as evidenced by comparison to ground test data and helped guide the research directions of the scientific community. However, continued improvements in physical and numerical modeling, computational efficiency, and experimental techniques, coupled with a new generation of flight research programs now present a unique opportunity to assess and improve our aerothermodynamic flight prediction capabilities. This report presents the work of AVT-136, *Assessment of Aerothermodynamic Flight Prediction Tools Through Ground and Flight Experimentation*, which attempted to leverage current flight research programs based on the triangle model to advance the extrapolation of ground test and numerical simulation to flight conditions.

1.2 OBJECTIVES AND ORGANIZATION OF AVT-136

In 2005 the RTO Applied Vehicle Technology panel approved the organization of Task Group AVT-136, *Assessment of Aerothermodynamic Flight Prediction Tools Through Ground and Flight Experimentation.*

The objective of the Task Group is to *assess and improve the understanding and prediction of aerothermodynamic phenomena and aerothermal loads for space transportation and earth/planetary entry systems through ground and flight experimentation*.

The following activities were undertaken by the group:

- Define data needed from ground-based and in-flight experiments for assessment/calibration of computational aerothermodynamic tools for space transportation and earth/planetary entry.
- Assess/document lessons learned from past ground-based experiments and demonstrator flights, including measurement uncertainties.
- Assess aerothermodynamic prediction tools using the available database and quantify simulation uncertainties. Identify gaps in the experimental database.
- Assess the current state of the art in measurement techniques for flight/ground experimentation for addressing critical aerothermodynamic phenomena.
- Where possible, conduct additional ground and flight experiments, with well-defined test conditions and measurement uncertainties. Pay special attention to address gaps.
- Where possible, conduct computational simulations for the experiments.
- Document both experimental and computational results and make recommendations for the future work.

To achieve the above, AVT-136 organized its efforts around the following six scientific topic areas broadly relevant to the development of planned hypersonic capabilities. Each topic area functioned as a semi-autonomous group by independently establishing a program of work consistent with the objective and defined activities of the Task Group. Contributions to the topic programs of work were organized and led by pairs, or in a few cases, individuals, who were recognized leaders in the area and capable of motivating the community to significant contributions. A summary of the topic areas is provided below.

Table 1-1: AVT-136 Scientific Topic Areas and Leadership.

Topic		Lead – Organization	Co-Lead – Organization
1	Nose and Leading Edges	Brian Hollis – NASA Langley	Salvatore Borelli – CIRA
2	Shock Interactions and Control Surfaces	Doyle Knight – Rutgers U.	Jose Longo – DLR
3	Shock Layer Properties and Radiation	Joe Olejniczak – NASA Ames	
4	Boundary Layer Transition	Steve Schneider – Purdue U.	
5	Gas/Surface Interactions	Georg Herdrich – U. Stuttgart	
6	Base and Afterbody Flows	Michael Wright – NASA Ames	Louis Walpot – AOES

To facilitate the development of scientific contributions to the six thrust topics, AVT-136 elected to structure the program of work to initially emphasize the assessment of numerical simulation capabilities through comparison with high-quality archival experimental data sets, although in several cases new experimental data was collected as part of the AVT-136 effort. After completion of the initial validation stage, numerical simulation capabilities were to then be extended to comparison with flight research data made available by the various flight research programs from the participating countries. A schematic illustrating how this process was planned for utilization in the Boundary Layer Transition topic is shown in Figure 1-2. After assessment of the capability of semi-empirical estimation methods to predict transition in well-characterized ground test experiments, the method was to be evaluated against a series of data from planned flight research efforts characterized by increasing three-dimensionality in both geometry and flow characteristics. The flight data was to be provided by the AFRL/DSTO HIFiRE 1 (axisymmetric geometry), NASA HyBoLT (flat with rounded sides) and HIFiRE 5 (elliptic cross-section) flight experiments. Unfortunately, unforeseen issues related to the availability of the flight research data prevented the Task Group from accomplishing this goal.

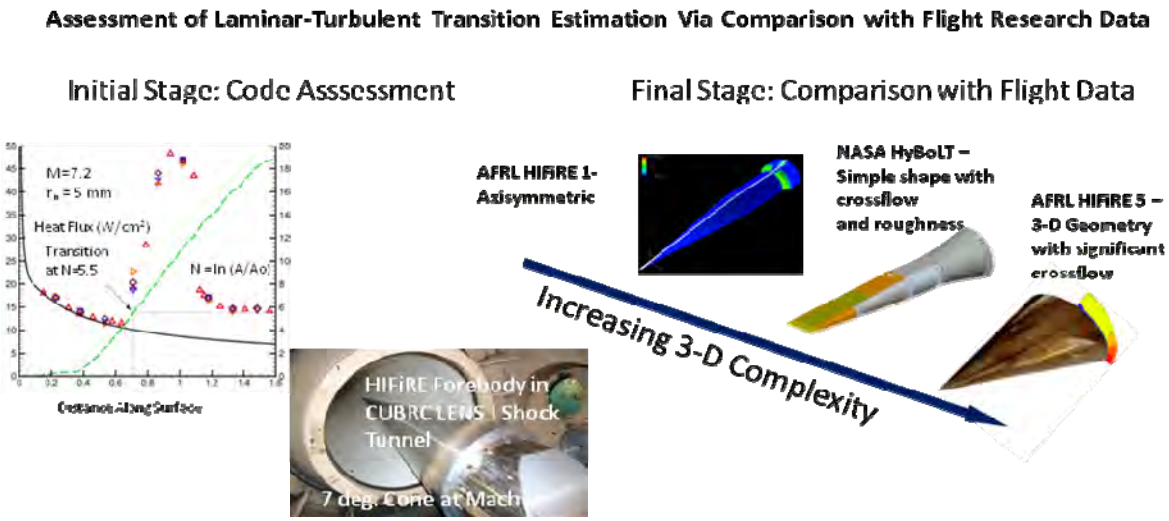

Figure 1-2: Example of the AVT-136 Planned Program of Work Comprised of Initial Code Assessment Followed by Comparison with Flight Research Data.

1.3 CHALLENGES ENCOUNTERED BY THE TASK GROUP

Although it was recognized from the onset of AVT-136 activities that reliance on flight research data yet to be collected posed significant risk to the achievement of Task Group objectives, the group concluded the significant benefit to be derived from comparison of computational simulations with flight data warranted pursuit of such a program of work. AVT-136 planned to acquire the following flight research data to facilitate accomplishment of the group objectives.

Table 1-2: Flight Research Data AVT-136 Planned to Utilize.

Flight Program	Agency	Flight Data to be Used by AVT-136
HIFiRE 1	AFRL/DSTO	- Boundary Layer Transition on cone forebody - Shock / Boundary Layer Interaction data generated by flare at aft of experiment
HyBoLT	NASA	- Boundary Layer Transition data
HIFiRE 5	AFRL/DSTO	- Boundary Layer Transition on elliptic shape

Unfortunately, both the HIFiRE and HyBoLT (Hypersonic Boundary Layer Transition) programs experienced significant technical difficulties that prevented AVT-136 from gaining access to the data. Following a series of unforeseen technical challenges associate with range access, telemetry and data acquisition issues, HIFiRE 1 is scheduled for launch in March, 2010, almost two years after it was originally planned. It is planned that the boundary layer transition and shock wave / boundary layer interaction flight data generated by HIFiRE 1 will eventually be provided to the research community for assessment of computational capabilities. As a result of the delays associated with HIFiRE 1, HIFiRE has also been pushed back beyond the scope of the AVT-136 effort. Finally, the HyBoLT experiment was launched aboard a developmental booster in August, 2008. The booster strayed from the planned trajectory and was destroyed on the ascent of the vehicle prior to achieving experimental conditions, resulting in no collection of experimental data.

AVT-136 keenly kept abreast of the developments associated with both the HIFiRE and HyBoLT programs. When it first became apparent that HIFiRE 1 was going to be delayed, a request for a one-year extension was made to the RTO AVT Panel. The request was granted and the Task Group proceeded with plans to quickly analyze the data when it finally became available. When HIFiRE 1 was delayed again in late 2008 it became apparent that flight data would not be available for use by AVT-136 and the group restructured its program of work to emphasize the comparison of numerical simulations with benchmark experimental data sets and eliminate plans to assess capabilities against flight data. Many members of the Task Group hope to eventually accomplish the flight data comparison goals, unfortunately, it will be outside the scope of the AVT-136 effort.

1.4 TASK GROUP CONTRIBUTIONS

Despite the unavailability of flight research data in accordance with the original AVT-136 program of work and the need to alter the program to emphasize the simulation assessment component, most of the scientific topic areas developed by the Task Group made significant progress in the assessment of current capabilities. The chapters following this introduction document the program of work and contributions of most of the topic areas and, thus, specific scientific conclusions and contributions will not be discussed here. However, it should be noted that the activities of AVT-136 generated substantial interest within the international scientific research community and the work of the Task Group was prominently featured in a total of six invited sessions dedicated to AVT-136 in the Sixth European Symposium on Aerothermodynamics for Space Vehicles and the 48th (2010) AIAA Aerospace Sciences Meeting. Section 6.4 of this report provides a list of the 33 conference papers presented by AVT-136 contributors at these two conferences.

1.5 SUMMARY OF TASK GROUP MEETINGS

A summary of the meetings of AVT-136 is presented in Table 1-3 below.

Table 1-3: Summary of Meetings of AVT-136.

Location	Date	Summary of Activity
Goettingen, GER	Spring 2006	Define PoW Technical Issues
Washington, DC	Fall 2006	Finalize PoW and Contributions
Florence, IT	Spring 2007	Review Progress on Contributions
NASA Ames	Fall 2007	Review Progress on Contributions
Loen, Norway	Spring 2008	Review Progress on Contributions
Versailles, FR	November 2008	Review Progress on Contributions
		6th European Aerothermodynamics Conf
VKI	July 2009	Review contents of draft final report
Orlando, FL	January 2010	Orlando AIAA Aerospace Sciences Meeting

1.6 REFERENCES

[1] Erbland, P., “Current and Near-Term RLV/Hypersonic Vehicle Programs”, RTO/AVT VKI Lecture Series on “Critical Technologies for Hypersonic Vehicle Development”, Brussels, Belgium, 10-14 May 2004.

[2] Muylaert, J., Kumar, A. and Dujarric, C., "Hypersonic Experimental and Computational Capability, Improvement and Validation", AGARD Advisory Report 319 (Final Report of AGARD Fluid Dynamics Panel's WG18), December 1998.

[3] "Technologies for Propelled Hypersonic Flight", NATO-RTO-AVT-WG10, 1998 – 2002.

Chapter 2 – SHOCK INTERACTIONS AND CONTROL SURFACES

Doyle Knight
Rutgers University
USA

Jose Longo
ESTEC
NETHERLANDS

2.1 INTRODUCTION

Renewed interest in hypersonic air vehicles such as the Boeing X-51 (Figure 2-1) has focused research on topics critical to hypersonic flight. The design of hypersonic air vehicles involves numerous engineering disciplines including aerothermodynamic analysis. In particular, the interaction of shock waves with the vehicle boundary layers can lead to regions of enhanced aerothermodynamic loading, and therefore accurate modeling of shock wave boundary layer interaction ("shock interactions") is essential.

Figure 2-1: Boeing X-51 Waverider.

During the past decade two NATO Research Technology Organisation (RTO) Working Groups (WGs) have assessed the capabilities for prediction of aerothermodynamic loads in high speed flight. AGARD Working Group 18 (WG18) examined the Computational Fluid Dynamics (CFD) capability for prediction of 2-D and 3-D perfect gas shock wave laminar and turbulent boundary layer interactions for three generic configurations: single fin (Figure 2-2), double fin (Figure 2-3) and hollow cylinder flare (Figure 2-4) [12]. The single and double fin configurations involved shock wave turbulent boundary layer interactions, while the hollow cylinder configuration included both laminar and turbulent shock boundary layer interactions. All cases were perfect gas flows. All turbulent flow simulations were performed using Reynolds-Averaged Navier-Stokes (RANS) models. The report concluded that laminar perfect gas shock interactions were accurately predicted. The report concluded that while turbulent perfect gas shock interaction predictions were accurate for 3-D mean pressure and primary separation locations, nevertheless the skin friction and heat transfer were poorly predicted.

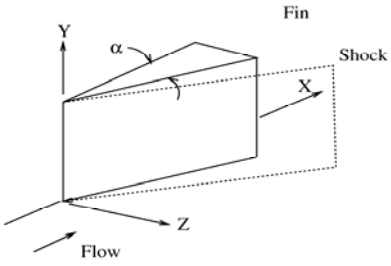

Figure 2-2: Single Fin.

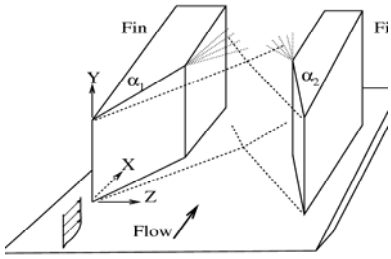

Figure 2-3: Double Fin.

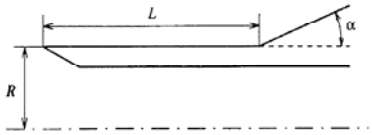

Figure 2-4: Hollow Cylinder.

RTO Working Group 10 (WG10) conducted a detailed examination of CFD capability for six areas relevant to hypersonic flight: boundary layer instability and transition, real gas flows, laminar hypersonic viscous-inviscid interactions, shock-shock interactions, shock wave-turbulent boundary layer interactions and base flows with and without plume interaction [13]. Sub-Group 3 of WG10 examined CFD capability for shock wave-turbulent boundary layer interactions focusing on five generic configurations: 2-D compression corner (Figure 2-5), 2-D compression-expansion corner (Figure 2-6), 2-D shock impingement (Figure 2-7), 3-D single fin (Figure 2-2) and 3-D double fin (Figure 2-3). All cases were perfect gas flows. All 2-D shock interaction flow simulations were performed using either Direct Numerical Simulation (DNS) or Large Eddy Simulation (LES) models, and all 3-D shock interaction flow simulations were performed using RANS methods. The report concluded that DNS and LES results for 2-D shock wave turbulent boundary layer interactions showed significant progress in predicting the flow; however, the Reynolds numbers of the simulations were relatively low due to computational resource requirements, and no comparison with experimental surface heat transfer measurements was performed. The report concluded that new RANS concepts for 3-D shock wave turbulent boundary layer interactions showed improvement in prediction of the flow; however, heat transfer was not accurately predicted.

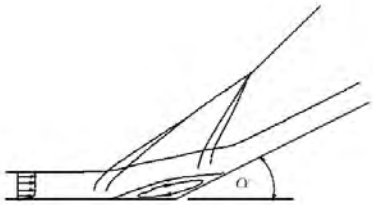

Figure 2-5: Compression Corner.

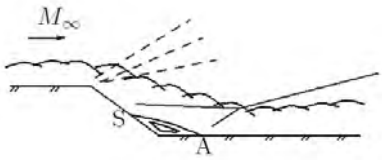

Figure 2-6: Compression-Expansion.

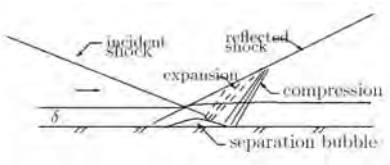

Figure 2-7: Shock Impingement.

RTO AVT Task Group 43 Topic No. 2 focuses on a further assessment of CFD for the specific issue of shock interactions and control surfaces in non-equilibrium flows. This report presents a comparison of computed and experimental results for two new configurations. The first configuration is a double cone (Figure 2-8) from CUBRC. The second configuration is a cylinder (Figure 2-9) from DLR. Experimental surface pressure and heat transfer data are available for two different enthalpy conditions under laminar flow conditions for each configuration, and constitute the primary measures for assessing the accuracy of the CFD simulations.

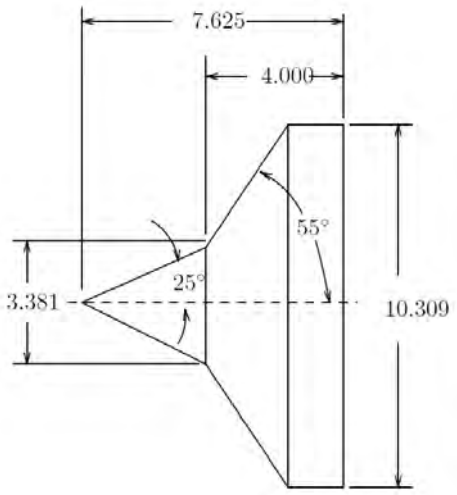

Figure 2-8: Double Cone.

Figure 2-9: Cylinder.

2.2 EXPERIMENTS

2.2.1 Double Cone

The experiments were conducted in the LENS I shock tunnel at CUBRC to obtain detailed surface and flow characteristics over a double cone configuration with semi angles of 25° and 55° and a base diameter of 10.3 inches (Figure 2-8). Measurements were made in nitrogen for total enthalpy conditions of 5.38 and 9.17 MJ/kg creating conditions with negligible dissociation. In allied studies, measurements were made to determine the velocity and NO concentration in the freestream for the airflows. The measured freestream velocity was in excellent agreement with non-equilibrium flow predictions using the nozzle code of Candler [3]. However, the measured NO concentration was measurably less than the predicted levels. The test conditions are shown in Table 2-1 where subscripts $_o$ and $_\infty$ represent reservoir and test section conditions, respectively. The values represent best estimates based on measurements made in the reservoir and freestream in flow calibration studies.

Table 2-1: Test Conditions for Double Cone.

Quantity	*Run 40*	*Run 42*	*Quantity*	*Run 40*	*Run 42*
h_o (MJ/kg)	5.38	9.17	T_∞ (K)	173	303
p_o (MPa)	17.3	17.9	$T_{\infty,vib}$ (K)	2735	3085
T_o (K)	4327	6611	$c[N_2]$	1.0000	0.9973
U_∞ (m/s)	3094	4065	$c[O_2]$	0.0000	0.0000
p_∞ (Pa)	129	121	$c[NO]$	0.0000	0.0000
ρ_∞ (kg/m^3)	$2.52 \cdot 10^{-3}$	$1.34 \cdot 10^{-3}$	$c[N]$	0.0000	0.0027
			$c[O]$	0.0000	0.0000

2.2.2 Cylinder

A test campaign [11] to investigate the flow past a cylindrical model was performed at the high enthalpy shock tunnel (HEG) of the German Aerospace Center (DLR). The cylindrical model, with a radius of 45 mm and a span of 380 mm, was mounted on the nozzle centerline with its axis transverse to the flow. It was equipped with 17 pressure transducers and the same number of thermocouples to measure surface pressure and heat flux distributions. The transducers were distributed along six rows located close to the plane of symmetry at the mid-span location (10, 20 and 30 mm to the left and right of the plane of symmetry, covering a circumferential angle of 60° with respect to the inflow direction).

The large shock stand-off distance of this configuration permits the application of optical measurement techniques for the determination of the gas properties in the shock layer. Holographic interferometry and time resolved Schlieren were applied to measure density distributions in the shock layer and the temporal evolution of the bow shock shape. Free stream static and Pitot pressures and stagnation heat transfer on a sphere were recorded at each run for calibration, normalization and statistical purposes.

The measurements on the cylinder were carried out at different total enthalpies (HEG conditions I and III, 22.4 MJ/kg and 13.5 MJ/kg, respectively) and with air as a test gas. The HEG reservoir and free stream data for the measurements are listed in Table 2-2.

Table 2-2: Test Conditions for Cylinder.

Quantity	*I*	*III*	*Quantity*	*I*	*III*
h_o (MJ/kg)	22.4	13.5	$p_{p\infty}$ (kPa)	52.9	70.8
p_o (MPa)	35.0	48.3	M_∞	8.98	8.78
T_o (K)	9200	7370	$c[N_2]$	0.7543	0.7356
U_∞ (m/s)	5956	4776	$c[O_2]$	0.00713	0.1340
p_∞ (Pa)	476	687	$c[NO]$	0.01026	0.0509
ρ_∞ (kg/m^3)	$1.547 \cdot 10^{-3}$	$3.26 \cdot 10^{-3}$	$c[N]$	$6.5 \cdot 10^{-7}$	0.0000
T_∞ (K)	901	694	$c[O]$	0.2283	0.07955

At the experimental conditions the flow in the shock layer is subject to non-equilibrium chemical relaxation processes that significantly affect the density distribution and hence the shock stand-off distance. Therefore, this test case represents a useful basis for the validation of the physico-chemical models used in CFD codes.

2.3 PARTICIPANTS

Computations of the double cone and cylinder were solicited from experts in the US and Europe. The participants are listed in Table 2-3. All aspects of the computations were determined individually by the participants including the selection of thermochemistry model, numerical algorithm, grid refinement study and convergence criteria. Details of the computations are presented in Section 2.4 organized by participant.

Table 2-3: Participants.

Name	*Organization*
Datta Gaitonde	Air Force Research Labs, Wright-Patterson AFB, OH, USA
Andrea Lani	Von Karman Institute for Fluid Dynamics, Brussels, Belgium
Dimitris Drikakis, Andrew Mosedale	Cranfield University, Cranfield, United Kingdom
Ioannis Nompelis	Dept Aerospace Engineering and Mechanics, Univ. of Minnesota, MN, USA
Bodo Reimann	German Aerospace Center (DLR), Braunschweig, Germany
Louis Walpot	Advanced Operations and Engineering Services, Netherlands

2.4 COMPUTATIONAL METHODS

2.4.1 Datta Gaitonde

All results were obtained with the GASP code. For the double cone cases, two grids were computed. The inviscid terms are discretized with the Roe scheme [26], extended to include high-temperature effects [21], and combined with the third-order upwind-biased MUSCL approach and the van Albada limiter. Viscous terms were computed in a centered fashion. The solution was marched in time with an implicit dual-stepping time-accurate algorithm. The simulation assumes fully catalytic walls with the Park I model which considers vibrational relaxation but neglects ionization [24]. Radiation has been ignored in all calculations.

For the cylinder cases, the flow was simulated in both 3-D and 2-D (centerplane) but assuming horizontal symmetry. The 3-D slice corresponding to the spanwise center of the cylinder shows essentially the same result as the 2-D computation. The inviscid terms are discretized with the AUSM+ method [17] combined with the third-order upwind-biased MUSCL approach and the minmod limiter. Viscous terms were computed in a centered fashion. The solution was marched in time with an implicit dual-stepping time-accurate algorithm. The simulation assumes fully catalytic walls with the Park I model which considers vibrational relaxation but neglects ionization [24]. Radiation has been ignored in all calculations.

2.4.2 Andrea Lani

The double cone Run 40 and Cylinder (I and III) test cases were computed with a parallel implicit cell-centered Finite Volume solver for unstructured meshes [16] implemented within the COOLFluiD collaborative software environment [14], [15], [16], [27]. In particular, we have used a modified AUSM+ scheme [16], [17] in combination with a multi-dimensional weighted least square reconstruction [1] and Venkatakhrisnan's limiter [29]. The results for double cone Run 42 have been computed with a parallel implicit vertex-centered Conservative Residual Distribution solver [4], [16] again implemented in COOLFluiD [16]. In particular, the second order accurate blended Bxc scheme has been employed [5]. In Runs 40 and 42, the flow is modeled as a neutral nitrogen mixture (N_2-N) in thermo-chemical non-equilibrium with a two temperature model. The corresponding reaction rate coefficients are given in Nompelis [22]. A three temperature model (including roto-translational *T*, vibrational temperatures of N_2 and O_2) has been applied to the cylinder test cases. In this case, the flow is treated as a five species air mixture with reaction rate coefficients given by Park [25]. More details about the modeling of transport, thermodynamics, chemistry and energy relaxation can be found in [16], [19] and [23].

2.4.3 Dimitris Drikakis, Andrew Mosedale

The computations at Cranfield University were performed using the code CNS3D [6], [7], [8]. The code comprises a library of numerical methods, including second- and fifth-order MUSCL schemes with low-Mach corrections and very high-order WENO schemes up to ninth-order accurate, for spatial discretization. The time integration is obtained by TVD Runge-Kutta schemes, third- and fifth-order accurate. The code can be used for Unsteady Reynolds-Averaged Navier-Stokes (URANS) and Implicit Large Eddy Simulations (ILES). CNS3D is fully parallelized using MPI systems and has been ported onto several high-performance computing facilities including Cranfield's 7.8 Tflops machine and the United Kingdom's national HPCx among others. The code employs the two temperature model by Park for non-equilibrium thermochemistry assuming that the translational and rotational modes of energy as well as the vibrational and electronic modes of energy are in equilibrium. Other capabilities of the code include ablation modeling, coupling of solid and fluid mechanics as well as coupling of molecular dynamics with CFD.

2.4.4 Ioannis Nompelis

The Navier-Stokes equations with chemistry are solved for a mixture of perfect gases that is in non-equilibrium. We solve a separate conservation equation for each of the five species and Park's rates are used as well as Park's TTv model for vibration-dissociation coupling [24]. A separate vibrational energy equation for the mixture is solved together with the momentum and total energy equations. A Simple Harmonic Oscilator (SHO) model is used, assuming that all vibrational models are in equilibrium. The Landau-Teller model [30] with Millikan and White [20] rates is employed for energy relaxation. The equations are solved with a finite volume code that uses the modified Steger-Warming flux splitting [18]. To achieve second order spatial accuracy a MUSCL [9] extrapolation is done to the primative variables. The viscous fluxes are evaluated with a finite difference form and viscosity coefficients are calculated from Blottner fits [2] with Wilke's mixing rule for the mixture. The equations are integrated with a fully implicit line-relaxation method [31].

2.4.5 Bodo Reimann

The flow solver is the DLR TAU code [28]. The Reynolds-averaged Navier-Stokes equations are discretized by a finite volume scheme. The AUSMDV second order upwind scheme with MUSCL reconstruction is used for the inviscid fluxes. For time discretization, local and dual time stepping, with a three-stage Runge-Kutta method, as well as an implicit, approximately factored LU-SGS scheme have been used. For acceleration, multi-grid and explicit residual smoothing are available. Furthermore, parallel computing is possible via domain splitting and Message Passing Interface (MPI) communication. To model the thermochemical behavior of the flow, the Gupta et al. [10] five species chemical non-equilibrium model was applied to the cylinder case. For the double cone case, the reaction rates for nitrogen given by Park [25] have been used. Thermal non-equilibrium is accounted for by a two temperature model according to Park. The relaxation of the vibrational energy of the nitrogen molecules is described by a Landau-Teller formulation using the Millikan-White relaxation times. The structured cylinder grid has 49 x 93 x 121 grid points. The grid is refined at the location where the shock is expected. For the double cone the fine mesh with 1024 x 513 grid points given by Nompelis is used.

2.4.6 Louis Walpot

The full unsteady laminar Navier-Stokes equations are solved using a finite volume algorithm. The double cone computations assume a two species (N_2 and N) mixture, and the cylinder computations assume a five species (N_2, O_2, NO, N, O) mixture. Viscosity is specified using Wilke's Mixing Rule. A two temperature thermochemistry model is utilized. The algorithm is second order accurate. Van Albada limiter is used.

2.5 RESULTS

2.5.1 Flowfield Structure

The structure of the double cone flowfield for the cases considered is illustrated in Figure 2-10. The first cone generates an incident shock wave which is close to the cone surface. The incident shock interacts with the shock wave generated by the second cone to form a shock-shock interaction. The impingement of the incident shock upon the cone surface causes a rapid pressure rise and concommitant separation. A recirculation region forms with separation and reattachment points. The increase in displacement thickness caused by the separation region induces the formation of a separate separation shock. The separation point is indicated in the experiment by a rapid decrease in heat transfer, and similarly the reattachment point is identified by a rapid increase in heat transfer. The separation region is identified by a plateau in surface pressure.

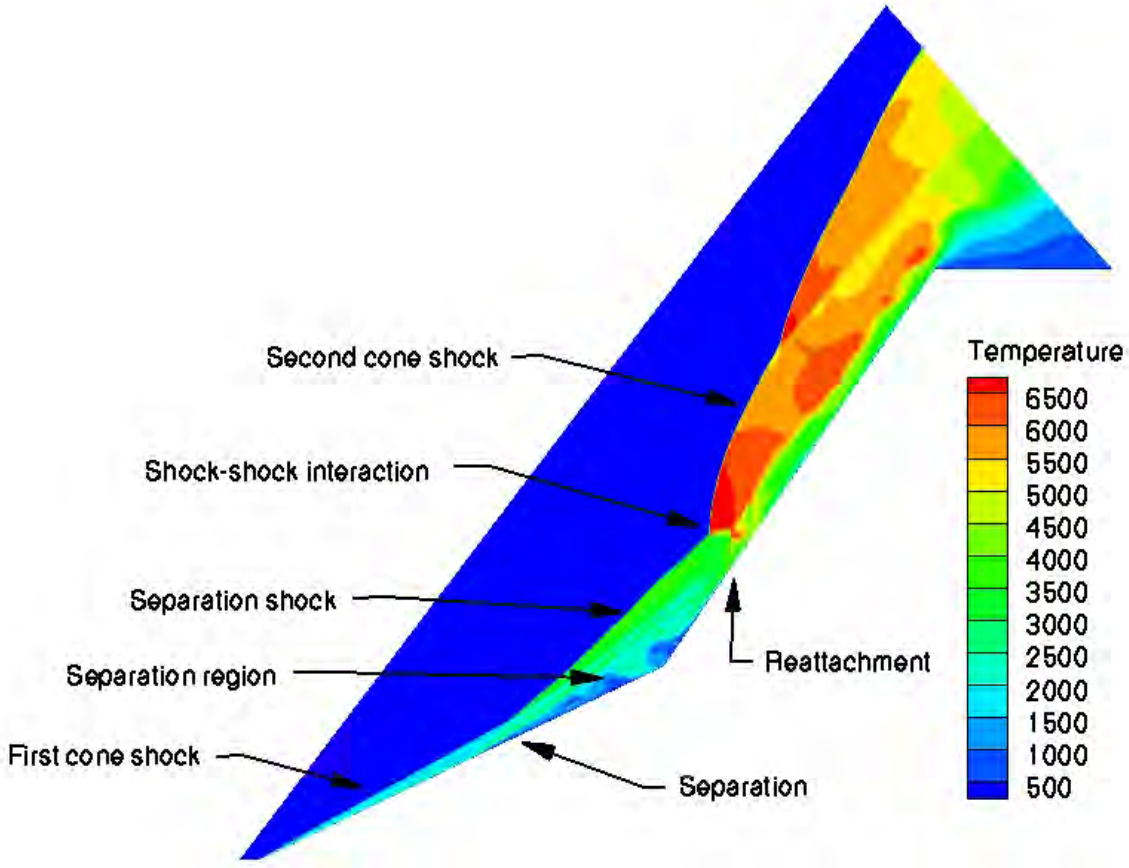

Figure 2-10: Double Cone Flowfield Structure (from Gaitonde).

The structure of the cylinder flowfield in the symmetry (center) plane is illustrated in Figure 2-11. The blunt body shock wave and streamlines are indicated. The stagnation point corresponds to the maximum surface pressure and heat transfer. The flow in the shock layer experiences significant non-equilibrium chemical and thermal relaxation processes which influences the shock stand-off distance.

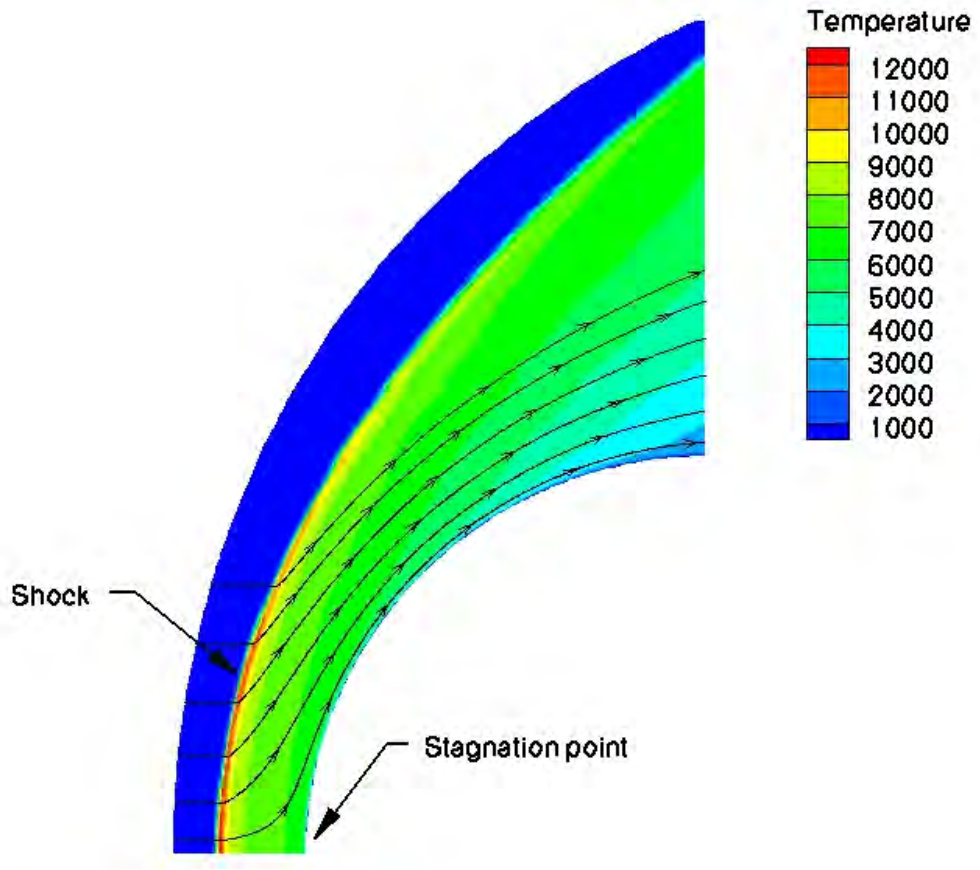

Figure 2-11: Cylinder Flowfield Structure (from Gaitonde).

2.5.2 Double Cone

2.5.2.1 Run 40

The computed surface pressure is compared with experiment in Figure 2-12 to Figure 2-17. The results of Gaitonde (Figure 2-12), Nompelis (Figure 2-15) and Walpot (Figure 2-17) indicate strong unsteadiness in the flowfield with a strongly unsteady separation region at the corner. Gaitonde, Nompelis and Walpot observed that their computations did not achieve steady state. The results of Lani (Figure 2-13), Drikakis et al. (Figure 2-14) and Reimann (Figure 2-16) are instantaneous “snapshots” of the surface pressure. In private communication, all three indicated that the computed flowfield was unsteady and did not achieve a steady state. The computed surface heat transfer is compared with experiment in Figure 2-18 to Figure 2-23. The results of Gaitonde (Figure 2-18), Nompelis (Figure 2-21) and Walpot (Figure 2-23) show similar unsteadiness as expected from the surface pressure computations. The results of Lani (Figure 2-19), Drikakis et al. (Figure 2-20) and Reimann (Figure 2-22) are instantaneous “snapshots” as previous.

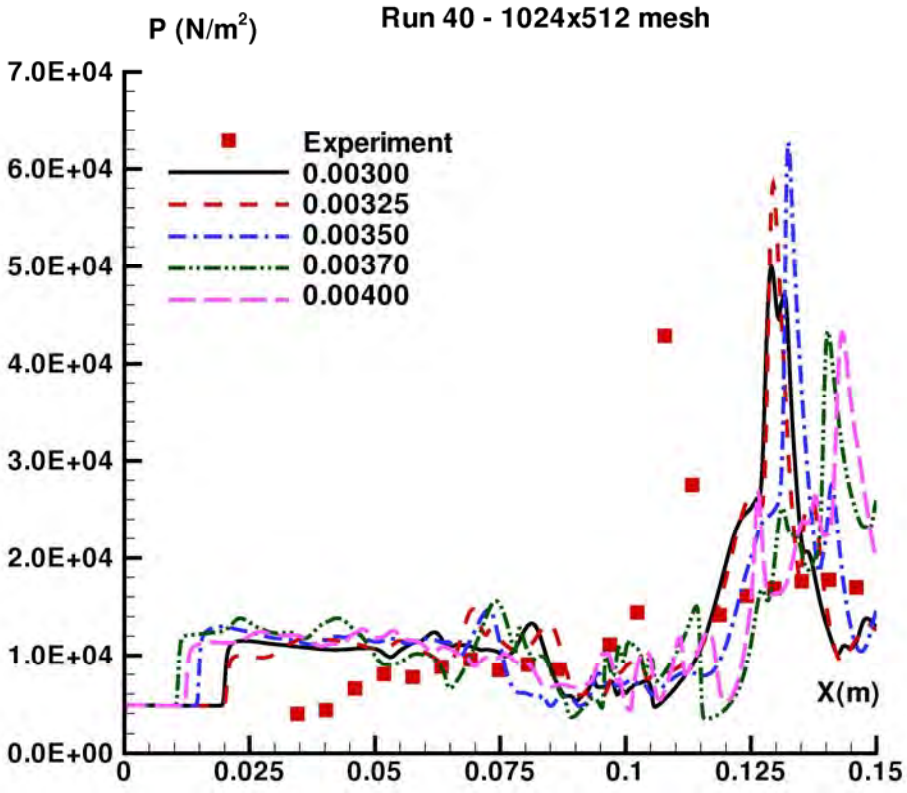

Figure 2-12: p_w for Run 40 (Gaitonde) [Time counter is notional and does not represent absolute time].

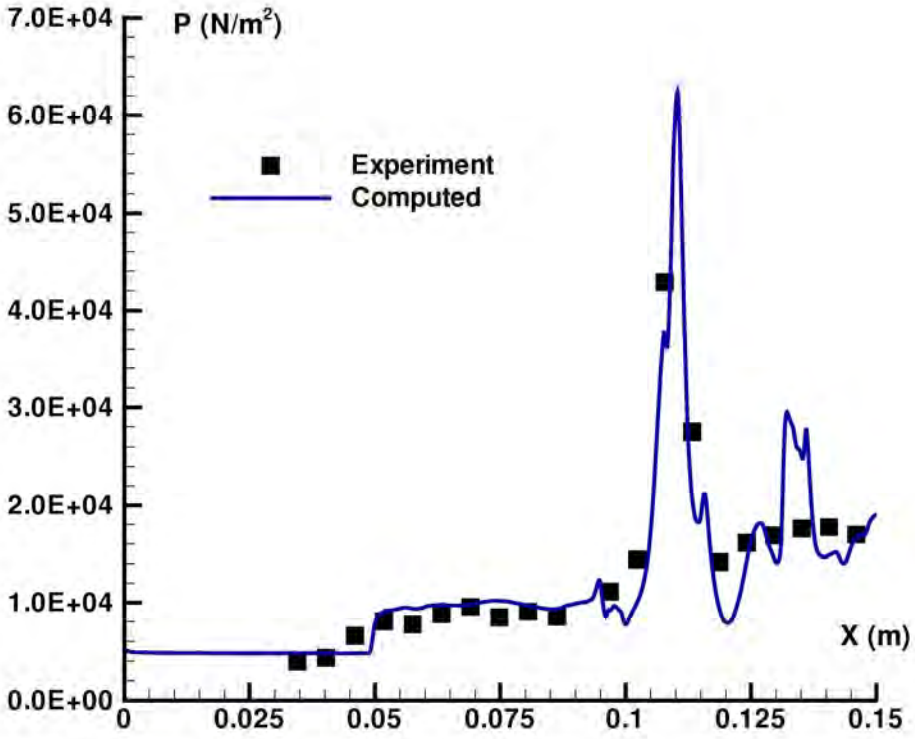

Figure 2-13: p_w for Run 40 (Lani).

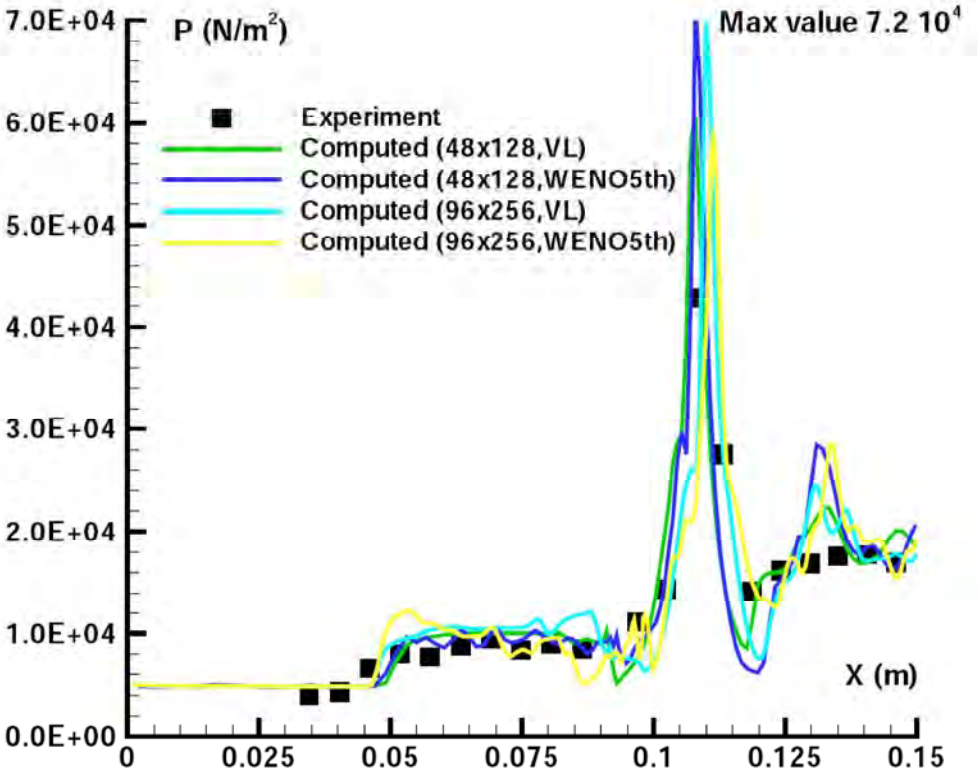

Figure 2-14: p_w for Run 40 (Drikakis et al.).

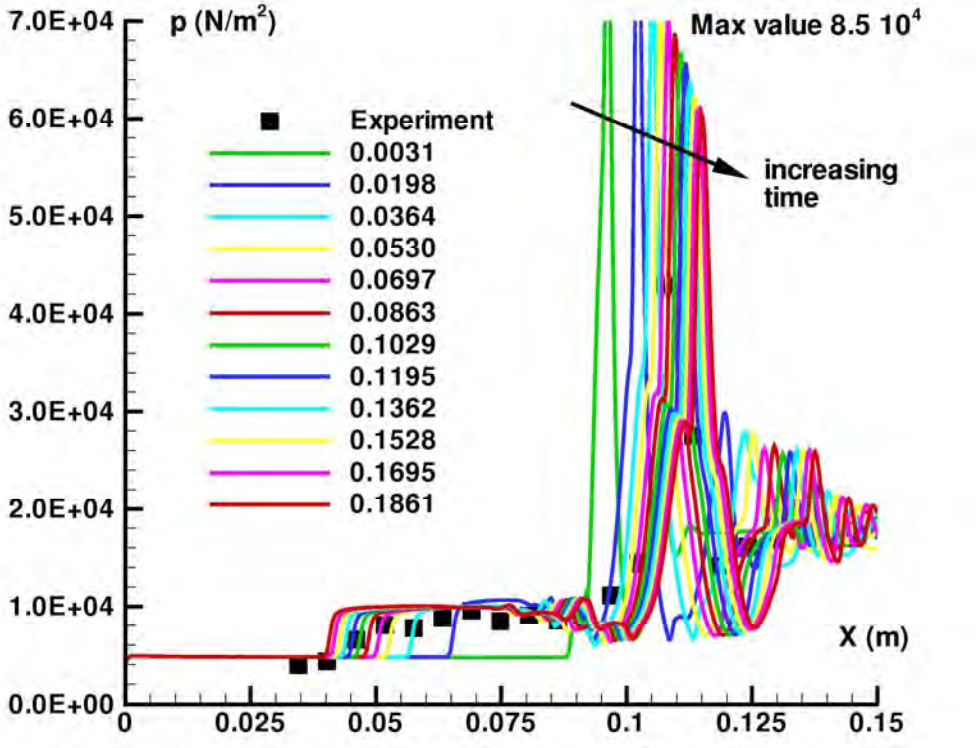

Figure 2-15: p_w for Run 40 (Nompelis).

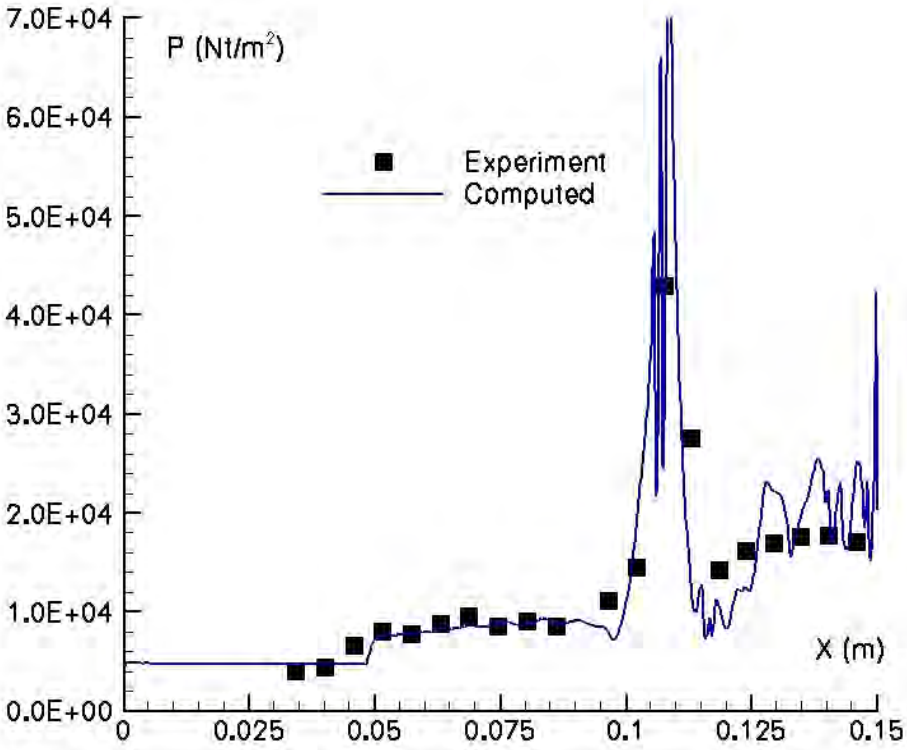

Figure 2-16: p_w for Run 40 (Reimann).

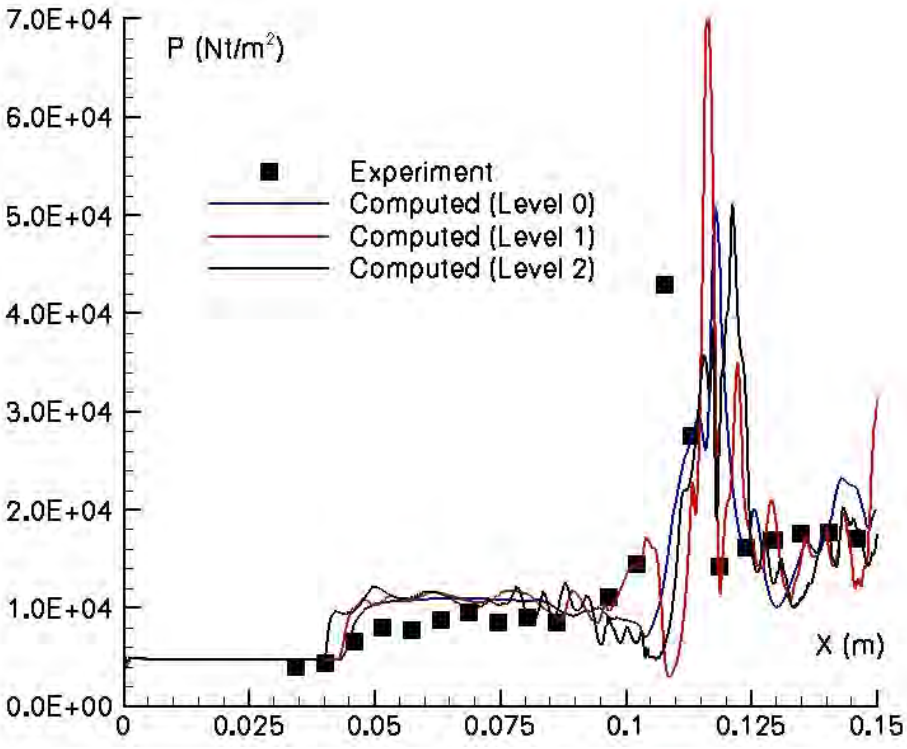

Figure 2-17: p_w for Run 40 (Walpot).

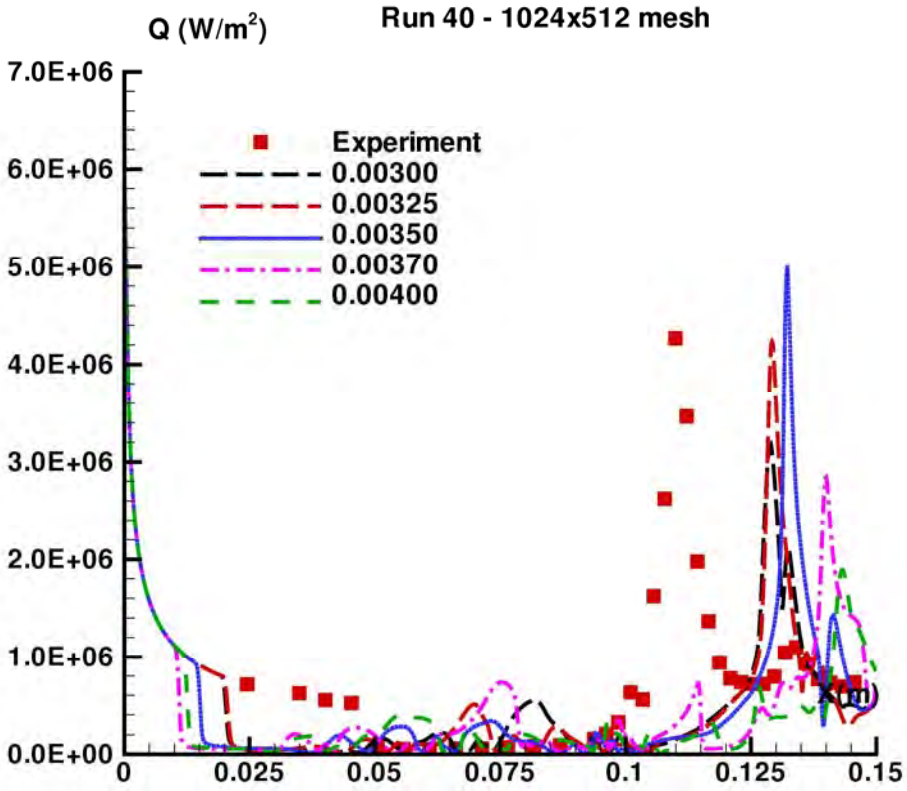

Figure 2-18: q_w for Run 40 (Gaitonde) [Time counter is notional and does not represent absolute time].

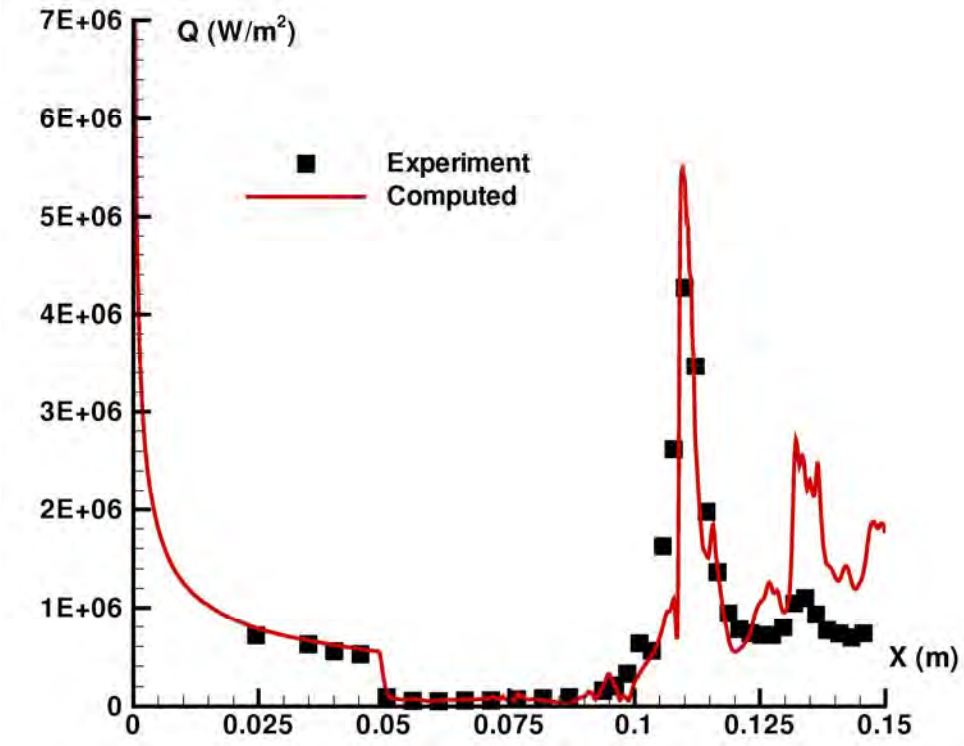

Figure 2-19: q_w for Run 40 (Lani).

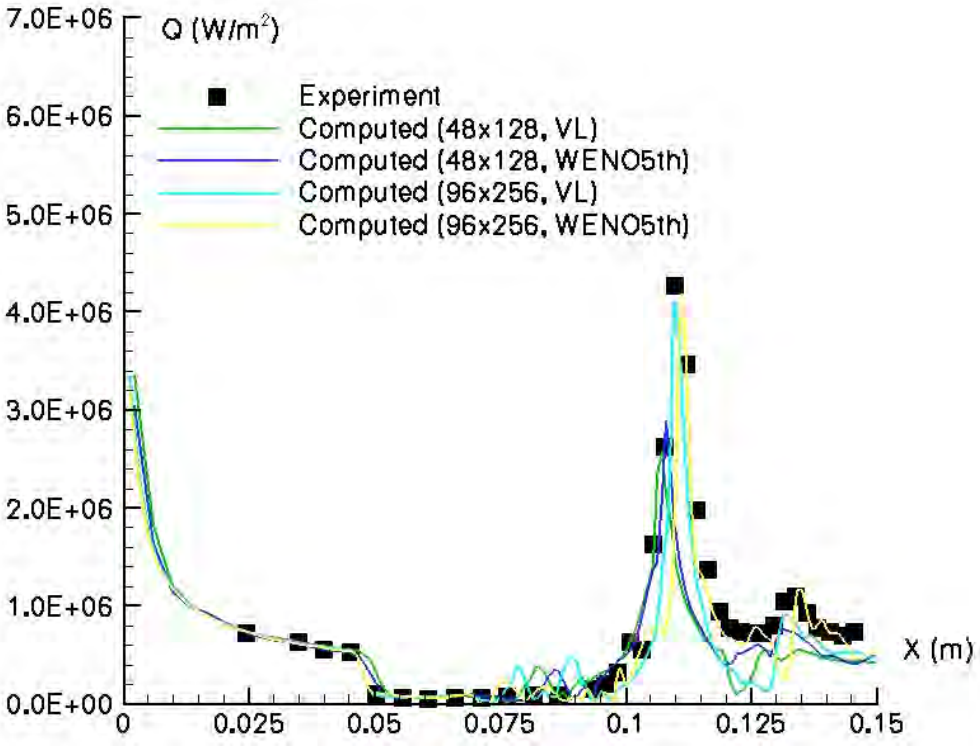

Figure 2-20: q_w for Run 40 (Drikakis et al.).

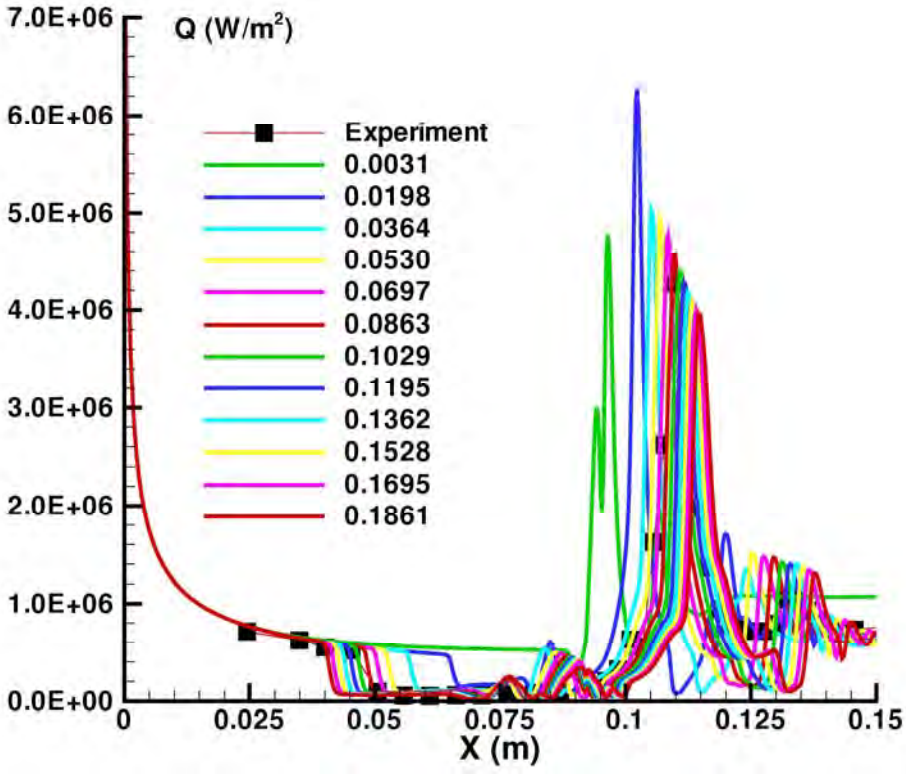

Figure 2-21: q_w for Run 40 (Nompelis).

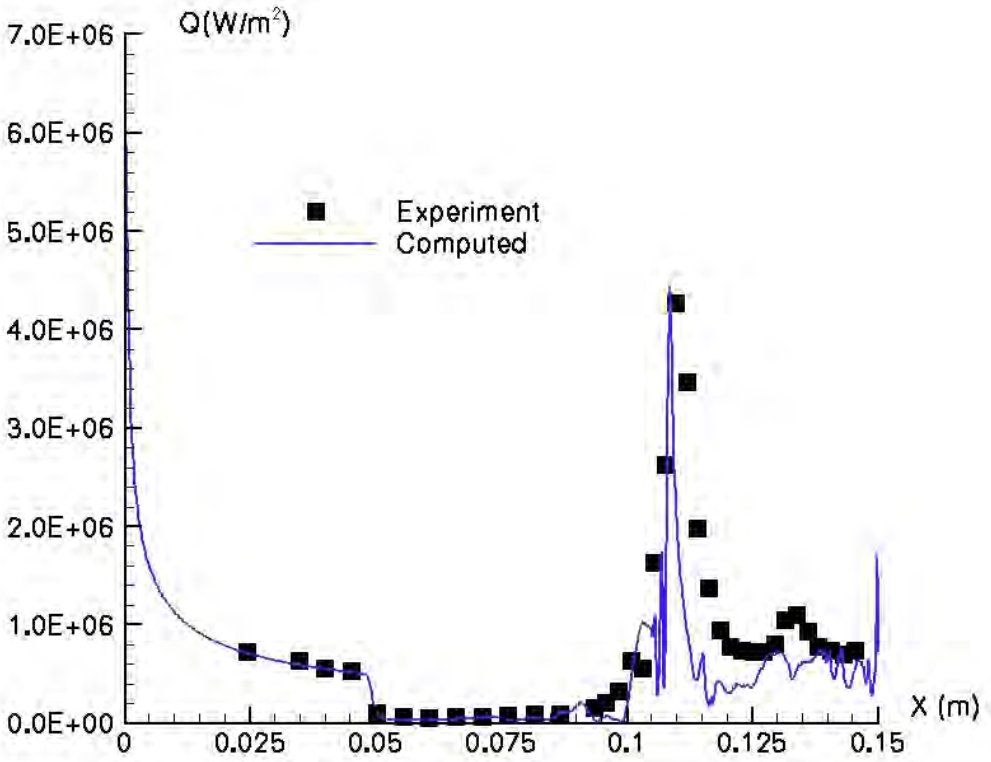

Figure 2-22: q_w for Run 40 (Reimann).

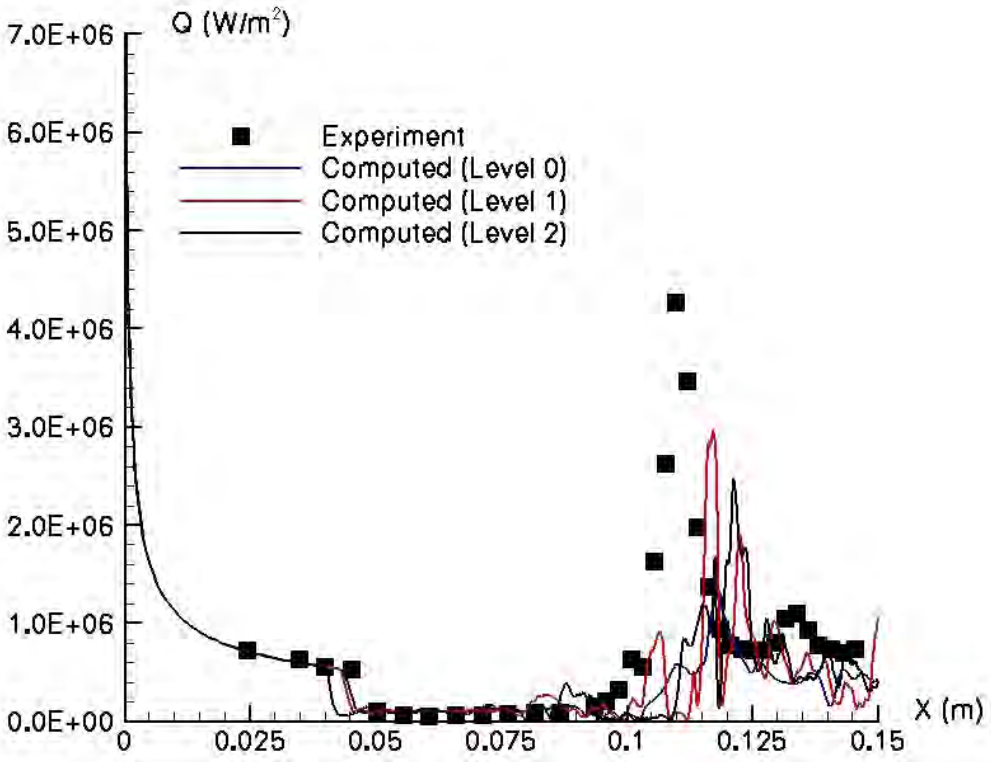

Figure 2-23: q_w for Run 40 (Walpot).

The substantial unsteadiness observed in all computations is in direct contrast to the experimental measurements of surface pressure and heat transfer which indicated a steady flowfield had been achieved. There is no clear explanation for this disagreement between the computations and experiment. It is certainly not attributable to a particular numerical flux algorithm since a variety of different algorithms were used. Also, it is certainly not attributable to a particular grid since several different grid convergence studies were performed by the participants. It may be conjectured that the particular inflow conditions, coupled with the double cone geometry, are close to a configuration of instability and the computations have tended towards this unsteady solution. Further computations and experiments are needed to assess this conjecture.

2.5.2.2 Run 42

The computed surface pressure is compared with experiment in Figure 2-24 to Figure 2-29. All participants observed that the computed flowfield achieved steady state. The location of upstream propagation of the surface pressure (x = 0.050 m) is accurately predicted by the fine grid solution of Gaitonde (Figure 2-24) and the computation of Drikakis et al. using a 5th order WENO scheme (Figure 2-26). All other solutions predict a pressure rise downstream of the experimental location. The plateau pressure associated with separation region (x = 0.05 m to 0.10 m) is accurately predicted by all participants. All computations accurately predict the location of the beginning of the second pressure rise. It is, of course, not necessarily evident that the peak experimental pressure measurement corresponds to the peak surface pressure since the pressure gradient is very large and the surface pressure transducer has finite size. Therefore, it is only possible to assess whether or not the computed peak surface pressure equals or exceeds the experimental value, since an under-prediction of peak surface pressure would indicate a shortcoming in the computation, while a peak computed surface pressure exceeding the peak measured surface pressure may in fact be accurate. Some discrepancies between computations and experiment in the expansion region (x = 0.115 m to 0.125 m) are evident. The computed secondary plateau pressure (x > 0.130 m) appears accurately predicted in all cases.

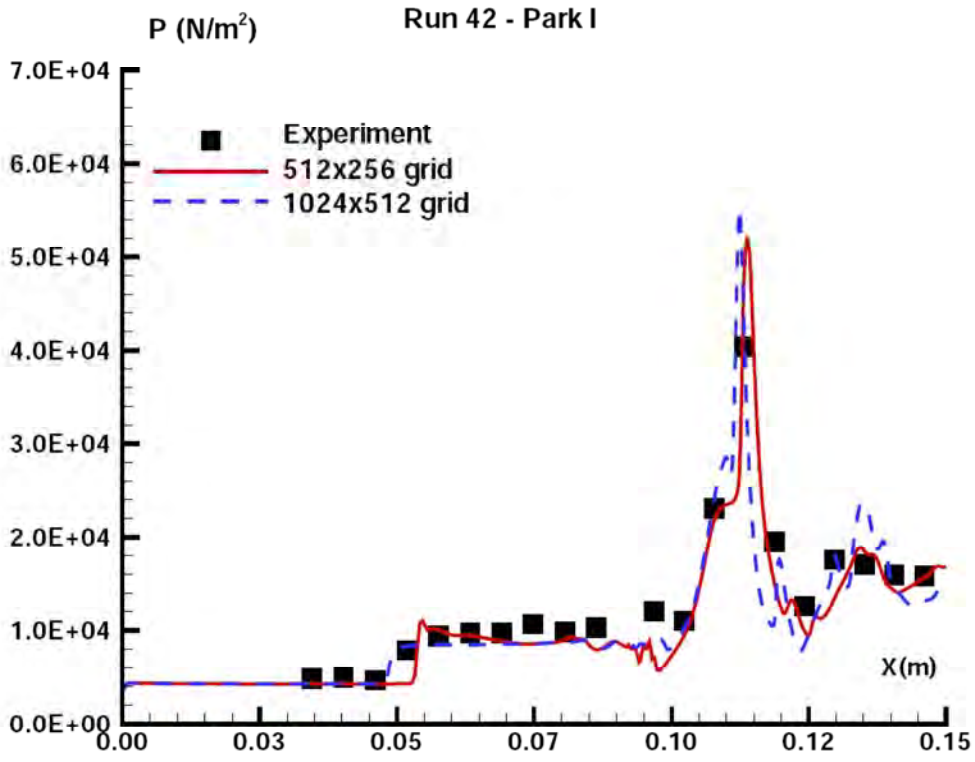

Figure 2-24: p_w for Run 42 (Gaitonde).

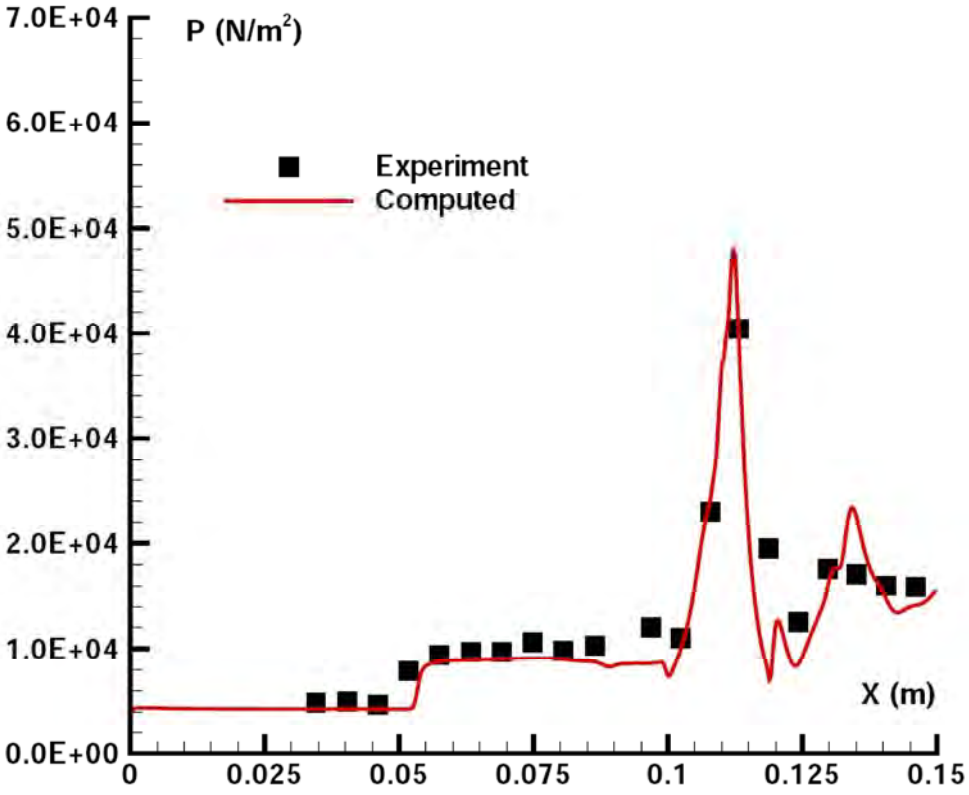

Figure 2-25: p_w for Run 42 (Lani).

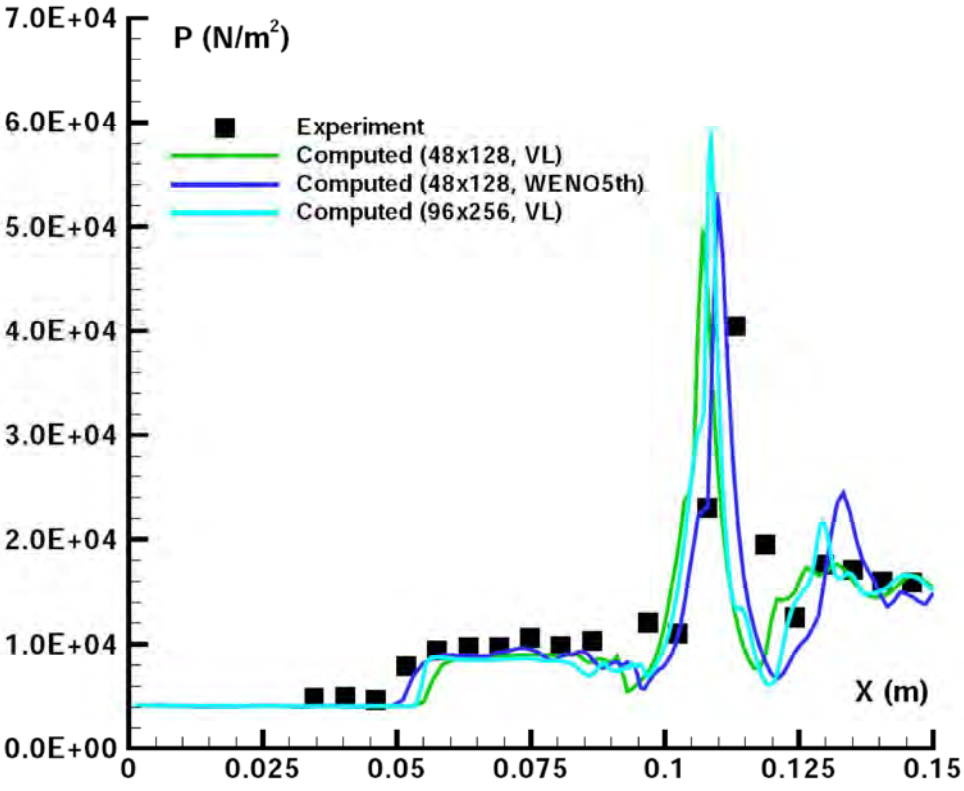

Figure 2-26: p_w for Run 42 (Drikakis et al.).

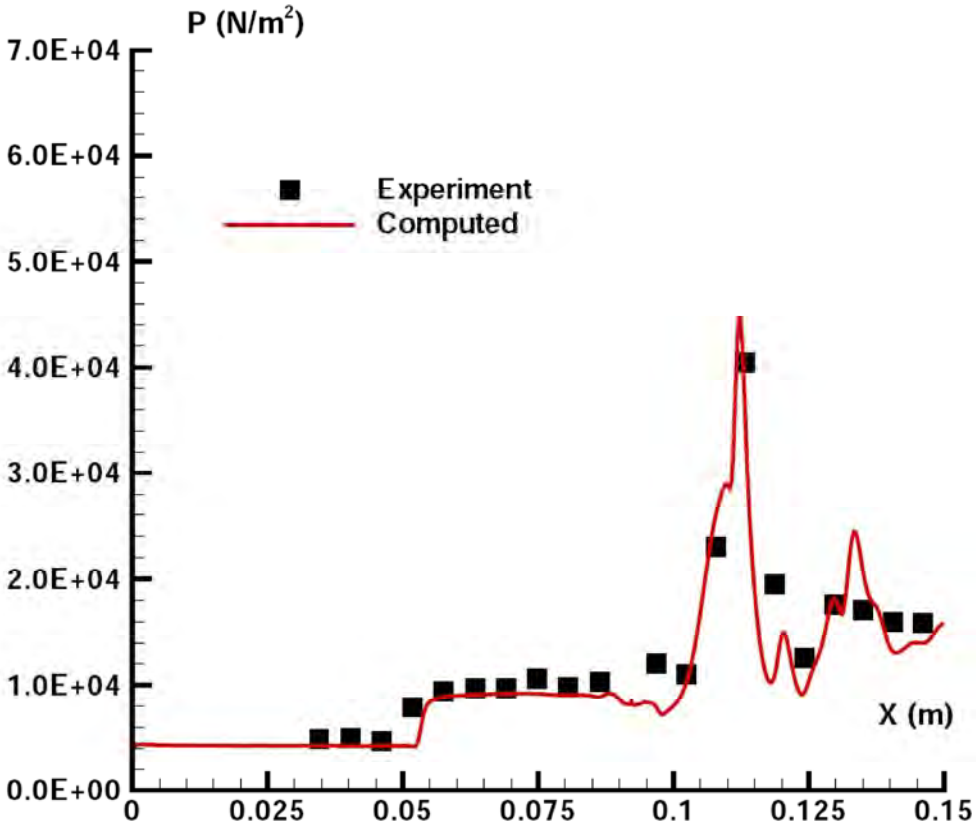

Figure 2-27: p_w for Run 42 (Nompelis).

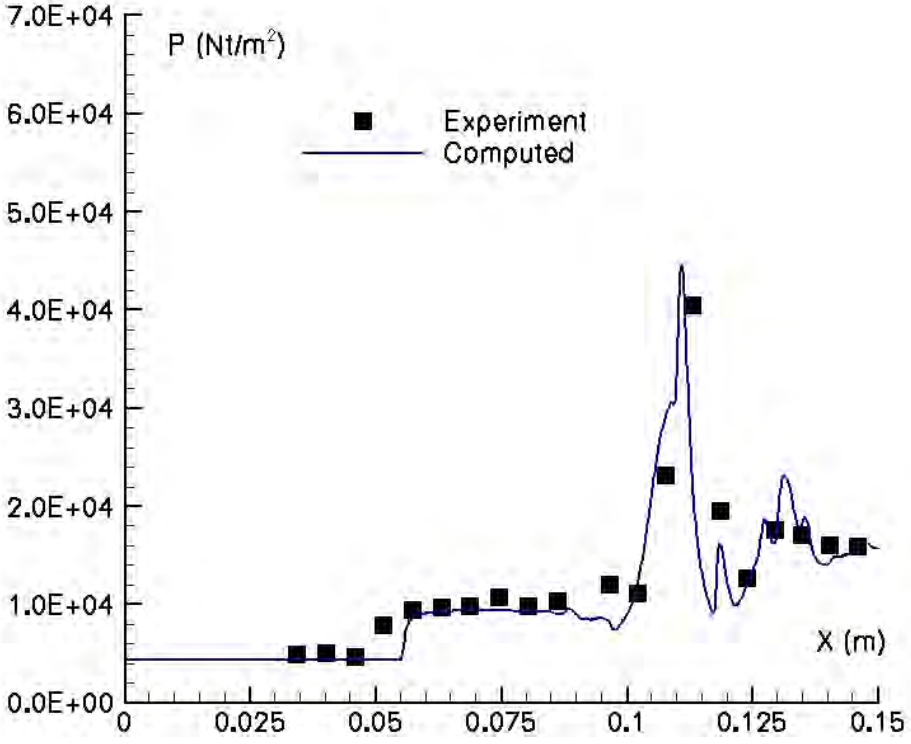

Figure 2-28: p_w for Run 42 (Reimann).

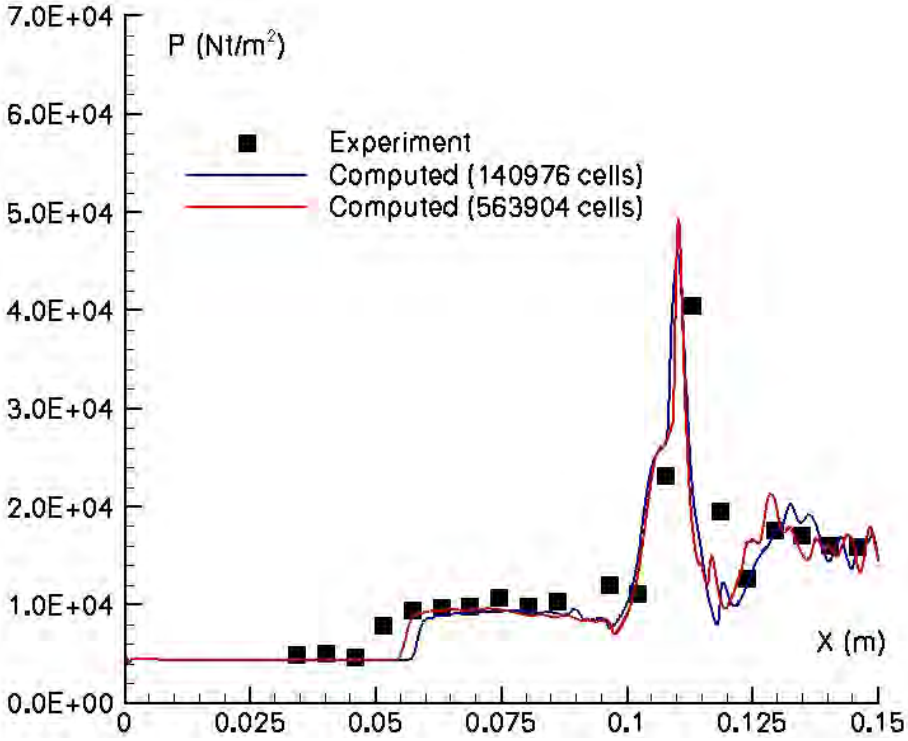

Figure 2-29: p_w for Run 42 (Walpot).

The computed surface heat transfer is compared with experiment in Figure 2-30 to Figure 2-35. The heat transfer upstream of the separation at x = 0.055 m is accurately predicted by all participants. The refined grid (1024 x 512) computation by Gaitonde (Figure 2-30) and the computation of Drikakis et al. using a 5th order WENO scheme (Figure 2-32) show separation at x = 0.050 m while all other solutions show separation at the experimental position (for the finer grid in Figure 2-35). This observation is interesting since these are the two solutions which more closely match the experimental pressure distribution as discussed above. All computations show good agreement with the low level of heat transfer in the separated region, and reasonable agreement with the location of the heat transfer rise at x = 0.105 m. Analogous to the previous discussion regarding peak surface pressure, it is only possible to assess whether or not the computed peak heat transfer equals or exceeds the experimental value. In this regard, the computations of Nompelis (Figure 2-33) and Reimann (Figure 2-34) under-predict the peak experimental heat transfer by 14%, and the fine grid computation by Walpot (Figure 2-35) by 5%.

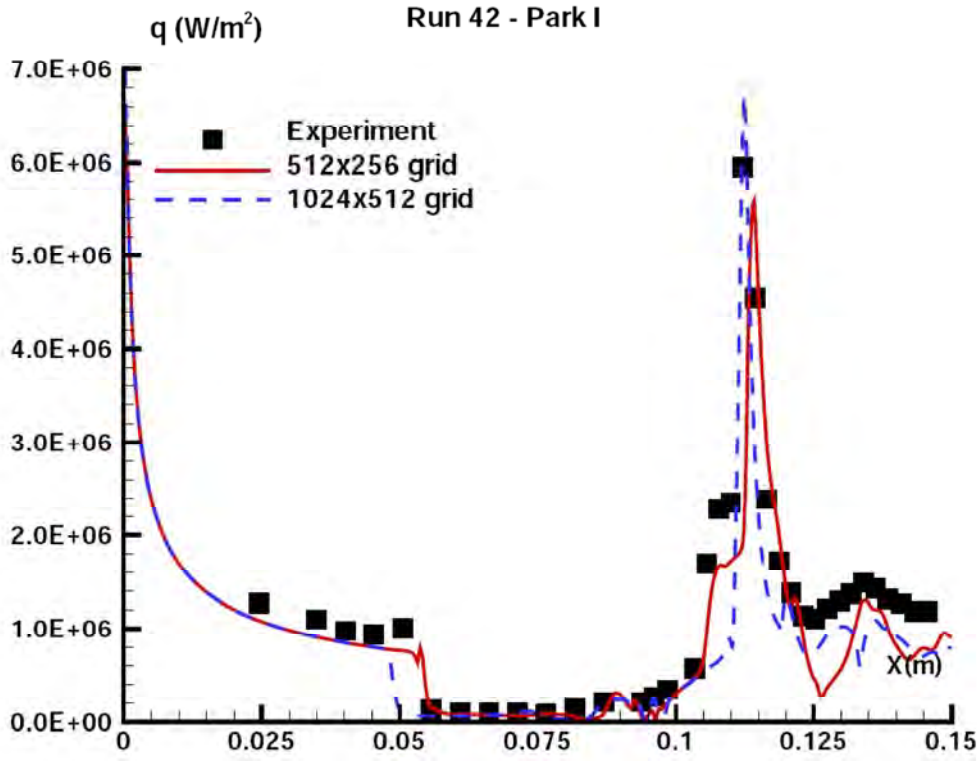

Figure 2-30: q_w for Run 42 (Gaitonde).

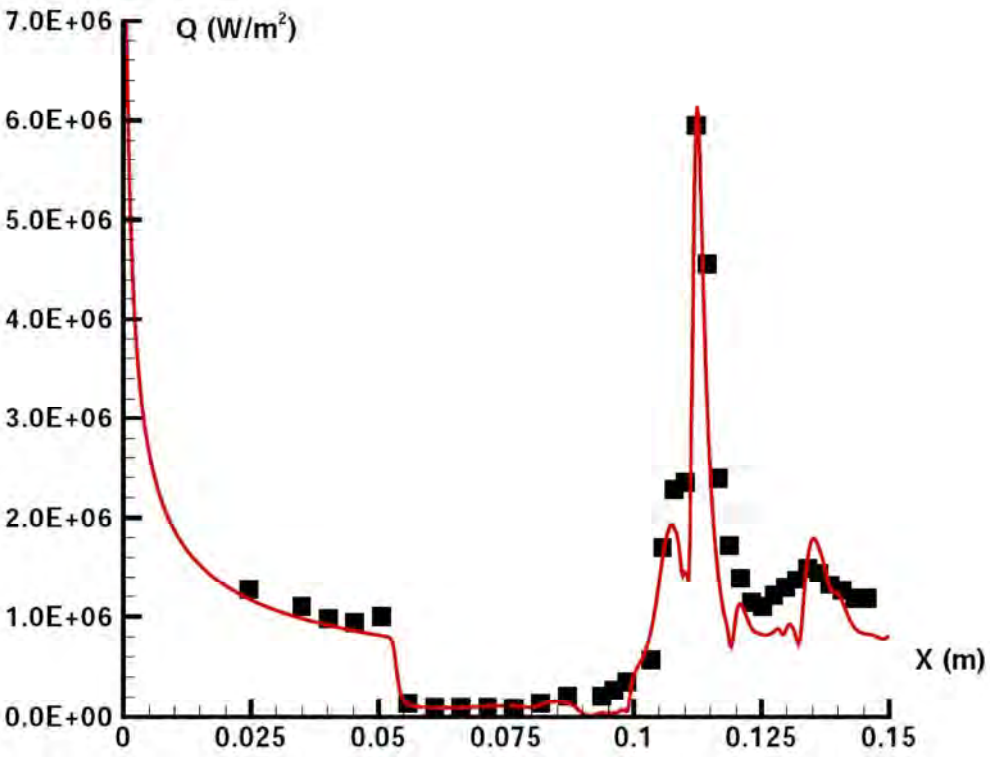

Figure 2-31: q_w for Run 42 (Lani).

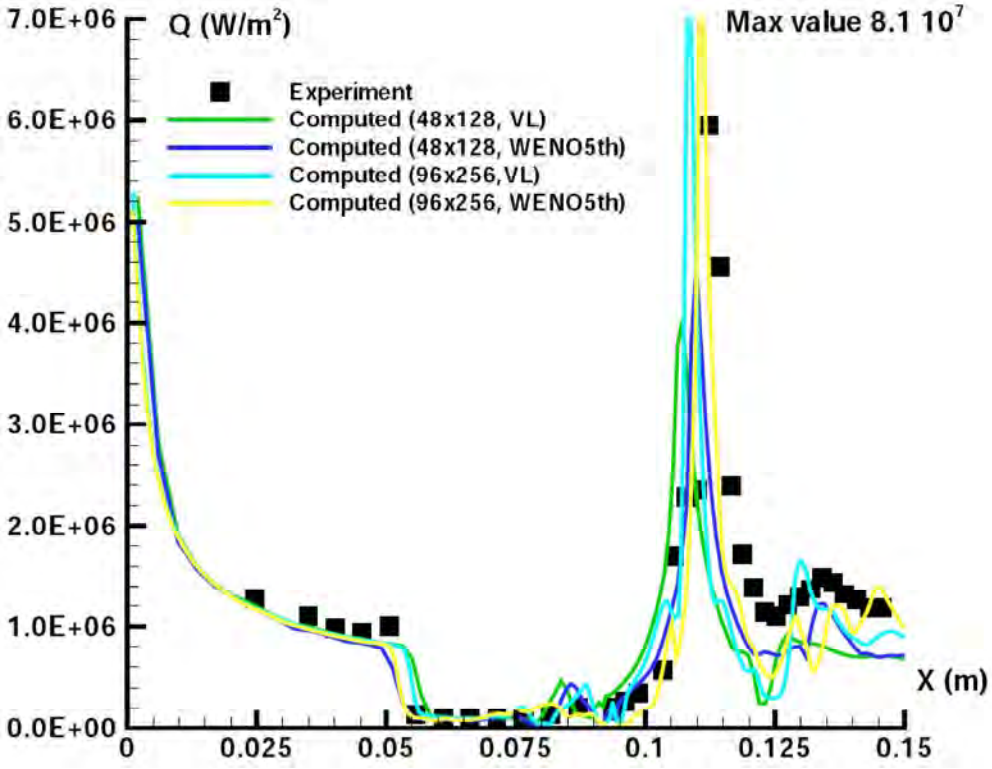

Figure 2-32: q_w for Run 42 (Drikakis et al.).

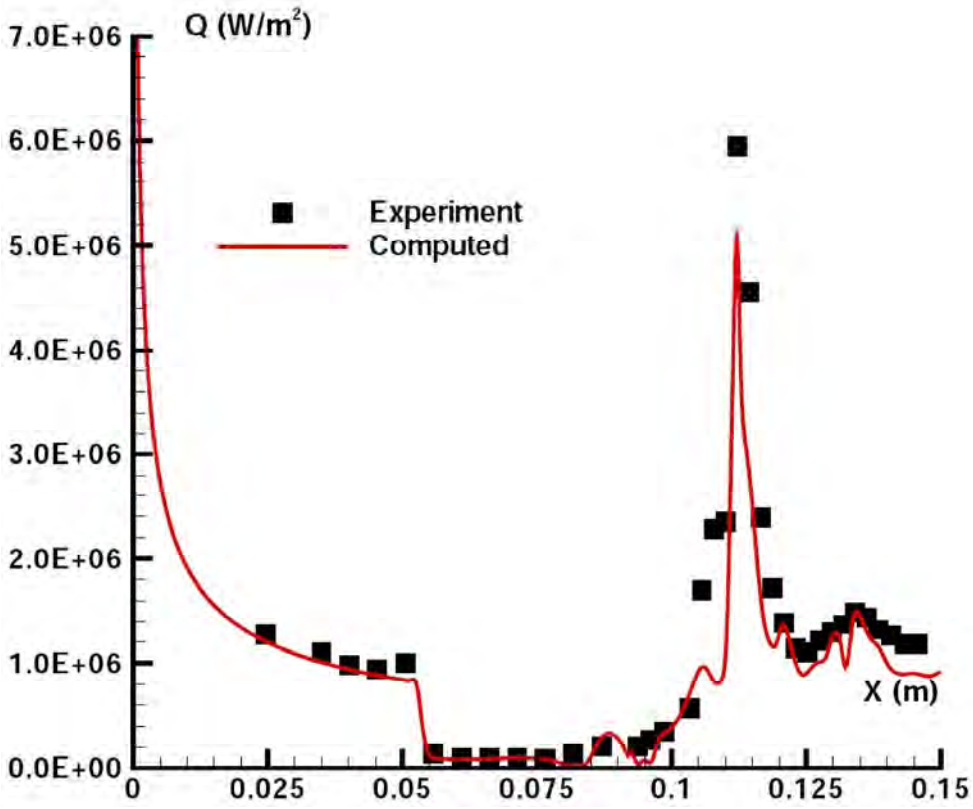

Figure 2-33: q_w for Run 42 (Nompelis).

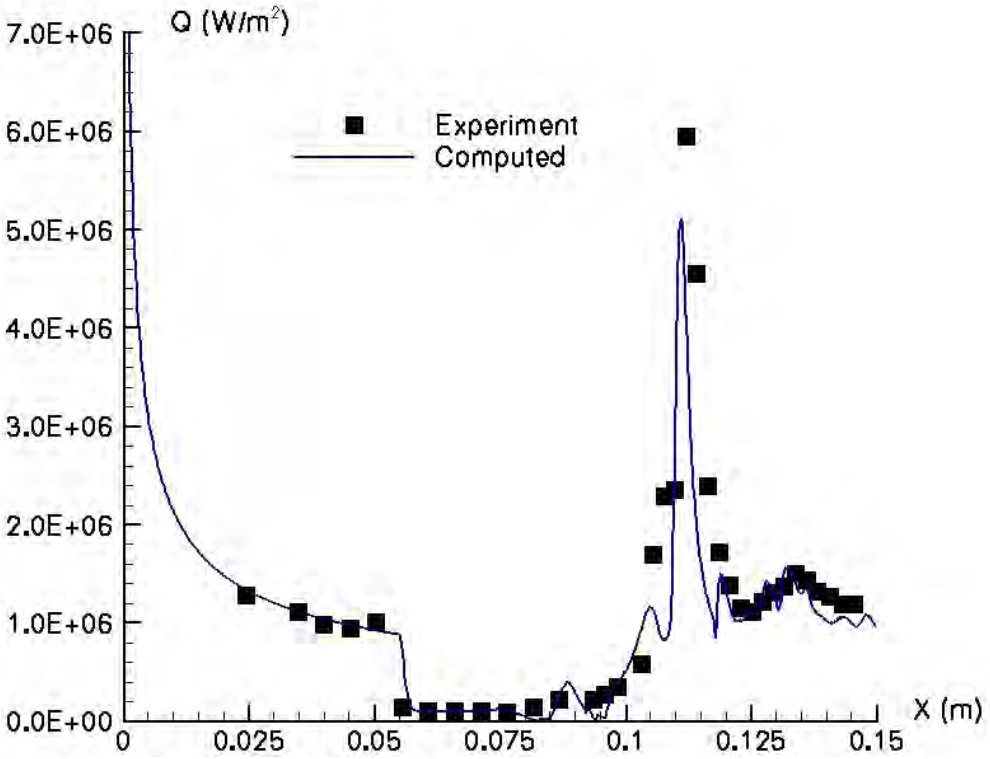

Figure 2-34: q_w for Run 42 (Reimann).

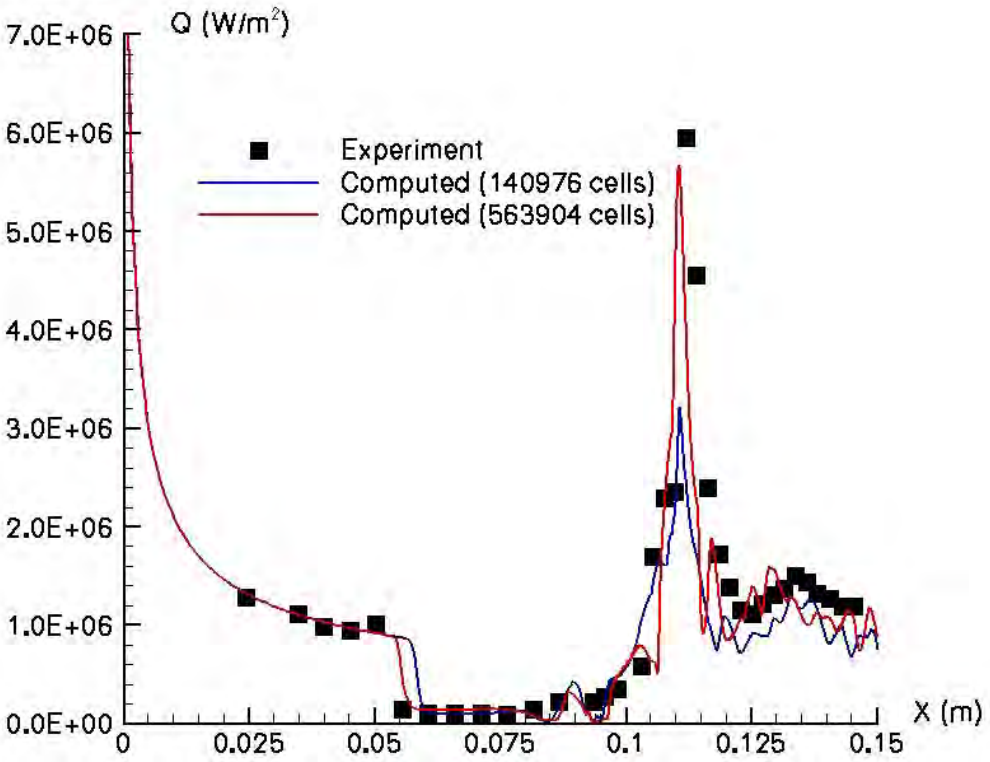

Figure 2-35: q_w for Run 42 (Walpot).

2.5.3 Cylinder

2.5.3.1 Case I

The computed surface pressure is compared with experiment in Figure 2-36 to Figure 2-40. Overall, there is excellent agreement between with experiment for all computations. Virtually identical results are obtained by Nompelis (Figure 2-38) for surface accommodation factor $\gamma = 0$ (non-catalytic) and $\gamma = 1$ (fully catalytic for radicals). All computed flowfields converged to steady state. The computed surface heat transfer is compared with experiment in Figure 2-41 to Figure 2-45. The computed peak heat transfer by Gaitonde (Figure 2-41) under-predicts the experimental peak heat transfer by 25%. The predictions of Lani (Figure 2-42) show closer agreement with experiment, while the fully catalytic predictions of Nompelis (Figure 2-43, $\gamma = 1$) display excellent agreement with experiment. The non-catalytic result of Nompelis, however, under-predicts the peak heat transfer by 25% similar to the results of Gaitonde. The predictions of Walpot (Figure 2-45) also underestimate the peak heat transfer. These results indicate that accurate modeling of surface catalysis is a critical to the prediction of peak heat transfer for this case.

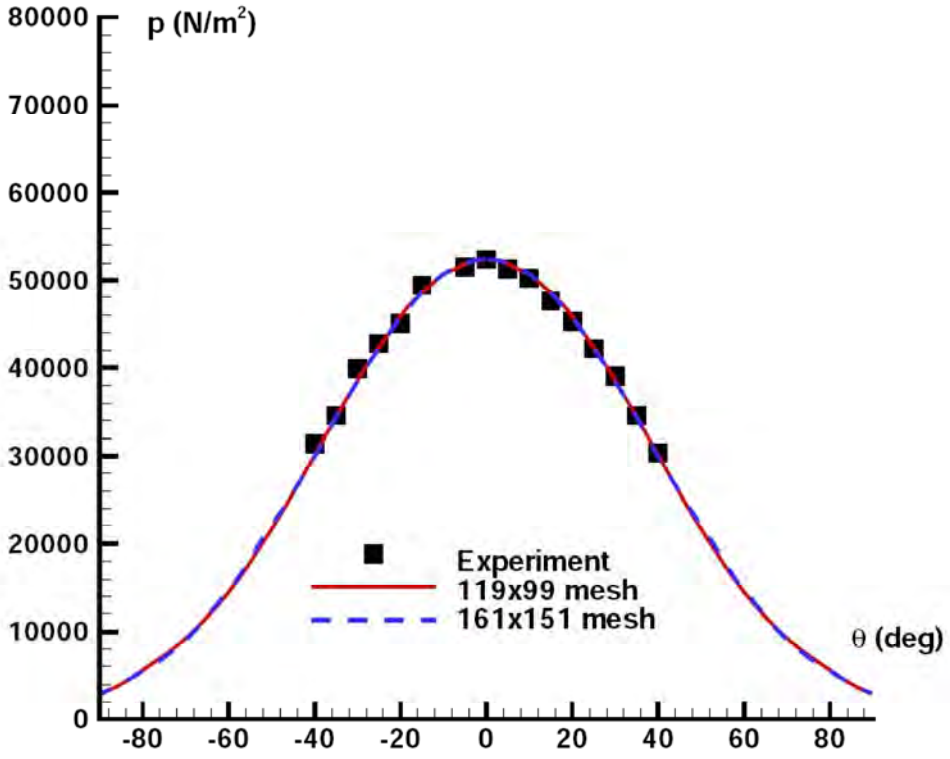

Figure 2-36: p_w for Case I (Gaitonde).

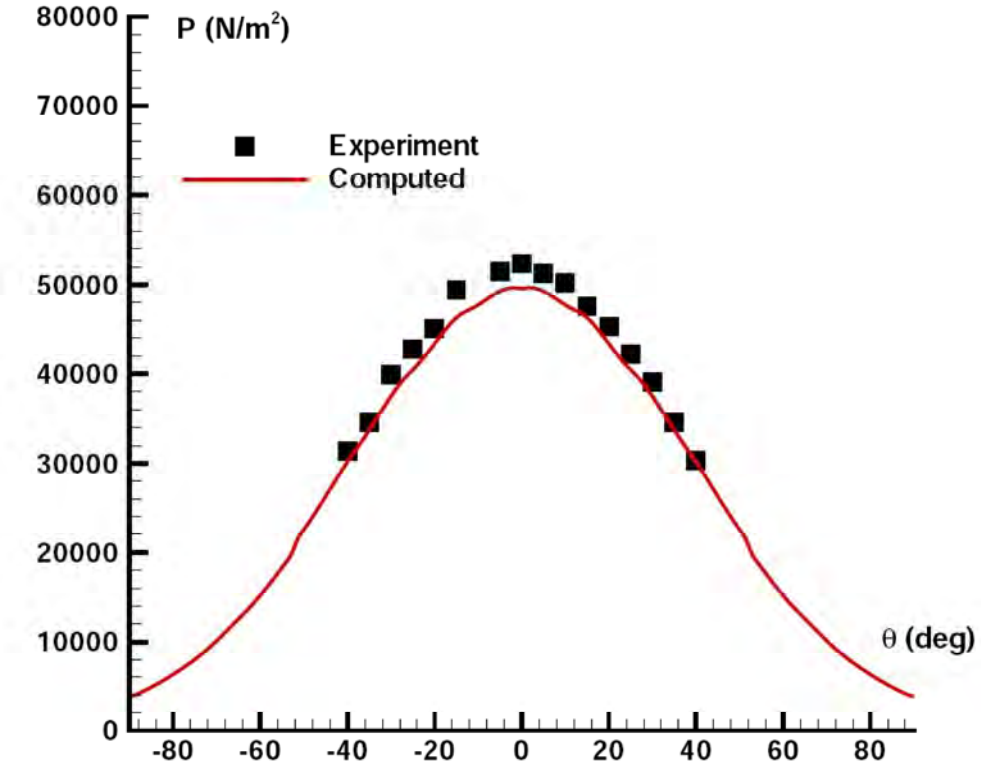

Figure 2-37: p_w for Case I (Lani).

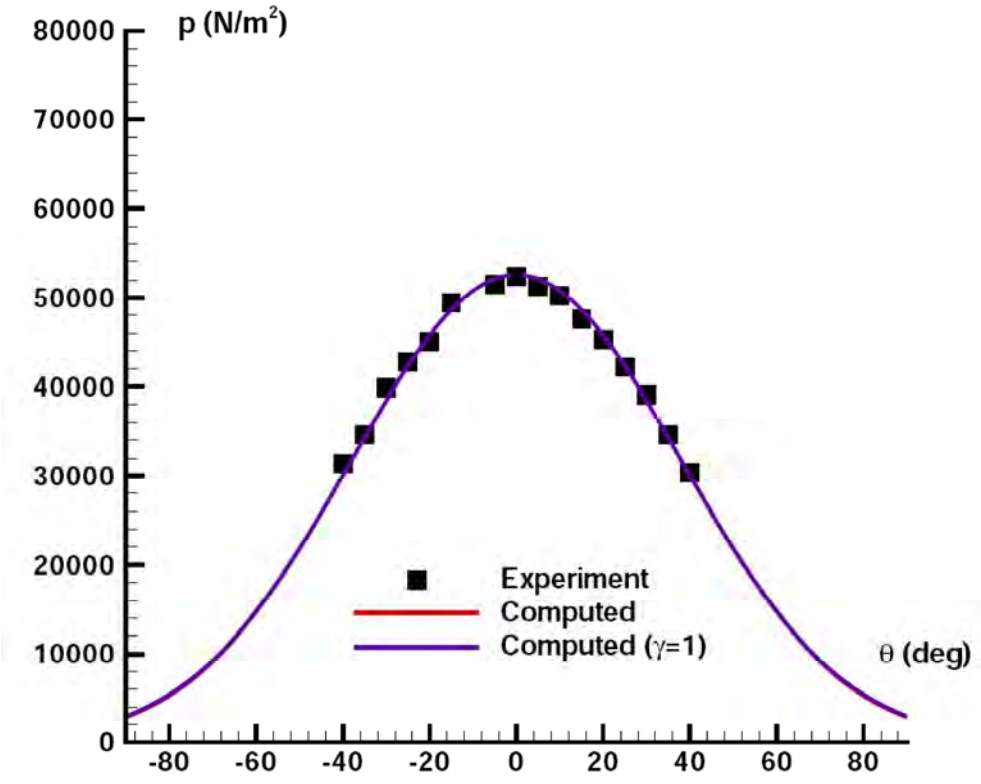

Figure 2-38: p_w for Case I (Nompelis).

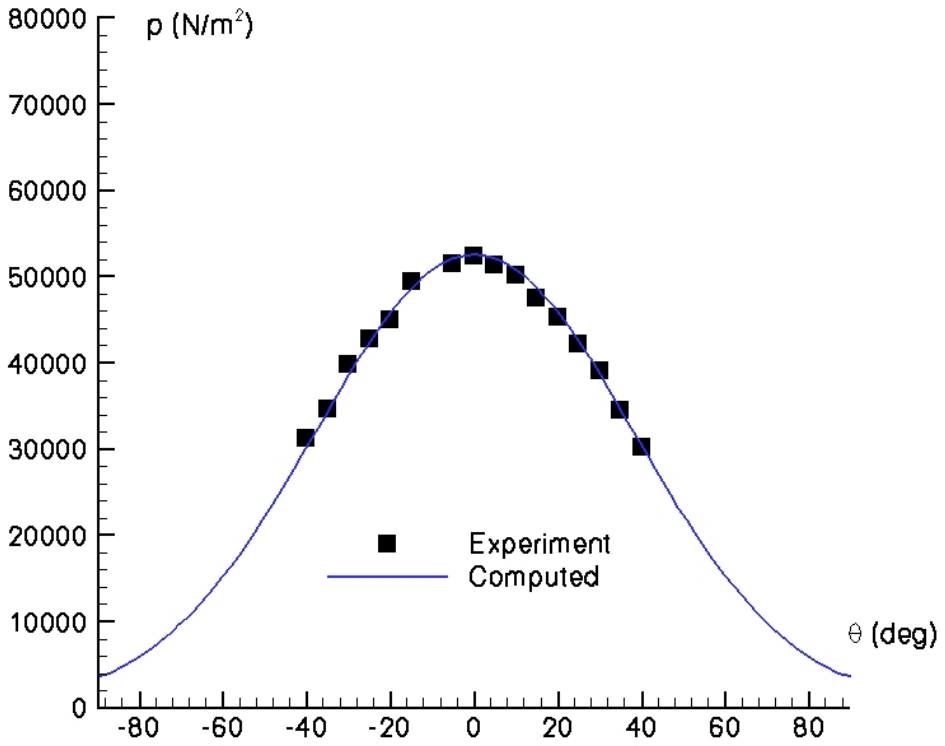

Figure 2-39: p_w for Case I (Reimann).

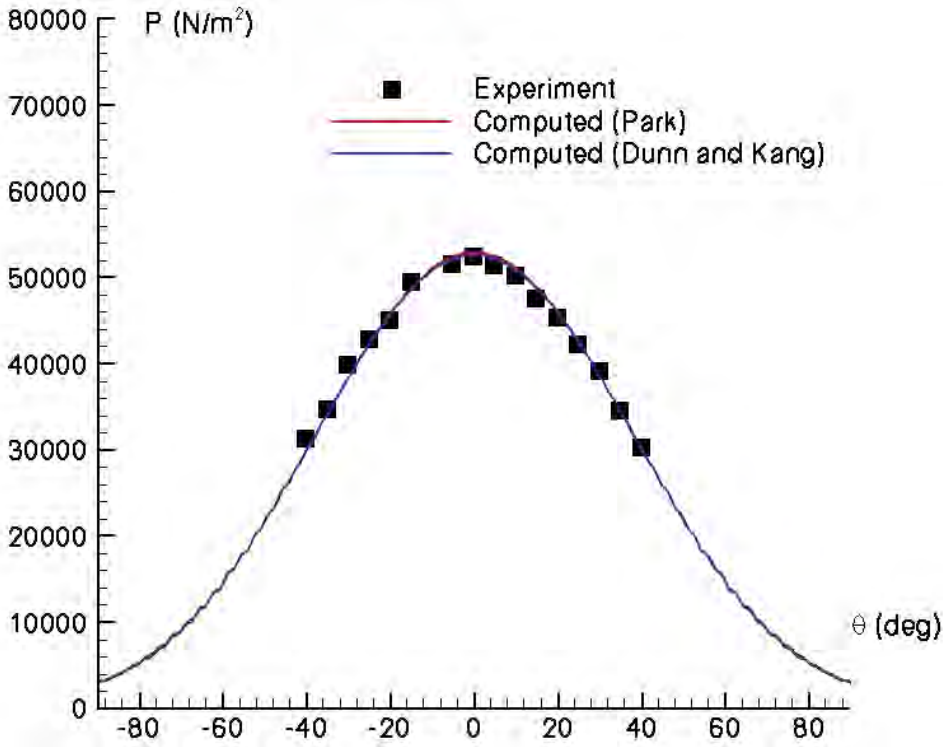

Figure 2-40: p_w for Case I (Walpot).

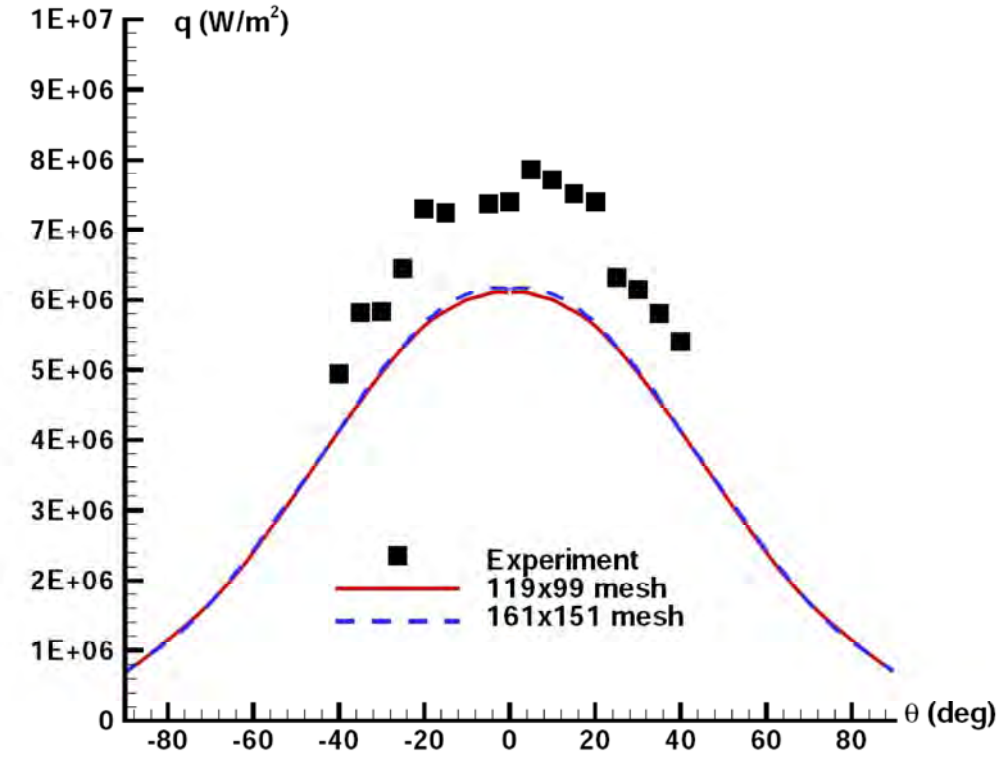

Figure 2-41: q_w for Case I (Gaitonde).

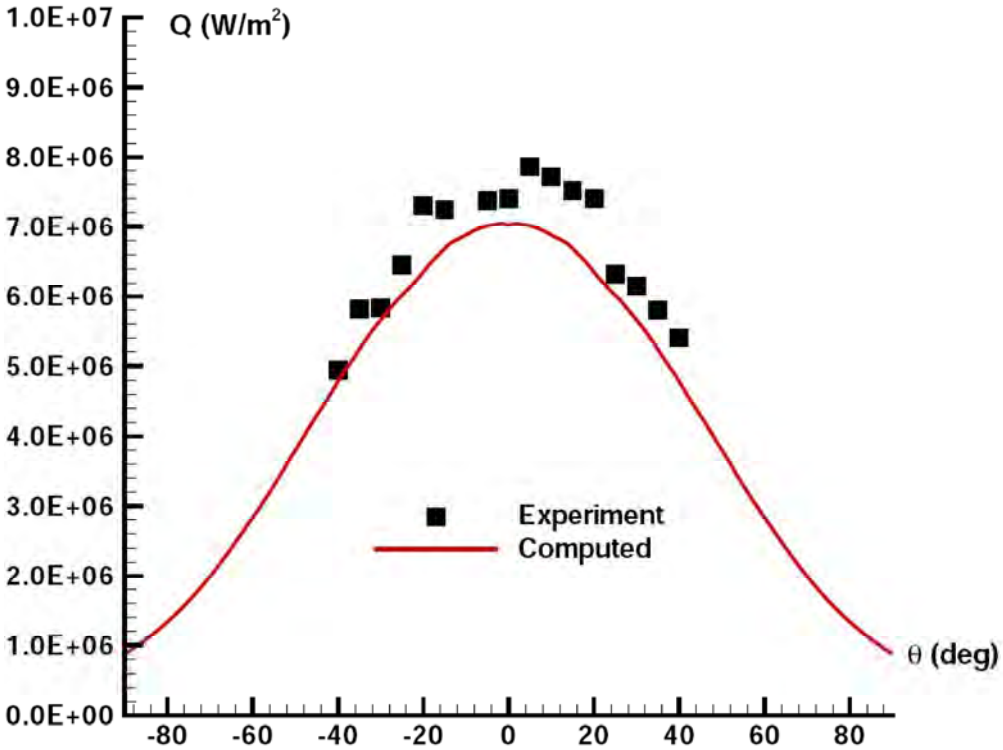

Figure 2-42: q_w for Case I (Lani).

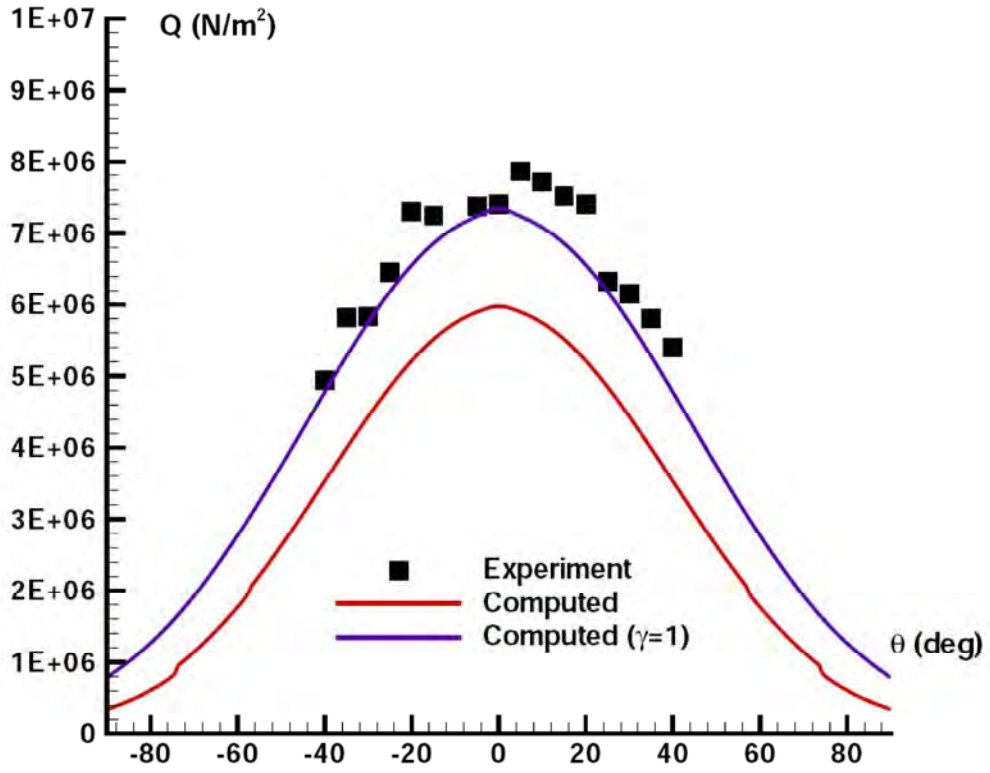

Figure 2-43: q_w for Case I (Nompelis).

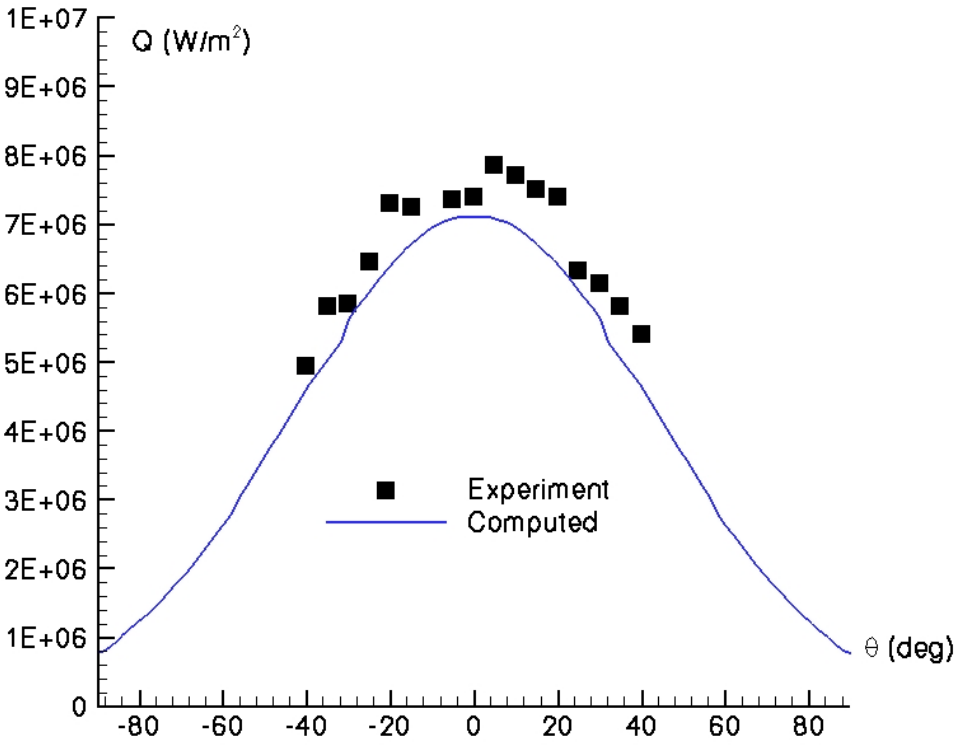

Figure 2-44: q_w for Case I (Reimann).

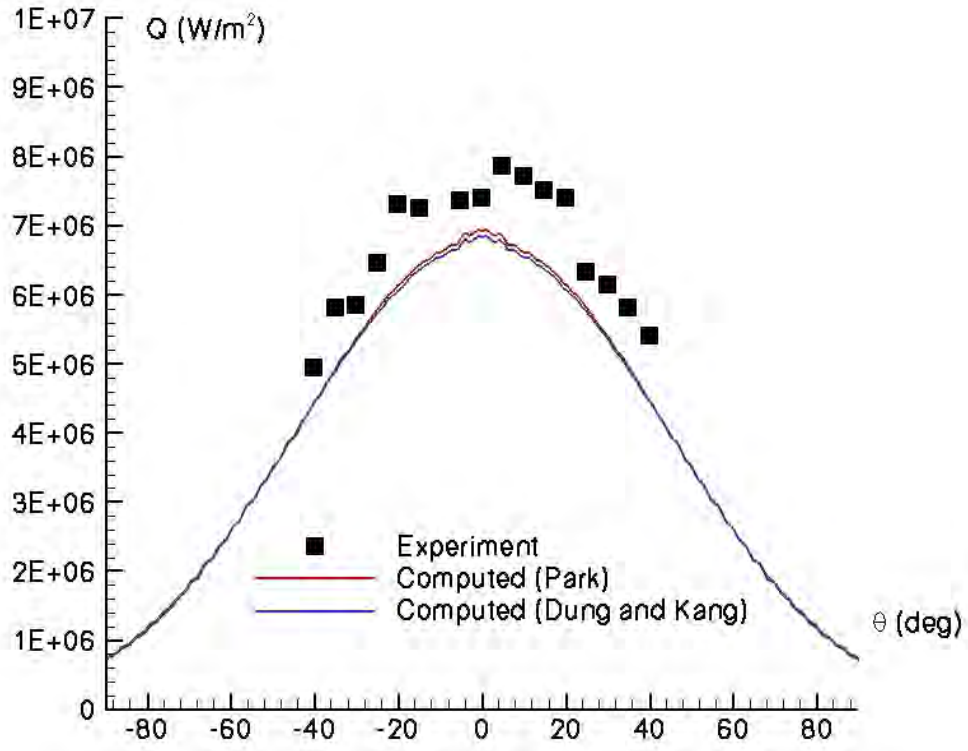

Figure 2-45: q_w for Case I (Walpot).

2.5.3.2 Case III

The computed surface pressure is compared with experiment in Figure 2-46 to Figure 2-50. Overall, there is good agreement with the pressure distribution on the surface for all computations. The predictions of Nompelis (Figure 2-48) for both non-catalytic ($\gamma = 0$) and catalytic ($\gamma = 1$) cases are virtually identical. The computed surface heat transfer is compared with experiment in Figure 2-51 to Figure 2-55. The peak experimental heat transfer is lower than for Case I as expected from the lower freestream total enthalpy in this case (Table 2-2). All predictions are in reasonable agreement with experiment. In particular, the effect of catalycity in the computations of Nompelis (Figure 2-53) are significantly less than in Case I.

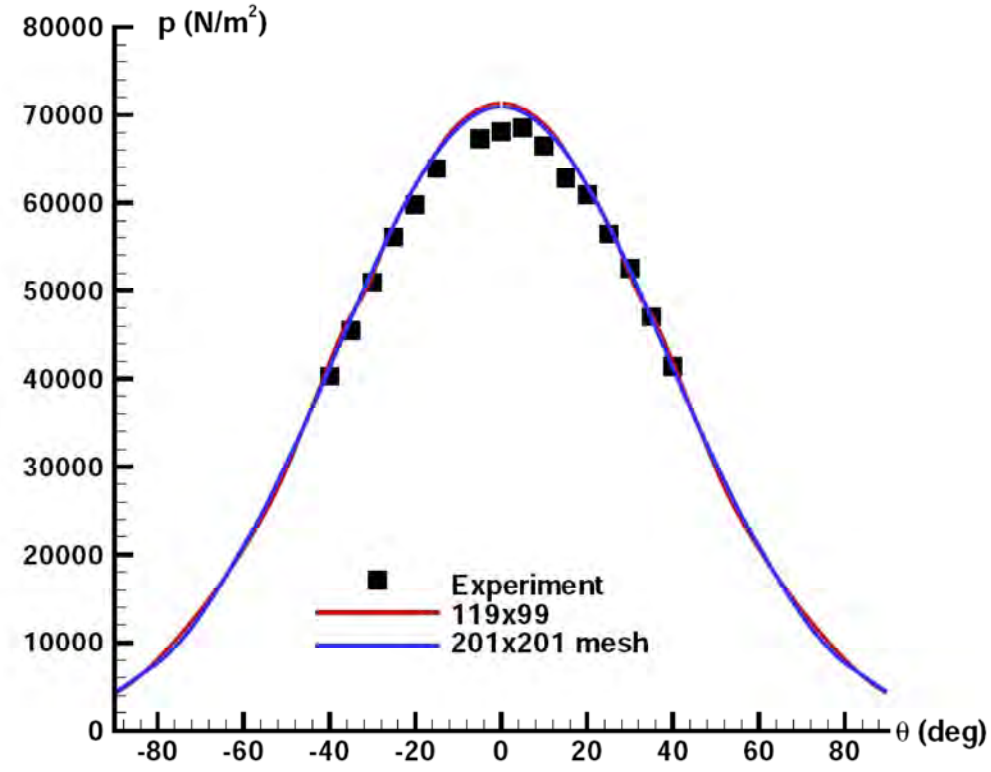

Figure 2-46: p_w for Case III (Gaitonde).

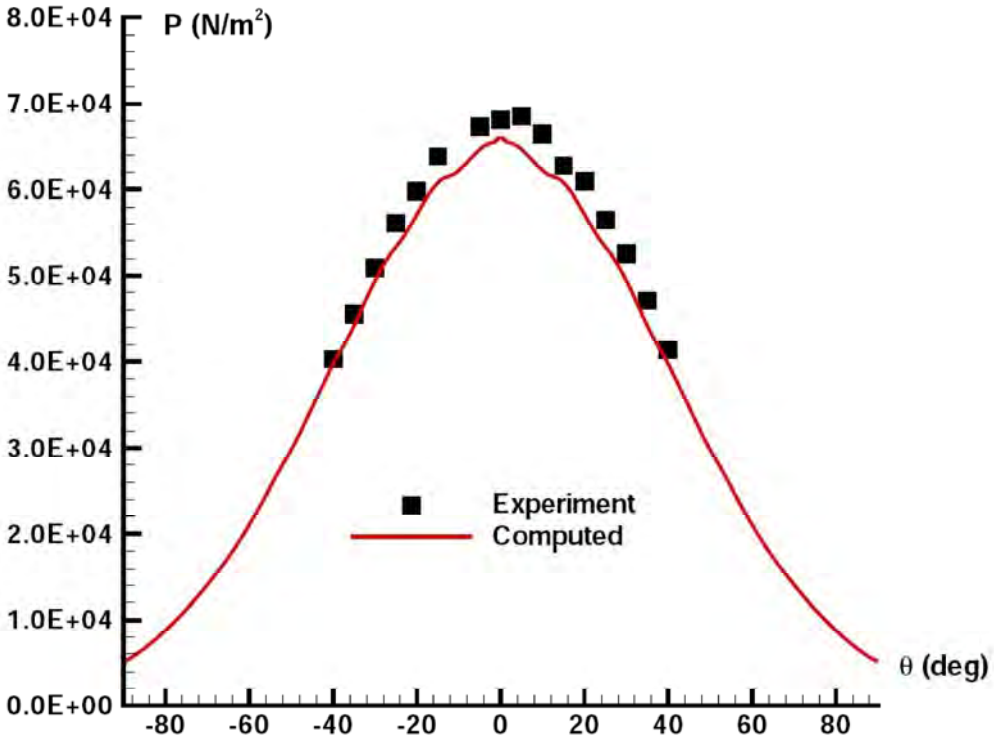

Figure 2-47: p_w for Case III (Lani).

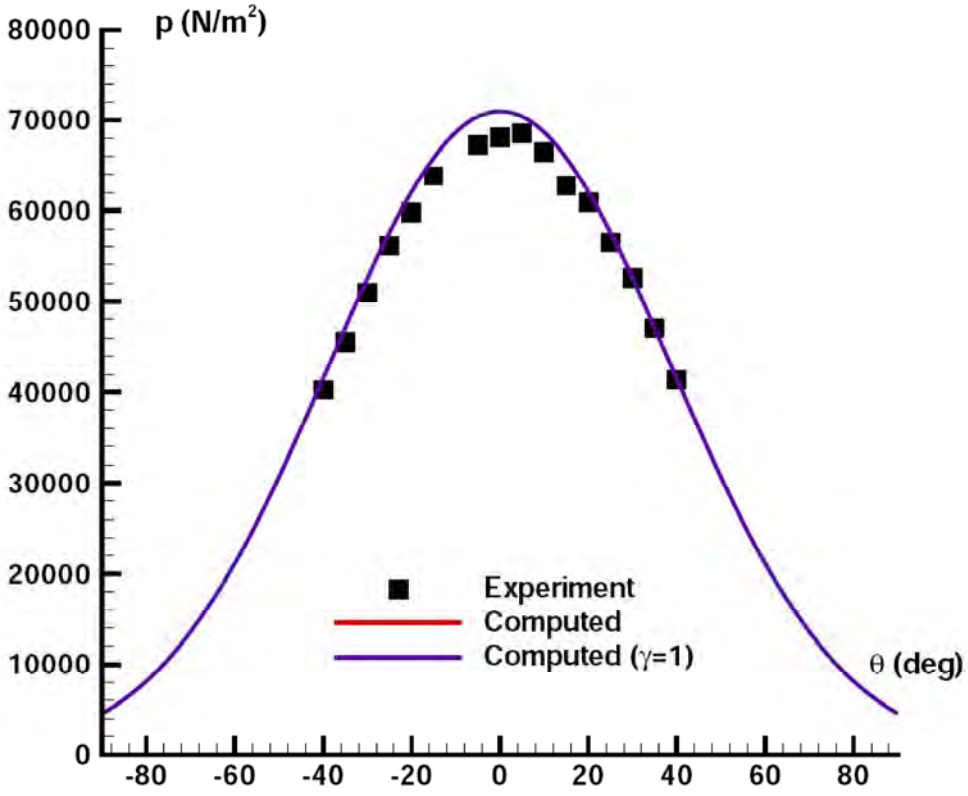

Figure 2-48: p_w for Case III (Nompelis).

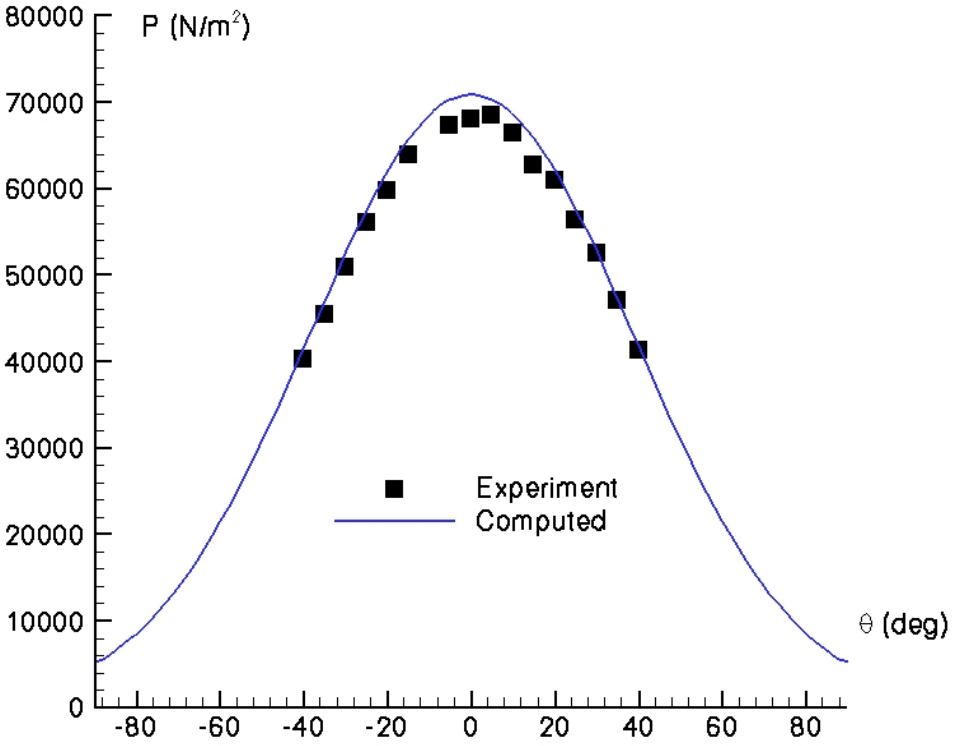

Figure 2-49: p_w for case III (Reimann).

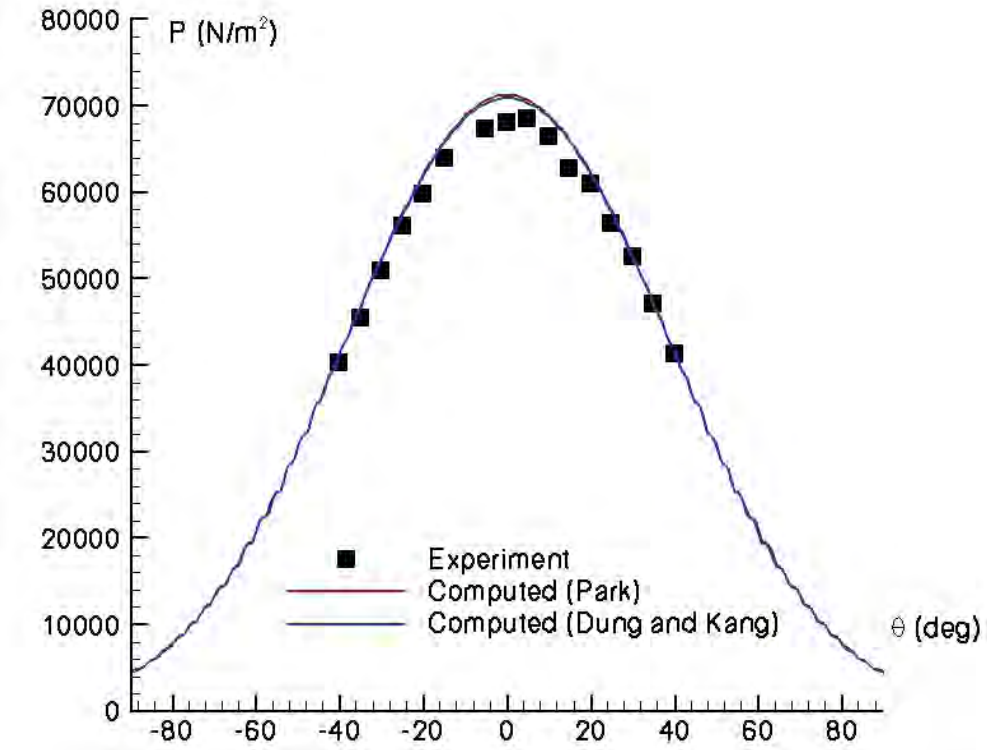

Figure 2-50: p_w for Case III (Walpot).

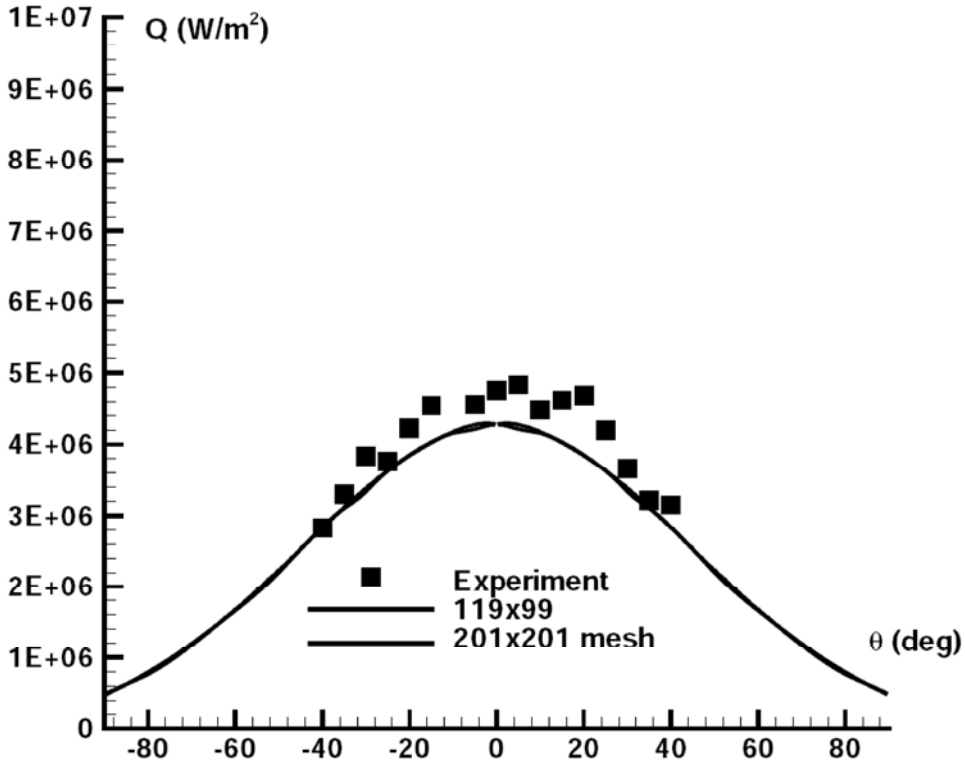

Figure 2-51: q_w for Case III (Gaitonde).

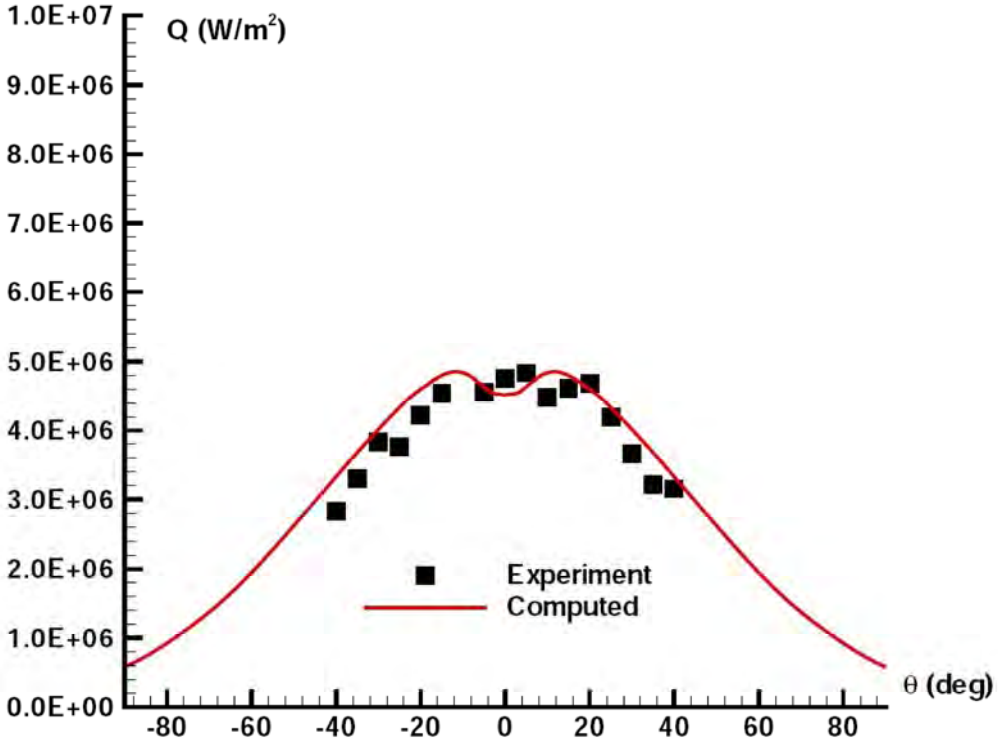

Figure 2-52: q_w for Case III (Lani).

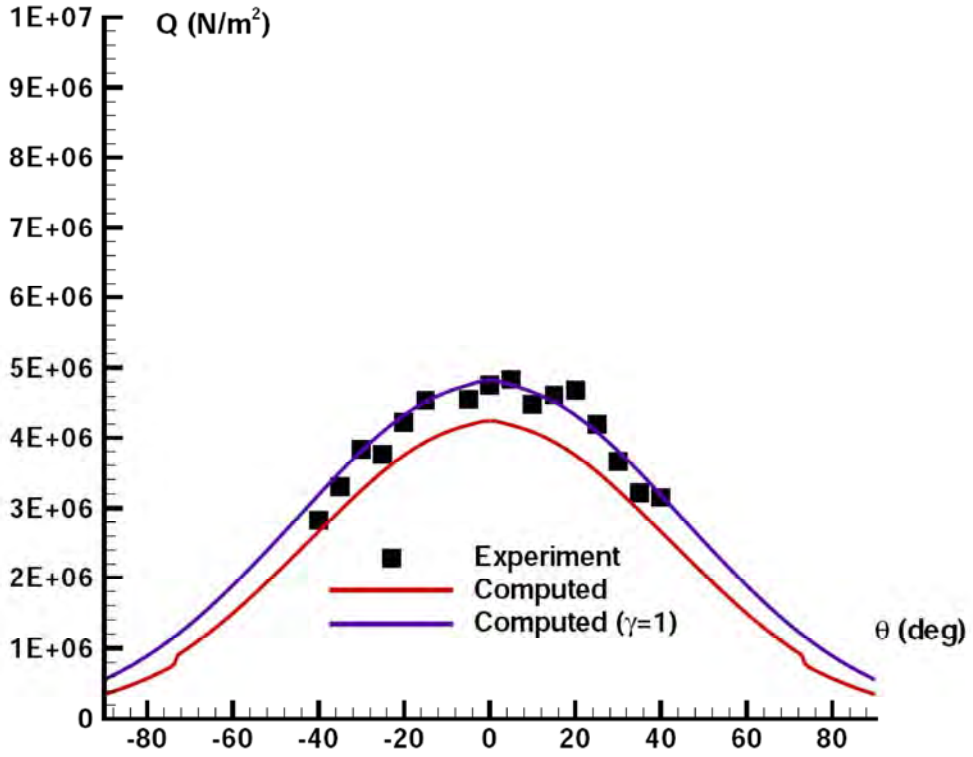

Figure 2-53: q_w for Case III (Nompelis).

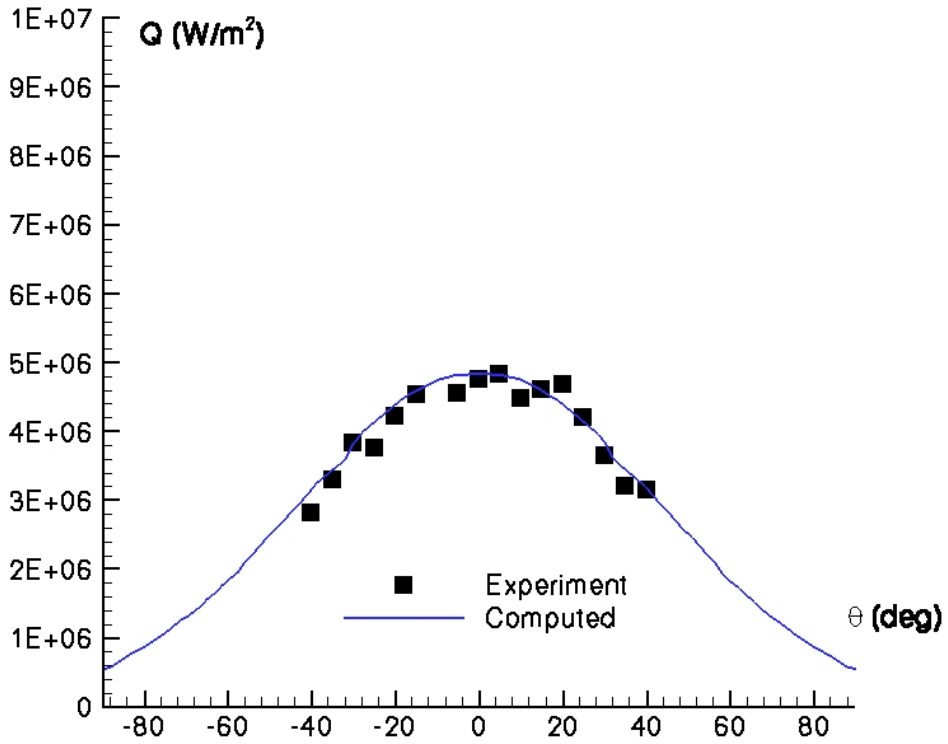

Figure 2-54: q_w for Case III (Reimann).

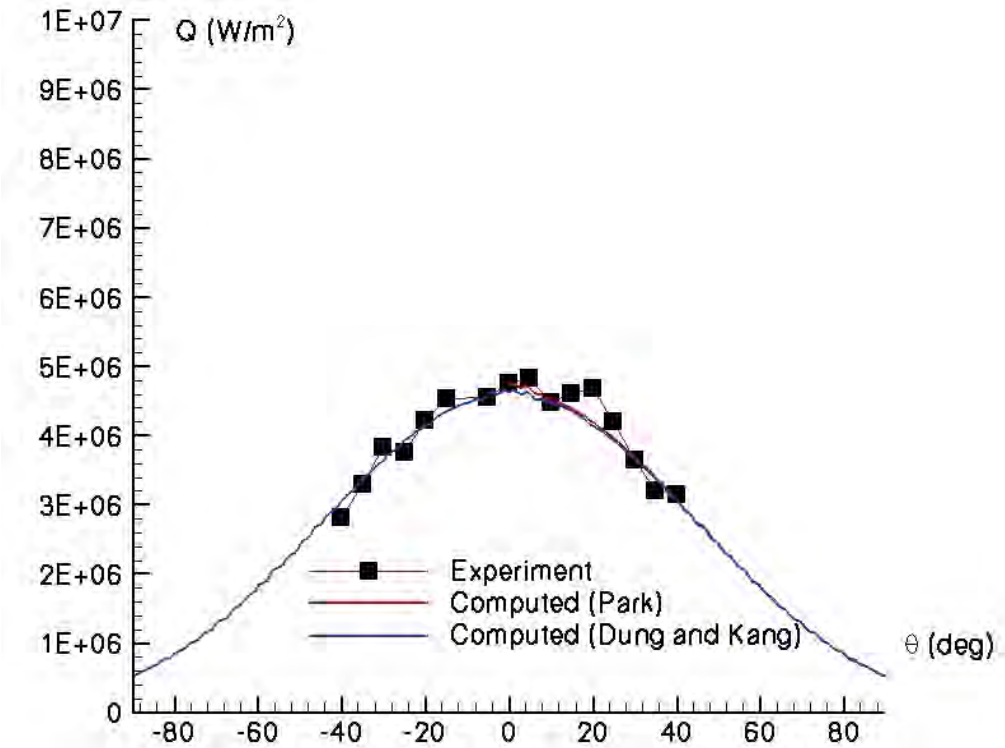

Figure 2-55: q_w for Case III (Walpot).

2.6 CONCLUSIONS

A collaborative effort on assessment of CFD capability for prediction of shock interactions was performed. A matrix of two test configurations (double cone and cylinder) was selected with two separate flow conditions for each configuration. Experimental data for surface pressure and heat transfer was provided for each configuration. Six CFD experts from Europe and the United States performed computations for most or all of the configurations and the results are compared with the experimental data. For the double cone configuration, a surprising result was observed for the first test case (Run 40). The experiment indicated that a steady flowfield had been achieved, while all computations indicated that a steady state solution had not been reached. This is a critically important result which requires further detailed investigation. For the second test case (Run 42), generally good agreement was obtained for surface pressure and heat transfer. For the cylinder configuration, close agreement was achieved for the surface pressure for both test conditions. However, the computed peak heat transfer was typically under-predicted by up to 25% for the higher freestream enthalpy configuration (Case I) in the absence of catalytic effects in the surface boundary conditions. This emphasizes the need for further research in modeling gas-surface interactions at high freestream enthalpy conditions. The computed heat transfer was in reasonable agreement for the lower freestream enthalpy case (Case III).

2.7 REFERENCES

[1] Barth, T., "Aspects of Unstructured Grids and Finite Volume Solvers for the Euler and Navier-Stokes Equations", Von Karman Institute for Fluid Dynamics, Lecture Series No. 1994-05, 1994.

[2] Blottner, F., Johnson, M. and Ellis, M., "Chemically Reacting Viscous Flow Program for Multicomponent Gas Mixtures", Technical Report SC-RR-70-754, Sandia National Laboratories, Albuquerque, NM, USA, 1971.

[3] Candler, G., "Hypersonic Nozzle Analysis Using an Excluded Volume Equation of State", AIAA Paper No. 2005-5202, American Institute of Aeronautics and Astronautics, January 2005.

[4] Csik, A., Ricchiuto, M. and Deconinck, H., "A Conservative Formulation of the Multidimensional Upwind Residual Distribution Schemes for General Nonlinear Conservation Laws", *Journal of Computational Physics*, Vol. 179, No. 2, pp. 286-312, 2002.

[5] Dobes, J. and Deconinck, H., "A Shock Sensor-Based Second-Order Blended (Bx) Upwind Residual Distribution Scheme for Steady and Unsteady Compressible Flow", In *Hyperbolic Problems: Theory, Numerics, Applications*, 978-3-540-75711-5 (print), 978-3-540-75712-2 (online), pp. 465-473, Springer, Berlin, 2008.

[6] Drikakis, D., "Advances in Turbulent Flow Computations Using High-Resolution Methods", *Progress in Aerospace Sciences*, Vol. 39, pp. 405-424, 2003.

[7] Drikakis, D., Hahn, M., Mosedale, A. and Thorber, B., "Large Eddy Simulation Using High Resolution and High Order Methods", *Philosophical Transactions Royal Society A*, 367, pp. 2985-2997, 2009.

[8] Drikakis, D. and Tsangaris, S., "An Implicit Flux-Averaging Scheme for the Euler Equations for Real Gases", *International Journal for Numerical Methods in Fluids*, Vol. 12, pp. 711-726, 1991.

[9] Druguet, M.-C., Candler, G. and Nompelis, I., "Effect of Numerics on Navier-Stokes Computations of Hypersonic Double-Cone Flows", *AIAA Journal*, Vol. 43, No. 3, pp. 616-623, March 2005.

[10] Gupta, R., Yos, J., Thompson, R. and Lee, K.-P., "A Review of Reaction Rates and Thermodynamic and Transport Properties for an Eleven-Species Model for chemical and Thermal Nonequilibrium Calculations to 30,000 K", Reference Publication No. 1232, NASA, 1990.

[11] Karl, S., Martinez-Schramm, J. and Hannemann, K., "High Enthalpy Cylinder Flow in HEG: A Basis for CFD Validation", AIAA Paper No. 2003-4252, American Institute of Aeronautics and Astronautics, June 2003.

[12] Knight, D. and Degrez, G., "Shock Wave Boundary Layer Interactions in High Mach Number Flows: A Critical Survey of Current Numerical Predictions", AGARD Report 319, AGARD, pp. 1-1 to 1-35, December 1998.

[13] Knight, D., RTO WG 10: "Test Cases for CFD Validation of Hypersonic Flight", AIAA Paper No. 2002-0433, American Institute of Aeronautics and Astronautics, January 2002.

[14] Lani, A., Quintino, T., Kimpe, D., Deconinck, H., Vandewalle, S. and Poedts, S., "The COOLFluiD Framework: Design Solutions for High Performance Object Oriented Scientific Computing Software", In *Computational Science ICCS 2005*, Sloot, P., Sunderan, V., van Albada, G. and Dongarra, J. (Eds.), Vol. 1 of LNCS 3514, pp. 28-286, Atlanta, GA, USA, Springer, May 2005.

[15] Lani, A., Quintino, T., Kimpe, D., Deconinck, H., Vandewalle, S. and Poedts, S., "Reusable Object Oriented Solutions for Numerical Simulation of PDEs in a High Performance Environment", *Scientific Programming*, Special Edition on POOSC 2005, Vol. 14, No. 2, pp. 111-139, 2006.

[16] Lani, A., "An Object Oriented and High Performance Platform for Aerothermodynamics Simulation", PhD Thesis, Université Libre de Bruxelles, 2008.

[17] Liou, M., "A Sequel to AUSM: AUSM+", *Journal of Computational Physics*, Vol. 129, No. 2, pp. 364-382, December 1996.

[18] MacCormack, R. and Candler, G., "The Solution of the Navier-Stokes Equations Using Gauss-Seidel Line Relaxation", *Computers and Fluids*, Vol. 17, No. 1, pp. 135-150, 1989.

[19] Magin, T. and Degrez, G., "Transport Algorithms for Partially Ionized Unmagnetized Plasmas", *Journal of Computational Physics*, Vol. 198, pp. 424-449, 2004.

[20] Millikan, R. and White, D., "Systematics of Vibrational Relaxation", *Journal of Chemical Physics*, Vol. 39, pp. 3209-3213, 1953.

[21] Morrison, J., "Flux-difference Split Scheme for Turbulent Transport Equations", AIAA Paper No. 1990-5251, American Institute of Aeronautics and Astronautics, October 1990.

[22] Nompelis, I., "Computational Study of Hypersonic Double-Cone Experiments for Code Validation", PhD Thesis, Department of Aerospace Engineering and Mechanics, University of Minnesota, MN, USA, May 2004.

[23] Panesi, M., "Physical Models for Nonequilibrium Plasma Flow Simulations at High Speed Re-entry Conditions", PhD Thesis, Universita di Pisa, Von Karman Institute of Fluid Dynamics, 2008.

[24] Park, C., "Non-equilibrium Hypersonic Aerothermodynamics", Wiley-Interscience, New York, NY, USA, 1990.

[25] Park, C., "Review of Chemical-Kinetic Problems of Future NASA mission, I: Earth Entries", *Journal of Thermophysics and Heat Transfer*, Vol. 7, pp. 385-398, July-September 1993.

[26] Roe, P., "Approximate Riemann Solvers, Parametric Vectors and Difference Schemes", *Journal of Computational Physics*, Vol. 43, pp. 357-372, 1981.

[27] Quintino, T., "A Component Environment for High-Performance Scientific Computing: Design and Implementation", PhD Thesis, Katholieke Universiteit Leuven, 2008.

[28] Schwamborn, D., Gerhold, T. and Heinrich, R., "The DLR TAU Code: Recent Applications in Research and Industry", In *ECCOMASS CFD 2006*, Wesseling, P. et al. (Eds.), TU Delft, Netherlands, 2006.

[29] Venkatakrishnan, V., "Convergence to Steady State Solutions of the Euler Equations on Unstructured Grids with Limiters", *Journal of Computational Physics*, Vol. 118, pp. 120-130, 1995.

[30] Vincenti, W. and Kruger, C., "Introduction to Physical Gas Dynamics", Krieger Publishing Company, Malabar, FL, USA, 1965.

[31] Wright, M., Bose, D. and Candler, G., "A Data-Parallel Line Relaxation Method for the Navier-Stokes Equations", *AIAA Journal*, Vol. 36, No. 9, pp. 1603-1609, September 1998.

Chapter 3 – AEROTHERMODYNAMICS OF BLUNT BODY ENTRY VEHICLES

Brian R. Hollis
NASA Langley Research Center
USA

Salvatore Borrelli
CIRA Italian Aerospace Research Centre
ITALY

3.1 INTRODUCTION

In this chapter, the aerothermodynamic phenomena of blunt body entry vehicles are discussed. Four topics will be considered that present challenges to current computational modeling techniques for blunt body environments: turbulent flow, non-equilibrium flow, rarefied flow, and radiation transport. Examples of comparisons between computational tools to ground and flight-test data will be presented in order to illustrate the challenges existing in the numerical modeling of each of these phenomena and to provide test cases for evaluation of Computational Fluid Dynamics (CFD) code predictions.

3.1.1 Blunt Body Entry Vehicles Overview

Blunt body configurations are the most common geometries employed for entry into planetary atmospheres. Examples of manned blunt-body entry vehicles include the Mercury, Gemini, and Apollo capsules. Examples of unmanned flight test or interplanetary probe blunt-body entry vehicles are more numerous and include the Viking, Pioneer, FIRE II, ARD, OREX, Stardust, etc. An overview of major programs that includes vehicle and mission descriptions in which blunt body entry vehicles have been employed is given in [1].

In broad terms, a blunt-body entry vehicle is comprised of a large heat shield that protects a smaller crew cabin or robotic probe payload. The heat shield is generally axisymmetric with either a large-angle, sphere-cone geometry (e.g., the Mars Viking probe) or a large radius-of-curvature spherical cap (e.g., the Apollo command module), although asymmetric shapes have sometimes been considered (e.g., the cancelled Aeroassist Flight Experiment).

The geometry of the heat shield produces large amounts of aerodynamic drag that decelerate the vehicle from orbital or interplanetary speeds. A small amount of aerodynamic lift for maneuverability and cross-range capability may also be provided by offsetting the center-of-gravity of the vehicle to trim it at a non-zero angle of attack.

The heat shield material, which is either a high-temperature insulator or an ablative material, protects the payload from the high levels of convective heating, and in some cases, radiative heating experienced during atmospheric entry. The large effective radius of the blunt body heat shield acts to mitigate the effects of convective heat transfer. However, the large radius actually has the opposite effect with respect to radiative heating, but radiation is typically a smaller fraction of the maximum heat rate and an even smaller fraction of the total integrated heat load.

The effects of non-equilibrium chemical and vibrational processes and of radiation transport have long been recognized as challenging applications of Computational Fluid Dynamics (CFD) tools used in the simulation of blunt body flow-fields. More recently, it has been recognized that some vehicles now in the developmental stage, e.g., the Mars Science Laboratory and Orion Crew Exploration Vehicle, will also experience environments that will be dominated by turbulent flow owing to their large sizes, high re-entry velocities, and non-zero angle of attack lifting trajectories. The modeling of turbulent flow fields in the subsonic or low Mach number flow behind the bow shock of such vehicles presents a new challenge for CFD since experimental data on such flows are sparse. Research into radiative transport phenomena has

also generally languished since the 1970's (after work on the Jupiter Galileo program) without any actual missions in which aerothermodynamic radiation was a significant factor. More recently, missions such as Stardust, Huygens, and Orion have renewed the need for research and development of better computational models for radiative transport processes.

In this discussion of blunt-body aerothermodynamic phenomena, ground and flight test programs and supporting computational analyses will be discussed for several programs: the Mars Science Laboratory, the Orion Crew Exploration Vehicle, and the Fire II flight test. Brief overviews of each vehicle and mission are presented below.

3.1.1.1 MSL Background

The Mars Science Laboratory (MSL) mission [2], to be launched in 2011, will deliver the largest (> 900 kg) rover ever to Mars (Figure 3-1). The MSL will fly a controlled, lifting trajectory (α = 16 deg) to deliver the payload to within 10 km of the target location. The entry vehicle (Figure 3-2) is comprised of a 4.5 m diameter spherically-blunted, 70-deg half-angle cone forebody heat shield that protects the aftbody payload from entry heating and provides a Lift-to-Drag (L/D) ratio of 0.24 for aerodynamic control and maneuvering. The MSL vehicle will enter the Martian atmosphere at a velocity of 5.6 km/sec, which is greater than that of any other Mars probe except Mars Pathfinder. Because of the vehicle's large heat shield diameter and the high angle of attack and velocity of its entry trajectory, it is expected that the vehicle will experience boundary-layer transition to turbulent flow well before the peak heating point on its trajectory. Therefore the vehicle's Thermal Protection System (TPS) was designed [3], [4] with a conservative assumption of turbulent flow throughout the entire trajectory. Extensive aerothermodynamic ground-testing was conducted in support of MSL development, including testing in the AEDC Hypervelocity Tunnel 9, CUBRC LENS, CalTech T5, and the NASA Langley 20-Inch Mach 6 Air Tunnel and is discussed in [5]-[12].

Figure 3-1: Size Comparison of Mars Rovers – from left: Mars Science Laboratory (2011); Mars Exploration Rover (2003); Mars Pathfinder (1996).

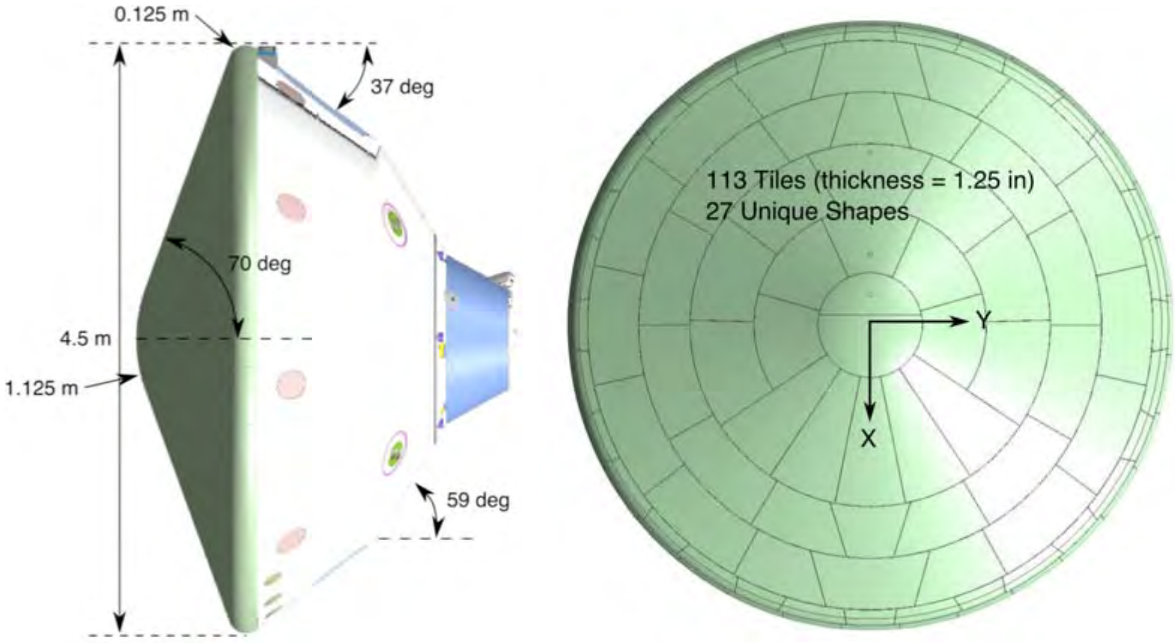

Figure 3-2: Mars Science Laboratory Entry Vehicle.

3.1.1.2 CEV Background

The Project Orion Crew Exploration Vehicle (CEV) was defined by NASA's Exploration Systems Architecture Study [13] as NASA's next manned space vehicle (Figure 3-3). The CEV will support NASA's exploration missions by providing crew access to the International Space Station, the moon, and Mars. The geometry of the CEV (Figure 3-4) is similar to that of Apollo – a spherical segment heat shield that protects a truncated-cone shaped crew compartment – but is considerably larger. The maximum diameter (current design iteration) of the CEV is 5 m, as compared to that of 3.912 m for Apollo.

Figure 3-3: Orion CEV.

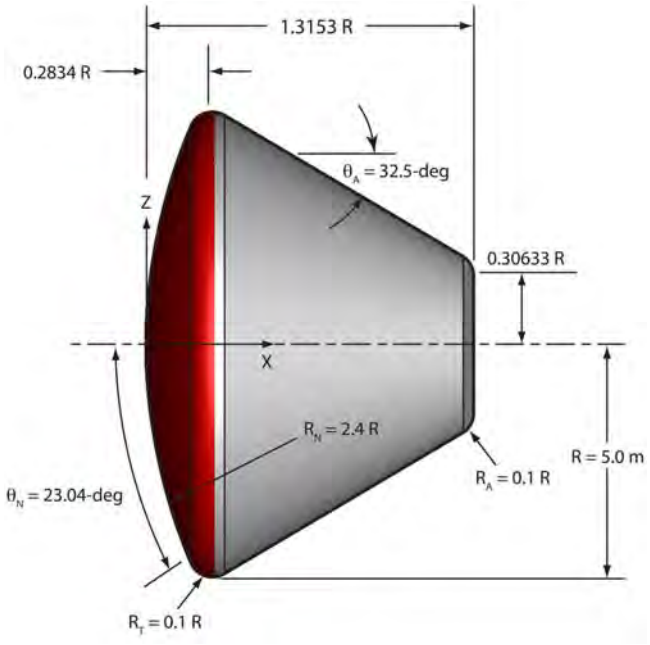

Figure 3-4: Orion CEV Crew Module Dimensions.

The design of the CEV TPS must account for the high heating rates generated at lunar return velocities and the aerothermodynamic challenges of non-equilibrium thermo-chemistry, turbulent flow, and radiation transport. As with MSL, the CEV is being designed with the conservative assumption of fully-turbulent flow throughout its trajectory. Although not discussed herein, the CEV TPS design must also account for ablation effects, including shape change, flow field radiation-ablation coupling, and ablated surface roughness heating augmentation. Ground testing conducted in support of CEV development is discussed in [14]-[22] and a summary of the overall test program is presented in [23].

3.1.1.3 FIRE-II Background

Project FIRE (Flight Investigation of the Reentry Environment) was conducted expressly for the purpose of measuring radiative heating at Lunar return velocities. The FIRE-II mission, which flew in 1965, is generally considered to be the best documented data set available on radiative heating since the mission was explicitly designed for the measurement of radiative heat-transfer in a non-ablating environment. The FIRE-II vehicle (Figure 3-5) was equipped with 3 separate beryllium heat shields that were each jettisoned before they reached temperatures at which ablation would begin. Data were obtained with both integrated and spectrally-resolved radiometers and with total heat flux calorimeters on each heat shield. Mission details for FIRE-II are presented in [24], [25] and flight test data are presented in detail in [26]-[28].

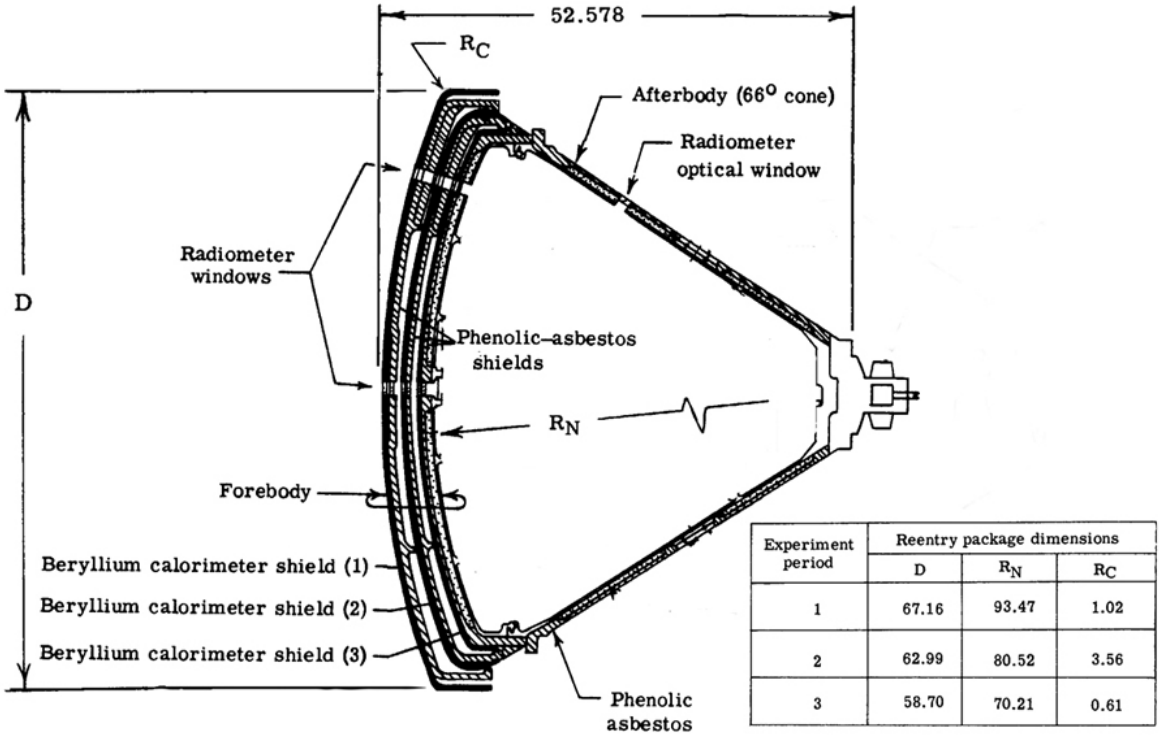

Experiment period	Reentry package dimensions		
	D	R_N	R_C
1	67.16	93.47	1.02
2	62.99	80.52	3.56
3	58.70	70.21	0.61

Figure 3-5: Project FIRE Vehicle Dimensions.

3.2 TURBULENT BLUNT-BODY FLOW

Historically, turbulent flow at hypersonic speeds has generally been considered to be a design issue for moderate to high lift-to-drag ratio lifting bodies and winged vehicles, such as the Shuttle Orbiter. Such vehicles travel at high Reynolds numbers and their large size provides sufficient length over which turbulent flow can develop. In contrast, blunt-body re-entry vehicles generally are smaller and have high drag coefficients that cause rapid deceleration, which thus decreases the likelihood of producing turbulent

flow. However, the problem of turbulent heating has become important in recent blunt-body vehicle designs, notably the Mars Science Laboratory (MSL) and the Orion Crew Exploration Vehicle (CEV). Both these vehicles are, in comparison to past blunt-body vehicles, quite large: the MSL is 4.5 m diameter and the CEV will be ~5 m diameter. Furthermore, both vehicles will experience atmospheric entry (at Mars and Earth, respectively) at high speeds (~11 km/s for CEV and ~5 km/s for MSL) and fly high angle-of-attack (for blunt bodies) lifting trajectories (11-deg to 16-deg range for MSL and 16-deg to 24-deg range for CEV). These factors all tend to promote transition to turbulent flow and thus the conservative design philosophy applied in both projects is to assume turbulent flow throughout their trajectories.

This assumption of turbulent flow led to the requirement to conduct high-Reynolds number hypersonic aeroheating testing on each vehicle in order to obtain turbulent heat transfer data for use in the evaluation of the CFD models employed in the design of each vehicle. Several examples of these experimental studies will be presented in which comparisons with CFD results have been performed.

3.2.1 Mars Science Laboratory Turbulent Flow

An investigation of turbulent aeroheating on the MSL vehicle [12] was conducted in the Arnold Engineering Development Center (AEDC) Hypervelocity Wind Tunnel No. 9 [29]. In this study, aeroheating data were collected on a 6-in. (0.1524 m) diameter, coaxial thermocouple instrumented MSL model in perfect-gas N_2 flow at the tunnels Mach 8 and Mach 10 test conditions. Data were obtained at free stream Reynolds numbers of 4×10^6/ft to 49×10^6/ft at Mach 8 and at 1×10^6/ft to 19×10^6/ft at Mach 10 with angles-of-attack between 0-deg and 24-deg. Turbulent flow was produced over the leeside of the heat shield at the highest Mach 10 Reynolds number, while turbulent flow was produced over the entire heat shield (both leeside and windside) at the highest mach 8 Reynolds number. The experimental uncertainty of the data was estimated to be ±12%.

Laminar and turbulent perfect-gas comparisons to these data were performed using the LAURA code [30] with the algebraic Cebeci-Smith turbulent model being used for the turbulent cases. Comparisons between centerline data and predictions are shown for selected α = 16-deg cases in Figure 3-6 and Figure 3-7. Free stream conditions for these cases are listed in Table 3-1. For the Mach 10 cases, the laminar predictions and data were in close agreement at $Re_\infty = 4 \times 10^6$/ft case, while at $Re_\infty = 19 \times 10^6$/ft, the laminar predictions matched the data on the windside of the forebody and the turbulent predictions matched the data on the leeside. For both Mach 8 cases, the turbulent predictions matched the data. Although the agreement between predictions and data was generally good for these cases, there were discrepancies around the stagnation point (x/R ~ 0.4) for all cases where measured heating rates were higher than either laminar or turbulent predictions.

Table 3-1: MSL Test Conditions for AEDC Tunnel 9.

Run	α (deg)	Re_∞ (1/ft)	M_∞	P_∞ (Pa)	T_∞ (K)	ρ_∞ (kg/m^3)	U_∞ (m/s)
3022	16	4.62E+06	9.80	656.1	54.4	0.0406	1474.9
3025	16	1.91E+07	10.32	2068.1	48.3	0.1444	1461.8
3047	16	3.04E+07	7.75	8231.8	73.8	0.3760	1356.4
3048	16	4.96E+07	7.98	11918.6	69.3	0.5792	1350.9

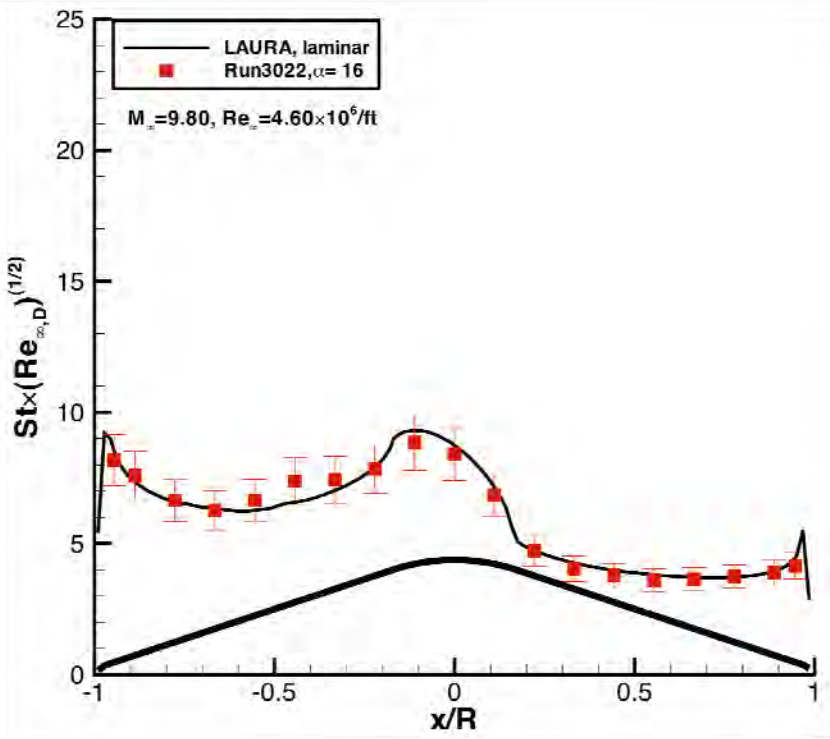

Mach 10, $Re_\infty = 4 \times 10^6$/ft

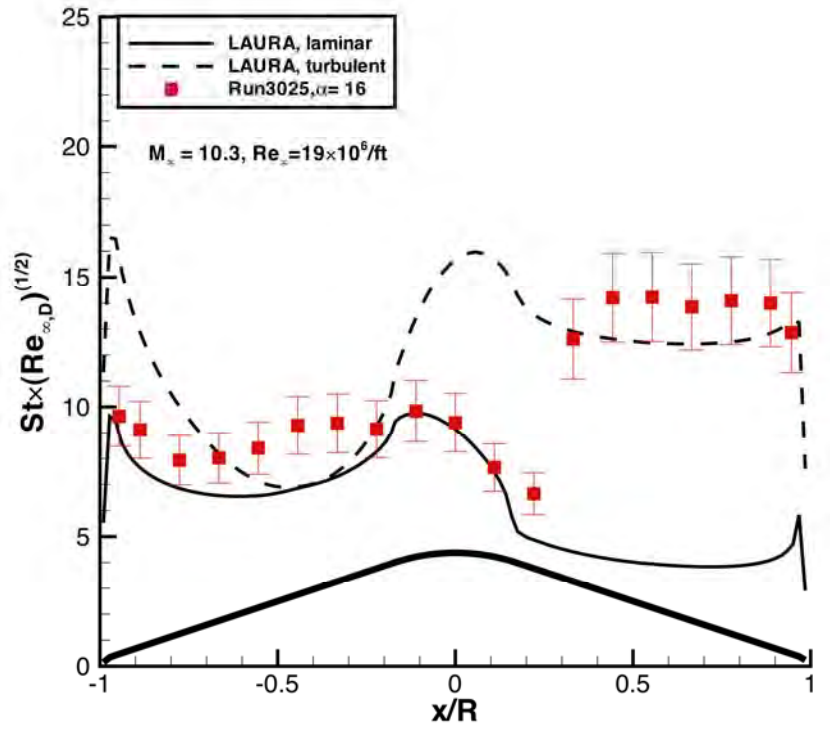

Mach 10, $Re_\infty = 19 \times 10^6$/ft

Figure 3-6: MSL Mach 10, α = 16-deg Data and Comparisons from AEDC Tunnel 9.

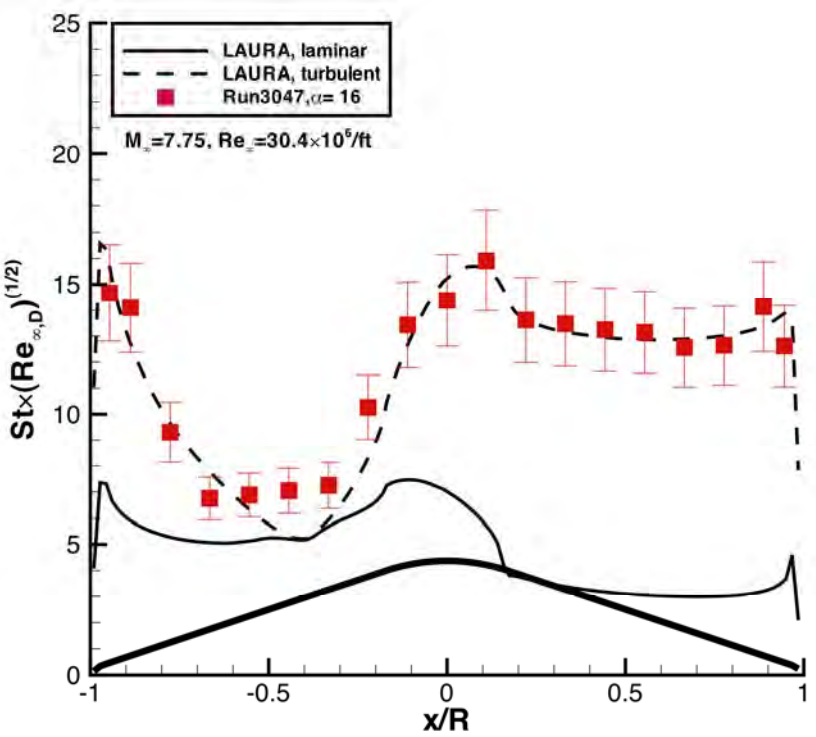

Mach 8, $Re_\infty = 30 \times 10^6$/ft

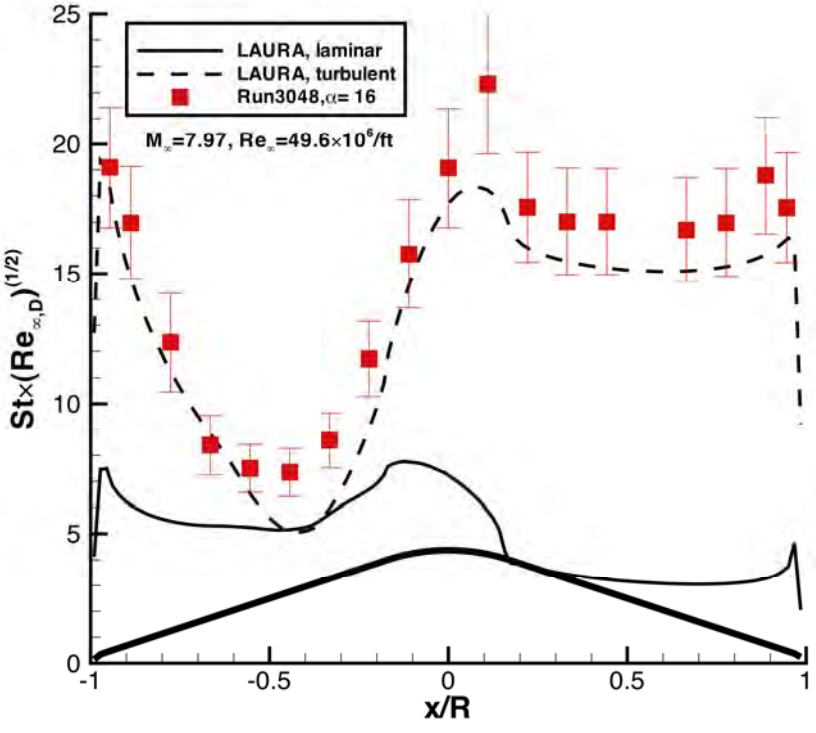

Mach 8, $Re_\infty = 50 \times 10^6$/ft

Figure 3-7: MSL Mach 8, α = 16-deg Data and Comparisons from AEDC Tunnel 9.

3.2.2 Orion Crew Exploration Vehicle Turbulent Flow

3.2.2.1 CUBRC LENS Testing of Orion CEV

Turbulent aeroheating testing of the Orion CEV vehicle was conducted [19] in the Calspan University of Buffalo Research Center (CUBRC) Large Energy National Shock Tunnel (LENS) I Hypervelocity Reflected Shock Tunnel [31]. The wind tunnel model was 14-in. (0.3556 m) in diameter and was instrumented with both coaxial thermocouples and thin-film gages. Runs were performed at Mach 8 with a 20-deg angle of attack for Reynolds numbers between 0.8×10^6/ft and 32×10^6/ft. Turbulent flow was produced on the leeside of the heat shield for Reynolds numbers of 9×10^6/ft and higher and turbulent flow was produced over the entire heat shield for Reynolds numbers of 23×10^6/ft and higher.

Predictions were performed using the DPLR [32] code for laminar flow and turbulent flow with Menter's SST model used for the turbulent cases at the conditions given in Table 3-2. Comparisons are shown in Figure 3-8 and Figure 3-9. Good agreement was achieved, although the turbulent data for the windward corner are not shown due to multi-dimensional conduction effects in the wind tunnel model for which corrections have not yet been generated.

Table 3-2: CEV Test Conditions for CUBRC LENS-I.

Run	α (deg)	Re_∞ (1/ft)	M_∞	P_∞ (Pa)	T_∞ (K)	ρ_∞ (kg/m^3)	U_∞ (m/s)
5	20	8.65E+05	7.64	260.8	79.8	0.0134	1371
11	20	3.10E+07	8.12	7791	74.4	0.366	1405
15	20	3.25E+07	7.96	8756	76.1	0.398	1396
21	20	29.7E+07	8.21	7033	71.7	0.339	1396

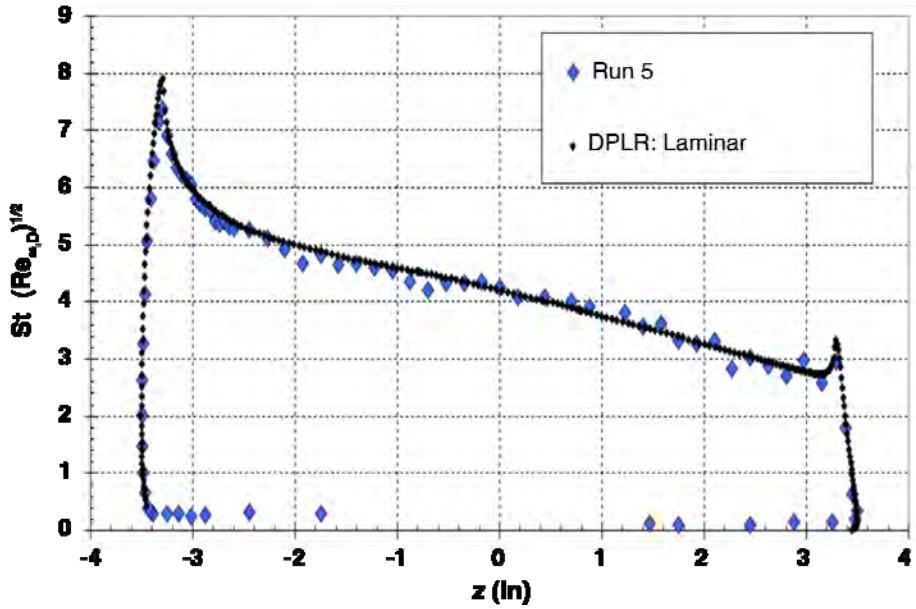

Figure 3-8: CEV Mach 8, α = 20-deg Laminar Data and Comparisons from CUBRC LENS-I.

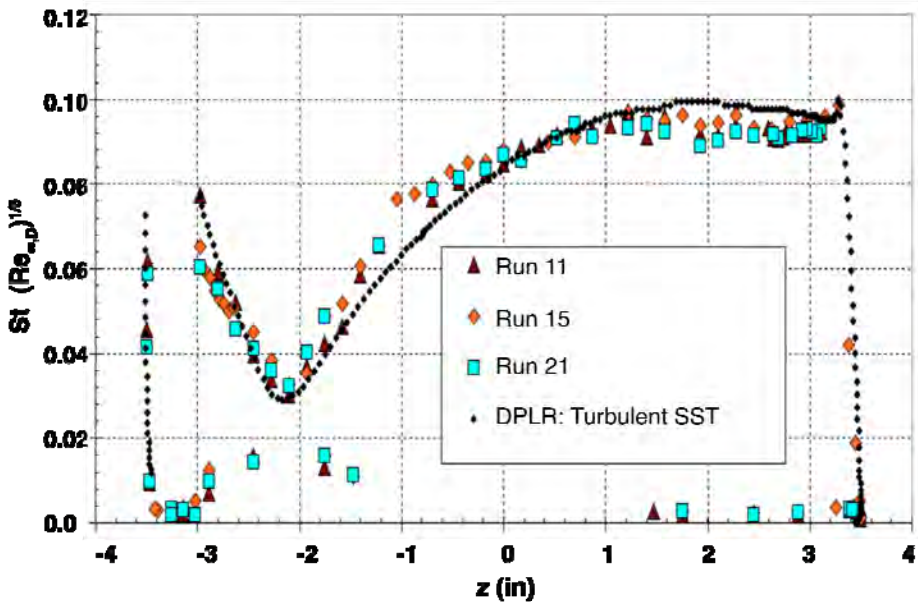

Figure 3-9: CEV Mach 8, α = 20-deg Turbulent Data and Comparisons from CUBRC LENS-I.

3.2.2.2 AEDC Tunnel 9 Testing of Orion CEV

Turbulent aeroheating testing of the Orion CEV vehicle was also conducted [22] in the AEDC Hypervelocity Wind Tunnel No. 9 on a 7-inch diameter, thermocouple-instrumented model in perfect-gas N_2 flow at the tunnels Mach 8 and Mach 10 test conditions. Angles-of-attack were varied from 16-deg to 32-deg. Free stream Reynolds numbers ranged from 8×10^6/ft to 48×10^6/ft at Mach 8 and from 2×10^6/ft to 20×10^6/ft at Mach 10. Transitional or turbulent flow was produced on the heat shield leeside for $Re_\infty \geq 10 \times 10^6$/ft for both Mach 8 and Mach 10, while for the higher Mach 8 Reynolds numbers ($Re_\infty \geq 32 \times 10^6$/ft), turbulent flow was also produced on the wind side of the heat shield. The experimental uncertainty of the data was estimated to be ±12%.

Laminar and turbulent perfect-gas comparisons to these data were performed using the LAURA code [30] with the algebraic Cebeci-Smith turbulent model being used for the turbulent cases. Comparisons between centerline data and predictions are shown for selected α = 28-deg cases in Figure 3-10 and Figure 3-11. Free stream conditions for these cases are listed in Table 3-3. For the Mach 10 cases (Figure 3-10), the laminar predictions and data were in close agreement at the $Re_\infty = 4 \times 10^6$/ft case, while at $Re_\infty = 19 \times 10^6$/ft, the laminar predictions matched the data on the windside of the forebody and the turbulent predictions matched the data on the leeside. For both Mach 8 cases (Figure 3-11), the turbulent predictions matched the data.

Table 3-3: CEV Test Conditions for AEDC Tunnel 9.

Run	α (deg)	Re_∞ (1/ft)	M_∞	P_∞ (Pa)	T_∞ (K)	ρ_∞ (kg/m^3)	U_∞ (m/s)
3058	28	4.58E+06	9.85	622	54.4	0.0358	1483
3061	28	1.97E+07	10.42	2120	48.4	0.148	1478
3076	28	3.07E+07	7.80	8290	74.1	0.378	1367
3073	28	4.79E+07	7.96	11800	70.6	0.566	1360

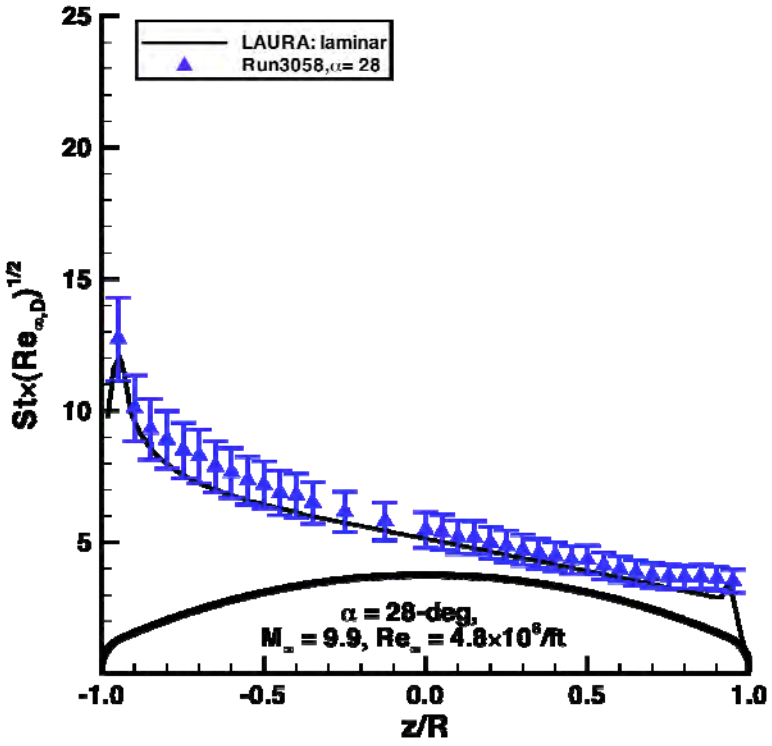

Mach 10, $Re_\infty = 4 \times 10^6$/ft

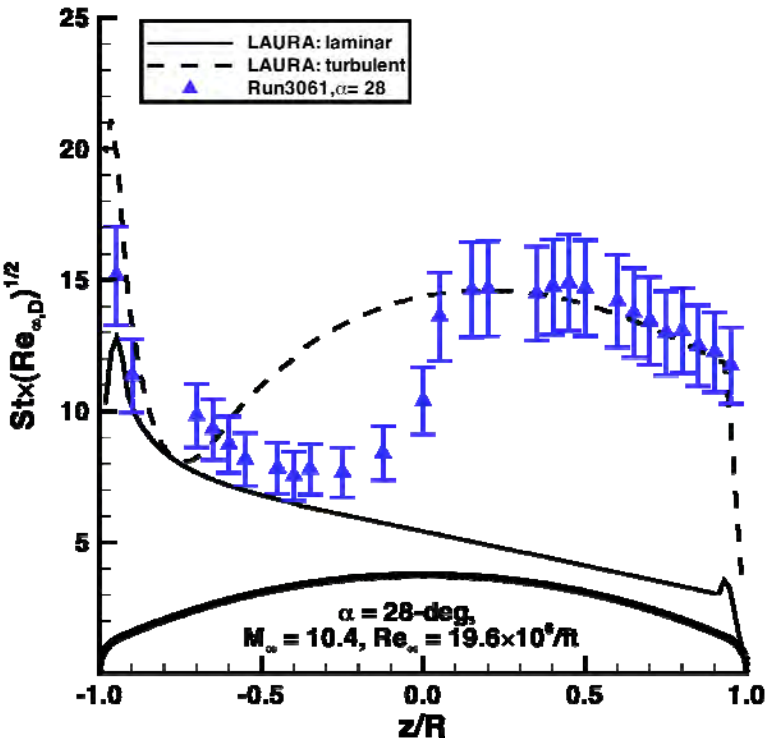

Mach 10, $Re_\infty = 20 \times 10^6$/ft

Figure 3-10: CEV Mach 10, α = 28-deg Data and Comparisons from AEDC Tunnel 9.

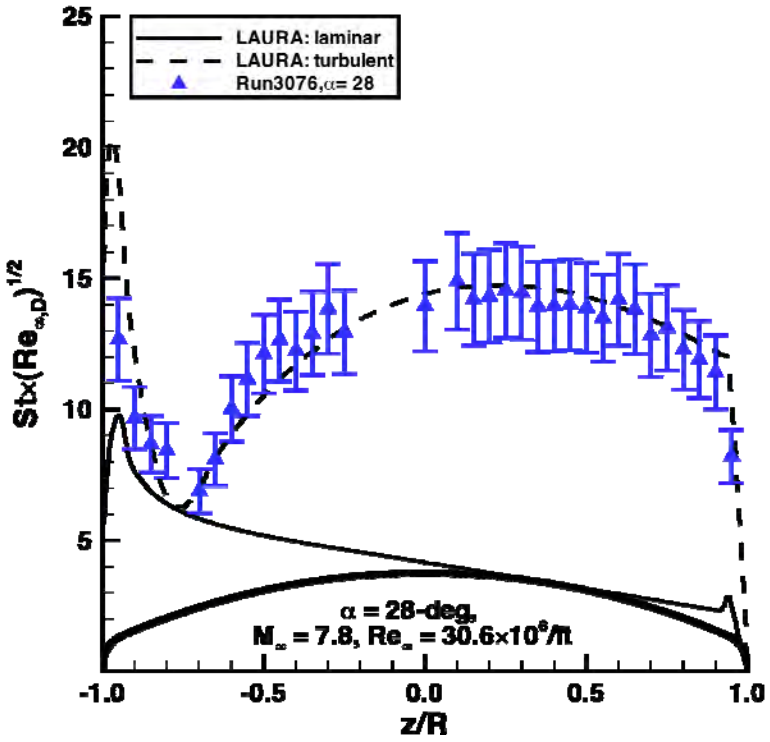

Mach 8, $Re_\infty = 31 \times 10^6$/ft

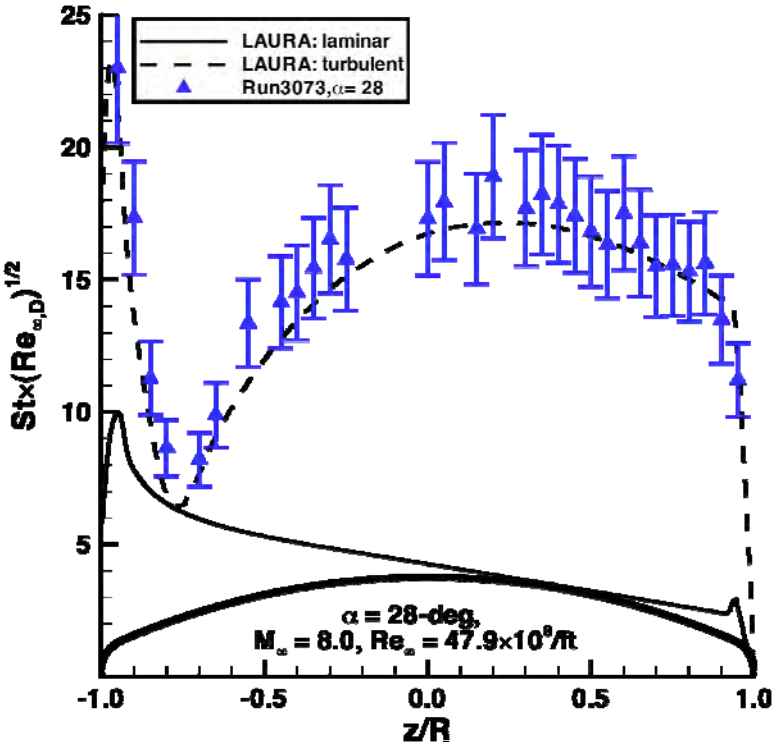

Mach 8, $Re_\infty = 48 \times 10^6$/ft

Figure 3-11: CEV Mach 10, α = 28-deg Data and Comparisons from AEDC Tunnel 9.

3.2.2.3 LaRC 20-Inch Mach 6 Air Testing of Orion CEV

An aeroheating test of the Orion CEV was conducted [21] in the NASA LaRC 20-Inch Mach 6 Air Tunnel [33]. Data were obtained on a 7-in. diameter model using the global phosphor thermography technique [34] with an estimated experimental uncertainty of ±10%. Testing was conducted at 28-deg angle of attack with free stream Reynolds numbers from of 2.0×10^6/ft to 7.3×10^6/ft. At these conditions, discrete boundary-layer trips located downstream of the stagnation point were required to produce fully-turbulent leeside flow.

Laminar and turbulent perfect-gas comparisons to these data were performed using the LAURA code [30] with the algebraic Cebeci-Smith turbulent model being used for the turbulent cases. Comparisons between centerline data and predictions are shown for selected α = 28-deg cases in Figure 3-12. Free stream conditions for these cases are listed in Table 3-4. Laminar predictions upstream of the trip locations were in good agreement with the data, as were both fully-turbulent and tripped boundary layer computations with the data downstream of the trip location.

Table 3-4: CEV Test Conditions for LaRC 20-Inch Mach 6 Air Tunnel.

Run	α (deg)	Re_∞ (1/ft)	M_∞	P_∞ (Pa)	T_∞ (K)	ρ_∞ (kg/m^3)	U_∞ (m/s)
3058	28	5.7E+06	6.0	1593	63.1	0.0881	958
3073	28	7.3E+07	6.0	2043	63.1	0.0113	959

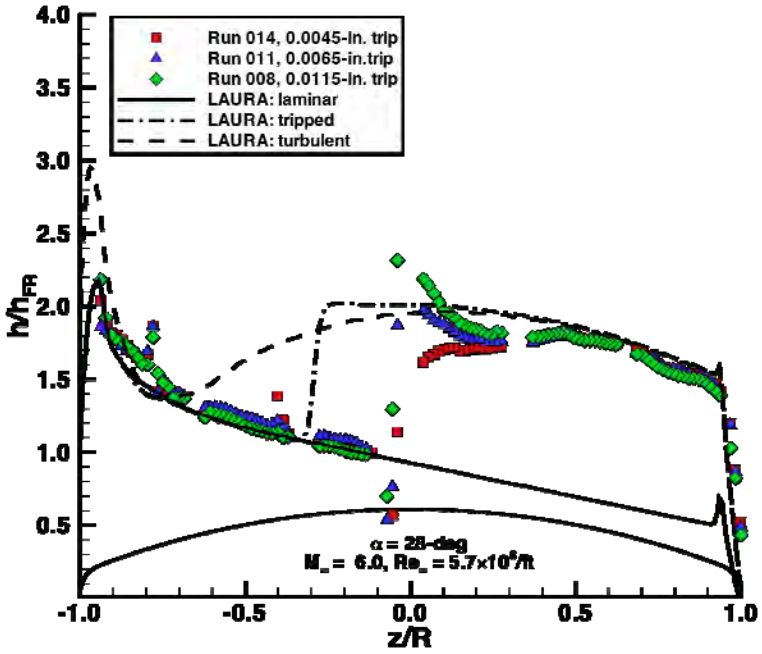

Mach 6, $Re_\infty = 5.7 \times 10^6$/ft

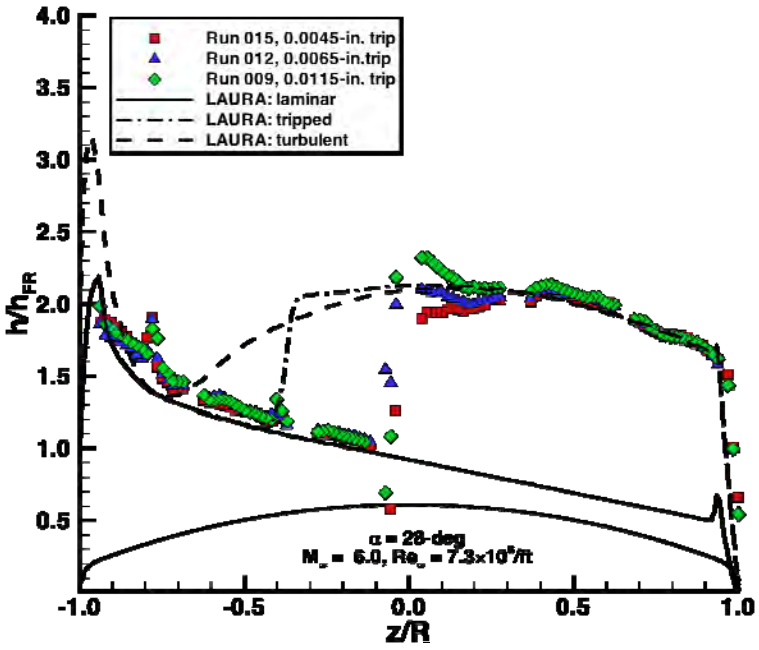

Mach 6, $Re_\infty = 7.3 \times 10^6$/ft

Figure 3-12: CEV Mach 6, α = 28-deg Data and Comparisons from LaRC 20-Inch Mach 6 Air Tunnel.

3.3 NON-EQUILIBRIUM BLUNT-BODY FLOW

At higher enthalpies such as experienced during atmospheric re-entry, chemical and vibrational non-equilibrium effects behind the shock wave become significant, especially for the strong shock waves

generated by blunt bodies. In comparison to perfect-gas or equilibrium problems, much more complex computational methods are required to model the various associated chemical reactions, vibrational excitation and relaxation rates, transport processes, and catalytic effects. Validation of these methods is challenging – few ground test facilities are capable of simulating these high enthalpies (let alone maintaining the correct Mach and Reynolds number levels) and collection of data from actual missions or flight tests is both expensive and technically complex.

As noted in the previous section, both the MSL and Orion CEV will experience atmospheric entry at relatively high speeds (CEV at ~11 km/s at Earth and MSL at ~5 km/s at Mars), which, in addition to producing transition to turbulence, will also produce thermochemical non-equilibrium effects. Test programs have been conducted for both missions with the goal of obtaining high-enthalpy heating data for code validation purposes.

3.3.1 Mars Science Laboratory Non-Equilibrium Flow

3.3.1.1 CUBRC LENS Testing of MSL

Testing of the MSL entry vehicle was performed with CO_2 as the test gas in the LENS I reflected shock tunnel [5]-[8] to obtain high-enthalpy, turbulent aeroheating data. Two tests were conducted; one with a 24-in. (0.6096 m) diameter model with thin-film gages and coaxial surface thermocouples and one with a 12-in. (0.3048 m) diameter model with coaxial surface thermocouples, thin-film gages, and calorimeter gages. Testing was conducted at enthalpies in the 5 MJ/kg to 10 MJ/kg range at angles-of-attack of 0-deg to 20-deg. Supporting CFD simulations for these tests were performed using both the DPLR [32] and LAURA [30] codes. Discussion herein will focus on a 5 MJ/kg, 0-deg angle-of-attack, 12-in. model case with conditions listed in Table 3-5.

Table 3-5: MSL Test Conditions for CUBRC LENS-I.

Run	α (deg)	Re_∞ (1/ft)	M_∞	P_∞ (Pa)	T_∞ (K)	ρ_∞ (kg/m^3)	U_∞ (m/s)	$[CO_2]$	[CO]	$[O_2]$	[O]
8	0	1.14E+05	6.2	1613	892	0.00896	2871	0.8630	0.0872	0.0497	0.0001

Owing to the presence of significant levels of free stream vibrational non-equilibrium these tests were not ideal for the stated goal of obtaining high-fidelity data for CFD validation. The presence of free stream vibrational non-equilibrium was noted when comparisons of predicted and measured shock shapes (e.g., Figure 3-13) were found to have large differences that were not evident in CO_2 tests in other facilities or in the LENS-X expansion tunnel (Figure 3-14). However, these data did highlight several critical issues for CFD simulation of high-enthalpy flows including: the requirement for including free stream non-equilibrium vibrational excitation in a reflected shock tunnel simulation; the uncertainties in the application of Park's two-temperature model [35] to CO_2; the uncertainties in surface catalytic models for CO_2 (both for actual vehicle heat shield materials and for metallic wind tunnel model surfaces); and the interactions between vibrational excitation, transport processes, and surface catalytic effects on heating.

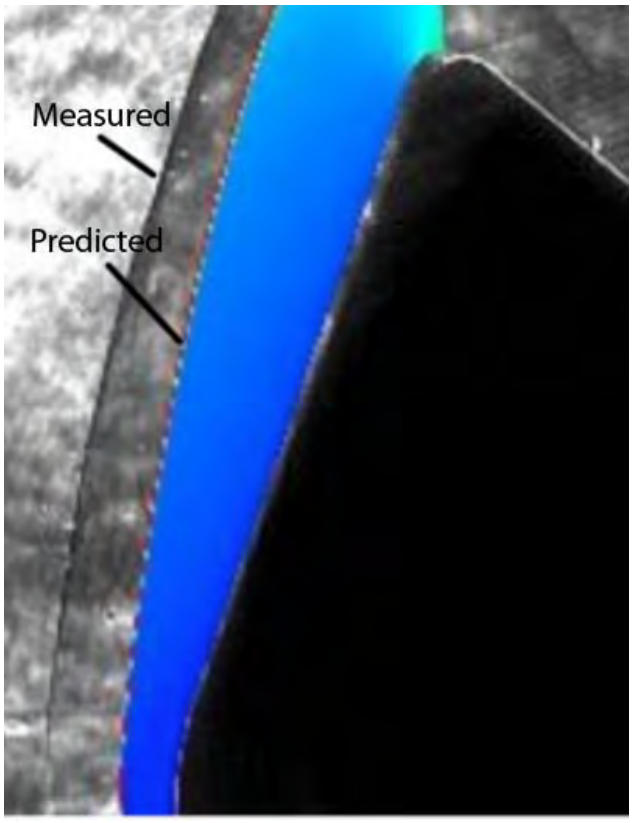

Figure 3-13: Comparison Between Measured and Predicted Shock Shape for MSL in CUBRC LENS-I.

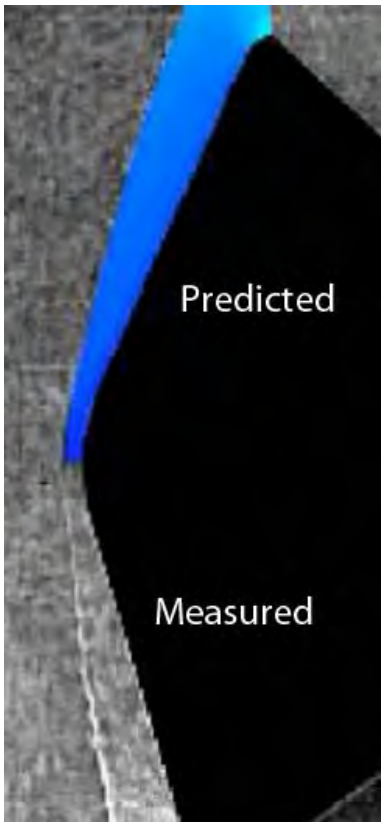

Figure 3-14: Comparison Between Measured and Predicted Shock Shape for MSL in CUBRC LENS-X.

The hypothesized presence of frozen vibrational flow in the free stream led to examination of the validity of Park's two-temperature translational/vibrational temperature model for simulation of CO_2. Unlike the diatomic N_2 and O_2 molecules for which Park developed this model, that have a single vibrational mode, the tri-atomic CO_2 molecule has three vibrational modes. Current CFD codes employed in the design of MSL (LAURA and DPLR) use variations of Park's model (with different options available for modeling the vibrational relaxation rates). It was estimated that the resultant sensitivities in the existing two-temperature model options could introduce at least a ±1% uncertainty in the MSL vehicle's trim angle during certain parts of the trajectory, while the actual accuracy of the two-temperature model itself is unknown. Such uncertainties have the potential to significantly affect the landing accuracy of the vehicle.

The wall boundary catalytic efficiency assumption was found to have a large effect on the predicted heat-transfer rates as shown in Figure 3-15. At laminar conditions, the predictions matched the data better when the assumption of a fully-catalytic wall (recombination to free stream species concentrations) was made, whereas predictions with a non-catalytic wall were much lower than the data. However, it is questionable whether the wind tunnel model material could truly behave as a super-catalytic surface.

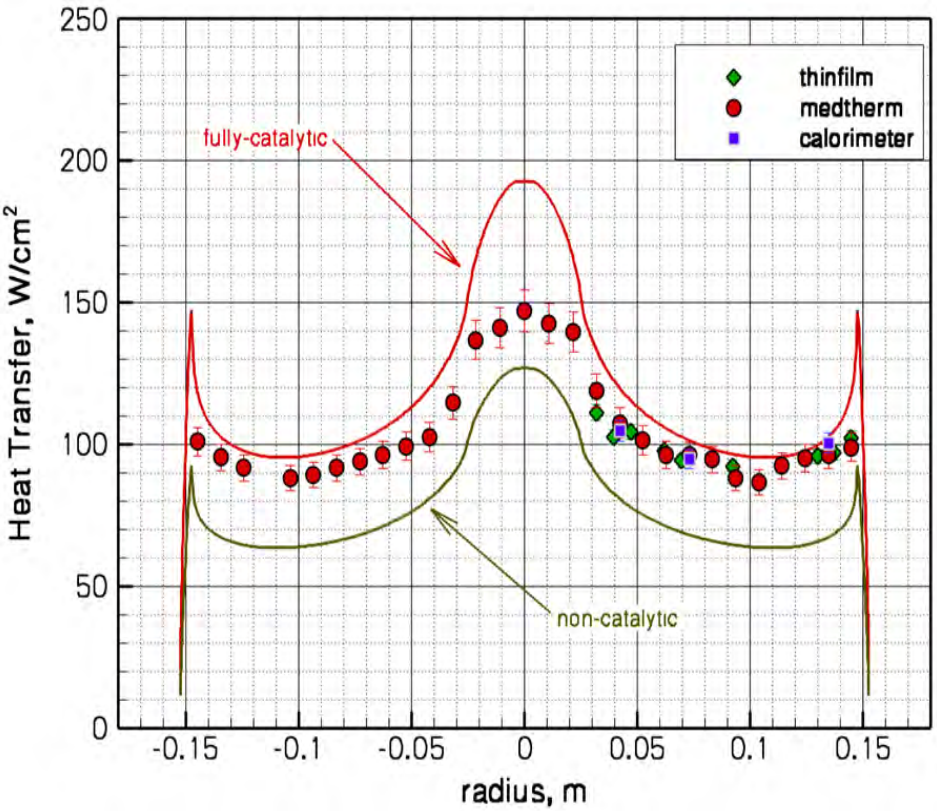

Figure 3-15: Comparison Between Super-Catalytic and Non-Catalytic Heating Predictions for MSL 12-in. Model, CUBRC Run 8.

As noted previously, differences in the predicted and measured shock shapes led to the theory that vibrational non-equilibrium effects were present in the free stream. While the actual free stream state in the facility could not be accurately determined, a parametric computational analysis [8] was performed using the DPLR [32] code in which the assumed energy in the vibrational mode was varied until the predicted shock-shapes could be brought into agreement with the measured data. As shown in Figure 3-16 the free stream vibrational non-excitation also had a significant effect on the computed stagnation region heating. It was found that an assumed free stream vibrational non-equilibrium level of ~42% was required to reconcile the measured and predicted shock stand-off distance; although these levels are high, they are smaller magnitude than the reservoir non-equilibrium levels. Similar effects were also found for assumed fractions of free stream chemical non-equilibrium.

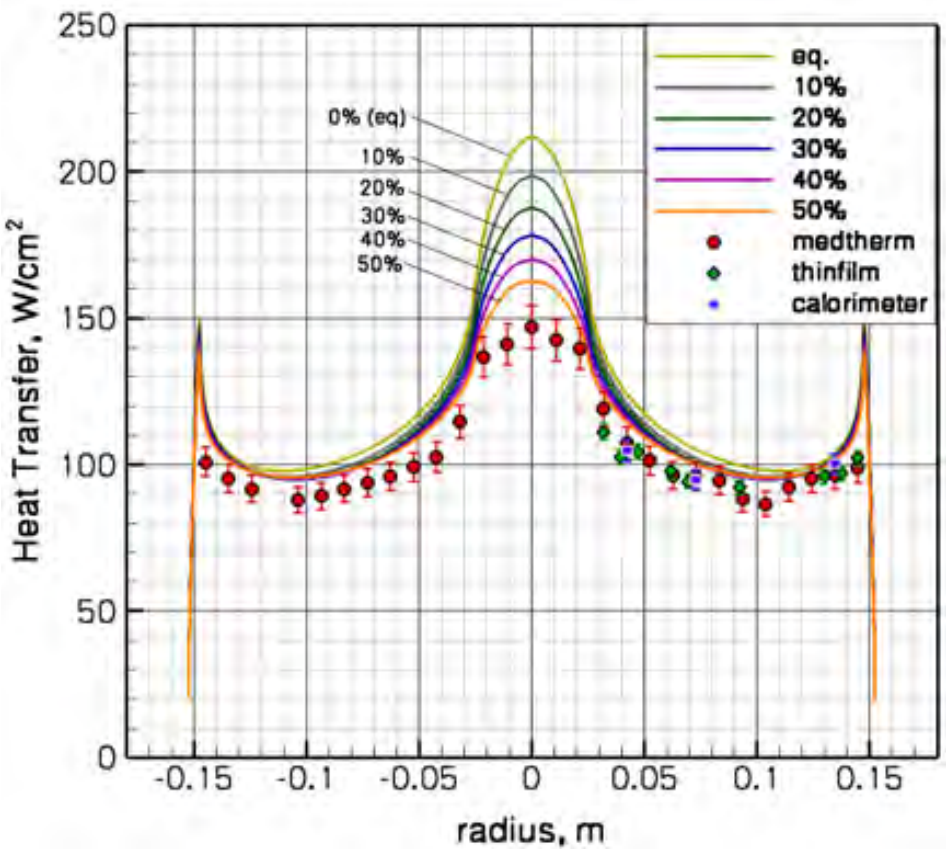

Figure 3-16: Effects of Free Stream Vibrational Non-Equilibrium on Heating Predictions for MSL 12-in. Model, CUBRC Run 8.

3.3.1.2 CalTech T5 Testing of MSL

Testing of the MSL entry vehicle was also conducted in CO_2 test gas in the California Institute of Technology (CalTech) T5 reflected shock tunnel [11]. The wind tunnel model had a 7-inch (0.1778 m) diameter and was instrumented with coaxial surface thermocouples. Enthalpy levels varied from 5 MJ/kg to 15 MJ/kg and angles-of-attack varied from 0-deg to 16-deg. Supporting CFD predictions were performed using the DPLR [32] code. Test conditions for sample cases are given in Table 3-6.

Table 3-6: MSL High-Enthalpy Test Conditions for CalTech T5.

Run	α (deg)	Re_∞ (1/ft)	T_∞ (K)	ρ_∞ (kg/m^3)	U_∞ (m/s)	H0 (MJ/kg)	$[CO_2]$	[CO]	$[O_2]$	[O]
2257	11	2.21E+05	2342	0.0549	3550	11.7	0.5379	0.2989	0.1357	0.0274
2258	11	6.68E+05	1351	0.0156	2552	4.9	0.9549	0.0301	0.0151	0.0000

At the test conditions generated in T5, the free-stream vibrational non-equilibrium problem experienced in the CUBRC LENS tests did not appear to be significant since predicted and measured shock shapes were found to be in close agreement. However, the question of surface catalysis was still found to be important. As shown in Figure 3-17, at conditions for which the boundary layer was assumed to be fully laminar,

the data and predictions were found to be in relatively close agreement with the assumption of a super-catalytic boundary wall boundary conditions – that is, full recombination to free stream species distributions. However, for conditions at which the boundary layer was assumed to be fully turbulent, the data and predictions were found to agree best when the opposite assumption of a non-catalytic wall boundary condition was made, as shown in Figure 3-18.

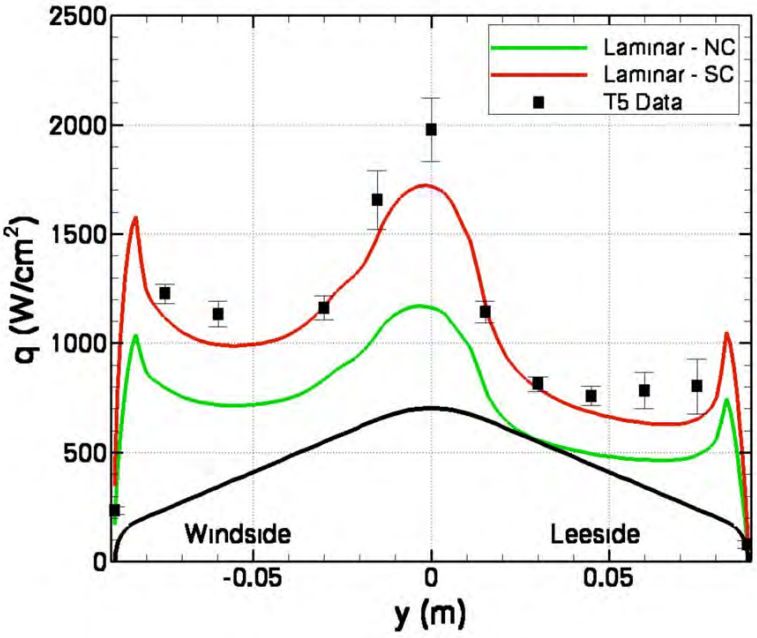

Figure 3-17: Comparison Between Super-Catalytic and Non-Catalytic Laminar Heating Predictions for MSL in CalTech T5 Run 2257.

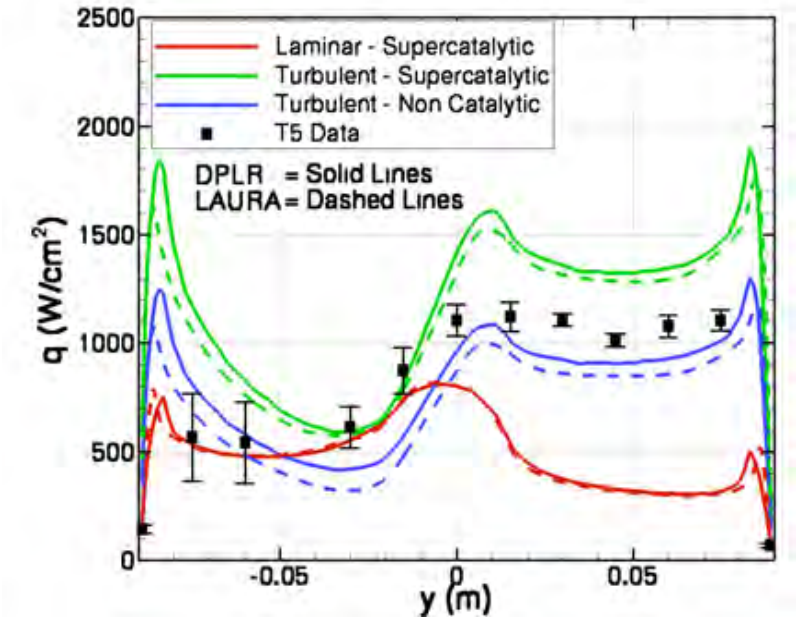

Figure 3-18: Comparison Between Super-Catalytic and Non-Catalytic Turbulent Heating Predictions for MSL in CalTech T5 Run 2258.

The comparison in Figure 3-18 is for turbulent predictions using the algebraic Baldwin-Lomax model, with an assumed turbulent Schmidt number of 0.5. A small, but noticeable effect on predicted heating levels for the super-catalytic case – but not the non-catalytic case – was noted when the turbulent Schmidt numbers was varied, as shown in Figure 3-19. Additional CFD analyses were performed in which the Baldwin-Lomax model was replaced with Menter's Shear-Stress Turbulent (SST) model as shown in Figure 3-20. While both factors were found to have significant effects on predicted turbulent heating levels, neither effect was large enough to reconcile super-catalytic predictions with the turbulent data.

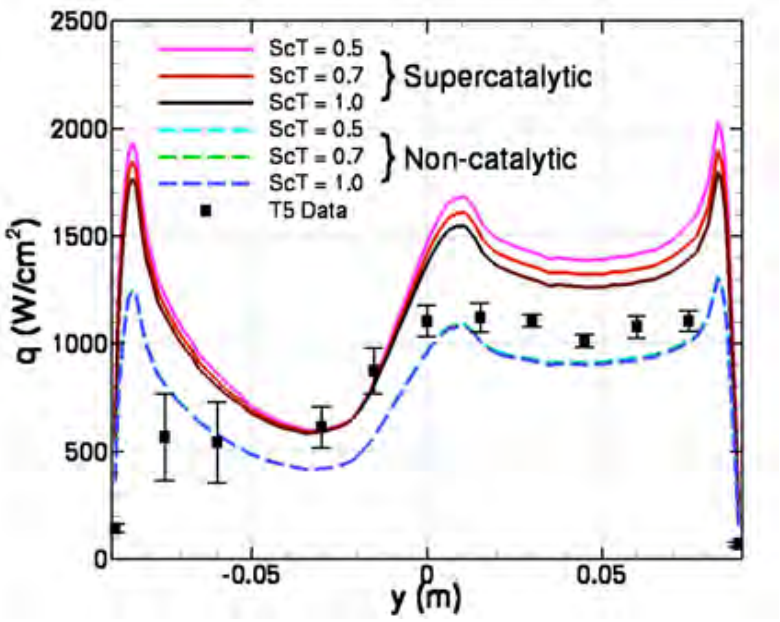

Figure 3-19: Effect of Turbulent Schmidt Number on Predictions for MSL in CalTech T5 Run 2258.

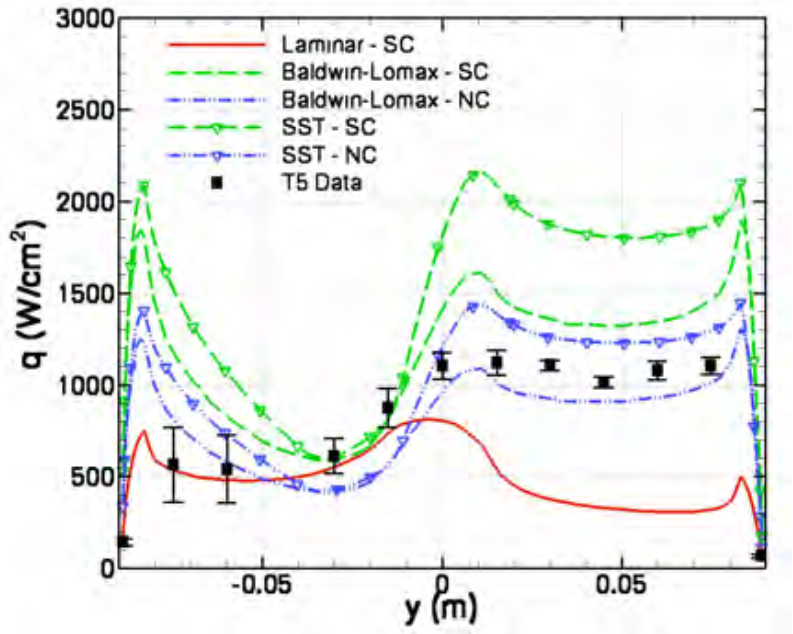

Figure 3-20: Comparison Between Turbulence Models Predictions for MSL in CalTech T5 Run 2258.

These results from CalTech T5 and the results from CUBRC LENS in the previous section further highlight the development and validation problems in the modeling of turbulence, catalysis, and chemical and vibrational rates that must be addressed to increase the fidelity on non-equilibrium CO_2 flow field prediction methods. This problem will become greater in importance as future Mars mission requirements call for larger landed masses that lead to greater entry velocities and thus higher heating levels.

3.3.2 Orion Crew Exploration Vehicle Non-Equilibrium Flow

High-enthalpy testing of an Orion CEV-like geometry was conducted in the CUBRC LENS-I facility in both air and nitrogen [17]. The model size 5.74-in. (0.167 m) in diameter and was instrumented with coaxial surface thermocouples. Data were obtained for angle-of-attack of 0-deg and 28-deg in N_2 at a ~10 MJ/kg total enthalpy and in air at total enthalpies of ~2 MJ/kg to 12 MJ/kg. Sample test conditions for air cases are given in Table 3-7.

Table 3-7: CEV High-Enthalpy Test Conditions for CUBRC LENS-I.

Run	α (deg)	T_∞, $T_{V\infty}$ (K)	U_∞ (m/s)	H_0 (MJ/kg)	$\rho_{\infty,N2}$ (kg/m^3)	$\rho_{\infty,O2}$ (kg/m^3)	$\rho_{\infty,NO}$ (kg/m^3)	$\rho_{\infty,O}$ (kg/m^3)
7	28	57	1805	1.7	6.798E-03	2.144E-03	0.000E+00	0.000E+00
8	28	191	2949	4.8	2.431E-03	6.529E-04	2.339E-04	1.902E-06
9	28	494	4054	9.2	1.214E-03	3.035E-04	9.108E-05	3.402E-05
10	28	631	4601	12.4	7.939E-04	1.493E-04	6.347E-05	6.949E-05

Predictions were performed using the DPLR [32] code with non-catalytic, finite-catalytic, and super-catalytic wall boundary conditions. For the N_2 cases, good agreement with data was observed with small levels of finite catalysis. Results (Figure 3-21 – Figure 3-24) were less consistent for the air cases; at the lower enthalpy levels, a close agreement was observed with the super-catalytic boundary condition, whereas at the higher enthalpy levels better agreement was observed with the non-catalytic boundary conditions. In these figures, it can also be seen that the disagreement between measured and predicted surface pressure increased with enthalpy. Additionally, increasing differences between the measured and predicted shock shapes (Figure 3-25) were observed with increasing enthalpy; this could indicate either the presence of un-accounted for chemical/vibrational freezing in the free stream or an inadequacy in the chemical/vibrational computational modeling for air.

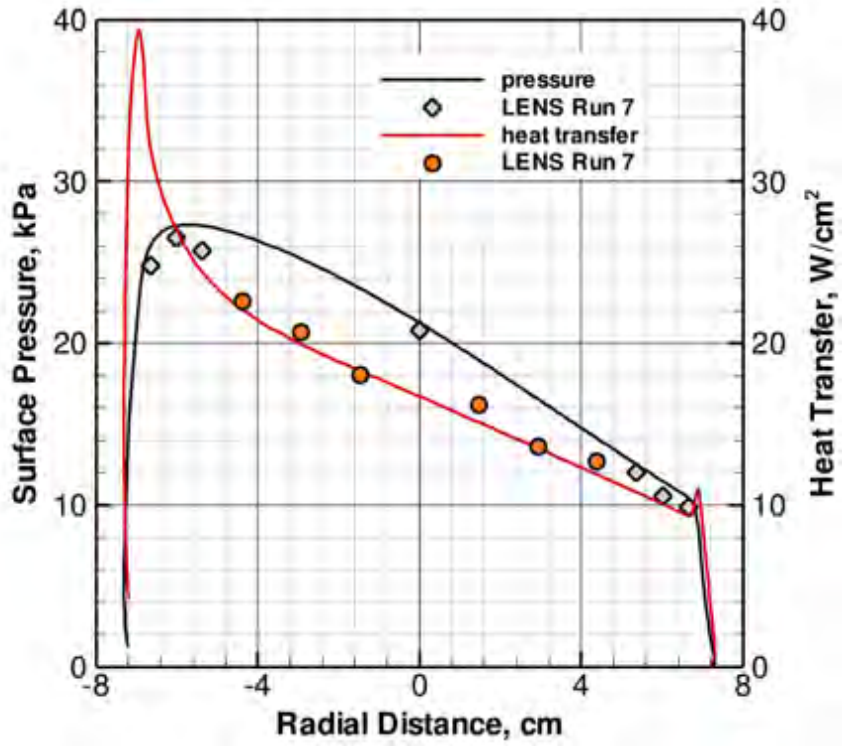

Figure 3-21: Comparison Between CEV Data and Predictions for CUBRC Run 7, 1.7 MJ/kg Enthalpy.

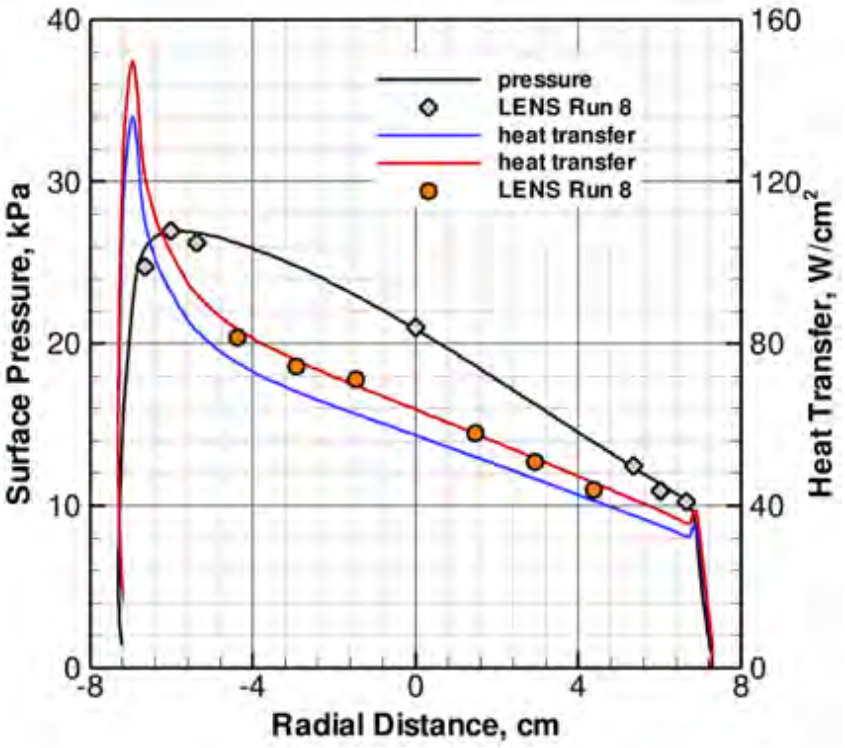

Figure 3-22: Comparison Between CEV Data and Predictions for CUBRC Run 8, 4.8 MJ/kg Enthalpy.

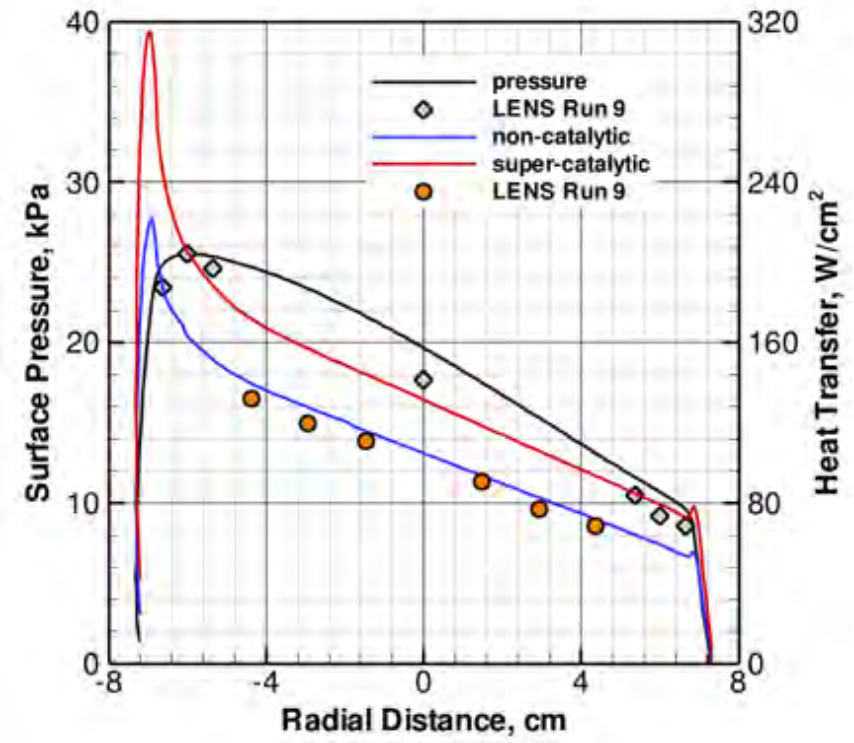

Figure 3-23: Comparison Between CEV Data and Predictions for CUBRC Run 9, 9.2 MJ/kg Enthalpy.

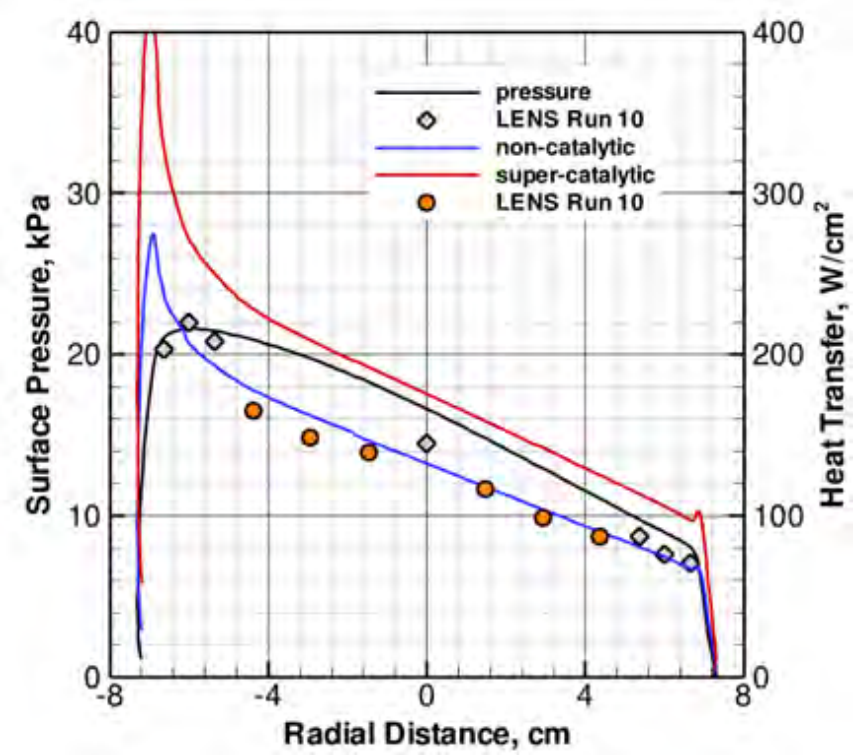

Figure 3-24: Comparison Between CEV Data and Predictions for CUBRC Run 10, 12.4 MJ/kg Enthalpy.

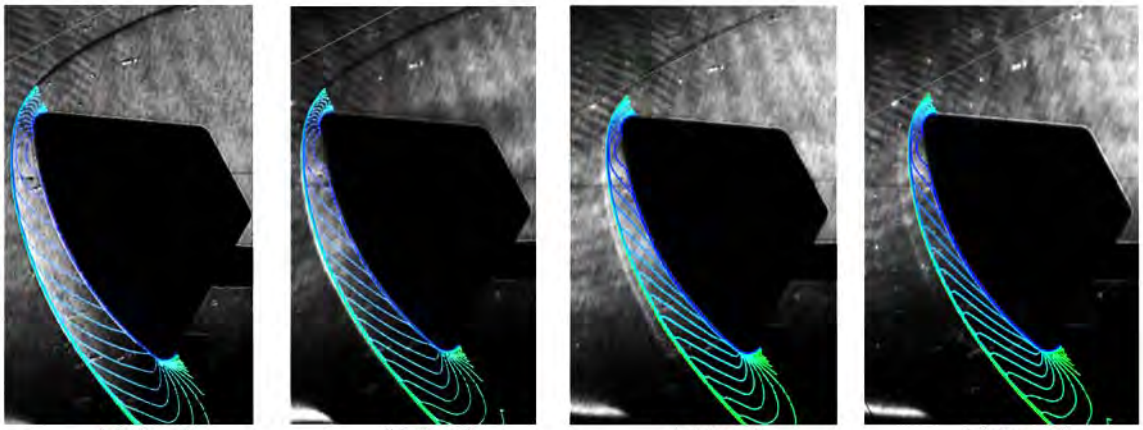

Figure 3-25: Comparison Between Measured and Predicted Shock Shape for CUBRC High-Enthalpy CEV Test.

3.4 RAREFIED FLOW

Rarefied flow effects are of importance in high-altitude hypersonic flows where the continuum assumptions inherent to Navier-Stokes based computational tools are inadequate. Comparisons of rarefied flow predictions with experimental data have been previously reported for an MSL-like configuration in [36] and [37] and little new work has since been performed. As for the CEV, there have as yet been no rarefied flow experiments performed and so aerothermodynamic analyses have been limited to computational studies.

A study [38] has been performed to investigate the overlap between rarefied-flow DSMC computations and continuum-flow Navier-Stoked computations. In this study, the baseline conditions (Table 3-8) suggested for the CEV are representative of conditions that would take place during the re-entry trajectory from the International Space Station (ISS).

Table 3-8: Representative ISS Mission Free-Stream Conditions.

Altitude (km)	α (deg)	T_∞ (K)	U_∞ (m/s)	ρ_∞ (kg/m^3)	n_∞ (#/m^3)	$X_{\infty,O2}$	$X_{\infty,N2}$	$X_{\infty,N}$	T_w (K)	Kn_∞	Computational Method
75	0	200	7600	4.34E-05	9.01E+20	0.2372	0.7628	0.0000	1464	0.0003	CFD
85	0	181	7600	7.96E-06	1.65E+20	0.2372	0.7628	0.0000	1184	0.0019	CFD & DSMC
95	0	189	7600	1.38E-06	2.90E+19	0.1972	0.7869	0.0159	951	0.01	CFD & DSMC
105	0	211	7600	2.30E-07	4.98E+18	0.1528	0.7819	0.0653	760	0.06	DSMC
115	0	304	7600	4.36E-08	9.86E+17	0.0979	0.7539	0.1484	618	0.32	DSMC
125	0	433	7600	1.31E-08	3.06E+17	0.0768	0.7117	0.2115	494	1.0	DSMC

The focus of this work was mainly on the 85 km and 95 km cases; for these two trajectory points, both DSMC and CFD computations were performed in order to evaluate a comparison between molecular approach (i.e., DSMC) and continuum one (i.e., CFD with and without slip flow boundary conditions).

As shown in Figure 3-26 and Figure 3-27, surface heating rates computed using DSMC were approximately 10% higher than the CFD results; it is also noticeable that the DSMC results do not indicate the slight rise in heating at the shoulder predicted by the CFD results.

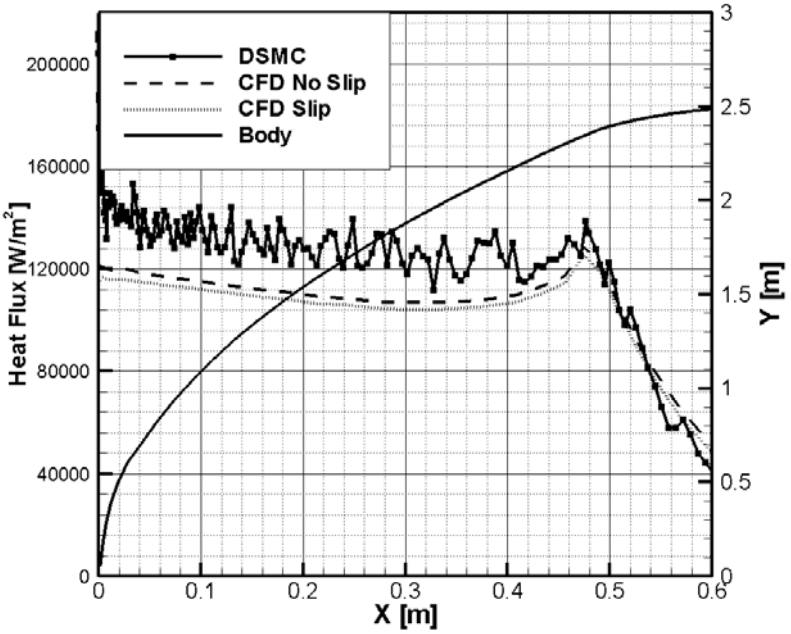

Figure 3-26: CEV Heat Flux at 85 km.

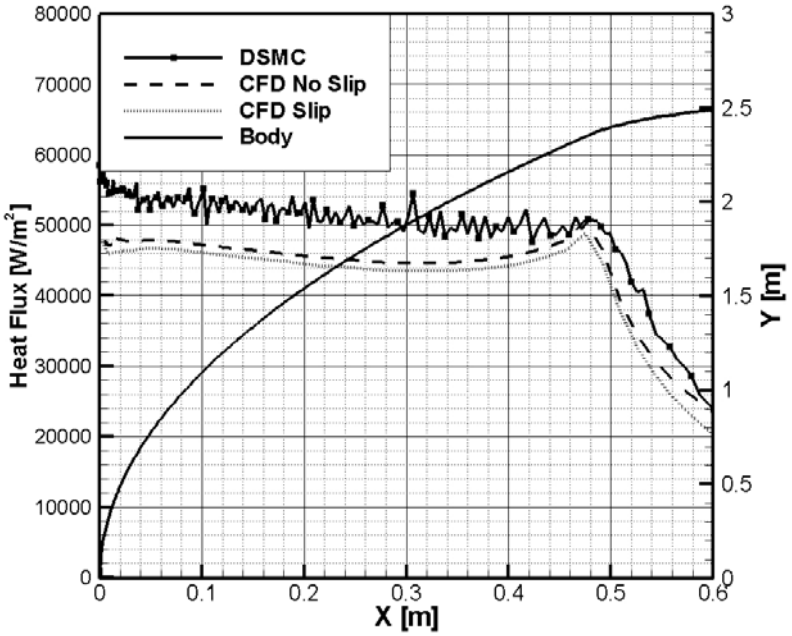

Figure 3-27: CEV Heat Flux at 95 km.

An evaluation of the chemical and conductive contributions to the global heat flux is shown in Figure 3-28 for a fully-catalytic boundary condition at 85 km. In particular, it can be seen that the chemical contribution to the heat flux calculated by CFD is very close to that from DSMC, while the conductive

contribution is much lower, thus generating a nearly 10% lower total heat flux as predicted by CFD. This difference in global heat flux is shown again for a non-catalytic wall case at 95 km in Figure 3-29. It is interesting to note that in the non-catalytic case the percentage difference between CFD and DSMC results increases from about 10% to 60%, but the absolute value of this difference is the same as for fully catalytic wall; this confirms that the discrepancy is not due to the chemical part of the heat flux, but from the conductive one. The same considerations apply to the altitude 95 km case.

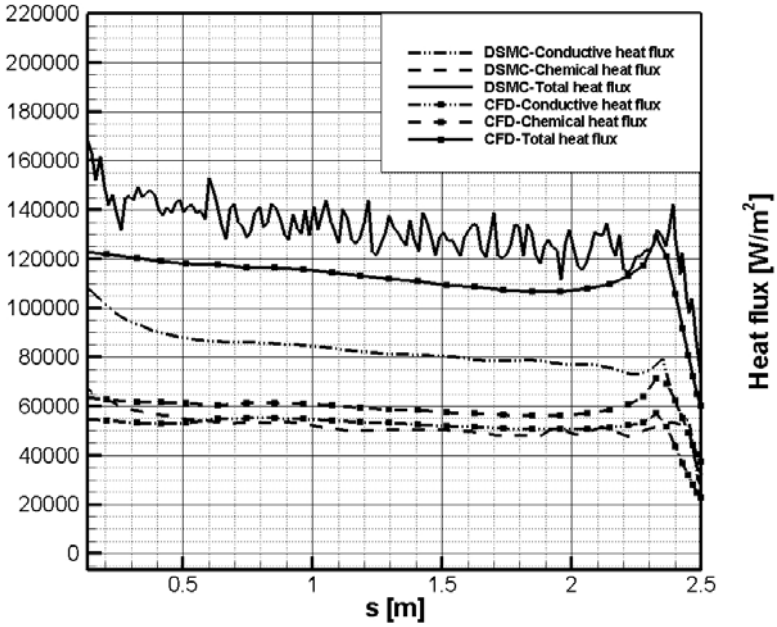

Figure 3-28: Chemical and Conductive Contributions to CEV Heat Flux at 85 km with Fully Catalytic Wall.

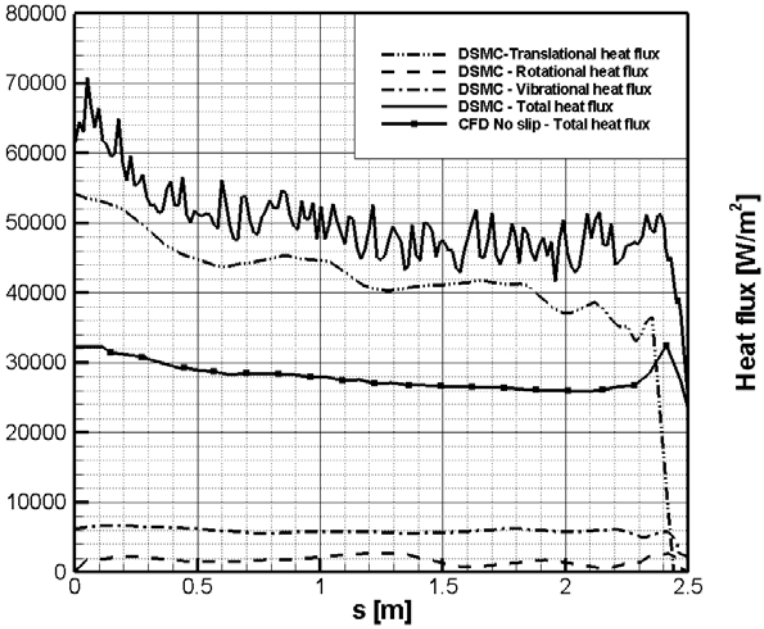

Figure 3-29: Chemical and Conductive Contributions to CEV Heat Flux at 95 km with Non-Catalytic Wall.

The stagnation point heat flux predictions for all cases are summarized in Figure 3-30. As a reference, results obtained through the Fay-Riddell formula, typically used for preliminary design of the Thermal Protection Systems, have been also reported. In the overlap (between 85 km and 95 km), where both modeling methods could be applied, DSMC results are to be preferred for the more correct modeling of rarefaction effects and for more conservative design margins.

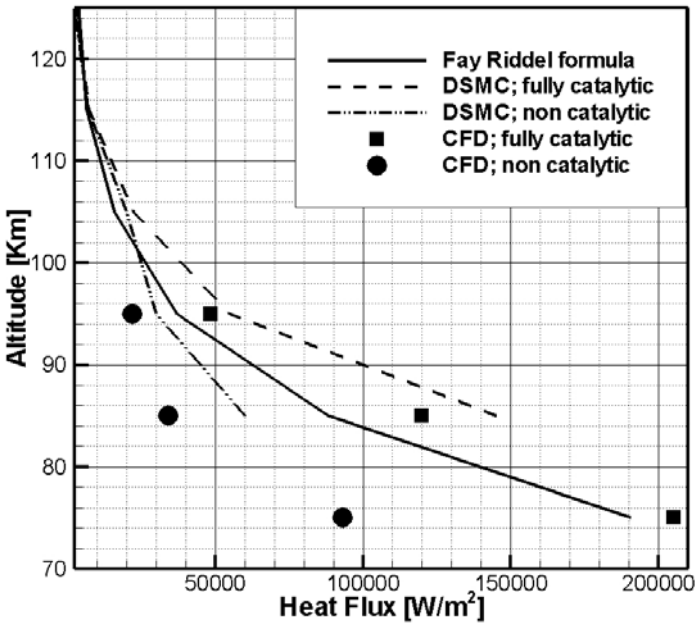

Figure 3-30: Stagnation Point Heat-Flux Predictions vs. Altitude.

3.5 RADIATION TRANSPORT

Radiation transport becomes an increasingly large contributor to the re-entry vehicle heating environment as either the entry velocity or body diameter increase. In the case of blunt re-entry vehicle such as Apollo or the Orion CEV, radiative heat-transfer can be of equal to, or greater, magnitude than the convective heating at points along the trajectory. Ground testing capabilities for radiative heating effects on entry vehicles are extremely limited; most ground testing in this field consists of optical diagnostics of shock-tube flows (e.g., [39]) rather than the testing of actual wind tunnel models with radiative heating measurements (e.g., [40]). The acquisition of flight test data is also challenging both due to the cost and complexity of instrumentation and measurements as well as the difficulty of separating radiative heating effects from those of convective heating and ablation cooling of real TPS systems.

3.5.1 FIRE-II Radiation Transport

Numerous studies have been published with comparisons to the FIRE II data; however most of these studies applied older computational tools and methods that are no longer in use. One of the most recent studies [41] was conducted using the HARA radiation transport code [42]-[43]. The HARA code includes detailed line radiation models based on the latest National Institute of Standards and Technology (NIST) atomic data, a smeared rotational band model for molecular radiation, and non-Boltzmann populations of excited states. In this study, the radiation transport code and a viscous shock-layer code were run in a loosely-coupled mode in order to account for the flow field energy loss due to radiation.

Computations were performed for each of the three heat-shields at the times given in Table 3-9. Radiation-flow field coupling was found to reduce the radiative heating by up to 30%. It was also found that the

radiation from the vacuum-ultraviolet region, which was neglected in some prior studies, was a significant contributor to the total flux. Comparisons were made between predicted and inferred radiative stagnation-point heat flux in the (0 eV – 6 eV) and in the (6 eV – 18 eV) ranges as shown in Table 3-10. The 'inferred' radiative heat flux for the (6 eV – 18 eV) range is taken to be the measured *total* heating at the calorimeter (radiative + convective) minus the integrated spectrometer measurement for the (0 eV – 6eV) range, minus the *predicted* convective heat flux computed using either non-catalytic or super-catalytic surface boundary conditions assumption. This inference was necessary because there were no direct measurements of total radiative heat-flux; rather, measurements were made of total heat flux and both spectral and integrated radiative intensities (over different frequency intervals). The actual heat-shield surface catalytic effective would have been somewhere between these two extremes; note that at the theoretical upper bound of super-catalytic effectiveness, it would actually be necessary for the radiative heating to be negative since the predicted super-catalytic convective result exceeds the total calorimeter measurement.

Table 3-9: FIRE-II Flight Test Points.

Time (sec)	Alt. (km)	ρ_∞ (kg/m^3)	U_∞ (km/s)	T_∞ (K)	T_{WALL} (K)	Heat-shield
1634.0	76.42	3.72E-5	11.36	195	6.15	First
1636.0	71.02	8.57E-5	11.31	210	810	First
1637.5	67.05	1.47E-4	11.25	228	1030	First
1640.5	59.62	3.86E-4	10.97	254	1560	First
1643.0	53.04	7.80E-4	10.48	276	640	Second
1645.0	48.37	1.32E-3	9.83	285	1520	Third
1648.3	41.60	3.25E-3	8.1	267	503	Third

Table 3-10: Comparison of Predicted and Inferred Absorbed Radiative Flux for FIRE-II.

	(0 eV – 6 eV) Range			(6 eV – 18 eV) Range				
Time (sec)	Measured Flux (W/cm^2)	Predicted Flux (W/cm^2)	% Difference	Inferred Super-Catalytic Flux (W/cm^2)	Inferred Non-Catalytic Flux (W/cm^2)	Predicted Flux (W/cm^2)	Super-Catalytic % Difference	Non-Catalytic % Difference
1634.0	3.4	4.5	32%	-45.4	58.6	10.1	NA	-83%
1636.0	12.9	14.2	10%	26.9	90	36.3	35%	-60%
1637.5	31.4	29.8	-5%	-1.6	126	71.3	NA	-43%
1640.5	81.7	95.2	17%	133	258	166.6	25%	-35%
1643.0	151	135.2	-10%	141	220	179.4	27%	-18%
1645.0	63.9	91	42%	259	345	85.8	-67%	-75%
1648.3	8.1	267	503	-16	64	10.5	NA	-84%

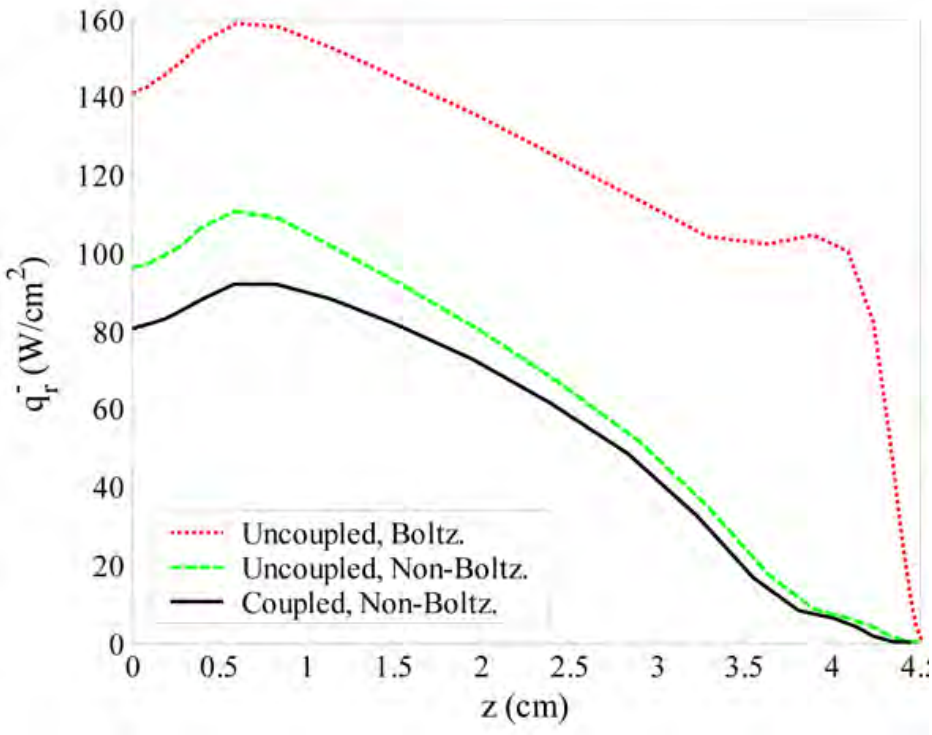

Figure 3-31: FIRE-II, t = 1636 sec: Stagnation Line Radiative Flux Computations Showing Effects of Flow Field / Radiation Coupling.

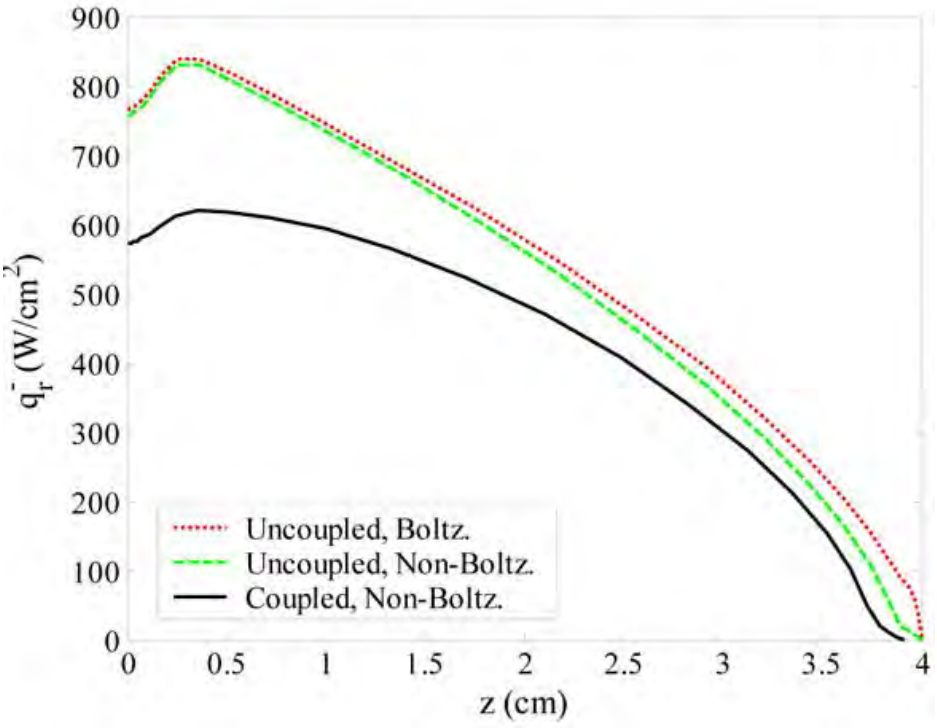

Figure 3-32: FIRE-II, t = 1643 sec: Stagnation Line Radiative Flux Computations Showing Effects of Flow Field / Radiation Coupling.

3.6 SUMMARY, CONCLUSIONS, AND RECOMMENDATIONS

Several examples have been presented in which modern computational tools and methods have been compared to either ground test or flight test data on blunt body re-entry vehicles. These comparisons have highlighted the effectiveness of the computations at predicting the effects of physical phenomena such as turbulence, chemical and vibrational non-equilibrium, rarefied flow, and radiation transport.

Of these phenomena, the best comparisons have been obtained for turbulent data. However these studies were all performed at perfect-gas conditions, and thus there still exists the need to validate computational models at non-equilibrium conditions for both Earth and Mars atmospheric environments.

With respect to non-equilibrium, greater discrepancies have been found between data and predictions. The accuracy of chemical and vibrational models has not been fully-validated, especially for Martian CO_2 environments. Additionally, there are difficulties in the analysis of the experimental data itself, both due to the issue of free stream non-equilibrium effects in the test facilities and due to the difficulty in determining the actual catalytic efficiency of the test model.

The validation of radiative transport models is the least advanced, owing both to the complexity of the physical phenomena and to the difficulty of performing ground test simulations or obtaining flight test data. Furthermore, computational predictions are challenging as both flow-field and radiation-transport methods must be coupled in order to properly model the physics of the problem.

Detailed information on each of the test cases presented herein is available and it is recommended that each be studied further in detail and used in the assessment of modern computational tools. However, these data sets themselves have significant uncertainties and are not inclusive enough of all physical situations to be considered adequate to fully-validate numerical tools used in the design of an actual re-entry vehicle. At best, these data can help to provide conservative upper bounds on the uncertainties of predictive methods. It is therefore recommended that both ground testing and flight testing of blunt body aerothermodynamic phenomena, coupled to computational predictions and analysis, be rigorously pursed, and that aerothermodynamic instrumentation be included as an integral part of all future missions.

3.7 REFERENCES

[1] Davies, C., “Planetary Mission Entry Vehicles Quick Reference Guide, Version 3.0”, NASA SP-2006-3401, 2006.

[2] Prakash, R., et al., “Mars Science Laboratory Entry, Descent, and Landing System Overview”, IEEE Paper 2008-1531, IEEE Aerospace Conference, Big Sky, MT, USA, March 1-8 2008.

[3] Edquist, K.T., Dyakonov, A.A., Wright, M.J. and Tang, C.Y., “Aerothermodynamic Design of the Mars Science Laboratory Heatshield”, AIAA Paper 2009-4075, 41st AIAA Thermophysics Conference, San Antonio, TX, USA, June 22-25 2009.

[4] Wright, M.J., Beck, R.A.S., Edquist, K.T., et al., “Sizing and Margins Assessment of the Mars Science Laboratory Aeroshell Thermal Protection System”, AIAA Paper 2009-4231, 41st AIAA Thermophysics Conference, San Antonio, TX, USA, June 22-25 2009.

[5] Hollis, B.R., Liechty, D.S., Wright, M.J., Holden, M.S., Wadhams, T.P. and MacLean, M., “Transition Onset and Turbulent Heating Measurements for the Mars Science Laboratory Entry Vehicle”, AIAA Paper 2005-1437, 43rd AIAA Aerospace Sciences Meeting and Exhibit, Reno, NV, USA, January 10-13 2005.

[6] MacLean, M., Wadhams, T., Holden, M. and Hollis, B.R., "Investigation of Blunt Bodies with CO_2 Test Gas Including Catalytic Effects", AIAA Paper 2005-4693, 38th AIAA Thermophysics Conference, Toronto, Ontario, Canada, June 6-9 2005.

[7] MacLean, M. and Holden, M., "Catalytic Effects on Heat Transfer Measurements for Aerothermal Studies with CO2", AIAA Paper 2006-0182, 44th AIAA Aerospace Sciences Meeting and Exhibit, Reno, NV, USA, January 9-12 2006.

[8] MacLean, M. and Holden, M., "Numerical Assessment of Data in Catalytic and Transitional Flow for Martian Entry", 9th AIAA/ASME Joint Thermophysics and Heat Transfer Conference, San Francisco, CA, USA, June 5-8 2006.

[9] Liechty, D.S., Hollis, B.R. and Edquist, K.T., "Mars Science Laboratory Experimental Aerothermodynamics with Effects of Cavities and Control Surfaces", *Journal of Spacecraft and Rockets*, Vol. 43, No. 2, pp. 340-353, March – April 2006.

[10] Hollis, B.R. and Liechty, D.S., "Transition Due to Heat-Shield Cavities on a Mars Entry Vehicle", *Journal of Spacecraft and Rockets*, Vol. 43, No. 2, pp. 354-366, March – April 2006.

[11] Wright, M.J., Olejniczak, J., Brown, J.L., Hornung, H.G. and Edquist, K.T., "Modeling of Shock Tunnel Aeroheating Data on the Mars Science Laboratory Aeroshell", *Journal of Thermophysics and Heat Transfer*, Vol. 20, No. 4, pp. 641-651, October – December 2006.

[12] Hollis, B.R. and Collier, B.R., "Turbulent Aeroheating Testing of Mars Science Laboratory Entry Vehicle", *Journal of Spacecraft and Rockets*, Vol. 45, No. 3, pp. 417-427, May – June-2008.

[13] Anon., "NASA's Exploration Systems Architecture Study, Final Report", NASA TM-2005-214062, November 2005.

[14] Grinstead, J.H., Wilder, M.C., Olejniczak, J., Bogdanoff, D.W., Allen, G.A., Dang, K. and Forrest, M.J., "Shock-Heated Air Radiation Measurements at Lunar Return Conditions", AIAA Paper 2008-1244, 46th AIAA Aerospace Sciences Meeting and Exhibit, Reno, NV, USA, January 7-10 2008.

[15] Amar, A.J., Horvath, T.J., Hollis, B.R., Berger, K.T., Berry, S.A. and Calvert, N., "Protuberance Boundary Layer Transition for Project Orion Crew Entry Vehicle", AIAA Paper 2008-1227, 46th AIAA Aerospace Sciences Meeting and Exhibit, Reno, NV, USA, January 7-10, 2008.

[16] Liechty, D.S., "Aerothermodynamic Testing of Protuberances and Penetrations on the NASA Crew Exploration Vehicle Heat Shield", AIAA Paper 2008-1240, 46th AIAA Aerospace Sciences Meeting and Exhibit, Reno, NV, USA, January 7-10 2008.

[17] MacLean, M., Mundy, E., Wadhams, T., Holden, M. and Parker, R., "Analysis and Ground Test of Aerothermal Effects on Spherical Capsule Geometries", AIAA Paper 2008-4273, 38th Fluid Dynamics Conference and Exhibit, Seattle, WA, USA, June 23-26 2008.

[18] Hollis, B.R., "Heating Augmentation in Laminar Flow Due to Heat-Shield Cavities on the Project Orion CEV", AIAA Paper 2008-6558, AIAA Atmospheric Flight Mechanics Conference and Exhibit, Honolulu, HI, USA, August 18-21 2008.

[19] Wadhams, T.P., Cassady, A.M., MacLean, M. and Holden, M.S., "Experimental Studies of the Aerothermal Characteristics of the Project Orion CEV Heat Shield in High Speed Transitional and Turbulent Flows", AIAA Paper 2009-0677, 47th AIAA Aerospace Sciences Meeting, Orlando, FL, USA, January 5-8 2009.

[20] Hollis, B.R., "Heating Augmentation Due to Compression Pad Cavities on the Project Orion CEV Heat Shield", AIAA Paper 2009-3843, 41st AIAA Thermophysics Conference, San Antonio, TX, USA, June 22-25 2009.

[21] Berger, K.T., "Aerothermodynamic Testing of the Crew Exploration Vehicle at Mach 6 and Mach 10", *Journal of Spacecraft and Rockets*, Vol. 46, No. 4, pp.758-765, July – August 2009.

[22] Hollis, B.R., Berger, K.T., Horvath, T.J., Coblish, J.J., Norris, J.D., Lillard, R.P. and Kirk, B.S., "Aeroheating Testing and Predictions for Project Orion Crew Exploration Vehicle", *Journal of Spacecraft and Rockets*, Vol. 46, No. 4, pp.766-780, July – August 2009.

[23] Berry, S.A., Horvath, T.J., Lillard, R.P., Kirk, B.S. and Cassady, A.M., "Aerothermal Testing for Project Orion Crew Exploration Vehicle", AIAA Paper 2009-3842, 41st AIAA Thermophysics Conference, San Antonio, TX, USA, June 22-25 2009.

[24] Lewis, J.H., Jr. and Scallion, W.I., "Flight Parameters and Vehicle Performance for Project Fire Flight II, Launched May 22, 1965", NASA TN-D-3569, August 1966.

[25] Richardson, N.R., "Project Fire Instrumentation for Radiative Heating and Related Measurements", NASA TN-D-3646, October 1966.

[26] Cornette, E.S., "Forebody Temperatures and Calorimeter Heating Rates Measured During Project Fire II Reentry at 11.35 Kilometers per Second", NASA TM-X-1305, November 1966.

[27] Cauchon, D.L., McKee, C.W. and Cornette, E.S., "Spectral Measurements of Gas-Cap Radiation During Project Fire Flight Experiments at Reentry Velocities Near 11.4 Kilometers per Second", NASA TM-X-1389, October 1967.

[28] Cauchon, D.L., "Radiative Heating Results from the Fire II Flight Experiment at a Reentry Velocity of 11.4 Kilometers per Second", NASA TM-X-1402, July 1967.

[29] Marren, D. and Lafferty, J., "The AEDC Hypervelocity Wind Tunnel 9", Advanced Hypersonic Test Facilities, Progress in Aeronautics and Astronautics, Vol. 198, American Institute of Aeronautics and Astronautics, Reston, VA, USA, pp. 467-477, 2002.

[30] Cheatwood, F.M. and Gnoffo, P.A., "User's Manual for the Langley Aerothermodynamic Upwind Relaxation Algorithm (LAURA)", NASA TM 4674, April 1996.

[31] Holden, M.S., Wadhams, T.P. and Candler, G.V., "Experimental Studies in the LENS Shock Tunnel and Expansion Tunnel to Examine Real-Gas Effects in Hypervelocity Flows", AIAA Paper 2004-0916, January 2004.

[32] Wright, M.J., Candler, G.V. and Bose, D., "Data-Parallel Line Relaxation Methods of the Navier Stokes Equations", *AIAA Journal*, Vol. 36, No. 9, pp. 1603-1609, 1998.

[33] Micol, J.R. "Langley Aerothermodynamic Facilities Complex: Enhancements and Testing Capabilities", AIAA Paper 98-0147, January 1998.

[34] Merski, N.R., "Global Aeroheating Wind-Tunnel Measurements Using Improved Two-Color Phosphor Thermography Methods", *Journal of Spacecraft and Rockets*, Vol. 36, No. 2, pp. 160-170, March – April 1999.

[35] Park, C., "Assessment of Two-Temperature Kinetic Model for Ionizing Air", *Journal of Thermophysics and Heat Transfer*, Vol. 3, No. 3, pp. 233-244, July 1989.

[36] "Hypersonic Experimental and Computational Capability, Improvement and Validation", Edited by Saric, W.S., Muylaert, J. and Dujarric, C., AGARD AR-319, Vol. I, May 1966.

[37] "Hypersonic Experimental and Computational Capability, Improvement and Validation", Edited by Muylaert, J., Kumar, A. and Dujarric, C., AGARD AR-319, Vol. II, December 1998.

[38] Votta, R., Schettino, A., Ranuzzi, G. and Borrelli, S., "Hypersonic Low Density Aerothermodynamics of Orion-Like Exploration Vehicle", *Journal of Spacecraft and Rockets*, Vol. 46, No. 4, pp. 781-787, AIAA-42663-356, July – August 2009.

[39] Grinstead, J.H., Wilder, M.C., Olejniczak, J., Bogdanoff, D.W., Allen, G.A., Dang, K. and Forrest, M.J., "Shock-Heated Air Radiation Measurements at Lunar Return Conditions", AIAA Paper 2008-1244, 46th AIAA Aerospace Sciences Meeting and Exhibit, Reno, NV, USA, January 7-10 2008.

[40] Capra, B.R., Leyland, P. and Morgan, R.G., "Subscale Testing of the FIRE II Vehicle in a Superorbital Expansion Tube", AIAA Paper 2004-1298, 42nd AIAA Aerospace Sciences Meeting and Exhibit, Reno, NV, USA, January 5-8 2004.

[41] Johnston, C.J., Hollis, B.R. and Sutton, K., "Nonequilibrium Stagnation-Line Radiative Heating for Fire II", *Journal of Spacecraft and Rockets*, Vol. 45, No. 6, pp. 1185-1195, 2008.

[42] Johnston, C.O., Hollis, B.R. and Sutton, K., "Spectrum Modeling for Air Shock Layers at Lunar Return Conditions", *Journal of Spacecraft and Rockets*, Vol. 45, No. 5, pp. 865-878, September – October 2008.

[43] Johnston, C.O., Hollis, B.R. and Sutton, K., "Non-Boltzmann Modeling for Air Shock Layers at Lunar Return Conditions", *Journal of Spacecraft and Rockets*, Vol. 45, No. 5, pp. 879-890, September – October 2008.

Chapter 4 – BOUNDARY-LAYER TRANSITION

Steven P. Schneider
Purdue University
USA

4.1 TOPIC OVERVIEW

Hypersonic laminar-turbulent transition is one of the key unresolved issues in aerothermodynamics. Since the AVT has no resources of its own, it can only serve to coordinate efforts that are funded by the various member countries. The problem is complex and difficult, so the AVT-136 effort could make only an incremental advance. Since transition often depends on many subtle factors, and is known to depend on the freestream disturbance environment, it is important to perform both experiments and computations in several locations using different facilities and personnel [14]. Each contributor benefits from iteratively comparing their results to the results of others. In addition, no single wind tunnel can simulate all aspects of hypersonic flight, so it is important to compare results from various facilities which can each simulate different aspects. This is particularly important because the facilities and associated instrumentation are very expensive and time consuming to develop. Computational simulations are also complex, involve numerous simplifying assumptions that differ between codes, and are time consuming to develop. Therefore, transition work under AVT-136 focused on developing an international cooperation that compares experiments and computations in several Nations, funded by the various national governments, and coordinated towards a goal of common interest. Such a cooperation is complex and time consuming, so the 3-year time-frame of AVT-136 could serve only as a beginning. Introductory information is omitted here, as the reader is assumed to be familiar with the field.

4.2 OVERVIEW OF AGREED FOCUS: TRANSITION ON CIRCULAR CONES NEAR ZERO ANGLE OF ATTACK IN WIND TUNNELS AND FLIGHT

This configuration has been chosen because it is relevant to efforts that can be funded in several NATO countries. The Italian team supporting USV is studying transition on circular cones. The German DLR has taken an interest in both computational simulations and experiments in the high-enthalpy shock tunnel HEG. The experiments in the HEG are to follow similar experiments in the high-enthalpy HIEST shock tunnel operated by JAXA in Japan, with which the DLR has an exchange agreement. The Technical University at Braunschweig in Germany has made measurements in their Mach-6 Ludwieg-tube tunnel. The Mach-6 blowdown tunnel at DLR Cologne has also been used for related measurements. In the U.S., a small-bluntness slender cone is to be flight tested as HIFiRE-1, which led to experimental measurements at the LENS shock tunnels at CUBRC, the Mach-6 blowdown tunnel at NASA Langley, and the Mach-6 quiet Ludwieg tube tunnel at Purdue. Sandia National Laboratory has an interest in the pressure fluctuations under transitional flow, which led to support for instability and transition measurements at Sandia and elsewhere. The HIFiRE-1 effort also led to computational simulations at the University of Minnesota and NASA Langley. The Minnesota STABL code is being used to compute instability-wave growth for comparison to the results at Langley, CUBRC, Purdue, Sandia, AEDC Tunnel 9, Braunschweig, HEG, and HIEST. The STABL code is also being used for comparisons to flight data. The DLR NOLOT code is being used for comparison to the STABL results.

The HIFiRE-1 flight geometry has a 7.0-deg. half angle and a 2.5-mm nose radius; the various researchers are all studying 7-deg. half-angle cones with small nose radii, although the actual nose radius that is used depends on scaling arguments and local conditions. In all cases, the second-mode instability is expected to dominate transition. The experimental research generally includes measurements of the second-mode wave amplitudes as well as the tunnel noise and transition location. At least three computational codes are

being used to compare the second-mode wave amplification. Different models are being built using the instrumentation and methods appropriate to the various facilities. Transition is to be measured with similar instrumentation, to the extent feasible. In most cases, the model includes transducers for measuring the surface pressure fluctuations. The surface pressure fluctuations under laminar flow will be used to estimate the noise level in the various tunnels, so both the transition location and the noise level can be compared, as in the classic work of Dougherty and Fisher (1980) [5] at lower speeds. Measurements are to be made at various unit Reynolds numbers. In HEG and HIEST, measurements are being made at various enthalpy levels, at the same Mach and Reynolds numbers, to improve understanding of the effect of gas chemistry. These high-enthalpy measurements are being compared to stability analyses provided by the University of Minnesota.

4.3 PLANNED HIFiRE-1 FLIGHT TESTS

Planning for the HIFiRE-1 flight test began ca. 2006, as described in [9]. A cone-cylinder-flare with a 7-deg. conical half-angle is to be flown from a Terrier-Orion launch vehicle at the Woomera range in Australia. Transition is to be measured on the nose-cone during re-entry, at a Mach number near 7. Although angle of attack is to be minimized, non-zero values remain probable during transition. The nose radius of 2.5 mm was selected as large enough to be readily survivable but small enough to permit relatively low-Reynolds number transition that should be dominated by second-mode instabilities. The conical section is about 1.1 m long. The flight has experienced the usual delays but is now expected during 2010. Of course, there are many difficulties involved in implementing flight tests; one of the bigger challenges will involve making useful measurements as the cone nutates during re-entry.

Kimmel (2008a) [10] discusses the surface roughness on the flight vehicle. The roughness on the nosetip and at the joints between the vehicle sections is to be smooth enough to avoid affecting transition. Near the nose, this may not be trivial to attain, given the uncertainty in the requirements and the various correlations, and also given the exotic materials needed to withstand the high temperatures expected on the small-radius non-ablating nose. Since there is much uncertainty about the location where transition may occur on the smooth body during re-entry, an isolated roughness was added to the design. This isolated roughness is to trip transition on one side of the vehicle even at relatively high altitude, so that trip-induced transition can be measured, even if the smooth side remains laminar to lower altitudes where the vehicle slows to supersonic speeds.

Kimmel (2008b) [11] provides a summary of the computations and experiments carried out for the aerothermal analysis. The effect of gas dissociation is insignificant, and vibrational excitation has a small effect. An N-factor of 10 was used to extrapolate the wind-tunnel measurements to flight. The effects of wall temperature, angle of attack and tunnel noise are all discussed.

4.4 CUBRC MEASUREMENTS AND COMPUTATIONS FOR HIFiRE-1

Wadhams et al. (2008) [20] describe the measurements in the large shock tunnel at Buffalo, over Mach 6.5 to 7.4. Thin-film heat-transfer gauges were used to characterize intermittency and transition, and pulsed laser Schlieren images are also shown. Fast PCB132 piezoelectric pressure sensors have been used to measure second-mode waves in blowdown tunnels and Ludwieg tubes, and were here used in the first such attempt in a shock tunnel, which was not yet successful. The model was a full-scale version of the HIFiRE-1 vehicle, with a 7-deg. half-angle cone that is 1.1 m long and 275 mm in diam. The cone is followed by a cylinder section and a flare, which is used for study of shock/boundary-layer interaction. Wadhams et al. measured with a sharp nose, a 2.5-mm nose radius, and a 5.0-mm nose. The flight velocity was duplicated along with the Mach number, so the freestream temperature is nearly the same as flight, although the wall temperature is lower than flight. Pitot-pressure measurements found freestream fluctuations of 0.25 – 0.5 %; the amplitude decreased with frequency.

Earlier measurements (reported in detail in [19]) were used to select the 2.5-mm nose radius, since a 5-mm nose radius delayed transition to the cone-cylinder junction. At Mach 6.5 to 7.2, and freestream Reynolds numbers of 16.4 to 9.8 million per meter, transition onset appears near 0.3 to 0.4 m from the nose, at zero angle of attack [20]. When the nosetip was heated from room temperature to about 440 K, transition was mostly unaffected. Wadhams et al. also show a sequence of Schlieren images and thin-film records which show the passage of turbulent spots along the cone.

A small diamond-shaped roughness is to be attached to the flight vehicle on one side, 525 mm from the tip, to ensure the occurrence of hypersonic transition despite limited Reynolds numbers. The trip is 10 mm on a side and 2 mm high. Although the run conditions are not labeled in [20] Figs. 25 – 27, it appears that the roughness generated transition onset midway down the cone, even at a freestream Reynolds number of 3 million per meter.

Computational efforts are reported in [12] and [20]. The Univ. of Minnesota STABL package was used to obtain Navier-Stokes mean-flow solutions and then linear parabolized stability analyses. The laminar heat transfer agreed well with the simulation. Transition onset appeared near where the most-amplified second-mode wave was computed to have a linear amplification of e^6 (N = 6). The seven cases computed in [12] yielded N factors of 4.9 to 6.8, with an average of 5.7. MacLean et al. (2008) [12] point out that the flight test should have lower noise than conventional ground tests, and also that the wall temperature in flight will be much higher than in the shock tunnel, perhaps near radiative equilibrium. Using radiative equilibrium, MacLean et al. compute a surface temperature in flight that falls from 1800 – 2100 K near the nose to about 1200 – 1300 K near 0.1 m to about 1000 K near the end of the cone. For the Mach 7.2 flight point, the cold ground-test wall-temperature distribution yielded N = 6.8 at about 0.45 m (their Figure 9), while the hot flight-test wall-temperature distribution yielded N of about 5 at 0.45 m (their Figure 12). The plots shown in [12] do not permit a more detailed comparison of the wall temperature effects; since the wall temperature varies dramatically with arclength during flight, the effect is not easy to estimate. Additional figures from MacLean (private communication, September 2009) show that when the wall temperature rises to radiative equilibrium from room temperature, the streamwise location at which N = 6 or N = 10 is reached increases by about 20%.

4.5 PURDUE MEASUREMENTS FOR HIFIRE-1

To reduce the risk of surprises in a flight test, it is generally advisable to make quiet-tunnel measurements under noise levels comparable to flight, to estimate the effect of tunnel noise on pre-flight ground tests in conventional facilities. However, available quiet tunnels cannot maintain laminar nozzle-wall boundary layers and the associated low noise levels to Reynolds numbers that are sufficient to achieve natural transition on a blunt cone at zero angle of attack [17]. In addition, the only existing hypersonic quiet tunnels are fairly small facilities that operate only with cold flow at Mach 6. Both the Purdue and Texas A&M tunnels can also operate with turbulent nozzle-wall boundary layers and noisy flow, by closing the valves providing suction to the bleed lips just upstream of the nozzle throat. Of course, the noise level under both conventional and quiet flow still varies with the tunnel and flow conditions. Even under quiet flow, the noise level is not zero and may still be higher than the unknown noise level in flight.

To study the effects of tunnel noise, Casper et al. (2008) [3] experiments with the HiFire-1 geometry in the Purdue Mach-6 quiet tunnel. The 7-deg. half-angle cone had a 4-inch base diameter and a 0.047-inch nose radius. Qualitative indications of heat transfer were measured using temperature-sensitive paint, and used to infer transition onset. Diamond-shaped roughness elements were applied at an axial location 5.1 inches from the nose.

As expected, the nominally smooth model remained laminar under quiet flow, to the maximum feasible Reynolds number of about 4 million, based on freestream conditions and cone length. Under noisy flow in

the Purdue tunnel at a freestream Reynolds number of 5.5 million per foot, transition occurred on the model at about 1 foot from the nose, which is generally similar to the location in the Langley tunnel. The N factor at transition in the Purdue tunnel under conventional noise was 5.8, while it was 6.0 in the Langley tunnel.

The effect of tunnel noise on transition induced by the isolated roughness element was of primary interest. For 'effective' roughness elements, it was previously thought that tunnel noise would have little effect [16]. Surprisingly, Casper's measurements showed a large effect of tunnel noise on roughness-induced transition, even under conditions where the roughness was 'effective' under noisy flow. Figure 4-1 summarizes the results. The roughness Reynolds number, Re_k, is based on the roughness height k and the conditions in the undisturbed boundary layer at that height. The axial distance to transition onset is x_{tr}. For the lowest value of Re_k, transition occurs only under noisy flow; the boundary layer is laminar to the end of the cone under quiet flow. For higher values of Re_k, the reduction in tunnel noise delays transition by factors of 2 – 6, even when the roughness is 'effective' under noisy flow. Further investigations of this effect should be carried out in the future.

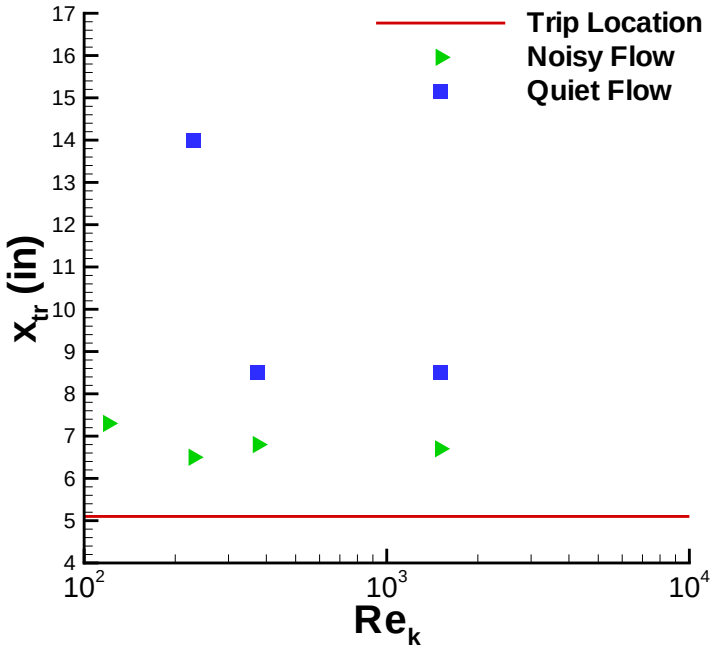

Figure 4-1: Effect of Trip Reynolds Number and Tunnel Noise on the Axial Location of Transition for the HIFiRE-1 Cone at Zero Angle of Attack and Mach 6.

4.6 NASA LANGLEY MEASUREMENTS FOR HIFIRE-1

Berger et al. (2008) [2] report measurements in the 20-inch Mach-6 blowdown tunnel at NASA Langley. The three models of the full vehicle were 20% scale. The nose radius was about 2.4 times larger than scale, due to the limitations involved in fabricating the ceramic phosphor models. There were also two models of the forecone alone, at 35% scale; one of these had a 0.047-in-radius nosetip (1.37 times scale), while the other had a 0.083-in.-rad. nosetip (2.4 times scale). Although this paper gives only the unit Reynolds numbers for each run, which are not sufficient to define the flow conditions, Table 1 in [1] gives the full flow conditions. The stagnation temperature is near 515 K for all the runs. Transition is inferred from heat-transfer measurements using thermographic phosphor images that are compared to laminar Navier-Stokes computations.

Berger's Figure 5 shows results for the 0.047-in-rad. forecone. At 2.5 million per ft., the flow is still laminar at 8.4 in. axially downstream from the nosetip. At 4 million per foot, transition onset occurs at about 0.6 ft., for a length Reynolds number of roughly 2.5 million. At 5.6 million per ft., it has moved upstream to about 0.45 ft. Data for transition on the other smooth forecones is not shown.

Berger et al. (2008) [2] also report measurements behind a diamond-shaped roughness 0.050-in. on a side. For the full-vehicle model with the 0.047-in. nose radius, and a roughness at 1.65 in. from the nosetip, transition did not occur for a roughness height of k = 0.0045 in.; the heat transfer behind the roughness is almost the same as the smooth-wall case. For a roughness height of 0.0065 in., transition onset occurs near 0.38 ft. A roughness of 0.0115 in. was nearly effective in tripping, at $k/\delta^* = 3.2$, where δ^* is the displacement thickness. This ratio was used to design the roughness in flight. The effect of the various model sizes is not examined in the paper.

4.7 MINNESOTA COMPUTATIONS FOR HIFIRE-1

Johnson et al. (2008) [8] report stability analyses for the earlier CUBRC experiments. A Navier-Stokes mean flow is analyzed using the linear Parabolized Stability Equations (PSE) as incorporated in the STABL code. Four Mach-7 runs are analyzed along with five Mach-10 runs, and all the conditions are tabulated. An e^N analysis with N = 5.5 gave good agreement with the measured transition-onset locations, while an analysis using $Re_\theta/M_e = 150$ scattered widely. Here, Re_θ is the local Reynolds number based on edge conditions and momentum thickness, and M_e is the local Mach number based on edge conditions. At 4.6 MJ/kg and Mach 10, including chemistry and vibrational non-equilibrium increased the N factor by less than 5%.

Alba et al. (2008) [1] report stability analyses for the Berger et al. (2008) [2] experiments. The Navier-Stokes equations are solved for the mean flow. Instability is analyzed using the linear PSE method. Their Table 1 lists 22 runs that were selected for simulation, including 9 runs at zero Angle of Attack (AoA). These include the two simple blunt cones, with axial lengths of 0.381 m and 1.19 or 2.10 mm nose radii, and the cone-cylinder-flare, with a nose radius of 1.19 mm and an axial cone length of 0.216 m. The simulations assume a uniform wall temperature of 300 K, which seems to be within about 10 – 20 % of the actual wall temperature.

Unfortunately, of the 9 candidate runs at zero AoA, only two were at Reynolds numbers high enough to clearly show the onset of transition. Three laminar runs had computed N factors of about 5 – 6 at the end of the cone, which is consistent with the observed laminar flow, since the onset of hypersonic transition in conventional-noise tunnels generally seems to occur near N = 5 – 6. When the larger nose radius of 2.10 mm was studied at a higher Reynolds number of 20 million per meter, the N factor at the end of the cone is similar to the value for a 1.19-mm nose radius at 7 million per meter.

When N = 5.5 was used to estimate the onset of transition, the two Langley runs with the 1.19-mm nose radius agreed well, as did 9 runs in the shock tunnels at CUBRC, as shown in Figure 4-2(b). In these figures, the caption gives the freestream Mach number and unit Reynolds number, along with the nose radius. By contrast, when the common simple correlation of $Re_\theta/M_e = 150$ is used, the data scatter widely, as shown in Figure 4-2(a), and the trend is not captured. Both figures are redrawn from those in [8], using additional data supplied by them. Transition Reynolds number generally increases with nose radius, for these small radii, or as transition moves closer to the nose. The CUBRC runs near Mach 7, shown in red, delivered the highest transition-onset Reynolds numbers, based on edge conditions and the axial length from the nose. This is curious, since higher Mach numbers are usually associated with higher transition Reynolds numbers, presumably because the noise is effectively smaller (see, for example, Pate 1980 [13] Figure 74). However, these higher transition Reynolds numbers are well correlated with N = 5.5. The CUBRC runs near Mach 10 provided the lowest transition Reynolds numbers, which is again curious with respect to Pate [13].

The NASA Langley Mach-6 data fall in between. Since the tunnel noise varies with tunnel, Mach number, and unit Reynolds number, the receptivity may vary with nose radius, and the non-linear second-mode breakdown amplitude may also vary, it's not obvious why N = 5.5 works as well as it does. Further investigation is needed; measurements of the wave amplitude would be particularly helpful.

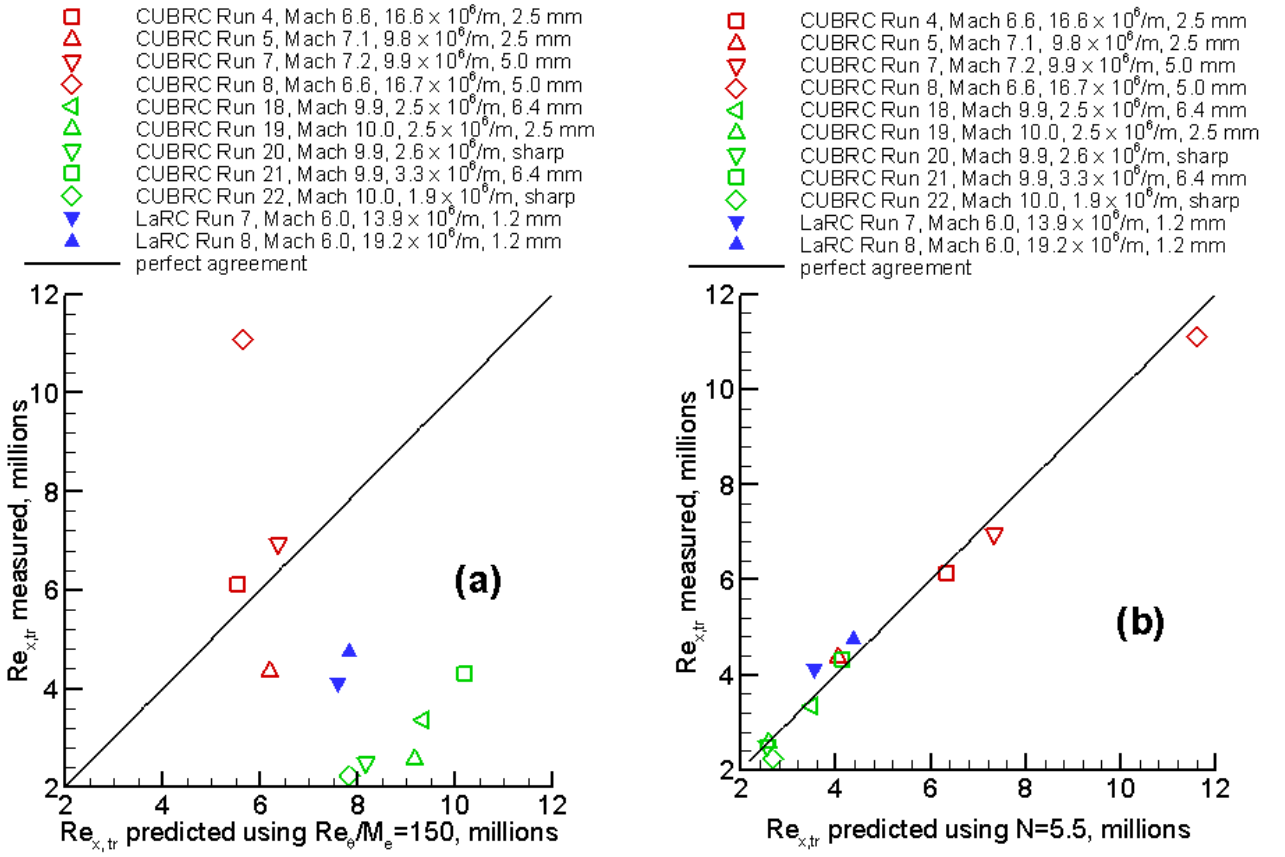

Figure 4-2: Correlations for Transition-Onset Reynolds Number for 7-deg. Half-Angle Cones with Small Nose Radii in Three Hypersonic Wind-Tunnel Nozzles.

4.8 MEASUREMENTS ON 7-DEG. CONE AT PURDUE AND BRAUNSCHWEIG

It has been well known for several decades that hypersonic tunnel noise affects transition on models [16]. When tunnel conditions are varied, the turbulent boundary layer on the nozzle wall varies, and the tunnel noise varies, along with the physics of instability and transition in the boundary layer on the model. It has been nearly impossible to separate the changes in boundary-layer instability from the changes in tunnel noise. Both affect transition, and usually only transition is measured. Measurements of the high-frequency instabilities required difficult and delicate instrumentation such as hot wires, which did not survive well enough in most hypersonic tunnels. However, if wave measurements could become feasible, it might be possible to separate the effects of tunnel noise from the effects due to changes in the boundary-layer instability.

As part of a study of hypersonic roughness effects, Fujii (2006) [7] found that it was possible to measure second-mode waves in a hypersonic tunnel using high-frequency piezoelectric pressure sensors that are

robust and inexpensive. This was surprising, since it was the first measurement of second-mode waves using surface pressure sensors, and the 1 MHz PCB-132 sensors were only designed to measure the passage of shock waves. Since this instrumentation promised a significant advance in general measurement of instability and transition, Estorf et al. (2008) [6] carried out further experiments at Braunschweig and Purdue. Second-mode instability waves were successfully measured in both tunnels. The frequencies and amplification rates agreed well with theory. Under noisy flow at Purdue and Braunschweig, the second-mode waves broke down to turbulence at about the same Reynolds number and the same amplitude, suggesting that non-linear breakdown is not too sensitive to the details of the tunnel noise environment. Second-mode waves were measured under quiet flow in the Purdue tunnel, for the first time; the wave amplitude under quiet flow was about 450 times lower than under noisy flow. The PCB-132 sensors are robust and easy to use, although reliable quantitative use will require further calibration efforts.

Similar measurements were also carried out using Atomic Layer Thermopile gauges that were invented in Germany (e.g., [15]). These surface heat-transfer sensors use the Seebeck effect to achieve very high sensitivity at frequencies to 1 MHz. Although they work better in flowfields with higher levels of heat transfer, second-mode waves were successfully measured in the Purdue Mach-6 tunnel under quiet and noisy conditions. As they become more readily available they may complement the pressure sensors for robust measurements of high-frequency instability waves and other phenomena.

4.9 SANDIA MEASUREMENTS ON 7-DEG. CONES

Casper et al. (2009) [4] measured the surface-pressure fluctuations on a sharp 7-deg. half-angle cone at Mach 5, 6 and 8, in the wind tunnels at Purdue and Sandia National Laboratory. Most measurements were carried out with a 0 – 50 kHz bandwidth, and were focused on the vibrations induced by transitional pressure fluctuations. The onset of transition was inferred from this peak in the streamwise distribution of the pressure fluctuations, which was previously measured to occur between the onset and end of transition. Under quiet flow at Mach 6, the boundary layer was laminar, so all measurements were obtained under conventional noise levels.

Casper et al. (2009) [4] also measured the surface pressure fluctuations using fast PCB132 quartz sensors, with an 11 kHz – 1 MHz bandwidth. For frequencies between 11 and 50 kHz, the two types of sensors agreed well. The PCB132 sensors were able to measure second-mode instability waves in all three nozzles. Prior to breakdown, the maximum second-mode amplitude increased from 5% at Mach 5 to 12 % at Mach 6 (under noisy flow) to 24% at Mach 8. The peak wave amplitude prior to transition clearly increased with Mach number, as did the tunnel noise level. More research is needed to understand these observations.

4.10 MEASUREMENTS ON 7-DEG. CONE AT HIEST

Work on the 7-deg. cone has stimulated further international interest. Existing measurements of second-mode waves have all been carried out in blowdown tunnels with low enthalpy and relatively long run times. Can the waves also be measured under high-enthalpy conditions, enabling a possible separation of tunnel noise effects from model boundary-layer effects? The large free-piston shock tunnels in Germany and Japan may be capable of generating and measuring second-mode waves under high-enthalpy conditions where aerothermochemistry affects instability and transition. Tanno et al. (2009) [18] report the first attempt at such measurements, in the large free-piston shock tunnel at the Kakuda Space Center in Japan. Transition is observed at a length Reynolds number of about 4 million, apparently based on freestream conditions. Power spectra obtained from PCB132 pressure signals suggest the presence of second-mode waves, although the data are not conclusive. Work continues.

4.11 SUMMARY: COLLABORATIVE EFFORTS INITIATED UNDER AVT-136

Hypersonic laminar-turbulent transition is a complex and difficult field in which significant progress is being made, using modern computational and experimental tools. No single ground-test facility can simulate all aspects of transition in flight. Likewise, computational models must make many assumptions in order to simulate flight. Efficient progress requires collaboration. Detailed comparisons between computational models and experimental measurements lead to improvements for all.

Second-mode wave measurements on a 7-deg. half-angle cone have been made in several wind tunnels, for comparison to stability results from several computational tools. New instrumentation has been developed to enable these measurements in the harsh environment typical of hypersonic tunnels. This progress has involved collaboration among researchers in the United States, Germany, Japan, and Russia.

AVT-136 efforts have initiated a number of continuing collaborations. The Technical University of Braunschweig is collaborating with Purdue University, Texas A&M University, the University of Minnesota, NASA Langley, and others to study cross-flow-induced transition on a sharp cone at angle of attack. Measurements of second-mode waves are being carried out with PCB and ALTP sensors at Braunschweig, Stuttgart Univ., the DLR in Göttingen, NASA Langley, Sandia National Laboratory, AEDC Tunnel 9, HIEST, CUBRC, Purdue and elsewhere, with computational comparisons provided by the Univ. of Minnesota, AFRL, and NASA Langley. Windside-forward transition on a blunt cone at angle of attack is being investigated by CIRA in Italy, DLR Cologne, and Purdue. The Von Karman Institute in Belgium is collaborating with Purdue regarding the effect of tunnel noise on roughness-induced transition. Comparisons to the HIFiRE-1 and HIFiRE-5 flights involve collaboration among AFRL, NASA Langley, CUBRC, Purdue, the University of Minnesota and others. For efficient progress, these efforts should continue.

4.12 REFERENCES

[1] Alba, C.R., Johnson, H.B., Bartkowicz, M.D., Candler, G.V. and Berger, K.T., “Boundary-layer stability calculations for the HIFiRE-1 Transition Experiment”, *J. Spacecraft and Rockets*, Vol. 45, No. 6, pp. 1125-1133, November – December 2008.

[2] Berger, K.T., Greene, F.A., Kimmel, R., Alba, C. and Johnson, H., “Aerothermodynamic Testing and Boundary-Layer Trip Sizing of the HIFiRE Flight 1 Vehicle”, *J. Spacecraft and Rockets*, Vol. 45, No. 6, pp. 1117-1124, November – December 2008.

[3] Casper, K.M., Wheaton, B.M., Johnson, H.B. and Schneider, S.P., “Effect of Freestream Noise on Roughness-Induced Transition at Mach 6”, AIAA Paper 2008-4291, June 2008.

[4] Casper, K.M., Beresh, S.J., Henfling, J.F., Spillers, R.W., Pruett, B. and Schneider, S.P., “Hypersonic Wind-Tunnel Measurements of Boundary-Layer Pressure Fluctuations”, AIAA Paper 2009-4054, June 2009 – See also M.S. Thesis, same title, Purdue University, August 2009.

[5] Dougherty, N.S., Jr. and Fisher, D.F., “Boundary-layer transition on a 10-deg. cone: wind tunnel/ flight data correlation”, AIAA Paper 80-0154, January 1980.

[6] Estorf, M., Radespiel, R., Schneider, S.P., Johnson, H.B. and Hein, S., “Surface-Pressure Measurements of Second-Mode Instability in Quiet Hypersonic Flow”, AIAA Paper 2008-1153, January 2008.

[7] Fujii, K., “Experiment of Two-Dimensional Roughness Effect on Hypersonic Boundary-Layer Transition”, *J. of Spacecraft and Rockets*, Vol. 43, No. 4, pp. 731-738, July – August 2006.

[8] Johnson, H.B., Alba, C.R., Candler, G.V., MacLean, M., Wadhams, T. and Holden, M., "Boundary-Layer Stability Analysis of the Hypersonic International Flight Research Transition Experiments", *J. Spacecraft and Rockets*, Vol. 45, No. 2, pp. 228-236, March – April 2008.

[9] Kimmel, R.L., Adamczak, D., Gaitonde, D., Rougeux, A. and Hayes, J.R., "HIFiRE-1 Boundary-Layer Transition Experiment Design", AIAA Paper 2007-0534, January 2007.

[10] Kimmel, R., "Roughness considerations for the HIFiRE-1 Vehicle", AIAA Paper 2008-4293, June 2008(a).

[11] Kimmel, R., "Aerothermal Design for the HIFiRE-1 Flight Vehicle", AIAA Paper 2008-4034, June 2008(b).

[12] MacLean, M., Wadhams, T., Holden, M. and Johnson, H., "Ground Test Studies of the HIFiRE-1 Transition Experiment, Part 2: Computational Analysis", *J. Spacecraft and Rockets*, Vol. 45, No. 6, pp. 1149-1164, November – December 2008.

[13] Pate, S.R., "Effects of Wind Tunnel Disturbances on Boundary-Layer Transition with Emphasis on Radiated Noise: A Review", AIAA Paper 80-0431, DTIC Citation AD-A384982; Not in AIAA Archive, March 1980.

[14] Reshotko, E., "A Program for Transition Research", *AIAA Journal*, Vol. 13, No. 3, pp. 261-265, March 1975.

[15] Roediger, T., Knauss, H., Estorf, M., Schneider, S. and Smorodsky, B., "Hypersonic Instability Waves Measured Using Fast-Response Heat-Flux Gauges", *J. of Spacecraft and Rockets*, Vol. 46, No. 2, pp. 266-273, March – April 2009.

[16] Schneider, S.P., "Effects of Roughness on Hypersonic Boundary-Layer Transition", *J. of Spacecraft and Rockets*, Vol. 45, No. 2, pp. 193-209, March – April 2008(a).

[17] Schneider, S.P., "Development of Hypersonic Quiet Tunnels", *J. of Spacecraft and Rockets*, Vol. 45, No. 4, pp. 641-664, July – August 2008(b).

[18] Tanno, H., Komura, T., Sato, K., Itoh, K., Takahashi, M. and Fujii, K., "Measurements of Hypersonic Boundary Layer Transition on Cone Models in the Free-Piston Shock Tunnel HIEST", AIAA Paper 2009-0781, January 2009.

[19] Wadhams, T.P., MacLean, M.G., Holden, M.S. and Mundy, E., "Pre-flight Ground Testing of the Full-Scale FRESH FX-1 at Fully Duplicated Flight Conditions", AIAA Paper 2007-4488, June 2007.

[20] Wadhams, T.P., Mundy, E., MacLean, M.G. and Holden, M.S., "Ground Test Studies of the HIFiRE-1 Transition Experiment, Part 1: Experimental Results", *J. Spacecraft and Rockets*, Vol. 45, No. 6, pp. 1134-1148, November – December 2008.

Chapter 5 – EXPERIMENTAL AND NUMERICAL TECHNIQUES TO ASSESS CATALYSIS

Georg Herdrich, Marcus Fertig, Dejan Petkow, Andreas Steinbeck
Institut fuer Raumfahrtsysteme
GERMANY

5.1 INTRODUCTION

Spacecrafts experience significant heat loads during atmospheric entry maneuvers. This is due to the considerable entry velocities and the corresponding mass specific enthalpies that have to be dissipated along the entry path through the atmosphere of the concerned celestial body. To withstand these loads, the vehicle requires a Thermal Protection System (TPS). In contrast to the amount of work done in the field of mechanical properties characterization and engineering development less experimental work has been conducted to characterize the catalytic and optical properties of such materials. However, these properties are of great importance because they are determining the thermo chemical behavior of the TPS during a given re-entry trajectory of a vehicle. Due to the high gas velocities in the entry phase, e.g., for Earth, the Oxygen and the Nitrogen molecules passing through the bow shock become at least partly dissociated. Depending on the environmental conditions (e.g., pressure and temperature of the TPS material) these atoms will recombine at different rates following different mechanisms. In any case, the released recombination energy of this exothermal chemical reaction results in an additional heat flux on the TPS and the gas phase in the boundary layer. The increase in heat flux can be as much as three times for an Air system, comparing a non-catalytic to a fully catalytic material [1], [2]. Correspondingly, at least two portions of heat flux have to be considered: The convective heat flux which does not directly depend on the material and the recombination heat flux which results from the chemical recombination of atoms, a process, which directly depends on the material of the space vehicle surface. If the ratio of the variable recombination and convective heat flux to a fully catalytic heat flux is taken a trend as shown in Figure 5-1 is obtained.

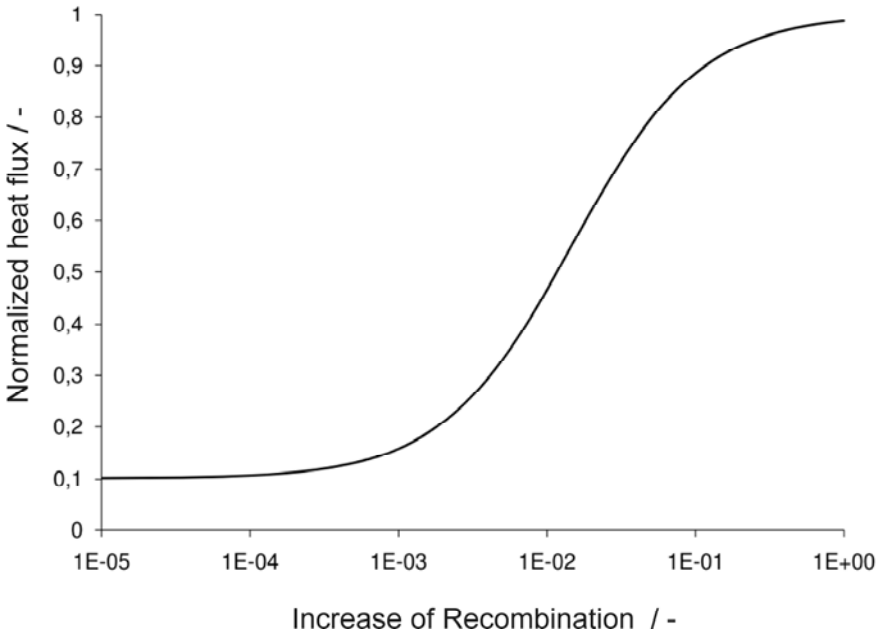

Figure 5-1: Normalized Heat Flux Depending on Increase of Recombination (as an example).

The impact of recombination is evident and the quantitative values of both minimum and maximum as well as the position of the heat flux increase depend on the catalysis properties of the surface material and on the conditions of the incident flow. In particular, the steep slope regime is of interests as the potential to manipulate the heat flux is most significant. In an overall consideration the process itself happens through the transport of atomic species (Oxygen and Nitrogen atoms in case of Air) to the material surface. Here, either at least one or more of the chemical precursors experience chemisorption. In a third step usually either the adsorpts react with each other (i.e., Langmuir-Hinshelwood mechanism) or one adsorpt reacts with a precursor that is still in the gas phase (i.e., Eley-Rideal mechanism). After that the resulting products (the molecules) are desorpted from the surface and then leave the surface zone [3], [4]. A more detailed description of these mechanisms is given in reference [5].

First theoretical investigations were performed by Fay and Riddell and Goulard leading to the formulation of algebraic formulations based on boundary layer models [6], [7]. It is interesting that such models are still quite powerful and still find their application within the group of the boundary layer based methodologies to derive the catalytic behaviour of candidate materials. From the understanding of the dominant mechanisms the importance of both the transported species and the fraction of these species recombining at and/or near the material surface become evident. Correspondingly the definition of the recombination coefficient γ_i as:

$$\gamma_i = \frac{\dot{N}_{Ai,recom}}{\dot{N}_{Ai,tot}} \tag{1}$$

related to the species can be defined. Here, the index recom is assigned to the respective number of recombining species while the index tot is assigned to the total number of particles that flow to the surface per second. Therefore, γ is always between 0 (non-catalytic) and 1 (fully catalytic). Correspondingly, and in consistence with the gradients in Figure 5-1, the following regimes can be defined:

- $\gamma < 1$: materials of low catalysis;
- $0.01 < \gamma < 0.1$: materials in with medium catalysis; and
- $\gamma > 0.1$: materials of high catalysis.

These considerations, however, still ignore the aspect of energy accommodation, i.e., the answer to the question which fraction of the heat flux derived from the recombination processes is experienced by the surface as it is evident that the other fraction still could stay with the molecule which is not necessarily in equilibrium with the surface. Correspondingly, the energy accommodation coefficient β defined as:

$$\beta = \frac{\dot{q}_{surface,recom}}{\dot{q}_{tot,recom}} \tag{2}$$

has to be taken into account and, eventually, the product of both γ_i and β. The aforementioned motivation of understanding the boundary layer and relevant parameter additionally necessitates knowledge on additional material properties such as, e.g., the emission coefficient and on the environmental conditions which usually leads to the operation of a set of adequate measurement techniques as well. This can be exemplarily outlined by the consideration of catalysis, the emission coefficient and the potential interaction between catalysis and other reaction schemes of a TPS material.

The heat flux onto a spacecraft itself becomes indirectly dependant on the TPS surface temperature. In case of common Silicon-based TPS materials, the raised temperatures may trigger another surface phenomenon, which interacts with catalysis: passive and active Oxidation along with a further rapid temperature increase and consequently a much higher mass loss rate.

This overall interaction between emissivity, catalysis and reaction schemes is in principal shown in Figure 5-2. It becomes clear that methodologies to assess surface reaction schemes require the precise knowledge of other material related properties. The emissivity is one of the most important of these parameters.

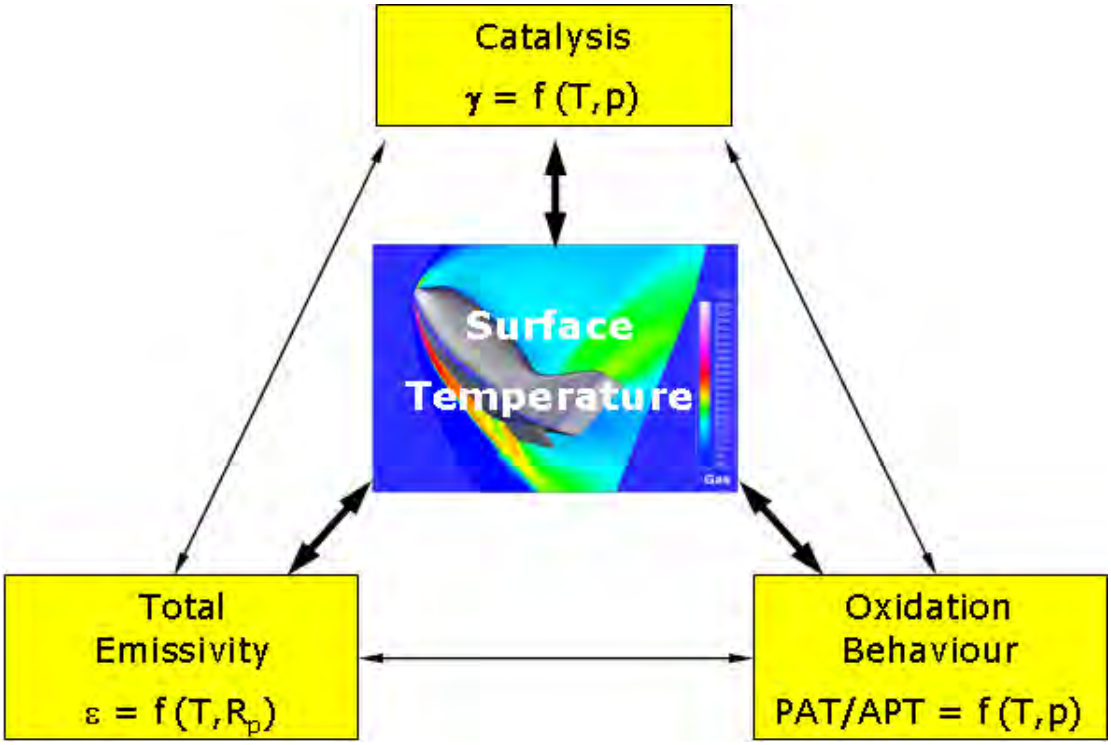

Figure 5-2: Catalysis, Emissivity and Reaction Scheme Interaction.

In order to develop and weight-optimized TPS for future, it is absolutely necessary to determine related material properties and closely investigate these surface phenomena and their interaction in ground tests and flight experiments. A promising assessment is the successful combination of experimental, in-flight data from the ballistic capsule MIRKA and numerical models as performed in Ref. [8]. In a further step, a critical consideration of catalysis data with respect to the different methodologies to determine catalysis has to be performed.

Through this motivation the works within RTO has been motivated with the aim to consolidate and to assess the theme of catalysis. The outcome will be incorporated to an RTO report which is currently in development. The paper gives an extraction of this report showing the facilities and capabilities world wide to assess catalysis data. A corresponding summary for the modelling activities can be found in reference [9].

For ballistic entry vehicles the altitude of maximum thermal load can be estimated by:

$$h\big|_{\dot{q}_{\max}} = H_B \ln\left(-\frac{3 H_B \rho_B}{\beta \sin\gamma_E}\right), \tag{3}$$

where H_B = 6700 m is the reference altitude, ρ_B = *1.752 kg/m*^{3} is the reference density, β is the ballistic coefficient of the vehicle in kg/m² and γ_E is the entry angle. Typically, the highest thermal loads of orbital as well as super-orbital re-entry vehicles arise at about 60 km of altitude or above. At such altitudes

chemical but also thermal non-equilibrium play an important role concerning vehicle heating. As an example, the temperatures along the stagnation line of the MIRKA re-entry capsule for peak heating conditions are shown in Figure 5-3.

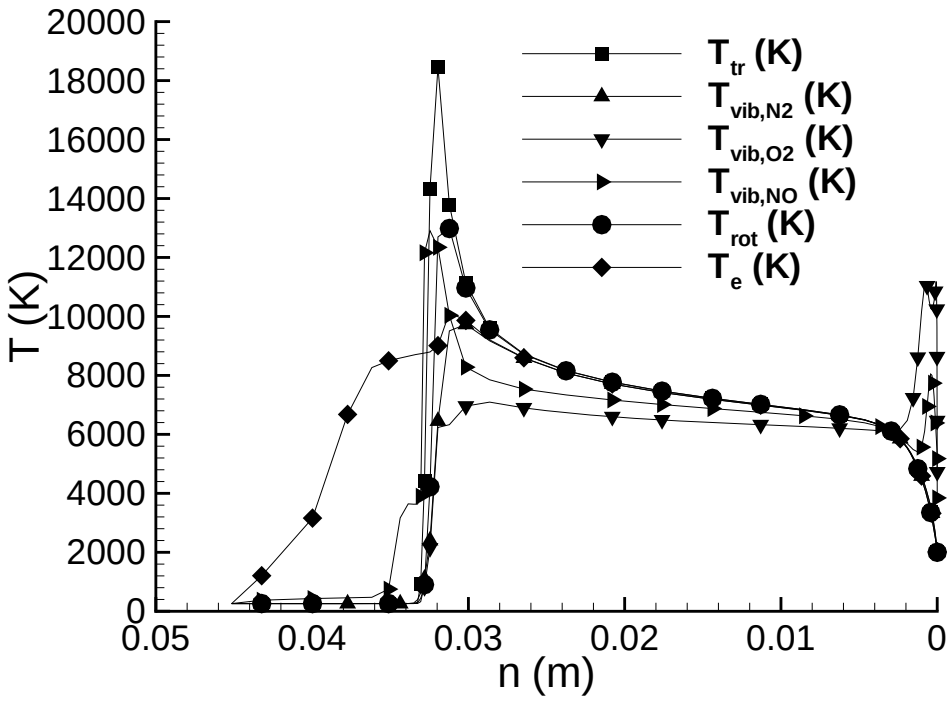

Figure 5-3: Temperature Distribution Along the MIRKA Stagnation Line for Peak Heating Conditions Employing the URANUS Non-Equilibrium Navier-Stokes Algorithm.

While the pressure and the density are sufficiently high to allow for nearly complete chemical relaxation in the flow field downstream of the shock, they are to low to allow for chemical equilibrium in the boundary layer near to the surface. Hence, the gas composition at the surface is significantly dissociated and a large amount of atomic species reaches the surface of the Thermal Protection System (TPS) of the re-entry vehicle. Depending on the catalytic properties of the TPS a part of the atomic species recombines at the surface.

The limiting cases for the recombination coefficient are 0, if no recombination occurs (non-catalytic) and 1, if all atoms recombine (fully catalytic). As a replacement for fully catalytic boundary conditions some CFD schemes apply so called super-catalytic boundary conditions where the composition at the inflow boundary is prescribed at the surface boundary.

As can be seen from Figure 5-4 the catalytic properties of the surface have a major influence on the chemical composition of the gas in the boundary layer.

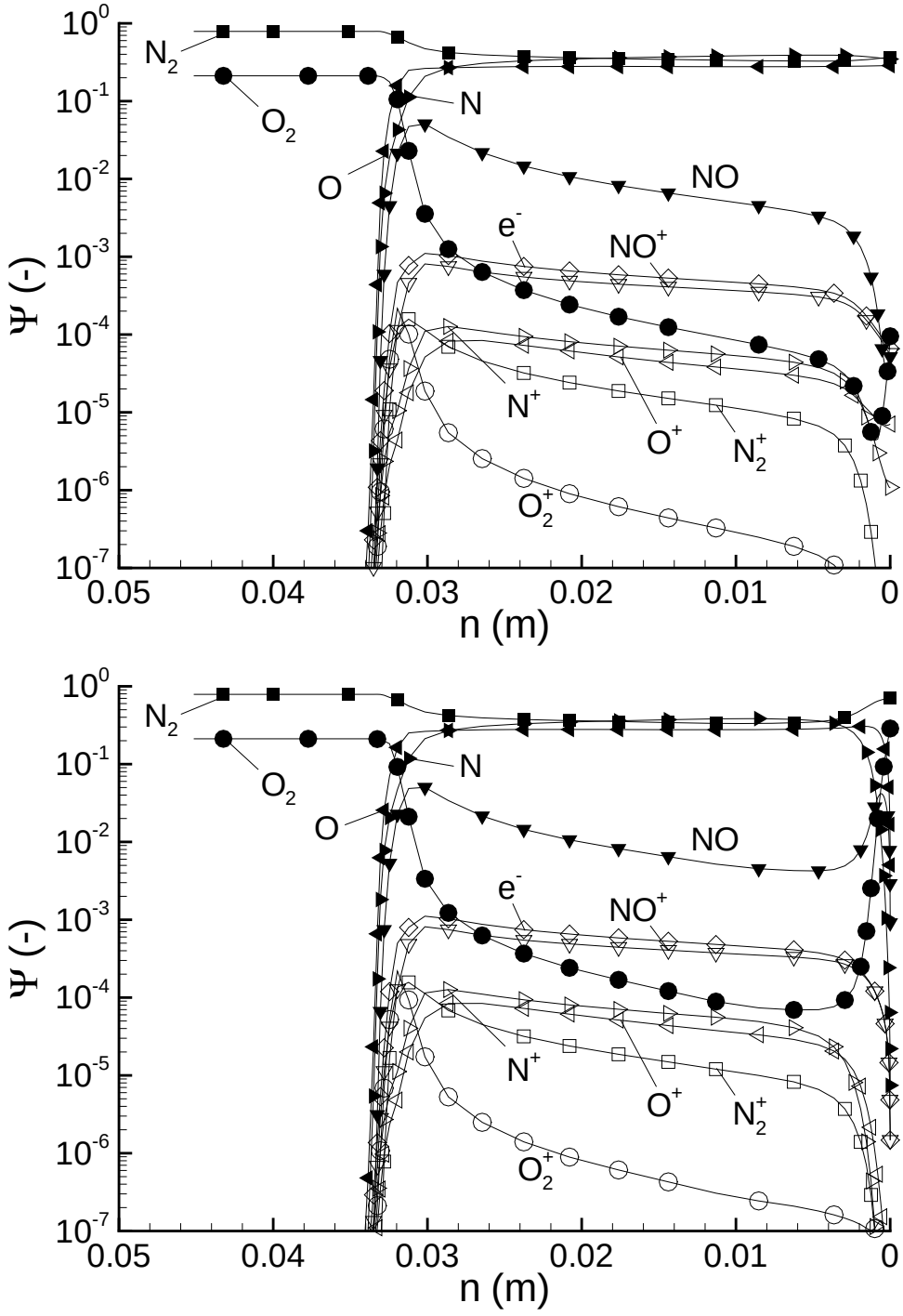

Figure 5-4: Mole Fraction Distribution versus Stagnation Stream Line for the MIRKA Re-entry Vehicle Under Peak Heating Conditions Comparing Non-Catalytic (top) and Fully Catalytic (bottom) Boundary Conditions Computed Employing URANUS.

Since the recombination of atoms is an exothermal process, the recombination of atoms is associated with the release of the dissociation energy at the TPS surface. As a result, the catalytic recombination of atoms at the TPS surface leads to an increase in surface heat flux as compared with the non-catalytic assumption. If no other reactions than catalytic recombination reactions are important at the TPS surface, the fully catalytic and the non-catalytic surface assumptions mark the limits for the heat flux onto the surface.

As shown in Figure 5-5 the computed heat flux onto the MIRKA surface at peak heating conditions varies between 0.75 MW/m² and 2.4 MW/m² for non-catalytic and fully catalytic surface boundary conditions, respectively. For re-entry into the Earth atmosphere, a ratio of 3 between fully catalytic and non-catalytic heat flux is a typical value.

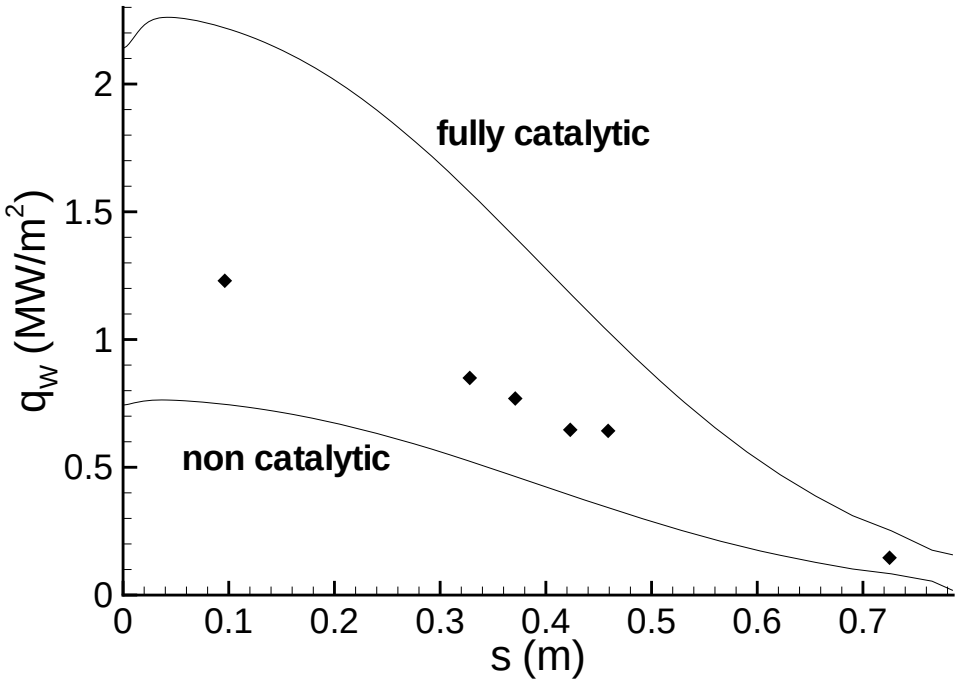

Figure 5-5: Comparison of Computed Surface Heat Loads for the MIRKA Vehicle at Peak Heating Conditions Employing Non-Catalytic and Fully Catalytic Surface Assumptions with Measurements of the HEATIN Experiment.

As can be seen from Figure 5-5 the heat flux measurement results in roughly one third the heat flux value of the fully catalytic boundary condition.

5.2 REALIZED EXPERIMENTAL METHODOLOGIES TO DERIVE CATALYSIS

The following section outlines institutions that have developed facilities and methodologies to experimentally derive catalysis data. It concentrates rather on the methodologies and facilities developed. They are considered qualified such that the discussion of measured data is a future item, see also section IV. The first four of the described methods are dominated by concentration measurements while the methods that use plasma wind tunnel facilities are dominated by energy balances. However, it is not in the ambition of the authors to categorize too strictly as some of the methods combine the two categories or could at least have an improvement, e.g., if concentration data for the plasma wind tunnel based methodologies would be measured.

5.2.1 Side-Arm Method

The side-arm method was first developed by Smith [10] in 1943 and was widely used in the 1950s and 1960s. Later the original measurement technique was modified and used by many others, e.g., 1959 by Greaves and Linnett [11], [12] or 1964 by Dickens and Sutcliffe [3]. It was one of the first procedures for the experimental determination of recombination coefficients.

The main part of the experimental setup consists on a quartz tube with a gas supply at the one side and a vacuum pump on the other side. Close to the vacuum pump connection a second tube diverged orthogonally from the main pipe. This second tube or side-arm gave the name for these kinds of apparatus. Between main pipe and second pipe the gas passes a plasma generator which generates dissociated and or ionized plasma. In literature side-arm reactors with electrodes and electrode-free plasma generators using high-frequency coils can be found.

For achieving higher degrees of dissociation the gas was often, e.g., mixed with water vapour which of course represents a contamination of the plasma which was done by Dickens and Sutcliffe [3].

By passing the side-arm the plasma diffuses towards the material sample in the measurement area of the side-arm. Depending on the type of side-arm reactor the isothermal properties of the measurement area in length can be up to a couple of decimeter. The recombination coefficient will be determined by measuring the decreasing amount of dissociated atoms along the material sample under inspection. The species concentration can be measured, e.g., using Pirani-Manometer, mass spectroscopy, laser induced fluorescence or other techniques. A principle scheme of a side-arm reactor can be seen in Figure 5-6 but represents only one possible configuration. Another method is to install several thermocouples with catalytic coatings. The greater the distance to the main pipe is the less is the concentration of the atoms in the side arm, hence, less atoms recombine at the surface of the catalytic coatings. This leads to a decrease of measured temperature along the side-arm. This type of side-arm reactor was used by Linnett and Marsden [13] as well as Greaves and Linnett [11], [12], [14].

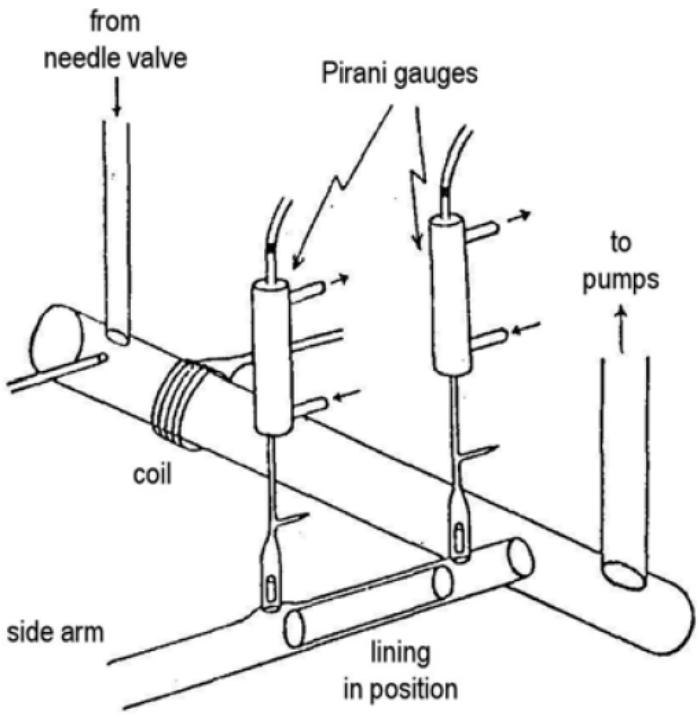

Figure 5-6: Side-Arm Reactor of Greaves and Linnett [11].

When the material sample is additionally equipped with heating elements the recombination coefficient over temperature can be obtained.

In the experimental setup in Figure 5-6 the material sample in the form of a hollow cylinder was installed inside the measurement area (lining in position). If the concentration of the atomic species is relatively low

and the temperature profile along the measurement area is isotherm, the catalytic property γ is given by the following equation:

$$\gamma = K\left(\frac{\ln\left(\alpha_A \alpha_B^{-1}\right)}{\Delta x}\right)^2 \tag{4}$$

Here, α_A and α_B are the atomic concentration at both ends of the material sample and Δx is the distance between them. The parameter K can be described as (4·S·D)/(Vav·D) with C as the circumference and S as the cross-sectional area of the side-arm. The size Vav is the average velocity of the atoms and D the coefficient of diffusion.

Although the side-arm method is one of the first measurement techniques used for determine the catalytic behaviour of different materials, it is still in use even today, e.g., Stewart and also Marschall [15], [16], [17].

The disadvantages of this method are the direct dependency of the knowledge of the coefficients of diffusion and the relatively low temperature range (up to 1000°C) achieved in these kinds of apparatus. The catalytic property of the material used for the tubes and side-arms must be known or determined in previous tests before installing the material sample. Furthermore the pressure level must be low to minimize the number of collisions of the atomic species in order to reduce the recombination reactions in the flow. Typical pressure levels are 4 Pa. As the recombination coefficient γ depends on temperature and pressure the γ obtained in these reactors are not representative for conditions during real re-entries. Nevertheless these values are important for the calibration of theoretical catalytic models.

5.2.2 Effusion Method

The Effusion Method was introduced 1966 by May and Linnett [18]. Hereby the gas streams through an aperture inside the evacuated tank in which the material sample is installed. The pressure and density should also be very low. Before crossing the aperture the gas become dissociated by passing a high frequency coil. Behind the aperture the material sample is placed coaxial and orthogonal to the flow direction. One part of the atomic species recombines to molecules at the surface of the sample.

Figure 5-7 shows a scheme of the arrangement of May and Linnett [18]. The sample under investigation consists of a thin Pyrex disc with the catalytic coating applied on one side of the disc. With known flow characteristics the total number of on the surface impinging particles can be calculated. The particle density can be measured similar to the techniques mentioned in the description of the side-arm method. Together with the temperature of the material sample and the total number of impinging particles the recombination coefficient can be determined. May and Linnett used resistance thermometers which were installed on the backside of the Pyrex disc. Like all measurement techniques which determine the catalysis by measuring the sample temperature and the heat flux respectively, the recombination coefficient and the energy accommodation factor cannot be separated but the effective recombination coefficient γ'.

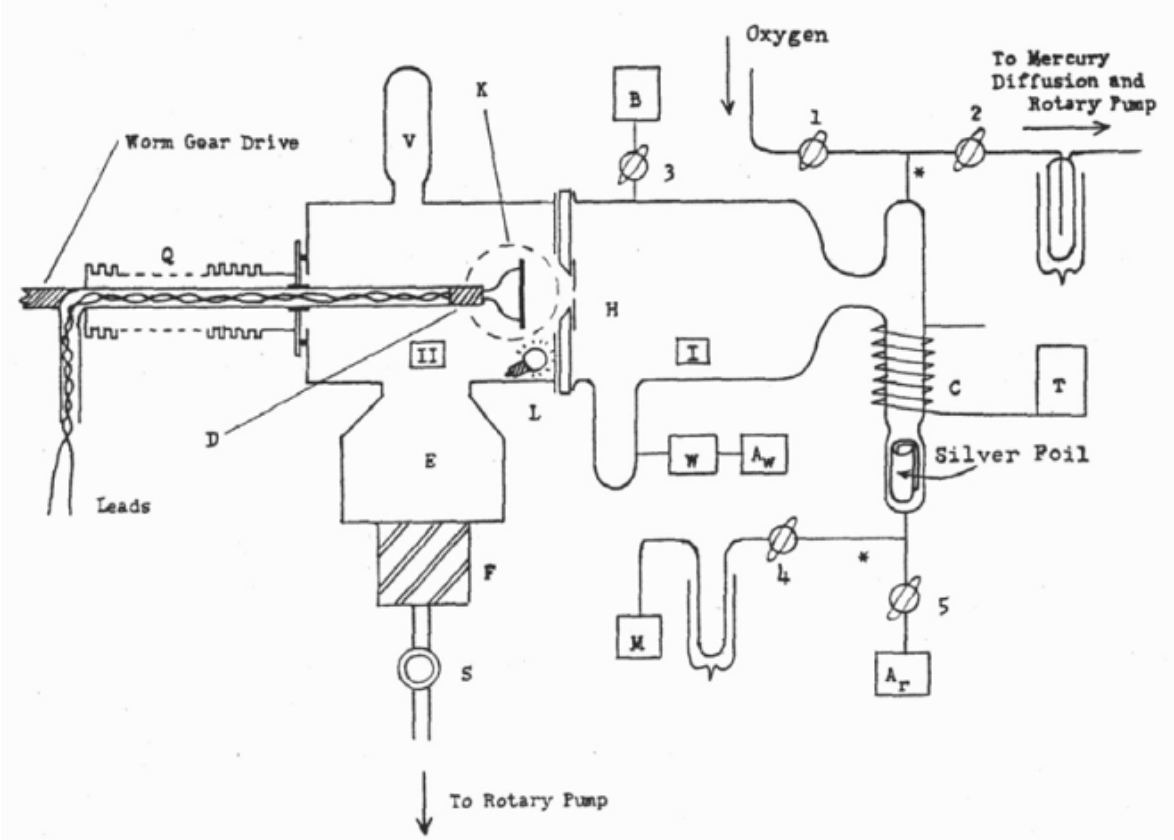

Figure 5-7: Scheme of Effusion Method by May and Linnett [18].

In comparison to the Side-arm Method, the Effusion Method is independent of the coefficient of diffusion. Additional it is suitable for high catalytic materials $\gamma > 0.1$.

Earlier versions of the Effusion Method were developed by Nakada [19] et al. in 1955. In their experiments metal samples were exposed to a partially dissociated hydrogen gas flow. In May and Linnetts assessment of these first experiments the driving force of the flow was not only related to effusion.

5.2.3 Chemical Luminescence Method

The method of species concentration measurements with the aid of chemical luminescence was introduced 1991 by Wickramanayaka, Meikle, Kobayashi, Hosokawa and Hatanaka [20]. The type of chemical reaction presumes Oxygen as working gas. The Oxygen gas streams through a Pyrex tube and by passing a high frequency coil become dissociated, see Figure 5-8. Directly in front of the material sample Nitrogen monoxide (NO) were added to the gas flow. As a result the Nitrogen monoxide reacts with the atomic Oxygen to high excited Nitrogen dioxide (NO_2) which, therefore, emits radiation:

$$NO + O \longrightarrow NO_2^* + h\nu \,. \tag{5}$$

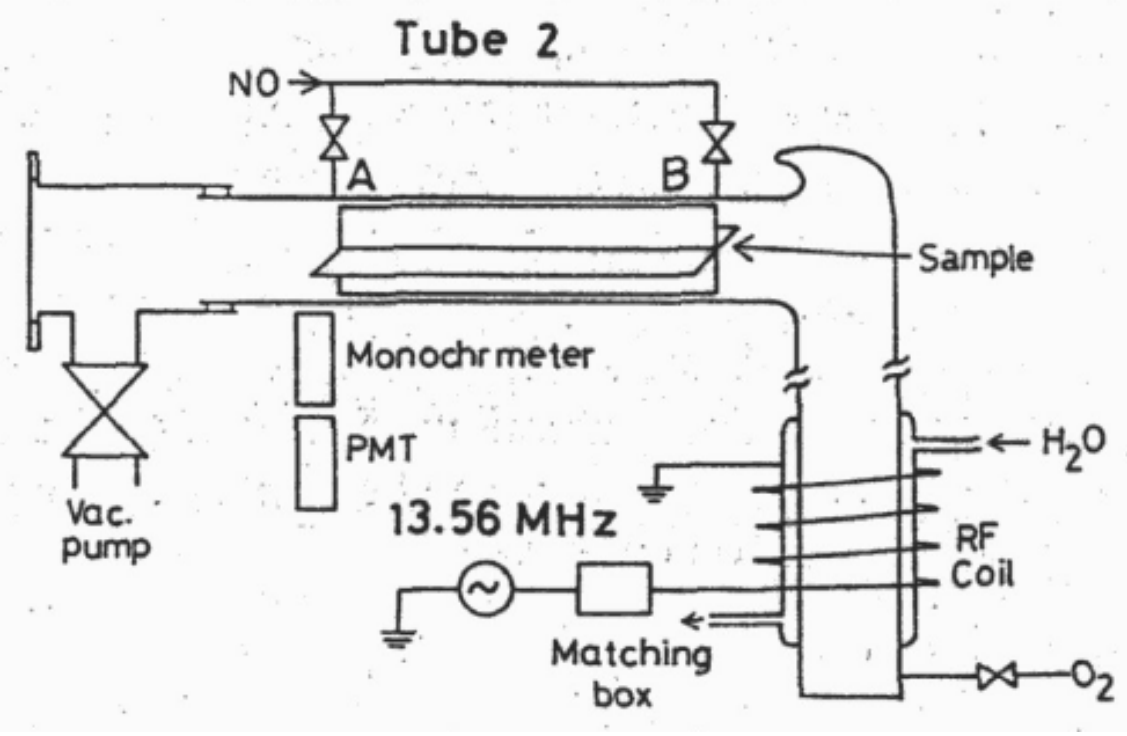

Figure 5-8: Scheme of Chemical Luminescence Method [20].

The number of reactions is proportional to the change of atomic Oxygen concentration, thus, it is a quantity for the determination of the recombination coefficient of the material sample, provided that at low pressures the number of chemical luminescence reactions in the gas phase is much smaller than the number of recombination reactions at the surface of the sample.

One disadvantage of this method should be mentioned is the change of surface properties of the investigated material sample through the adding of Nitrogen monoxide into the gas flow. On the other side the key benefits of this method are the selectivity of the measurement principle which allows the measurement of the concentration of atomic Oxygen only. This leads to accurate statements of the recombination coefficient corresponding to the working gas, in this case Oxygen, because impacts of other gas species can be neglected.

5.2.4 MESOX

The MESOX (Moyen d'Essai Solaire d'Oxydation) [21], [22], [23], [24] solar furnace facility introduced by Balat, Czerniak and Badie [21] represents an experimental setup of a plasma generator and a solar oven. Material samples of 3 mm in depth and 25 mm in diameter can be investigated and are installed coaxially inside a glass pipe in such a way that the sample is in the focus of the solar oven. The solar radiation concentrator is used for the sample heating and a microwave generator for the generation of the Air plasma. The glass tube has is 500 mm long and has a diameter of 50 mm. In this setup a maximum heat flux of 5.0 MW/m² and temperatures of 2500 K can be achieved. For a thermal insulation the sample holder is made out of Zirconium dioxide (ZrO_2). The plasma stream between inflow and vacuum pump system leads to a stagnation point flow to the material sample. The pressure level can be varied between 100 Pa and 10000 Pa. The temperature increase is determined with optical reflectors at both sides by optical pyrometers. The principle setup can be seen in Figure 5-9. With the MESOX setup it is possible to measure simultaneously the thermal and chemical contributions of the atomic recombination on surfaces at high temperatures on the same setup which allows a good accuracy.

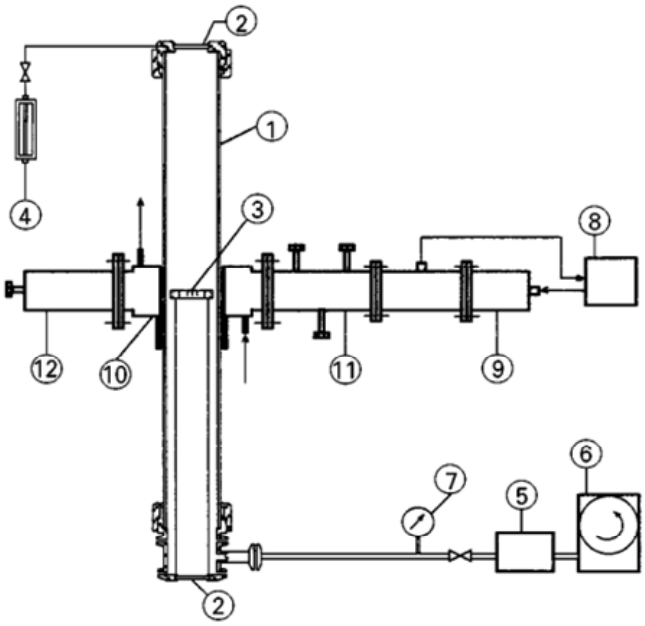

1 quarts chamber
2 viewports
3 sample holder
4 flow meter
5 pressure regulator
6 vacuum pump
7 pressure gauge
8 microwave generator
9 isolator
10 refrigerated wave guide
11 three stubs tuner
12 plunger

Figure 5-9: Scheme of the MESOX Experimental Setup by Balat [21].

For the evaluation of the recombination coefficients it is referred to two different procedures, the mesoscopic and the microscopic approach. The first is based upon the balancing of heat fluxes onto the material sample and allows for the qualitative determination of catalysis effects. The second evaluation involves additionally the concentration of all species. These values are measured by means of actinometry. For this reason the recombination coefficients can also be determined quantitatively.

For mesoscopic approach it is necessary to balance the heat fluxes for several conditions. For this purpose the circulation of the sample with Air, Air plasma, Argon and Argon plasma have to be performed, see also Figure 5-10. In every of these four series of experiments heat is conducted and radiated from the sample. But the energy impact onto the sample arises from different mechanisms. During Air and Argon tests the heating of the material sample is only affected by solar radiation. During Argon plasma tests an additional amount of heat will be released due to the microwave radiation producing ionized Argon plasma. A further test with Air plasma causes recombination reactions of the dissociated species, hence, the temperature of the sample increases further on. By comparing the energy balances of all four tests the thermal flux of recombination can be derived.

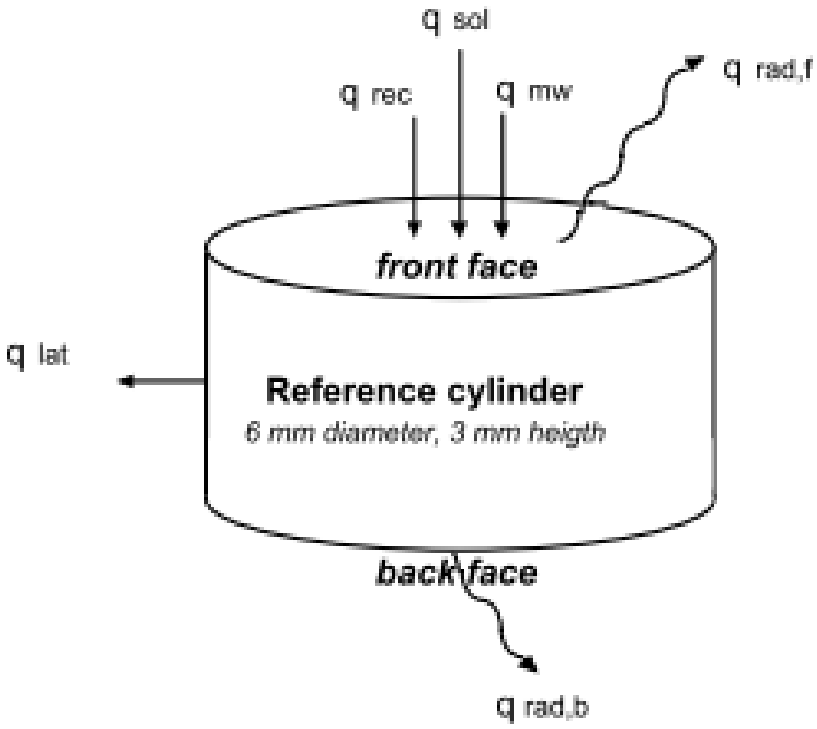

Figure 5-10: Heat Flux Balancing According to Balat [21].

The microscopic approach is used to measure the recombination coefficient quantitatively. The actinometry technique is used to identify the relative atomic concentration profile. This is done by introducing a small but known amount of Argon into the Air plasma. Then the ratio of the intensities of the dissociated species and an Argon line is measured. The ratio of these intensities is assumed to be proportional to the atom concentration. Further assumptions are needed for this measurement technique. The Argon should not disturb the Air plasma, the excited species must be solely produced by electronic impacts from ground state, the de-excitation of the species should be essentially by radiation and the cross-sections of the investigated atoms and Argon must be the same and the energy thresholds must be similar.

Furthermore by neglecting convection and radial fluxes the concentration is only varying along the x-axis:

$$D\frac{\partial^2 c}{\partial x^2} = 0 \tag{6}$$

The boundary condition for this equation are the ratio I_A/I_{Ar} is constant along the discharge and the at the surface sample, the mass balance in Oxygen atoms is established by the equality between the Oxygen arriving at the surface by diffusion and the atomic Oxygen recombined at the surface:

$$-D_{A,air}\left.\frac{\partial C_A}{\partial x}\right|_{x=0} - C_A(x=0)\frac{\gamma \cdot v}{4} = 0 \tag{7}$$

Here, v is the mean square velocity of atoms. Finally, the equation for the recombination coefficient can be derived:

$$\gamma = \left(\frac{\left. \frac{I_A}{I_{Ar}} \right|_{x=L}}{\left. \frac{I_A}{I_{Ar}} \right|_{x=0}} \frac{T_S}{T_L} - 1 \right) \frac{4D_{A,air}}{vL} \tag{8}$$

with I_A/I_{Ar} the ratio of the intensities respectively at the entrance of the reactor (x = L) and at the surface sample (x = 0), $D_{A,Air}$ the binary diffusion coefficient of the atomic species in Air and L the thickness of the concentration boundary layer.

5.2.5 Catalysis Measurements Using Plasma Wind Tunnels (such as IPM RAS, VKI and IRS)

The following section does not claim completeness in the sense that all available PWT facilities are covered.

5.2.5.1 Analytical Evaluation of Boundary Layer (IRS)

Measurements of recombination coefficients in Plasma Wind Tunnels (PWT) are another import method for the evaluation of catalytic phenomena. The advantage of using PWTs is that re-entry relevant conditions can be produced. First evaluations of the recombination coefficients utilizes the comparison of a fully catalytic material to the material to be investigated based on Goulard's Theory [7]. This method was used by many started with Scott [25] in 1980 and later on with Stewart [16] and the authors of references [26], [27]. As fully catalytic material reference material CuO was assumed to be close to being fully catalytic but this assumption of course contains some uncertainty. Further developments of this method avoid this assumption and will be described below.

At IRS tests to determine catalysis, particularly the measurement of Oxygen recombination coefficient, are performed in the inductively heated plasma wind tunnel PWK3. This plasma source produces subsonic and supersonic flows and has many advantages regarding other plasma sources, especially for material tests. With inductively heated plasma it is possible to generate pure Oxygen plasmas. In arc jets atomic Oxygen would lead to a fast corrosion of cathodes which leads on the one hand to a fast degenerating cathode and on the other hand to a polluted plasma. To prevent corrosion additional gases like Argon and/or Nitrogen are mixed to the Oxygen plasma in this kind of plasma sources. With pure Oxygen the measured recombination coefficients are much more accurate.

For employing Goulard's theory of stagnation point heat transfer the boundary layer is assumed to be frozen, hence, all recombination reactions occur on the surface. Due to low pressure and high stream velocities in Plasma Wind Tunnel tests this assumption is reasonable. The following analytical approach is valid for supersonic flows.

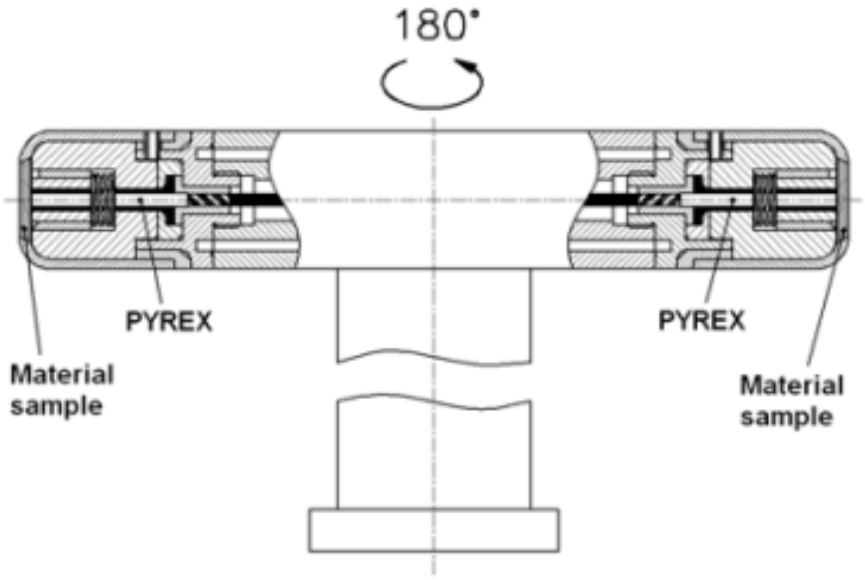

Figure 5-11: Material Double Probe with Mini-Pyrometer Pyrex [26].

The total heat flux to a catalytic surface excluding radiation is given by:

$$\dot{q} = \dot{q}_c + \dot{q}_{recom} \tag{9}$$

with $\dot{q}_c$ the convective part from ordinary molecular conduction and the released heat by atoms recombination at the surface which are balanced by the atoms diffusing though the boundary layer. The convective heat flux can be expressed by following equation:

$$\dot{q}_c = \lambda_w \left(\frac{\partial T}{\partial y} \right) = 0.47 \frac{\mu_w \rho_w}{(\mu_{se} \rho_{se})^{1/2}} (2\beta)^{1/2} \, \mathrm{Pr}^{-2/3} \, \bar{h}_{se} \tag{10}$$

The heat flux by recombination is simply the multiplication of the reaction rate constant, the heat of recombination of the atomic species and the partial density at the wall, thus:

$$q_D = h_R c_e \rho_e \frac{k_w}{\left(\frac{\mu_{se} \rho_{se}}{2\beta} \right) \frac{k_w Sc}{0.47 Sc^{1/3} \mu_w} + 1} \tag{11}$$

The correlation between the reaction rate constant and the recombination coefficient γ is:

$$k_w = \frac{2\gamma}{2-\gamma} \sqrt{\frac{\Re T}{2\pi M}} \tag{12}$$

so the recombination coefficient can be derived in case k_w is known.

The total heat flux can be obtained by measuring the temperature of the material sample in steady state condition. This has been done by pyrometric measurements. Following the heat flux can be achieved using

thermal analysis in combination with the relevant material properties such as, e.g., emissivity coefficient. Thus, by calculating the convective heat flux and subtracting the result from the total heat flux to the surface, the reaction rate constant yields:

$$k_w = \left[\frac{\Delta h_R c_{se} \rho_w}{\dot{q}_D} - \left(\frac{\mu_{se} \rho_{se}}{2\beta} \right)^{1/2} \frac{Sc_w^{2/3}}{0.47 \mu_w} \right]^{-1} \tag{13}$$

The frozen enthalpy $\overline{h_{se}}$ is given by:

$$\overline{h_{se}} = h_{tot}(x,0) - \frac{1}{2} u_e^2 - h_R c_e \,. \tag{14}$$

From Newtonian theory for the velocity gradient β follows:

$$\beta = \left(\frac{du_e}{dx} \right)_s = \frac{1}{R_{eff}} \sqrt{\frac{2(p_e - p_\infty)}{\rho_e}} \tag{15}$$

with R_{eff} the effective nose radius. For a supersonic plasma flow the Mach number can be derived by the well-known Raleigh-Pitot equation and the plasma temperature for example or by the use of relevant measurement techniques such as conical probes.

The density at the wall ρw in equation (9) which is needed for the evaluation of the reaction rate constant kw is itself depending on the species concentration at the wall; hence both parameters must be calculated simultaneously by an iterative procedure.

The Prandtl and Schmidt numbers and viscosity values in equation (10), (11), (13) were calculated according to Fertig et al. [28]. Finally with equation (5) and (7) the recombination coefficient can be derived.

Furthermore, the partial pressure of the dissociated species, which is the driving force for the chemical reaction. Generally a chemically reaction rate is calculated by the multiplication of a reaction rate constant and the species concentration of the concerning species or any collision partner.

$$\dot{\omega} = k_f \left[c_i \right] \left[c_j \right] \tag{16}$$

With the heat flux caused by catalytic reactions at the surface and the recombination coefficient it becomes possible to determine the species concentration at the wall. The diffusion part of the total heat flux is simply the net atom mass flux to the wall j_w multiplied with the heat of recombination h_R:

$$\dot{q}_D = h_R j_w = h_R k_w c_w \rho_w \,. \tag{17}$$

Since the mass fraction and the molar fraction are connected by:

$$c_w = \frac{\psi_A M_A}{\sum \psi_i M_i} \tag{18}$$

the partial pressure of the atomic species which is the driving force for the catalytic reaction is obtained by:

$$p_A = \psi_A p \tag{19}$$

Further quantities like absolute numbers of atoms hitting the wall and absolute number of recombining atoms as well as the atomic concentration gradient at the wall can be easily obtained:

$$N_r = \frac{j_w}{M_A u}, \tag{20}$$

$$N = \frac{N_r}{\gamma}, \tag{21}$$

$$\left(\frac{dc_A}{dy}\right)_w = \frac{j_w Sc}{\rho_w \mu_w}. \tag{22}$$

This method allows the determination of recombination coefficients depending on temperature and the partial pressure on the surface.

5.2.5.2 Numerical Evaluation of Boundary Layer to Derive Recombination Coefficients

Similar measurement techniques as described in the previous chapter with a stronger application of CFD simulations for numerically rebuilding of the free stream plasma, computation of non-equilibrium multi-component boundary layers and modelling of reacting plasma and gas flows within plasma torch and around sensor probes were performed by Kolesnikov [29], [30]. In their PWT tests with pure Oxygen and Nitrogen as well as CO_2 and Air were performed.

Measurements at the plasmatron facility at the VKI [31], [32] were performed and evaluated by means of numerical calculations with a boundary layer code. This PWT mainly uses Air plasma; hence, an effective recombination coefficient for Air is calculated. The recombination coefficients therefore of the single species Oxygen and Nitrogen are, therefore, difficult to distinguish.

The advantage of numerical evaluations is the deeper insight into single processes of hypersonic boundary layer flows. Nevertheless the numerical rebuilding of plasma wind tunnel flows around different sensor probes at different inflows still remains a difficult and time-consuming task. Also the use of numerical boundary layer codes only does not avoid assumptions such as chemical and thermal equilibrium at the edge of the boundary layer.

5.2.6 Catalysis Measurements Using Shock Tubes (CUBRC)

Besides Plasma Wind Tunnels (PWT), shock tubes can be used to determine the recombination coefficients of sample materials. At CUBRC, finite rate surface recombination coefficients are determined based on fitting numerical predicted heat fluxes to experimentally gained heat flux values. Currently the experiments are performed in the LENS-I and LENS-II facilities of CUBRC. The facilities represent reflected shock tunnels creating very high enthalpy flows. The capabilities of the LENS facilities are shown in Figure 5-12.

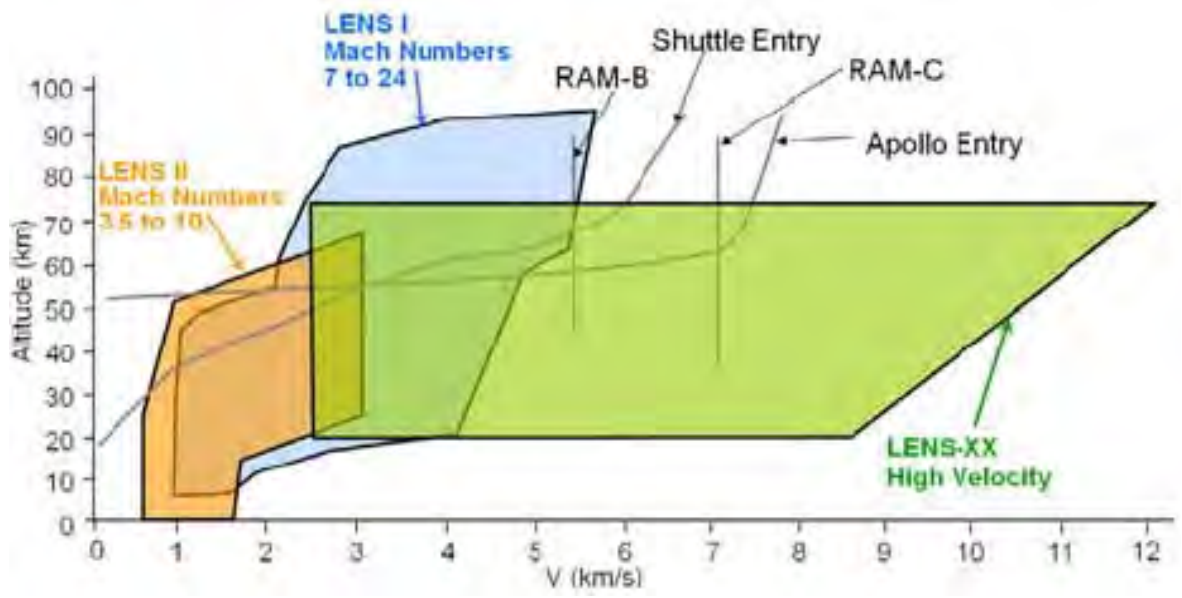

Figure 5-12: Velocity-Altitude Duplication Capabilities of CUBRC LENS Facilities [34].

For measurements reported in [34], the facilities were operated with Nitrogen, Air and Carbon Dioxide as test gas. The enthalpy was varied between 5 MJ/kg and 15 MJ/kg. All tests were performed using test articles made of stainless steel or aluminium, which represent the typical materials for shock tube testing. The investigated test articles were either in the shape of a spherical capsule or a sphere cone. In addition cylindrical test articles were tested. To measure the heat flux on the test article, they are equipped with heat flux sensors from type thin-film, coaxial thermocouple or calorimeter. In addition, pressure gauges in the test article are part of the experimental setup.

The measured heat flux is compared to numerically predicted heat flux curves computed under variation of the finite rate surface recombination coefficient. The tool used for the numerical predictions is the DPLR code of NASA Ames Research Center. The code solves reacting Navier-Stokes equations including finite rate chemistry and finite rate vibrational non-equilibrium effects. A limitation of the code is that only homogeneous surface reactions are considered. Therefore, besides the variation of the recombination coefficient for the homogenous surfaces reactions, a further case, the super-catalytic wall, is considered. The super-catalytic wall is defined by their characteristics of recombining completely O_2/N_2 and CO_2.

Exemplarily, the results for the spherical capsule model in a 10.3 MJ/kg Nitrogen flow are shown in Figure 5-13. Besides the measured pressure and heat flux distribution, the figure reports the numerically calculated pressure and the numerically predicted heat flux under variation of the recombination coefficient. It is evident that the numerically obtained results for $\gamma = 0.01$ fits best to the measurement. This showcase illustrates the finding of MacLean and Holden, who report that in all their test cases in Nitrogen, the catalytic recombination probability was fount to be most likely between 0.001 and 0.01. Unlike for Nitrogen, for Air the numerical predictions show best agreement with the experiment in case of the super catalytic wall assumption. This conclusion is limited to the test cases with lower enthalpy (5 MJ/kg), because the CFD results of MacLean and Holden rebuilt the high enthalpy flows only insufficient, e.g., wrong bow shock stand-off. For reliable results improvement of the CFD computations is required. Similar conclusion is drawn from the CO_2 test cases.

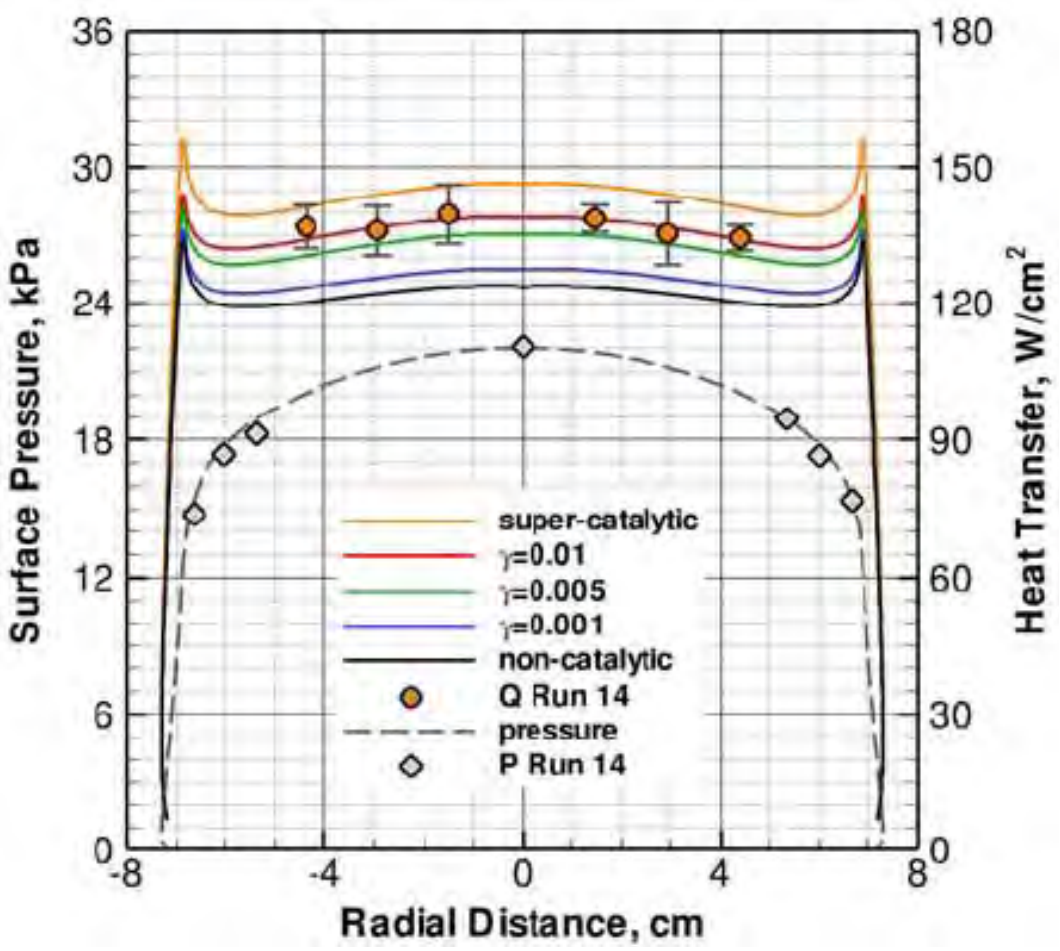

Figure 5-13: Nitrogen, 10.3 MJ/kg, Spherical Capsule [34].

5.2.7 Comparison

In the last years several analytical solutions have been introduced to model recombination probabilities, e.g., Fertig [35]. The main advantage of these much more sophisticated methods is obvious. With the knowledge of recombination coefficients only a global modelling of heat flux predictions due to atomic recombination is possible because the recombination coefficients are the result of the summation of several physical intermediate steps. With detailed analytical models it becomes possible to model these elementary reaction steps like adsorption, desorption, Eley-Rideal-Chemistry and also Langmuir-Hinshelwood-Chemistry directly. The problem occurring with such detailed modelling is the need of a good database to correlate parameters which are introduced by these models and which are unknown a priori or have a wide fluctuation range. In other words the analytic models need a calibration with measurement data.

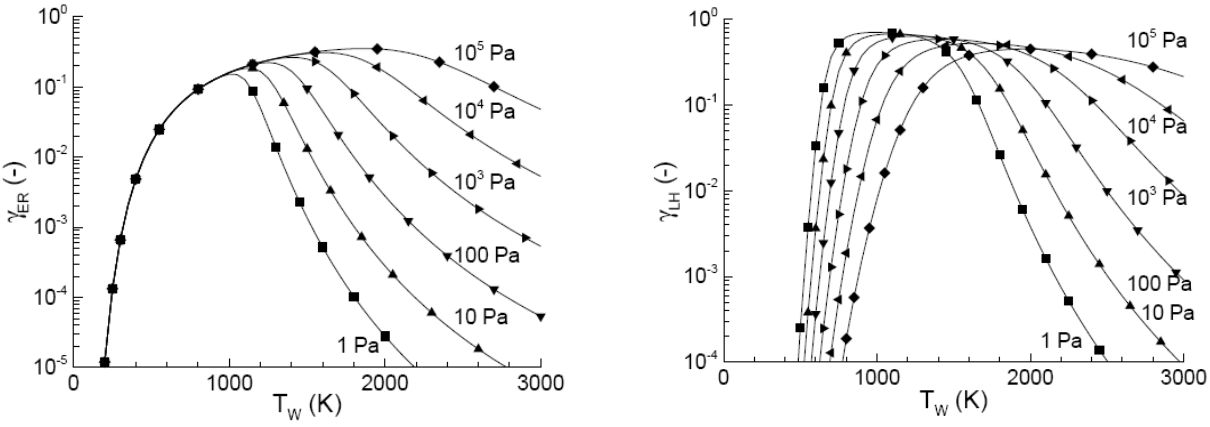

Figure 5-14: Analytical Calculated Partial Pressure Dependency of γER and γLH [35].

Nowadays there are only few materials which provide such a good database which is suitable for this calibration. Such materials are SiC or SiO_2 for example, which are widely investigated in the past. In literature recombination coefficients were usually presented with a dependency only on temperature. This information is not adequate enough because recombination probabilities also depend strongly on partial pressures. Additional information like absolute reaction rates or chemical heat fluxes would also help creating such a database to calibrate analytic models.

In the figure below Oxygen recombination coefficients on SiO_2 can be seen as an example of comparison. Depending on the temperature the deviation of data which can be found in literature differs up to two orders of magnitude. This is mainly due to missing information of pressure data, energy accommodation coefficients and differences of the crystalline structure of the used SiO_2 material.

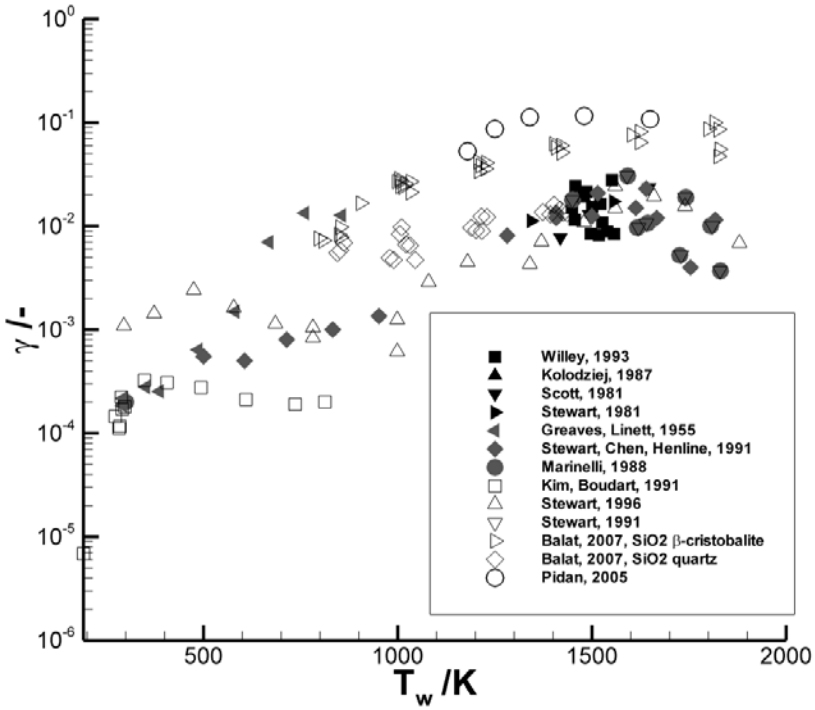

Figure 5-15: Comparison of Oxygen Recombination Coefficients of SiO_2.

Table 5-1: Comparison of Different Experimental Measurement Techniques.

	Category		Temperature Level /°C	Pressure Level /Pa	Recombination Coefficient /-	Energy Accommodation Factor /-
Measurement Technique	**Energy Balance**	**Concentration Measurement**				
Side-Arm	–	X	RT – 1200	< 4	X	X
Effusion	X	–	RT – 1700	< 4	X	–
Chemical Luminescence	–	X	RT – 1200	< 100	X	–
Mesox	(X)	X	Up to 2500	100 – 100000	X	X
PWT	X	–	500 – 2500	10 – 50000	X	–
Shock Tunnel	X	–	RT	1000 – 10000	X	–

5.2.8 Recommendations

During the past two decades several institutions have gathered extensive expertise in the field of recombination and/or chemical accommodation coefficient measurement techniques. This document gives a first preliminary review of the facilities and the accompanying methodologies. This in turn is then a basis for the later evaluation of collaboration potential enabling an improvement of the overall catalysis measurements. A sufficiently detailed review of the reported recombination coefficient data has not been performed so far and still requires an open exchange of data.

In a first step a combination of the existing expertise would lead to a creation of confidence in the methodologies and, in addition, to a potential improvement of the discussed methods. Methodologies that make use of boundary layer models often lack in detailed experimental and numerical characterization of the boundary layers and, in addition, they often use equilibrium derived parameters which somehow contradicts the situation of investigating a non-equilibrium effect (i.e., catalysis). In addition, the representation of the data has to be evaluated religiously as, e.g., a majority of the published data neglects the necessity to include both the wall temperature and the pressure information within the data sets.

The development of an open data base enabling the comparison and evaluation data is of utmost importance. Such open data and the open discussion would at least minimize uncertainties resulting from the derivation of data out of respective data and documents. These assessments would be a prerequisite for a harmonization process which would lead to an evaluation, verification and validation of the data. In addition overlaps of the different methodologies (example: Comparison IRS Oxygen condition with data from moderate enthalpy Air condition from VKI was promising and approved convergence of the Kolesnikov model towards the IRS methodology) could be assessed. Correspondingly, the creation of a working group either on an international level (as a “continuation” of the RTO Task Group), an ESA level or an EU level which may even allow including partners from the Americas and Russia as well is very imperative.

A further step is the comparison and/or (mutual) verification with numerical models and, most important, the development and realization of catalysis-based instrumentations within flight campaigns. One good example is MIRKA where heat flux data were successfully correlated to relevant plasma-surface interactions using the URANUS code. A very good occasion has to be seen in the non-equilibrium in-flight sensor systems aboard the European capsule EXPERT. The flight that can be expected from the junction experiment (VKI),

the catalysis-based experiment PHLUX and the overall on board heat flux sensors will enable rebuilding activities along the trajectory using the CFD codes that include plasma-surface modeling. These activities would then lead to a catalysis data base that is verified and validated to a maximum extend.

In the section **"Analytical Evaluation of Boundary Layer (IRS)"** two improvements are outlined: One refers to the aforementioned derivation of pressure, i.e., the partial pressure, the second refers to the elimination of a highly catalytic reference material (such as in Smith's methodology) to improve the accuracy. First data have already been derived and published.

A further point is the energy accommodation. Only a minority of the referenced methodologies is capable to derive the energy accommodation coefficient. Therefore, an assessment of the significance of b as, e.g., in [33] and the qualification level of existing experimental data is strongly recommended.

5.3 MODELLING APPROACHES FOR GAS-SURFACE INTERACTIONS

This chapter has the following set-up: in the first sub-chapter we discuss the main catalysis processes, Eley-Rideal and Langmuir-Hinshelwood more in detail. Then surface oxidation processes of SiC-based TPS materials are focussed as they are typical example for the interaction between oxidation and catalysis. In the last section we present some numerical implementations which take into account modelling approaches such as finite rate surface reaction models as they are, e.g., implemented within the 2-D CFD code URANUS [36], electronic structure computations as, e.g., in reference [37] and kinetic Monte Carlo simulations such as in reference [38] and as, e.g., implemented in the IRS DSMC code LASVEGAS [38].

5.3.1 Catalysis Models / Dominant Processes (To Implement)

Although the pressure at the luv side of the vehicle is relatively high, the collision frequency between the atoms in the boundary layer is too low to allow for their recombination, i.e., the boundary can be considered frozen concerning recombination under peak heating conditions. As already mentioned, the recombination of atoms might be catalysed by the heat shield material. Such heterogeneous catalytic processes consist of multiple elementary reactions. A general need for this kind of catalytic recombination is an increase of collision probability.

This arises, if the atoms stick at the surface for some time which required a bond between atom and surface. The residence time of adsorbed atoms at the surface depends mainly on bond strength and temperature. At high temperature the thermal desorption becomes dominant such that the surface coverage reduces. Depending on the bonding type one distinguishes physisorption and chemisorption. Physisorption arises due to Van der Waals forces between adsorbed particles and the surface. The bond energy is typically in the order of 20 kJ/mole. Since no chemical bond is necessary, multiple layers of adsorbed particles are possible. However, due to the low bond energy adsorption becomes dominant at temperatures significantly below 1000 K. For thermal protection systems under peak heating conditions which experience temperatures above 1000 K the chemisorption is the more important process since the bond energy is in the order of 200 kJ/mole.

The impact of recombination is evident and the quantitative values of both minimum and maximum as well as the position of the heat flux increase depend on the catalysis properties of the surface material and on the conditions of the incident flow. In particular, the steep slope regime is of interests as the potential to manipulate the heat flux is most significant. In an overall consideration the process itself happens through the transport of atomic species (Oxygen and Nitrogen atoms in case of Air) to the material surface. Here, either at least one or more of the chemical precursors experience chemisorption. In a third step usually either the adsorpts react with each other (i.e., Langmuir-Hinshelwood mechanism) or one adsorpt reacts with a precursor that is still in the gas phase (i.e., Eley-Rideal mechanism). After that the resulting products (the molecules) are desorpted from the surface and then leave the surface zone.

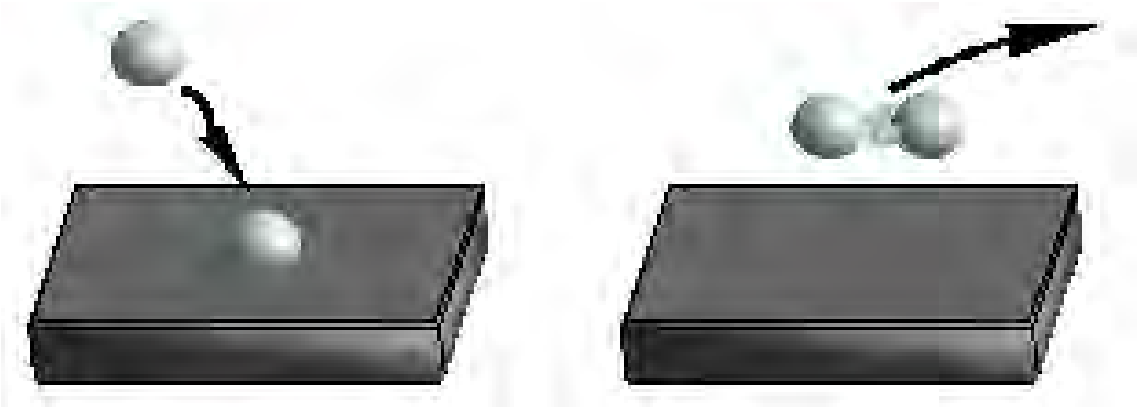

Figure 5-16: Eley-Rideal Mechanism.

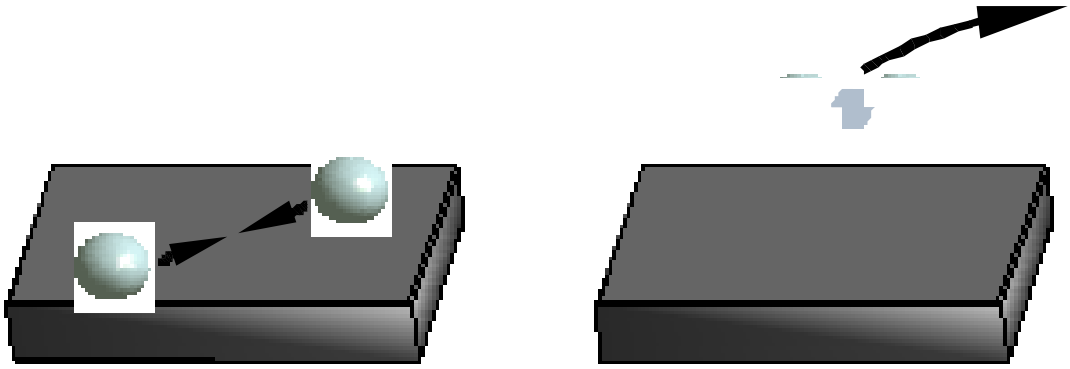

Figure 5-17: Langmuir-Hinshelwood Mechanism.

5.3.2 Surface Oxidation Models

For the development of re-entry vehicles, a detailed prediction of the surface loads during hypersonic flight is essential. In the high temperature areas of the surface temperature may exceed 2000 K. Therefore, TPS materials based on SiO_2 such as RCG can not be used there. Ceramics based on SiC withstand much higher temperatures and have a high emissivity as well, which allows for an effective radiation cooling of the surface. As compared to SiO_2-based materials the catalytic efficiency of SiC concerning Oxygen and Nitrogen atoms is significantly higher at high temperatures. Furthermore, SiC may react with Oxygen or Nitrogen forming the gaseous species SiO, SiN, CO and CN. If the surface temperature is sufficiently low and the Oxygen partial pressure is sufficiently high, a solid SiO_2 layer may form at the surface, which acts as a protection layer for the underlying SiC. All of the reactions described so far are exothermal, i.e., chemical energy is transferred towards the surface. Therefore, a protective SiO_2 layer is desirable at the surface since SiO_2 not only protects the SiC from further oxidation but is also less catalytic. Ambient conditions leading to the formation of a protective SiO_2 layer are called ‘passive’. Unfortunately, the protective SiO_2 layer is removed from the surface in the temperature range of 1600 K – 2100 K depending on Oxygen partial pressure. As a consequence, the bare SiC is exposed to the highly reactive, partially dissociated gas flow. In this case, the reaction behavior is called ‘active’.

5.3.3 Brief Overview on Numerical Implementations

Three major (basic) approaches can be identified for the description of surface chemistry models:

- Finite rate surface reaction models as, e.g., described in reference [36].
- Kinetic Monte Carlo as, e.g., applied in reference [38].
- Molecular dynamics as, e.g., in reference [37].

As depicted in Figure 5-18 all numerical approaches have spatial and temporal domains in which they are valid or applicable. For the treatment of practical problems one needs to focus on large scales. The chemical and physical data for the implemented models is either obtained by experiments or by theoretical/numerical considerations at (much) smaller scales. From a technical point of view, the Molecular Dynamics (MD) and Kinetic Monte Carlo (KMC) methods are bridging technologies which enable an accurate treatment of realistic engineering problems by producing data needed as input parameters for other numerical tools. Due to the scope of the present work we limit ourselves to brief introductions of existing catalysis related MD and KMC investigations. For the sake of clarity, we start with the large scales which are the domains of macroscopic approaches represented by CFD and DSMC.

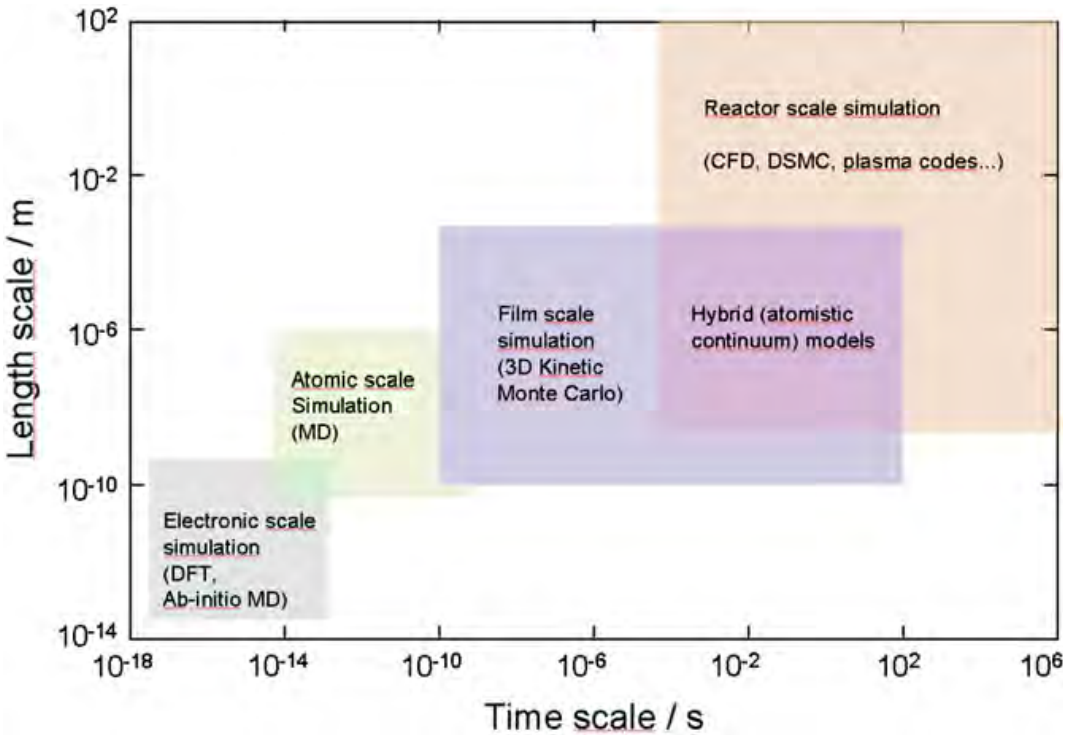

Figure 5-18: Spatial and Temporal Scaling Classification of Different Numerical Methods.

Reference [36] applies finite rate surface models to the situation of the atmospheric entry. In order to predict the thermal and mechanical loads during re-entry, the URANUS (Upwind Relaxation Algorithm for Non-equilibrium Flows of the University of Stuttgart) code has been being developed at the Institute of Space Systems (IRS) of the Universität Stuttgart. For the accurate determination of the thermochemical conditions, advanced thermochemical relaxation models for the gas-phase as well as sophisticated gas-surface interaction models have been developed. The Navier-Stokes equations for the 11-component Air flow which consists of N_2, O_2, NO, N, O, N^+_2 ,O^+_2 , NO^+, O^+, N^+ and e have been derived by the Chapman-Enskog method from the Boltzmann equation. The linearized system of equations is solved fully

coupled and fully implicitly, employing Newton's method. A global catalysis model, which assumes complete chemical energy accommodation at the surface, is presently used in the 3-D version of the URANUS code. The catalytic behavior of the implemented technical surfaces (SiC, SiO_2) is modeled by overall recombination coefficients which were measured by Stewart in a large surface temperature range.) For design approaches, non- and fully-catalytic cases can also be simulated by the 3-D URANUS code. More advanced gas-surface interaction models, which allow for a detailed simulation of the elementary reactions as well as of active and passive oxidation of SiC, are available in the 2-D/axisymmetric code. Ceramics based on SiC withstand temperatures above 2000 K and have a high emissivity, which allows for an effective radiation cooling of the surface. Hence, the nose caps of the US Shuttle orbiter, X-38 and Hope-X are all based on silicon carbide. In comparison to SiO_2-based materials, the catalysis of SiC concerning Oxygen and Nitrogen atoms is significantly higher at high temperatures. Furthermore, SiC may react with Oxygen or Nitrogen, forming the gaseous species SiO, SiN, CO and CN. If the surface temperature is sufficiently low and the Oxygen partial pressure is sufficiently high, a solid SiO_2 layer may form at the surface and acts as a protection layer for the underlying SiC. All of the reactions described so far are exothermal, i.e., chemical energy is transferred towards the surface. Therefore, a protective SiO_2 layer is desirable at the surface since SiO_2 not only protects the SiC from further oxidation but is also less catalytic.

At sufficiently low pressures and/or at sufficiently strong disturbances the continuum hypothesis fails due to highly reduced particle interactions leading to a non-negligible reduction of collision-based relaxation processes. Accordingly, at high Knudsen numbers even small deviations from equilibrium lead to problems for continuum approaches. Macroscopic properties exhibit large statistical fluctuations. However, such high Knudsen regimes can be treated numerically by the use of DSMC methods. At the IRS, a 2-D axi-symmetric DSMC code with flexible chemistry was developed. Typical problems treated are atmospheric re-entry flows and nozzle expansion flows into a low pressure environment. A detailed description of the physico-chemical models are given in [39].

Concerning the catalysis effect, focus is on the ER mechanism since Seward [41] showed that for TPS materials in Air the LH mechanism is negligible compared to ER as the relevant temperatures are in the range of 1000 K – 2000 K. In our DSMC code we modeled so-called active sites as surface elements which can be identified with the Si atoms. Recombination may occur only in case of an already adsorbed atom j. In such cases the recombination probability for an incoming atom i is given by:

$$P_{rec,ij} = \gamma_{ij}\left[1 - \exp(-N_{ad,j})\right]. \tag{23}$$

Here, $N_{ad,j}$ gives the number of adsorbed atoms j. However, as the main (i.e., critical) surface reactions are expected to occur at high pressure regions where DSMC in unfeasible compared to CFD codes the catalysis implementations are of minor importance.

The second numerical methodology (Kinetic Monte Carlo – KMC) can be addressed via a statistical approach 3: The gas-surface-interaction that takes place in the chemically reacting flow around an atmospheric re-entry vehicle is investigated. It turns out that the currently very often used approach employing a recombination coefficient has a limited applicability. Serious concerns arise when the interaction model is extrapolated from ground to flight tests.

The KMC approach can be facilitated in order to provide macroscopic rate coefficients which are obtained from such simulations. Contrary to the other particle methods, KMC is a zero-dimensional approach without any (typical) particle positions or velocities. Instead, surface areas are discretized and initialized. Each surface element is able to adsorb particles, i.e., to be covered by particles. The particles exist only as surface particles in case that a respective microscopic process or transition occurs. The master equation which governs the microscopic surface transitions is:

$$\frac{dP_\alpha}{dt} = \sum_\beta (W_{\alpha\beta} P_\beta - W_{\beta\alpha} P_\alpha) \tag{24}$$

and can be derived from first principles or empirically, see, e.g., [40]. Here, α and β are surface configurations, P_α is the probability to find the system in configuration α, $W_{\alpha\beta}$ is the (microscopic) rate coefficient of the process leading to configuration α which is usually given in Arrhenius form. An exception is the rate coefficient for the adsorption process which has the form:

$$W_{ads} = \frac{pA_{site}\sigma}{\sqrt{2\pi m k_B T}} \tag{25}$$

with σ being the sticking coefficient. This quantity (σ) describes the probability of a gas-phase atom or molecule to stick to the surface element and can be obtained, e.g., by MD simulations.

In a typical KMC simulation the surface elements are initialized as empty surfaces with a pre-defined temperature. After some simulation period a steady-state solution is obtained which, in combination with a spatial averaging process, leads to the macroscopic rate coefficients. Thömel et al. [38] extensively performed such simulations on basis of a platinum surface in a CO_2 environment, see Figure 5-19.

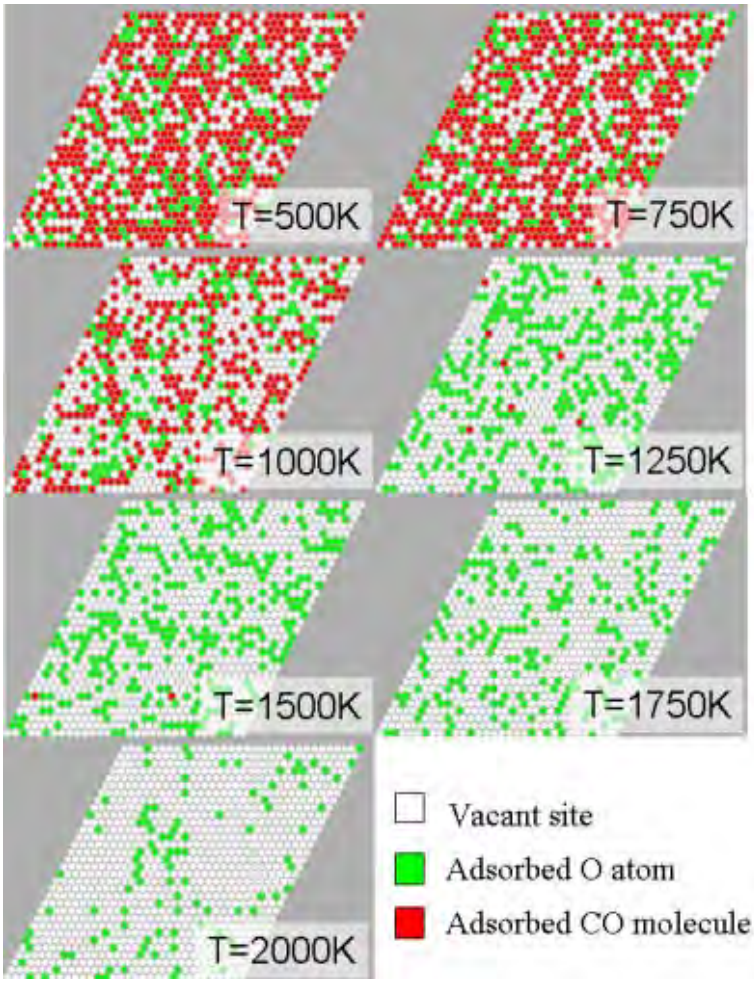

Figure 5-19: Steady-State Solutions as Functions of Platinum Surface Temperature T [37].

By considering 12 different surface events including (dissociative) adsorption, ER mechanism, LH mechanism, desorption and even surface diffusion they showed that the widely used approach employing recombination coefficients for the different atomic gas-phase species has a limited applicability. This is a result of the effect of changing the gas phase condition by desorption processes. Since diffusion processes of particles to and from the surface are usually neglected in macroscopic approaches. In [38] the obtained rate coefficients were applied to a continuum viscous flow simulation showing that at high temperatures the LH mechanism for atomic Oxygen dominates the ER mechanism, see Figure 5-20. In case of CO, the ER mechanism is the dominating process.

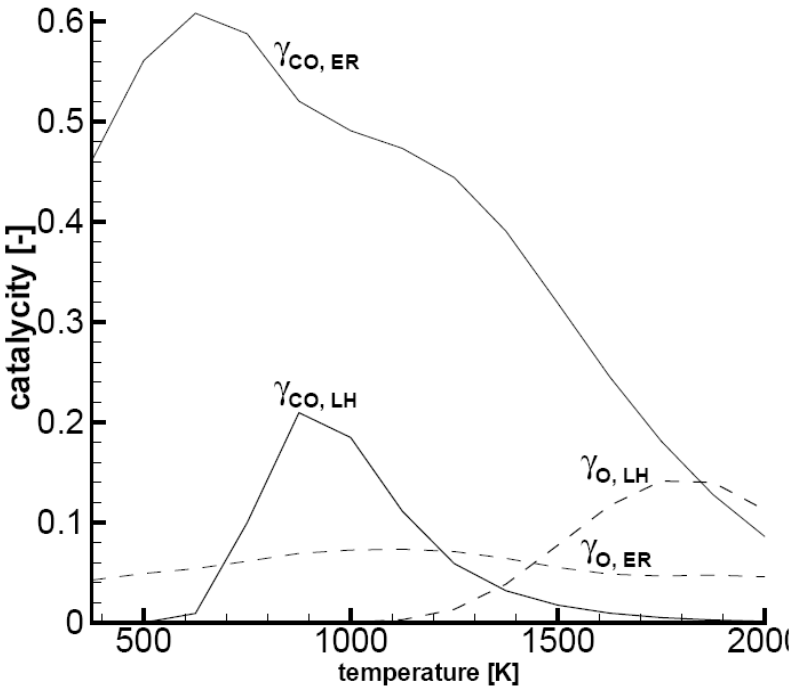

Figure 5-20: Catalysis of CO and O Over Temperature [37].

A catalysis-based KMC approach needs as input several parameters as, e.g., adsorption and recombination coefficients which can be obtained by Molecular Dynamics simulations. We have to distinguish between the classical MD approaches and the ab initio MD methods. The former uses a given, i.e., predefined, set of potential parameters in order to solve the Hamiltonian of a many body system, the latter additionally resolves the electronic structure (e.g., by Density Functional Theory – DFT), thereby delivering the potential information.

In [37] the authors studied N_2 creation of adsorbed N atoms at a Silica surface with T = 1000 K by use of semi-classical MD simulations. The fitted potentials of the interactions between N and N_2 and Si_xO_y clusters were pre-computed by DFT calculations on basis of a size-scalable approach. Semi-classical MD means here that additionally to the classical MD scheme surface phonon excitations of the crystal structure were quantum-mechanically self-consistently treated. Focus was set on the ER mechanism:

$$N(s) + N(g) \rightarrow N_2(g) + \Delta E\,. \tag{26}$$

The key question was the energy share of ΔE after the recombination and desorption process in terms of internal and translational energy of N_2(g) and the energy transferred to the surface. The results are given in Figure 5-21.

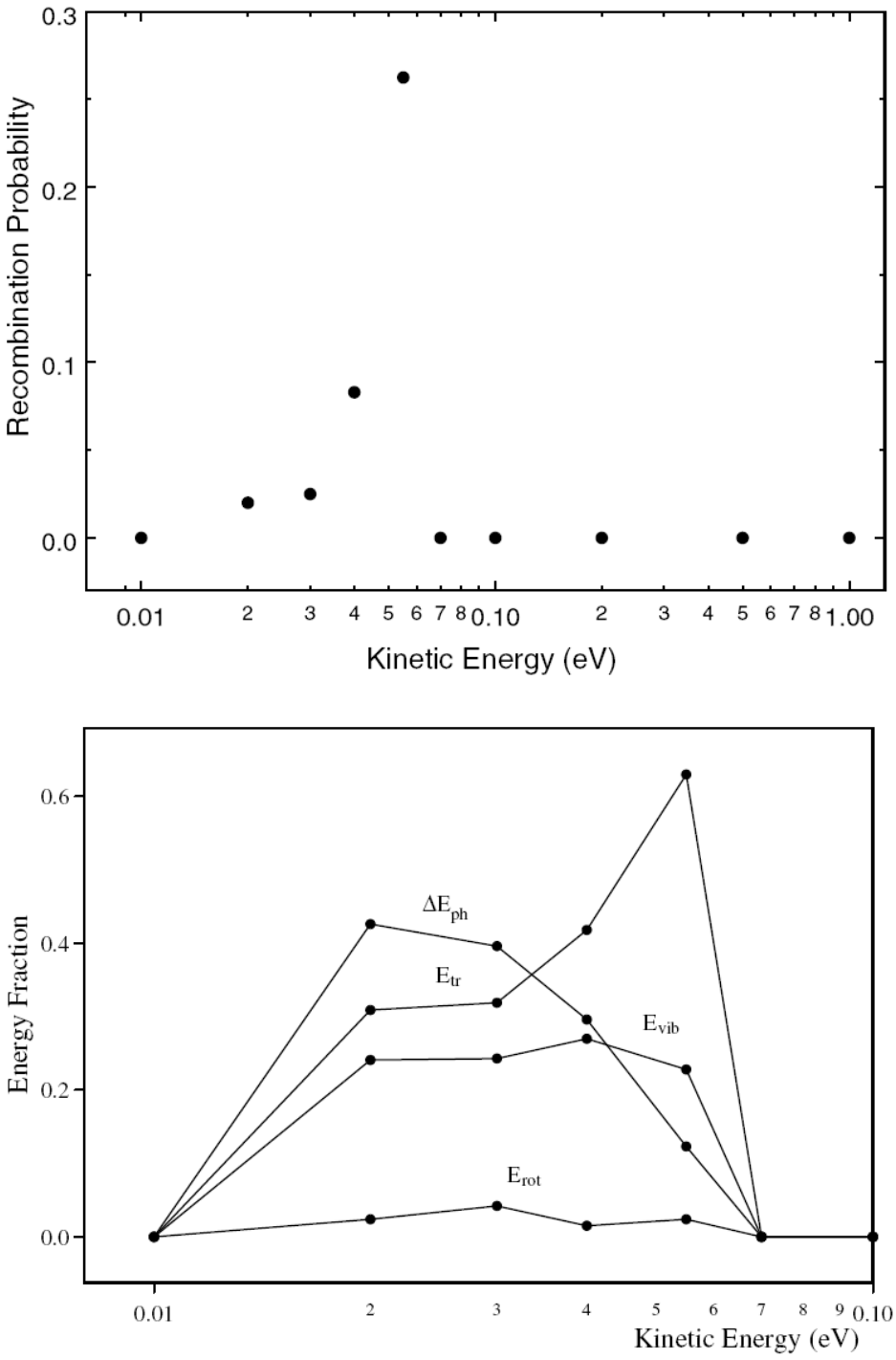

Figure 5-21: Theoretical Recombination Probability (top) and the Energy Fractions (bottom) as a Result of the Semi-Classical MD Simulations of Nitrogen-Based ER Mechanism at a Silica Surface [36].

The recombination probability for the discussed reaction is depicted over the kinetic energy of N_2(g). Obviously, a non-vanishing recombination probability exists only in the range between 0.02 eV < E_{kin} < 0.55 eV. A trajectory analysis showed that the most favourable condition for the ER mechanism exists when the adsorbed N atom desorbs in the gas-phase into the direction of the

incoming N atom. Averaging the impact energies of the incoming atoms over a Boltzmann distribution at $T_{gas} = T_s = 1000$ K yields a theoretical recombination coefficient of $\gamma = 3.99.10^{-2}$. Due to the lack of comparable experiments an adequate validation of these results is still difficult.

The bottom image of Figure 5-21 shows the total energy partitioning as a function of the kinetic energy of the incoming atoms. Here, E_{tr}, E_{vib}, E_{rot} and ΔE_{ph} represent the translational, vibrational and rotational energies of the created N_2 molecule as well as the phonon modes of the lattice atoms. One can see that at lower energies the largest energy part (approx. 40%) is absorbed by the surface. The trajectory analysis showed that the recombination is very close to the surface such that the coupling between phonon excitations and particles is strong. At higher energies the largest fraction is transferred to the translational mode. Over a large energy range the vibrational energy friction is about 20% while there is nearly no transfer to the rotational degree of freedom.

Similar computations were performed by Sayòs et al. [42]. Instead of Nitrogen they investigated the gas-surface interaction between atomic and molecular Oxygen and a Silica surface. They chose two temperatures, 300 K and 1000 K. Unfortunately; most published results are based on the low temperature (in combination with O_2) such that for our discussion here only the results given in Figure 5-22 are of practical interest.

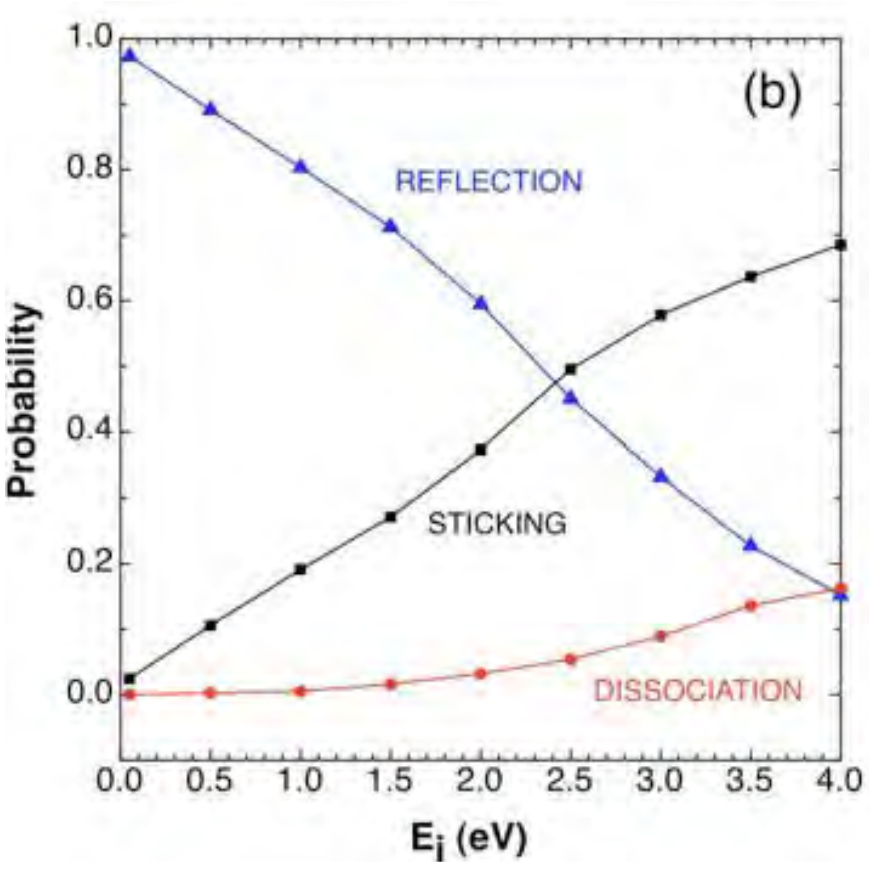

Figure 5-22: Reflection, Sticking and Dissociation Probability of Incoming O_2(v = 0, j = 1) Over its Kinetic Energy at T_s = 1000 K [36].

The probability coefficient for different processes shows that surface dissociation increases with increasing kinetic energy. The same behaviour is observed for the sticking probability while the reflection probability decreases.

Typical MD and KMC simulations initialize the surface as a plane element. However, real surfaces are not plane at all such that advanced modelling of surface roughness [43], [44] is expected to improve the fitting of numerical results according to experimental measurements.

5.4 CONCLUSIONS AND WORK PLAN CONSIDERATION

In principal, three quite diverse assessments of methodologies are available to enable the numerical calculation of catalysis. Often these assessments are hybridized and the evaluation of these methods and their respective validation is difficult as relevant non-equilibrium flight data are rare. However, some attempts were performed successfully, e.g., using the MIRKA flight data (not shown here, but published).

Having in mind all these results we claim that it is generally possible to drastically improve macroscopic catalysis models by a stepwise increase of the temporal and spatial scale of the applied numerical tools as depicted in Figure 5-18. Future work must be dedicated towards an exchange between the different communities and respective comparisons. The corresponding activities are at their very beginning and should be addressed within a working group of international level.

Figure 5-23 gives an overview on the present situation (without pretension of completeness). However, all of the shown examples in the three regimes “Modeling”, “Ground Tests” and “Flight Experiments” belong to well-documented research groups/projects such that they somehow identify the basis for a future multi-year work plan to assess catalysis. The overall ambition has to be seen in a set of activities assigned to a maximum of verification and validation of relevant catalysis data which is more or less a synthesis activity for the examples given in Figure 5-23.

- Establishment of an international catalysis working group. This group will give an umbrella for the following activities and, in addition, informal meetings will allow the identification of potential advancements in both fields (experiment and model) and, e.g., definition of reference test cases and conditions.
- Correspondingly, a first research proposal could be the realization of a relational data base for experimental catalysis data- at least as long as the catalysis data (recombination coefficients and energy accommodation) have not already been established, e.g., in the models by the use of measured recombination coefficients. For this the review in this report has to be used in order to link the origin of the data, the methodology, i.e., how the data were measured and relevant issues such as assumptions, measurement technique used and modelling support. This will guarantee a traceability of the data and statements of their relevance on the theme of atmospheric entry.
- A similar assessment has to be performed with models that derive catalysis data. Of, course flight data have to be included within the combined data base.
- The obtained data bases have to be cross-linked in order to have a verification tool.

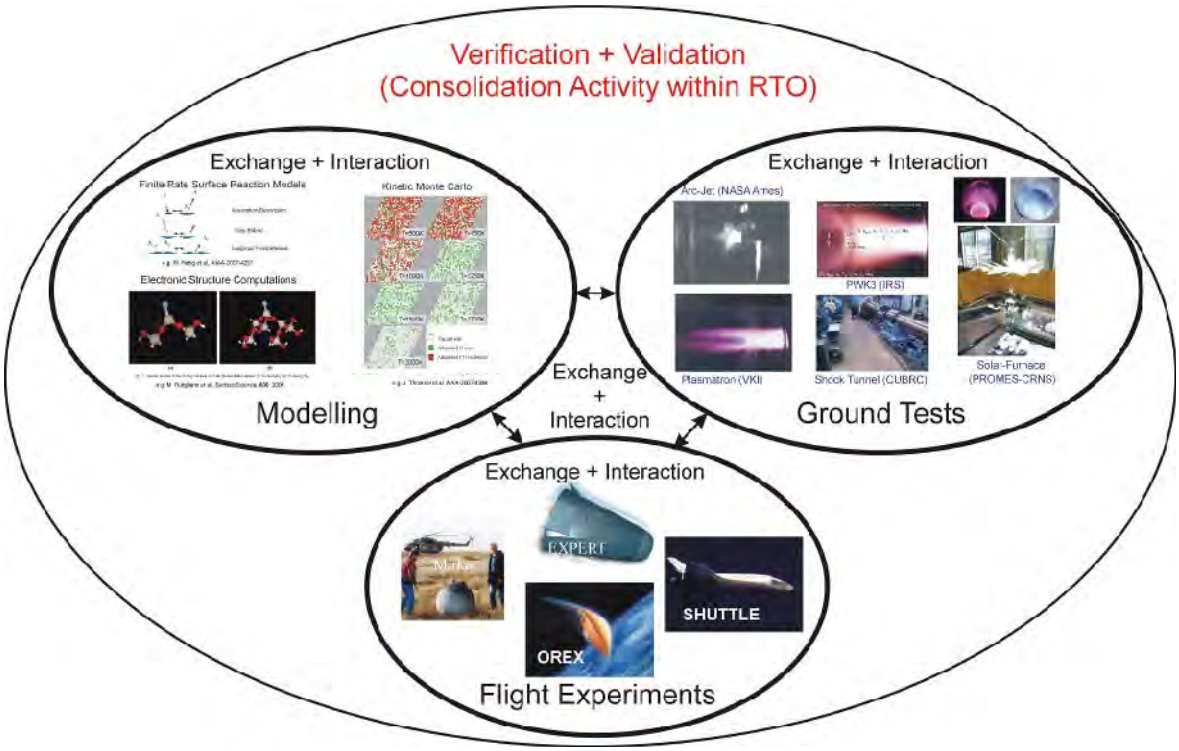

Figure 5-23: Motivation Scheme for the Proposed Work Plan.

For all of the three aforementioned fields a first step programmatic for research projects is needed: This should consist of the development of a relational data base on catalytic coefficients including the data themselves, the methodology used, the (reviewed) reference of the data, a field identifying the verification and validation levels achieved through cross-links and comparisons. An analogue assessment should be performed for flight data and experimental data which are then to be linked to the aforementioned data base. Overall in a following step a metrological analysis of the methodologies should be performed.

5.5 REFERENCES

[1] Kolesnikov, A.F., "Combined Measurements and Computations of High Enthalpy and Plasma Flows for Determination of TPM Surface Catalycity", RTO AVT/VKI Special Course on "Measurement Techniques for High Enthalpy Plasma Flows", von Karman Institute for Fluid Dynamics, RTO EN-1, Rhode-Saint-Genèse, Belgium, October 1999.

[2] Stöckle, T., "Untersuchung der Oberfächenkatalyzität metallischer und keramischer Werkstoffe in Hochenthalpieströmungen", Dissertation (in German), Institute for Space Systems, Universtät Stuttgart, 2000.

[3] Dickens, P.G. and Sutcliffe, M.B., "Recombination of Oxygen Atoms on Oxide Surfaces – Part 1 – Activation Energies of Recombination", *Transactions of the Faraday Society*, Vol. 60, pp. 1272-1285, 1964.

[4] Reggiani, S., Barbato, M., Bruno, C. and Muylaert, J., "Model for Heterogeneous Catalysis on Metal Surfaces with Applications to Hypersonic Flows", 31st AIAA Thermophysics Conference, New Orleans, LA, USA: AIAA – 96-1902, 1996.

[5] Herdrich, G., Fertig, M., Petkow, D. and Steinbeck, A., "Modeling Approaches for Gas-Surface Interactions", AIAA Paper, 48th AIAA Aerospace Sciences Meeting including the New Horizons Forum and Aerospace Exposition, Orlando, FL, USA, 4-7 January 2010.

[6] Fay, J.H. and Riddell, F.R., "Theory of Stagnation Point Heat Transfer in Dissociated Air", *Journal of the Aeronautical Sciences*, 25, Nr. 2, S. 73-85, ISSN 0021-9142 /0095-9812, 1958.

[7] Goulard, R., "On Catalytic Recombination Rates in Hypersonic Stagnation Heat Transfer, Jet Propulsion", 28, Nr. 11, S. 737-745, ISSN 0095-8751, 1958.

[8] Herdrich, G., Auweter-Kurtz, M., Fertig, M., Löhle, S., Pidan, S. and Laux, T., "Oxidation Behaviour of SiC-based Thermal Protection System Materials using newly developed Probe Techniques", *Journal of Spacecraft and Rockets*, pp. 817-824, Vol. 42, No. 5, September – October 2005.

[9] Herdrich, G., Fertig, M., Petkow, D. and Steinbeck, A., "Modelling Approaches for Gas-Surface Interactions", 48th AIAA Aerospace Sciences Meeting including the New Horizons Forum and Aerospace Exposition, Orlando World Center Marriott, FL, USA, 4-7 January 2010.

[10] Smith, W., "The Surface Recombination of H Atoms and OH Radicals", *Journal of Chemical Physics*, Volume 11, pp. 110-125, 1946.

[11] Greaves, J.C. and Linnett, J.W., "Recombination of Atoms at Surfaces – Part. 6 – Recombination of Oxygen Atoms on Silica from 20°C to 600°C", *Transactions of the Faraday Society*, Vol. 55, pp. 1355-1361, 1959.

[12] Greaves, J.C. and Linnett, J.W., "Recombination of Atoms at Surfaces – Part. 5 – Oxygen Atoms at Oxide Surfaces", *Transactions of the Faraday Society*, Vol. 55, pp. 1346-1354, 1959.

[13] Linnett, J.W. and Marsden, D.G.H., "The kinetics of the recombination of Oxygen atoms at glass surface", Proceedings of the Royal Society, A234, 1956.

[14] Greaves, J.C. and Linnett, J.W., "The Recombination of Oxygen Atoms at Surface", *Transactions of the Faraday Society*, Vol. 54, pp. 1323-1330, 1958.

[15] Stewart, D., "Determination of Surface Catalytic Efficiency for Thermal Protection Systems – Room Temperature to Their Upper Limit", AIAA-Paper 96-1863, 31st Thermophysics Conference, New Orleans, LA, USA, 1996.

[16] Stewart, D.A. and Bouslog, S., "Surface Characterization of Candidate Metallic TPS for RLV", 33rd Thermophysics Conference, Norfolk, VA, USA, AIAA 99-3458, 1999.

[17] Marschall, J., "Laboratory Determination of Thermal Protection System Materials Surface Catalytic Properties", Experiment, Modeling and Simulation of Gas-Surface Interactions for Reactive Flows in Hypersonic Flights, RTO-EN-AVT-142, Paper 11, pp. 11-1 – 11-32, 2007.

[18] May, J.W. and Linnett, J.W., "Recombinations of Atoms at Surfaces – An Effusion Method Applied to Oxygen Atom Recombination", *Journal of Catalysis*, Vol. 7, pp. 324-341, 1967.

[19] Nakada, K., Sato, S. and Shida, S., "Recombination of Hydrogen Atoms on the Copper Single Crystal Surfaces", Proceedings of the Japan Academy, Vol. 31, No. 7, pp. 449-454, 1955.

[20] Wickramanayaka, S., Meikle, S., Kobayashi, T., Hosokawa, N. and Hatanaka, Y., "Measurements of catalytic efficiency of surfaces for the removal of atomic Oxygen using NO2 continuum", *Journal of Vacuum Science and Technology*, Vol. 9, Issue 6, pp. 2999-3002, November 1991.

[21] Balat, M., Czerniak, M. and Bladie, J-.M., "Thermal and chemical approaches for Oxygen catalytic recombination on ceramic materials at high temperature", *Applied Surface Science*, 120, pp. 225-238, 1997.

[22] Bedra, L. and Balat-Pichelin, M., "Comparative modeling study and experimental results of atomic Oxygen recombination on silica-based surfaces at high temperature", *Aerospace Science and Technology*, Vol. 9, pp. 318-328, 2005.

[23] Balat-Pichelin, M., "Interaction of Reactive Gas Flows and Ceramics at High Temperature – Experimental Methods for the Measurement of Species Recombination during Planetary Entry", Experiment, Modeling and Simulation of Gas-Surface Interactions for Reactive Flows in Hypersonic Flights, RTO-EN-AVT-142, Paper 12, pp. 12-1 – 12-26, 2007.

[24] Balat-Pichelin, M., Passarelli, M., Scatteia, L. and Alfano, D., "Catalycity of Zirconia and of ZrB2-based Ultra-High Temperature Ceramics", 6th European Symposium on Aerothermodynamics for Space Vehicles, Versailles, France, 3-6 November 2008.

[25] Scott, C.D., "Catalytic Recombination of Nitrogen and Oxygen on High-Temperature Reusable Surface Insulation", *Progress in Astronautics and Aeronautics*, Vol. 77, pp. 192-212, 1981.

[26] Pidan, S., Auweter-Kurtz, M., Herdrich, G. and Fertig, M., "Recombination Coefficients and Spectral Emissivity of Silicon Carbide-Based Thermal Protection Materials", *Journal of Thermophysics and Heat Transfer*, Vol. 19, No. 4, pp. 566-571, October – December 2005.

[27] Steinbeck, A., Fertig, M., Herdrich, G. and Röser, H.-P., "Enhanced Evaluation of Recombination Coefficient Measurements in Plasma Wind Tunnels", 41st AIAA Thermophysics Conference, San Antonio, TX, USA, AIAA 2009-3933, 2009.

[28] Fertig, M., Dohr, A. and Fruehauf, H.-H., "Transport Coefficients for High Temperature Non-equilibrium Air Flows", *Journal of Thermophysics and Heat Transfer*, Vol. 15, No. 2, pp 148-156, 2001.

[29] Kolesnikov, A.F., Pershin, I.S., Vasil'evskii, S.A. and Yakushin, M.I., "Study of Quarts Surface Catalycity in Dossiated Carbon Dioxide Subsonic Flows", 7th AIAA/ASME Joint Thermophysics and Heat Transfer Conference, AIAA98-2847, 1998.

[30] Kolesnikov, A.F., Yakushin, M.I., Pershin, I.S. and Vasil'evskii, S.A., "Heat Transfer Simulations and Surface Catalycity Prediction at the Martian Atmosphere Entry Conditions", 9th International Space Planes and Hypersonic Systems and Technologies Conference, AIAA 99-4892, 1999.

[31] Panerai, F., Thoemel, J. and Chazot, O., "Ground Test Investigation on a Thermal Protection System Junction", 6th European Symposium on Aerothermodynamics for Space Vehicles, Versailles, France, 3-6 November 2008.

[32] Chazot, O., Thoemel, J. and Balat-Pichelin, M., "Air Catalycity Determination in Plasma Wind Tunnels and Diffusion Reactors", 6th European Symposium on Aerothermodynamics for Space Vehicles, Versailles, France, 3-6 November 2008.

[33] Fertig, M., Schäff, S., Herdrich, G. and Auweter-Kurtz, M., "Influence of Chemical Accommodation on Re-entry Heating and Plasma Wind Tunnel Experiments", AIAA 2006-3816, 9th AIAA/ASME Joint Thermophysics and Heat Transfer Conference, San Francisco, CA, USA, June 2006.

[34] MacLean, M. and Holden, M., "Assessment of Aerothermal Heating Augmentation attributed to Surface Catalysis in High Enthalpy Shock Tunnel Flows", Proc. 'The 6th European Symposium on

Aerothermodynamics for Space Vehicles', Versailles, France, 3-6 November 2008 (ESA SP-659, January 2009).

[35] Fertig, M., Herdrich, G. and Auweter-Kurtz, M., "SiO_2 Modelling for CFD Calculations", AIAA 2007-4257, 39th AIAA Thermophysics Conference, Miami, FL, USA, June 2007.

[36] Fertig, M. and Herdrich, G., "The Advanced URANUS Navier-Stokes Code for the Simulation of Nonequilibrium Re-entry Flows", 26th International Space Symposium on Technology and Science, Hamamatsu, Japan, 1-8 June 2008, Selected papers from the 26th International Symposium on Space Technology and Science, Transactions of Japan Society for Aeronautical and Space Sciences, Space Technology Japan, Vol. 7, No. ists26, pp.Pe_15-Pe_24, 2009.

[37] Rutigliano, M., Pieretti, A., Cacciatore, M., Sanna, N. and Barone, V., "N atoms recombination on a silica surface: A global theoretical approach", *Surface Science*, 600, 4239-4246, 2006.

[38] Thömel, J., Panesi, M., Lukkien, J.J. and Chazot, O., "A Multiscale Approach for Building a Mechanism based Catalysis Model for High Enthalpy CO_2 Flow", 39th AIAA Thermophysics Conference, Miami, FL, USA, June 2007.

[39] Laux, M., "Direkte Simulation verdünnter, reagierender Strömungen", Dissertation (German), Institut für Raumfahrtsysteme, Universität Stuttgart, Germany, 1996.

[40] Jansen, A.P.J., "Monte Carlo simulations of chemical reactions on a surface with time-dependent reaction-rate constants", *Comp. Phys. Comm.*, Vol. 86, Issues 1-2, pp. 1-12, April 1995.

[41] Seward, W.A., "A Model for Oxygen Atom Recombination on a Silicon Dioxide Surface", PhD Thesis, AFIT/DS/AA/85-1, Air Force Institute of Technology, Wright-Patterson Air Force Base, OH, USA, 1985.

[42] Sayòs, R., Moròn, V., Arasa, C. and Busnengo, H.F., "Theoretical Dynamics of Several Atomic and Molecular Oxygen Processes over a Silica Surface", Proc. of "The 6th European Symposium on Aerothermodynamics for Space Vehicles", Versailles, France, 2008, ESA SP-659 2009.

[43] Thoemel, J., Chazot, O. and Barbante, P., "Aspects of advanced catalysis modeling for hypersonic flows, Center for Turbulence Research", Proceedings of the Summer Program, 2008.

[44] Park, C., "Numerical Implementation of Surface Catalysis, Reactions, and Sublimation", In "Experiment, Modeling and Simulation of Gas-Surface Interactions for Reactive Flows in Hypersonic Flights", Educational Notes RTO-EN-AVT-142, pp. 16-1 – 16-20, Neuilly-sur-Seine, France, 2007.

5.5.1 References for Figure 5-15

Willey, R.J., "Comparison of Kinetic Models for Atom Recombination on High-Temperature Reusable Surface Insulation", *Journal of Thermophysics and Heat Transfer*, Vol. 7, No. 1, pp. 55-62, 1993.

Kolodziej, P., and Stewart, D.A., "Nitrogen Recombination on High-Temperature Reusable Surface Insulation and the Analysis of its Effects on Surface Catalysis", 22nd AIAA Thermophysics Conference, Honolulu, HI, USA, June 1987.

Scott, C.D., "Catalytic Recombination of Nitrogen and Oxygen on High-Temperature Reusable Surface Insulation", *Progress in Astronautics and Aeronautics*, Vol. 77, pp. 192-212, 1981.

Stewart, D.A., “Catalytic surface effects experiment on the Space Shuttle”, Palo Alto, 16th Thermophysics Conference, June 1981.

Greaves, J.C. and Linnett, J.W., “Recombination of Atoms at Surfaces – Part. 6 – Recombination of Oxygen Atoms on Silica from 20°C to 600°C”, Transactions of the Faraday Society, Vol. 55, pp. 1355-1361, 1959.

Stewart, D.A., Chen, Y.-K. and Henline, W.D., “Effect of Non-Equilibrium Flow Chemistry and Surface Chemistry on Surface Heating to AFE”, 26th AIAA Thermophysics Conference, Honolulu, HI, USA, 1991.

Marinelli, W.J., “Collisional quenching of atoms and molecules on spacecraft thermal protection surfaces”, AIAA-1988-2667 Thermophysics, Plasmadynamics and Lasers Conference, San Antonio, TX, USA, June 1988.

Kim, Y.C. and Boudart, M., “Recombination of O, N and H Atoms on Silica: Kinetics and Mechanism Langmuir”, Vol. 7, pp. 2999-3005, 1991.

Stewart, D.A., “Effect of non-equilibrium flow chemistry and surface catalysis on surface heating to AFE”, Palo Alto, 26th Thermophysics Conference, June 1991.

Stewart, D.A., “Determination of Surface Catalytic Efficiency for Thermal Protection Materials – Room Temperature to Their Upper Use Limit”, AIAA-Paper 96-1863, 31st AIAA Thermophysics Conference, New Orleans, LA, USA, 1996.

Bedra, L. and Balat-Pichelin, M., “Comparative modeling study and experimental results of atomic oxygen recombination on silica-based surfaces at high temperature”, *Aerospace Science and Technology*, Vol. 9, pp. 318-328, 2007.

Pidan, S., Auweter-Kurtz, M., Herdrich, G. and Fertig, M., “Recombination Coefficients and Spectral Emissivity of Silicon Carbide-Based Thermal Protection Materials”, *Journal of Thermophysics and Heat Transfer*, Vol. 19, No. 4, pp. 566-571, October – December 2005.

Chapter 6 – BASE FLOW INVESTIGATION OF THE APOLLO AS-202 COMMAND MODULE

Louis. M.G. Walpot
AOES Netherlands BV
NETHERLANDS

Michael J. Wright
NASA Ames Research Center
USA

Peter Noeding
EADS Astrium Bremen
GERMANY

Ferry Schrijer
TU Delft
NETHERLANDS

6.1 INTRODUCTION

In recent years, both Europe and the US are developing hypersonic research and operational vehicles. These include (re)entry capsules (both ballistic and lifting) and lifting bodies such as ExoMars, EXPERT, ARV, CEV and IXV. The research programs are meant to enable technology and engineering capabilities to support during the next decade the development of affordable (possibly reusable) space transportation systems as well as hypersonic weapons systems for time critical targets. These programs have a broad range of goals, ranging from the qualification of thermal protection systems, the assessment of RCS performances, the development of GNC algorithms, to the full demonstration of the performance and operability of the integrated vehicles. Since the aerothermodynamic characteristics influence nearly all elements of the vehicle design, the accurate prediction of the aerothermal environment is a pre-requisite for the design of efficient hypersonic systems. Significant uncertainties in the prediction of the hypersonic aerodynamic and the aerothermal loads can lead to conservative margins in the design of the vehicle including its Outer Mould Line (OML), thermal protection system, structure, and required control system robustness. The current level of aerothermal prediction uncertainties results therefore in reduced vehicle performances (e.g., sub-optimal payload to mass ratio, increased operational constraints).

On the other hand, present computational capabilities enable the simulation of three dimensional flow fields with complex thermo-chemical models over complete trajectories and ease the validation of these tools by, e.g., reconstruction of detailed wind tunnel tests performed under identified and controlled conditions (flow properties and vehicle attitude in particular). These controlled conditions are typically difficult to achieve when performing in flight measurements which in turn results in large associated measurement uncertainties. Similar problems arise when attempting to rebuild measurements performed in “hot” ground facilities, where the difficulty level is increased by the addition of the free-flow characterization itself. The implementation of ever more sophisticated thermochemical models is no obvious cure to the aforementioned problems since their effect is often overwhelmed by the large measurement uncertainties incurred in both flight and ground high enthalpy facilities.

Concurrent to the previous considerations, a major contributor to the overall vehicle mass of re-entry vehicles is the afterbody thermal protection system. This is due to the large acreage (equal or bigger than that of the forebody) to be protected. The present predictive capabilities for base flows are comparatively lower than those for windward flowfields and offer therefore a substantial potential for improving the design of future re-entry vehicles. To that end, it is essential to address the accuracy of high fidelity CFD tools exercised in the US and EU, which motivates a thorough investigation of the present status of hypersonic flight afterbody heating.

This paper addresses the predictive capabilities of after body flow fields of re-entry vehicles investigated in the frame of the NATO/RTO – RTG-043 Task Group and is structured as follows:

- First, the verification of base flow topologies on the basis of available wind-tunnel results performed under controlled supersonic conditions (i.e., cold flows devoid of reactive effects) is performed. Such tests address the detailed characterization of the base flow with particular emphasis on separation/reattachment and their relation to Mach number effects. The tests have been performed on an Apollo-like re-entry capsule configuration.
- Second, the tools validated in the frame of the previous effort are exercised and appraised against flight-test data collected during the Apollo AS-202 re-entry.

6.2 EXPERIMENTAL DATA

6.2.1 Experimental Supersonic Data

Ground tests were performed to obtain flow field data of the AS-202 configuration under supersonic test conditions. Shadowgraph measurements provided insight into shock and shear layer patterns found under different angles of attack at Mach numbers between 2 and 4. The facility used in the ground experiments is the TST27 transonic/supersonic blow-down wind tunnel located at TU Delft in The Netherlands, (see Figure 6-1). This tunnel features a 27 x 28 cm^2 test section and sports two flexible nozzle walls that allow to continuously vary the Mach number between 0.5 and 4.2. The total pressure in the settling chamber can be varied from 2 bar at Mach 0.5 to 20 bar at Mach 4.2, which results in a unit Reynolds number range from 25 x 10^6 to 150 x 10^6. The maximum run-time of the facility is 300 s. Two 30 cm diameter schlieren windows in the side of the test section are available for optical access. In the current experiments, the wind tunnel was operated in the Mach 2 to 4 range with a total pressure ranging from 2.7 – 12 bar and a total temperature of 288 K. The capsule geometry used for the definition of the wind tunnel model is a scaled version of the AS-202 outer mold line as defined in Figure 6-1. The model has a diameter of 50 mm and is fabricated out of stainless steel, it is side-mounted on a stainless steel blade sting. Two models are used with mounting at respectively 0 and 25 degrees, (see Figure 6-1). Angles of attack other than 0 or 25 degrees were reached by deflecting the mounting sting according to the sought flow condition.

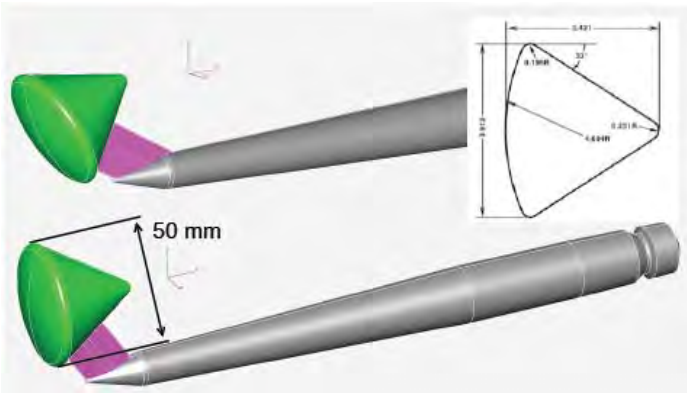

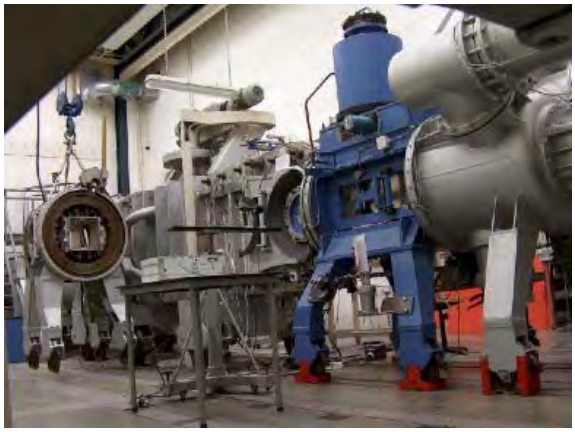

Figure 6-1: The 5-cm Diameter AS-202 for 0 and 25 deg in the TU Delft TST27 Wind Tunnel.

Shadowgraphs were obtained during the tests using a 3872 x 2592 pixel Nikon D80 camera. The illumination was provided by a Xenon spark light with an emission time of 20 *ns*, effectively freezing the flow in a single snapshot.

6.2.2 AS-202 Flight Data

The flight data used for assessment/comparison of heat flux data on the capsule were taken from the AS-202 flight test [1], [2], [3], which was performed as part of the Apollo program. Once the Apollo entry vehicle design was determined, two flight tests of the actual Command Module (AS-201 and AS-202) were conducted at super-orbital entry velocities resulting from sub-orbital boosted trajectories with an intentional skip maneuver. Although AS-201 did not carry an onboard Inertial Measurement Unit (IMU), one was carried during the AS-202 flight, which enabled a reconstruction of the flight trajectory and vehicle orientation as a function of time.

In this paper the afterbody heating environment for the Apollo Command Module shape as measured on the AS-202 mission is used as basis for comparison between CFD results and flight data.

Figure 6-2 shows the outer mould line of the AS-202 as modeled for the CFD analyses. The re-entry trajectory of AS-202 in terms of velocity and altitude vs. time is shown in Figure 6-3. The points in time and the related free-stream conditions used for comparison to flight data are tabulated in Table 6-1. The small side slip angle has been neglected in the current simulations. The locations of calorimeters used to determine the heat fluxes on the AS-202 conical afterbody are depicted in Figure 6-4. Table 6-2 contains the exact coordinates of each calorimeter position. Figure 6-2, Figure 6-3, Figure 6-4 and Table 6-1 and Table 6-2 are taken from Ref. [4].

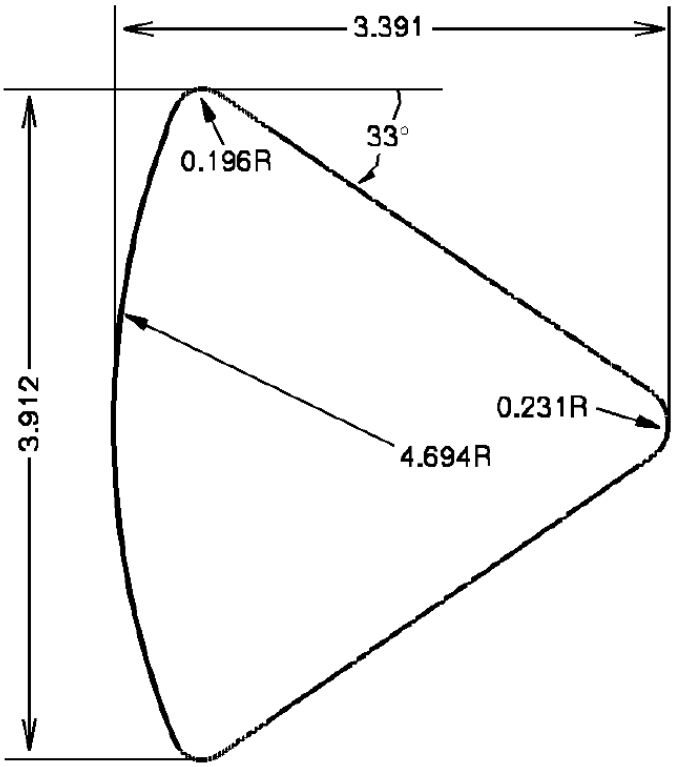

Figure 6-2: Schematic Drawing of the Outer Mold Line of AS-202 Capsule as Modeled in this Work.

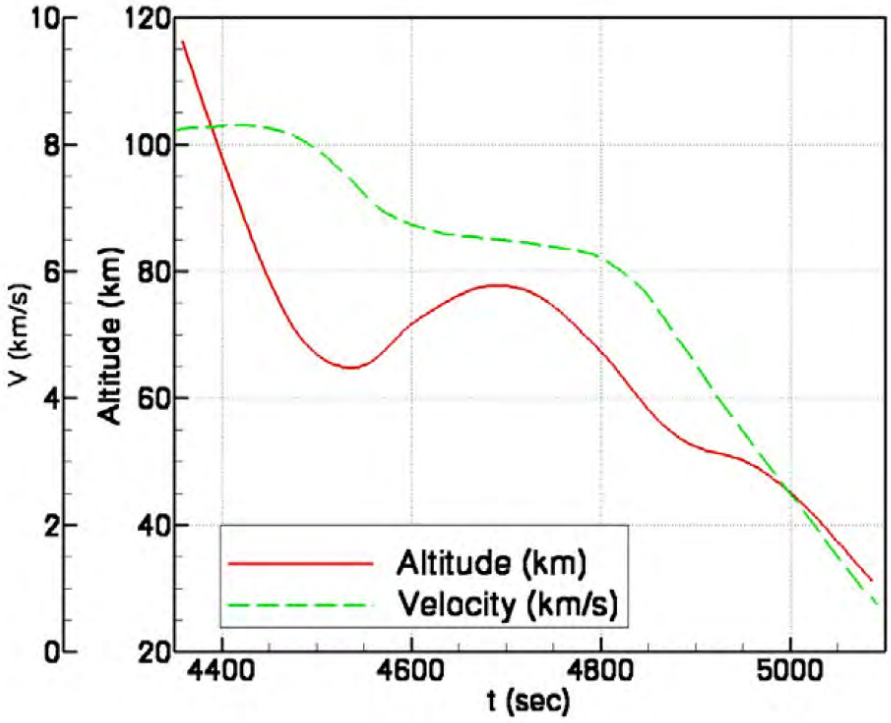

Figure 6-3: Altitude and Velocity as a Function of Time from Launch for AS-202.

Table 6-1: AS-202 Trajectory Points and Freestream Conditions.

Time[a] (s)	Alt. (km)	Re_D[b]	V (km/s)	M	ρ_∞ (kg/m^3)	T_∞ (K)	α (deg)	β (deg)
4455	76.8	7.5 x 10^4	8.24	28.6	3.38e-5	205	18.2	2.0
4475	71.3	1.8 x 10^5	8.15	27.6	8.76e-5	217	17.9	2.5
4500	70.0	3.0 x 10^5	7.92	26.2	1.52e-4	227	17.8	2.5
4510	66.0	3.2 x 10^5	7.80	25.6	1.69e-4	230	17.8	2.5
4530	64.9	3.4 x 10^5	7.53	24.5	1.84e-4	234	17.9	2.5
4560	66.0	2.7 x 10^5	7.07	23.2	1.53e-4	231	18.1	2.5
4600	71.6	1.3 x 10^5	6.74	22.9	7.19e-5	215	18.3	2.5
4650	76.2	5.7 x 10^4	6.56	22.8	3.24e-5	206	18.5	2.0
4700	77.2	4.3 x 10^4	6.49	22.7	2.45e-5	203	18.5	2.0
4750	74.5	7.6 x 10^4	6.39	22.0	4.50e-5	210	18.4	2.0
4800	67.3	2.1 x 10^5	6.21	20.5	1.37e-4	210	18.4	2.0
4825	62.9	3.5 x 10^5	5.97	19.2	2.81e-4	239	18.3	2.0
4850	58.2	5.3 x 10^5	5.62	17.6	4.14e-4	252	18.3	2.5
4875	54.6	6.9 x 10^5	5.07	15.6	6.16e-4	262	18.4	2.5
4900	52.4	7.6 x 10^5	4.53	13.2	8.00e-4	268	18.6	2.5

[a]Seconds after launch.
[b]Freestream Reynolds number based on body diameter.

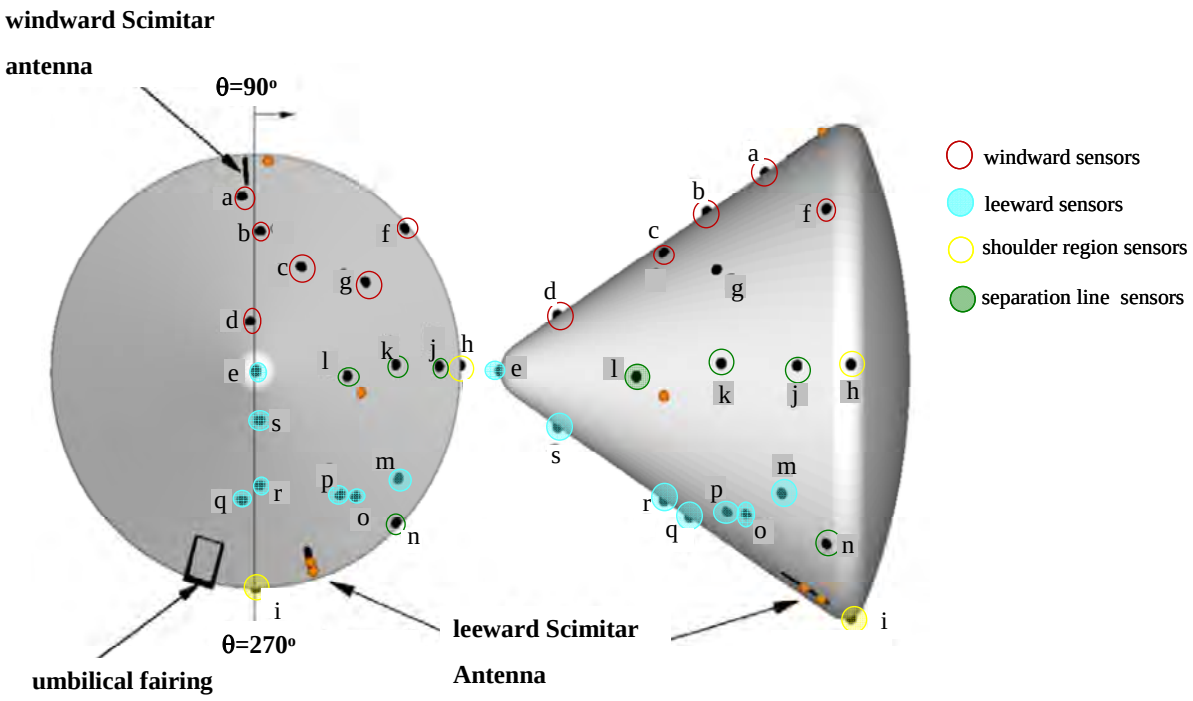

Figure 6-4: Locations of Calorimeters on AS-202 Conical Afterbody (orange symbols indicate inoperative instruments – letters correspond to the ID).

Table 6-2: Afterbody Calorimeter Locations for AS-202.

ID[a]	X[b] (cm)	θ^b (deg)	Range (W/cm^2)	ID[a]	X[b] (cm)	θ^b (deg)	Range (W/cm^2)
–	72.6	93.7	0 – 114	l	228.8	182.9	0 – 28
a	120.8	85.3	0 – 57	m	106.8	215.3	0 – 11.4
b	169.8	92.0	0 – 57	n	69.5	225.5	0 – 11.4
c	205.6	115.0	0 – 57	–	205.6	191.3	0 – 28
d	294.8	83.4	0 – 57	O	136.6	229.8	0 – 11.4
e	343.1	Apex	0 – 28	P	152.6	234.0	0 – 28
f	69.5	138.0	0 – 57	Q	184.3	276.4	0 – 28
g	161.5	142.8	0 – 28	R	205.6	267.8	0 – 28
h	54.5	178.5	0 – 28	S	294.8	265.0	0 – 28
i	54.5	270.0	0 – 11.4	–	74.1	253.0	0 – 28
j	94.1	178.6	0 – 28	–	88.0	253.0	0 – 57
k	157.6	177.5	0 – 28				

[a]Corresponds to Figure 17 in Ref. [1]. Those without letters were non-functional during AS-202.

[b]Refer to Figure 6-4 for coordinate system definition.

6.3 COMPUTATIONAL MODELING

AOES used the LORE [5] CFD code for the Navier-Stokes calculations presented in this paper. For a number of computational conditions, including wind tunnel and AS-202 flight test data, Navier-Stokes calculations have also been performed by ASTRIUM Bremen using the TAU code [6]. These results are hereafter compared to the test data and the LORE results. Finally, the existing CFD Results (DPLR CFD-Code) published by Wright et al. [4] for the AS-202 flight test data are also reported here for comparison.

LORE is a multi-block finite-volume Navier-Stokes solver augmented with finite rate chemistry and thermal non-equilibrium effects. For the present effort, turbulence effects have been modeled with Menter's SST (Shear Stress Transport) and Baldwin-Lomax models. LORE has been extensively validated against X-38 wind tunnel test data (obtained at ONERA S2Ma, Langley Research Center (LaRC) 16 ft and FFA's T1500) [5] and CARV [7].

For the LORE calculations presented here super-catalytic wall boundary conditions have been used, which represents a conservative approach often used for design. In this assumption the wall composition is forced to be equal to the freestream. This boundary condition is conservative in that the maximum chemical enthalpy is recovered at the wall, but it does not account for potential rate-limiting processes in the underlying surface chemistry (surface reaction rates are taken to be infinite). In the current flight test cases ranging from Mach 28 to Mach 4, it has been observed that there is no appreciable difference in base flow heating between supercatalytic and diffusion limited with LORE.

The DLR Navier-Stokes and Euler-Solver **TAU-Code** [6] has been used at EADS Astrium Bremen. The code has been extensively validated against test results and other CFD Codes in the past, see e.g., [7]. The three-dimensional CFD program was developed by the German Aerospace Center DLR for unstructured and structured grids (under participation of several branches of EADS Germany). The TAU flow solver

represents a three-dimensional parallel hybrid multi-grid code employing a finite volume scheme for solving the Reynolds-averaged Navier-Stokes equations. The inviscid fluxes are calculated using an AUSM or a Roe type 2nd-order upwind scheme. The gradients of the flow variables are determined by employing a Green-Gauss formula. Central differences are used to discretize the viscous fluxes. Treatment of viscous walls within the TAU-Code allows for adiabatic, constant wall temperature or radiation equilibrium conditions.

Turbulence Modeling – The TAU Code offers a choice of different one- and two-equation turbulence models (Spalart-Allmaras model, various versions of the k-ω-model). For AS-202, the Spalart-Allmaras model was used to cover turbulent flow situations.

Air Chemistry – Regarding the available thermo-chemical models for hypersonic flows, the following options are incorporated into the TAU-Code:

a) **Equilibrium Chemistry** – Air is considered as a five species ideal gas mixture. The temperature and pressure dependent equilibrium gas properties are modeled via appropriate fit functions. A temperature range between 50 K and 20000 K and a density range between 10 – 12 kg/m^3 and 10 kg/m^3 is covered by the fits currently in use.

b) **Chemical Non-Equilibrium** – The non-equilibrium model currently implemented in the TAU-Code consists of a five species and seventeen reactions air model employing the finite reaction rates according to Gupta et al. This can be easily replaced by more detailed models [8]. The diffusion is modeled according to Fick's law by a single diffusion coefficient for all species. The diffusion coefficient is connected to the local viscosity via a user-specified constant Schmidt number. Within AS-202 flow simulations chemical non-equilibrium in conjunction with a fully catalytic wall boundary condition was assumed (as opposed to the supercatalytic wall conditions in the LORE calculations. However, for the conditions considered here the dependency of the wall heat fluxes on either wall condition is considered small).

The CFD modeling published earlier, using the DPLR code for comparison to the AS-202 flight data is described in detail in [4]. DPLR is a parallel multi-block finite volume code that solves the reacting Navier-Stokes equations including finite-rate chemistry and the effects of thermal non-equilibrium. The Euler fluxes are computed using a modified (low-dissipation) form of Steger-Warming flux vector splitting, with third-order spatial accuracy obtained via MUSCL extrapolation. Viscous fluxes are computed to second-order accuracy using a central difference approach.

CFD Grids –Some TAU Code Calculations employed the same structured grids as used by LORE, so as to facilitate direct code comparison. Other TAU CFD meshes for the AS-202 analyses employed a hybrid grid approach consisting of structured prismatic grid layers in the wall regions to resolve the boundary layers as well as tetrahedral cells covering the rest of the computational domain. For the hybrid grids, in order to limit the impact of the grid density on the computed flow-field, the solution-dependent grid adaptation features of the TAU Code were used. Typically, a total of 2 to 3 grid adaptation cycles were performed to improve the solutions. Figure 6-5 shows the hybrid TAU grid after two adaptation cycles. Shock and shear layer structures are clearly reflected by the locally adapted/refined regions of the mesh. The lower left insert of Figure 6-5 shows the complete computational domain. The upper left insert shows the "structured" boundary layer mesh part in the shoulder region.

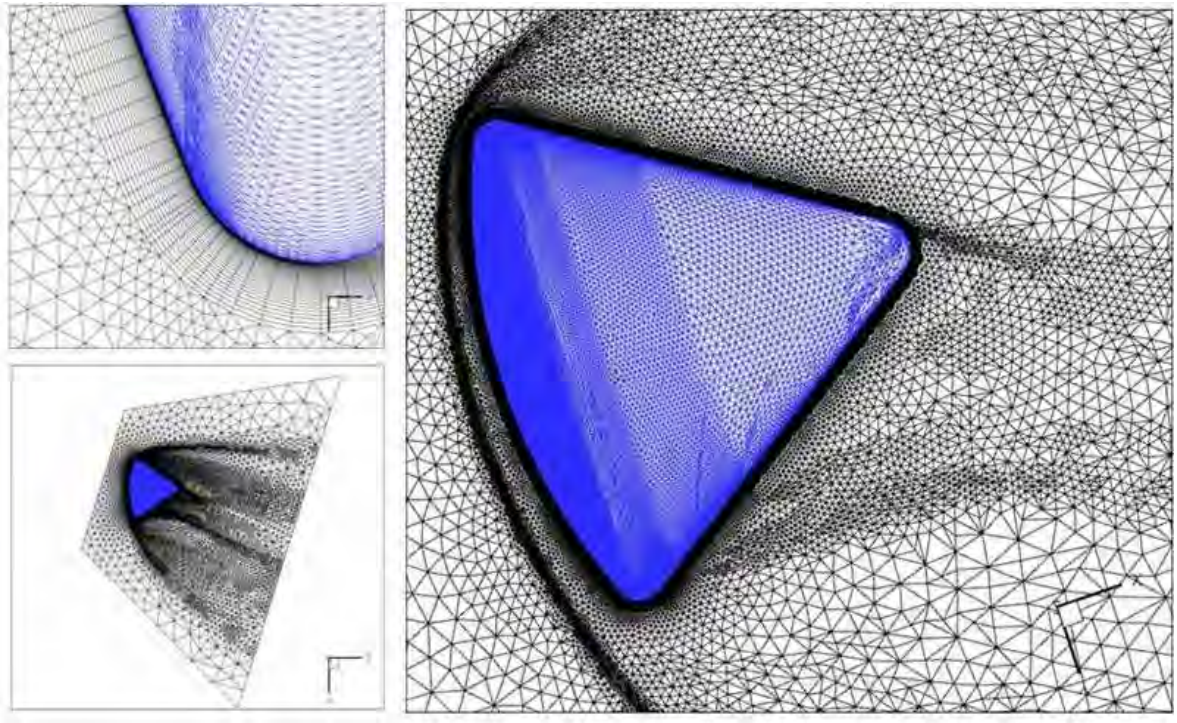

Figure 6-5: Hybrid TAU-Code CFD Grid for the AS-202 Flight Test Geometry.

The structured grids have been generated with GridPro. The meshes are featured with smoothness and are each shock adapted. The meshes for flight and wind tunnel w/o sting comprise 76 blocks and roughly 8 million cells. The meshes with sting have 151 blocks with 24 million cells, resp. 3 million cells for the undoubled mesh. In Figure 6-6 each other point has been plotted. The smallest distance at the wall is 1.e-6 m. Grid convergence is checked by comparing the solution in terms of separation/flow topologies for the WT mode and heat fluxes in front and base for the flight cases. It can bee seen in Figure 6-7, where the surface meshes are plotted for the fine and undoubled mesh, that the pressure contour lines on the front shield are independent of the mesh. Table 6-3 summarizes main differences in the modeling approaches for the AS-202 calculations between the LORE, TAU Code and DPLR analyses.

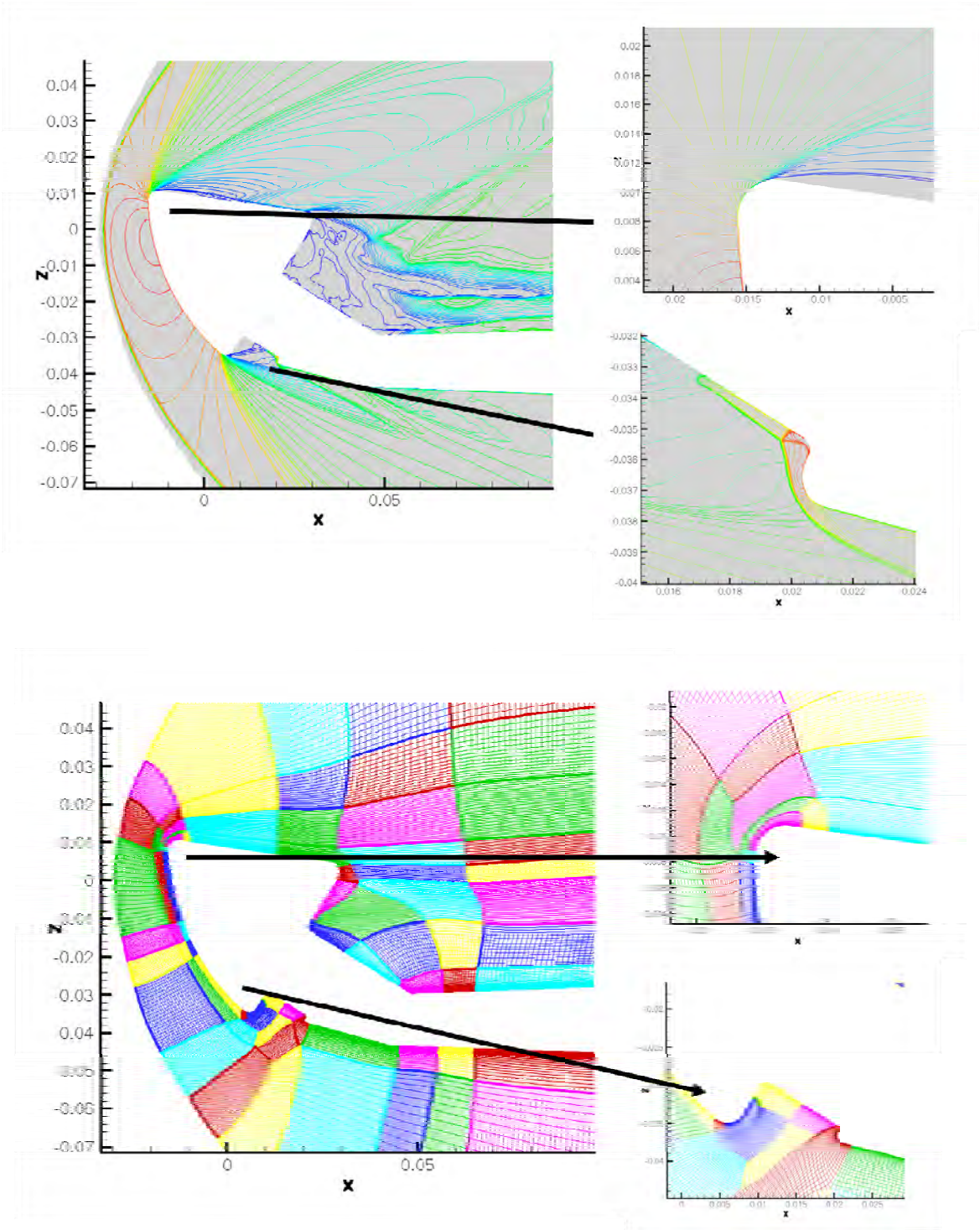

Figure 6-6: Structured Grid Used Both by LORE and TAU for the TST27 Supersonic Tests.

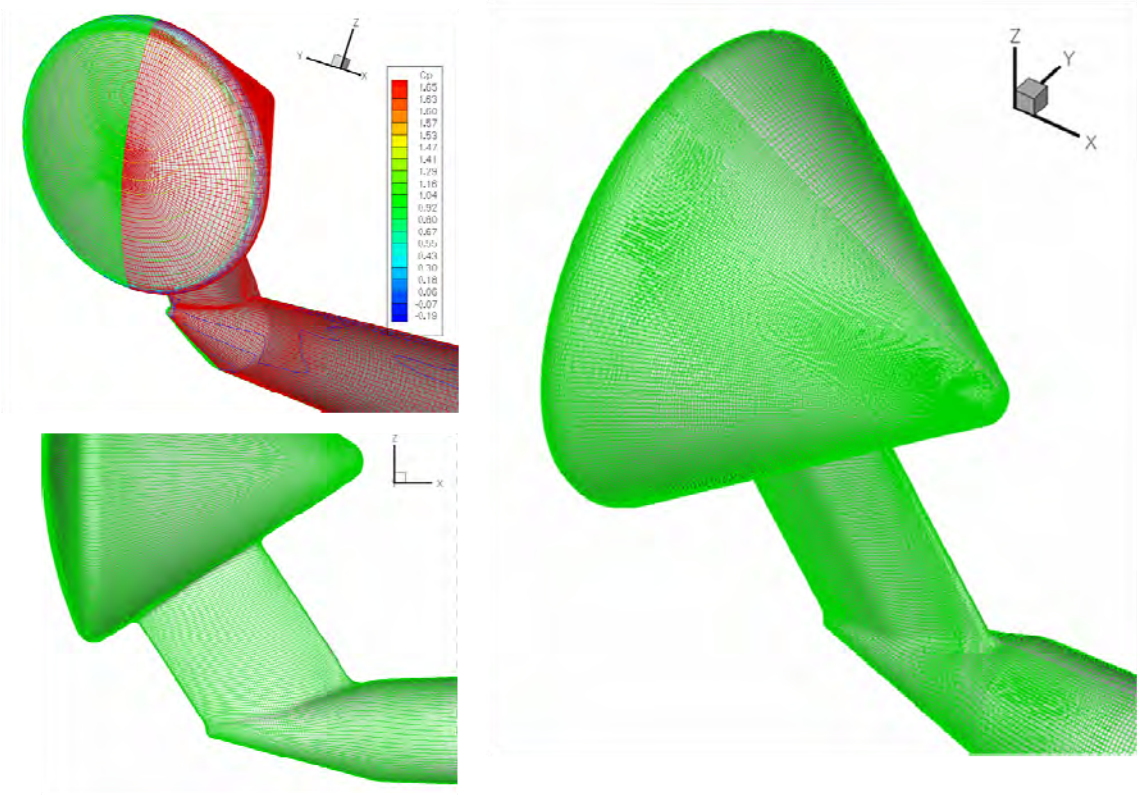

Figure 6-7: Structured Grid Used Both by LORE and TAU for the TST27 Supersonic Tests.

Table 6-3: Differences in Modeling of the AS-202 Flight Case: LORE, TAU Code, DPLR.

	CFD Meshes	Thermochemical Model	Transport Coefficients	Wall Catalycity	Turbulence Model
LORE	Block Structured Level 1: 1 Mio. Cells Level 2: 8 Mio. Cells	Thermochemical Non-equilibrium 5 Species Finite Rate [12]	Constant Lewis Number Le = 1.2 SCEBD	Super Catalytic	Baldwin-Lomax
TAU-Code	Structured 1 Mio. Cells(as Level 1/LORE), **or** Solution Adaptive, Hybrid/Unstructured 4 Mio. Cells	Chemical Non-equilibrium 5 Species Finite Rate [8]	Constant Schmidt Number for All Species Sc = 0.7	Fully Catalytic	Spalart-Allmaras
DPLR	Block Structured 1.5 Mio. Cells	Thermochemical Non-equilibrium 5 Species Finite Rate [12]	Mixing Mules [8] Diffusion Coefficients via SCEBD	Diffusion Limited	Baldwin-Lomax

6.4 RESULTS

6.4.1 Shadowgraphy Results from the TST27 Wind Tunnel and Related CFD Calculations

General flow pattern and shear layer separation at the capsule shoulder was investigated for various combinations of angle of attack and Mach number. Mach 2 and Mach 4 wind tunnel results and related CFD calculations for varying angles of attack are used to examine the flow topology with respect to:

- Shock patterns: Bow shock, shoulder region, wake areas.
- Shock-shock interactions/flow interferences due to the presence of a wind tunnel blade mounting.
- Local separation and reattachment of the capsule flow.
- Characteristic flow patterns of the leeside/wake flow.

The quality of the CFD codes with regard to the correct determination of flow separations in the base area is deemed very important in view of the accurate prediction of aerothermal heat fluxes on vehicle leeside during re-entry. The shadowgraphy images from the wind tunnel represent a useful basis for comparison here.

The shadowgraphy images taken for various angle of attack/Mach number combinations are shown in Figure 6-12 to Figure 6-16. These figures also contain the corresponding CFD results (calculated density fields), overlaid on the shadowgraphs. As evidenced by Figure 6-12 to Figure 6-16, the flow around the capsule is characterized by the bow shock forming in front of the spherical heat shield and by the expansion over the capsule shoulder. The flow over-expands and a lip shock is formed. At smaller angles of attack downstream of the shoulder a completely separated shear layer develops and it does not reattach on the model. The expansion from the low velocity region downstream of the bow shock over the model shoulder is clearly evident. Also the shock coming from the re-compression in the capsule wake is clearly visualized.

With increasing angles of attack it can be observed that the shear layer only partially separates from the upper side of the capsule or stays completely attached at sufficiently large angles of attack. At the model shoulder a small shock wave is present where separation occurs. Further downstream, a stronger shock is formed if and where the shear layer reattaches. Downstream of the capsule a strong shock is present where the wake is re-compressed. The shock emanating from the reattaching shear layer is also evident. The downstream region shows a three dimensional reattachment shock pattern that emanates from the wake behind the capsule.

Oblique shocks are visible at the tip of the lower side of the sting mounting. Shocks are also present at the edge of the mounting, at the location where the cone angle of the sting is reduced. However, no significant interference with the upper side of the capsule model, where the separation behavior at the cone vs. angle of attack is investigated is apparent from the blade mounting.

The shadowgraphs clearly show whether the flow was attached or separated from the windward side of the capsule. Figure 6-12 shows a separated and Figure 6-14 an attached case.

It was found that for increasing Mach numbers, the flow separation occurs at smaller angles of attack. Similar results were obtained by Kruse et al. [9] In Figure 6-8, the measurement points are given as a function of angle of attack and Mach number. A blue circle denotes the flow conditions for which the shear layer was found to be attached while the separated cases are represented by a red triangle. In Figure 6-8 also the curve-fit from Kruse et al. [9] is shown that forms the border between an attached or a separated shear layer. As can be seen, the separation angle of attack decreases with increasing Mach

number. However the angle of attack values found by Kruse et al. [9] are smaller for Mach 2. This is due to the fact that in those measurements models with sharp-edged shoulders were used, in those cases the separation point is defined and a more or less centered Prandtl-Meyer expansion is formed. In the current experiments, the flow expands more gradually and therefore is likely to separate more easily.

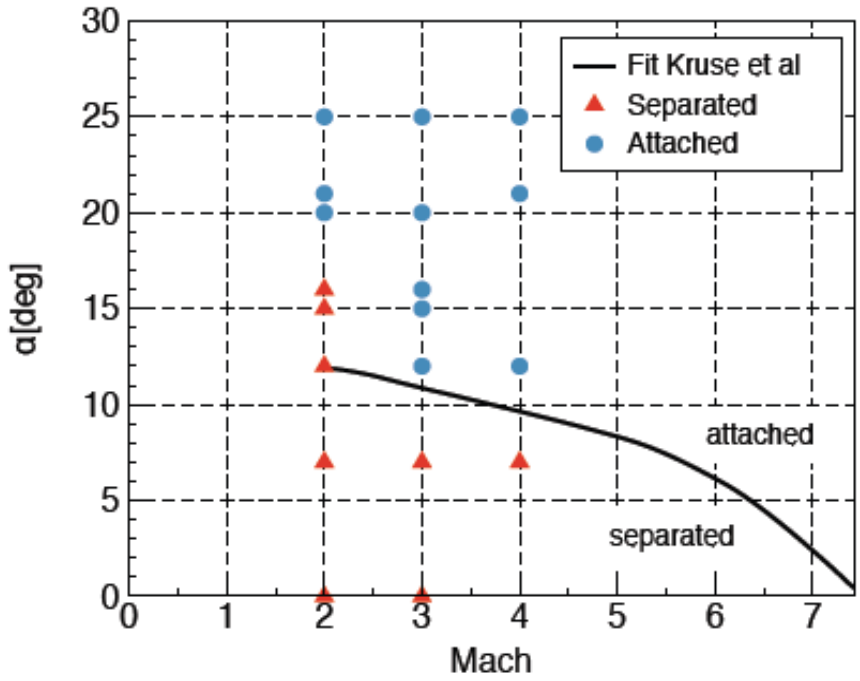

Figure 6-8: Boundary Layer Separation Condition as a Function of Mach Number and Angle of Attack.

Figure 6-12 to Figure 6-14 show a series of shadowgraphs for Mach 2 at varying angles of attack between 14 and 22 degrees. At 22 degrees a completely separated shear layer at the upper side of the rear cone of the model can be observed. The separation on the upper side of the cone begins when the angle of attack is reduced to about 19 degrees with a flat separation bubble starting just behind the shoulder with reattachment about halfway along the cone surface. A reattachment shock is visible at the downstream end of the separation bubble. The CFD results show excellent agreement regarding the onset of separation at 19 degree AoA as well as the reattachment position, as evidenced in Figure 6-13. This is true for the fine (8 million cells) as well as for the undoubled (1 million cells) mesh (Figure 6-9). As confirmed by the related CFD calculations performed without mounting and depicted in Figure 6-17 and Figure 6-18 (where the flow topology is probed downstream of the model by means of planar Mach contour cuts), the presence of the wind tunnel blade/sting does not significantly influence the separation behavior at the upper side of the cone. This is also evident from the calculated density contours in the symmetry plane, with and without sting/blade, as shown in Figure 6-11.

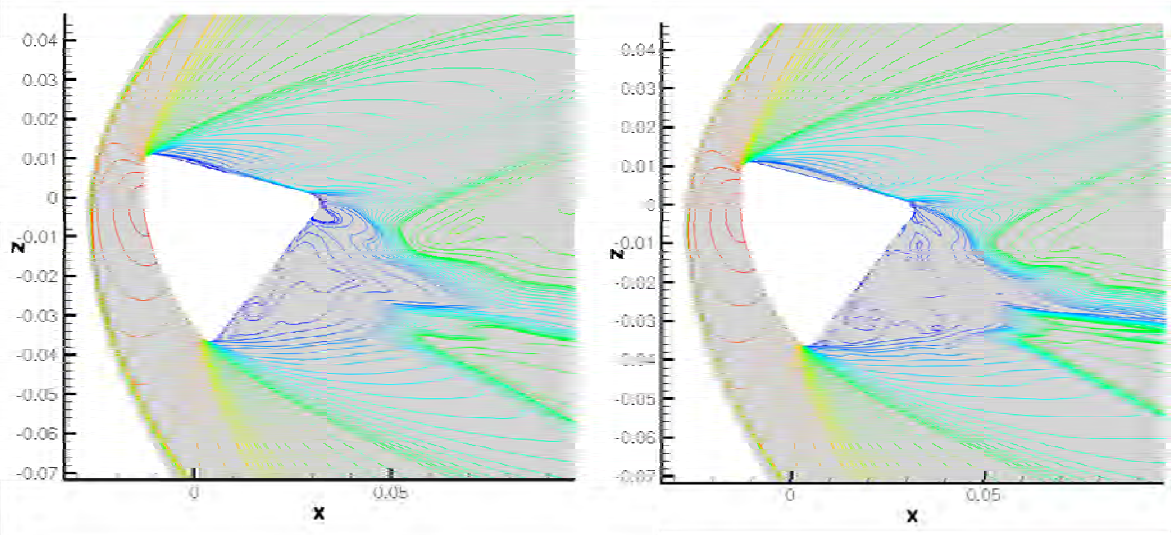

1M cells 8M cells

Figure 6-9: AS-202 in TST27 (Without Sting) Mach 2 AoA 19 Symmetry Plane Computed with LORE: Effect of Grid Refinement.

The LORE and TAU code calculations properly capture the separation bubble at 19 degrees angle of attack (Figure 6-10). At 14° angle of attack, the CFD calculations and related shadowgraphs show a completely separated shear layer on the upper side (Figure 6-12).

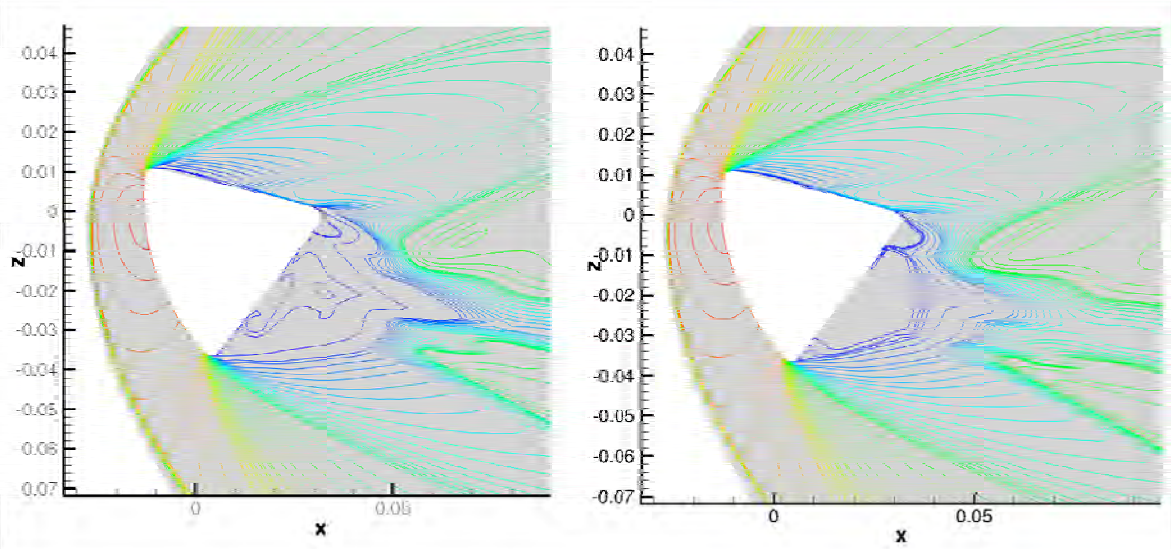

Figure 6-10: AS-202 in TST27 (Without Sting) Mach 2 AoA 19 Symmetry Plane Computed with LORE and TAU (1M Cells).

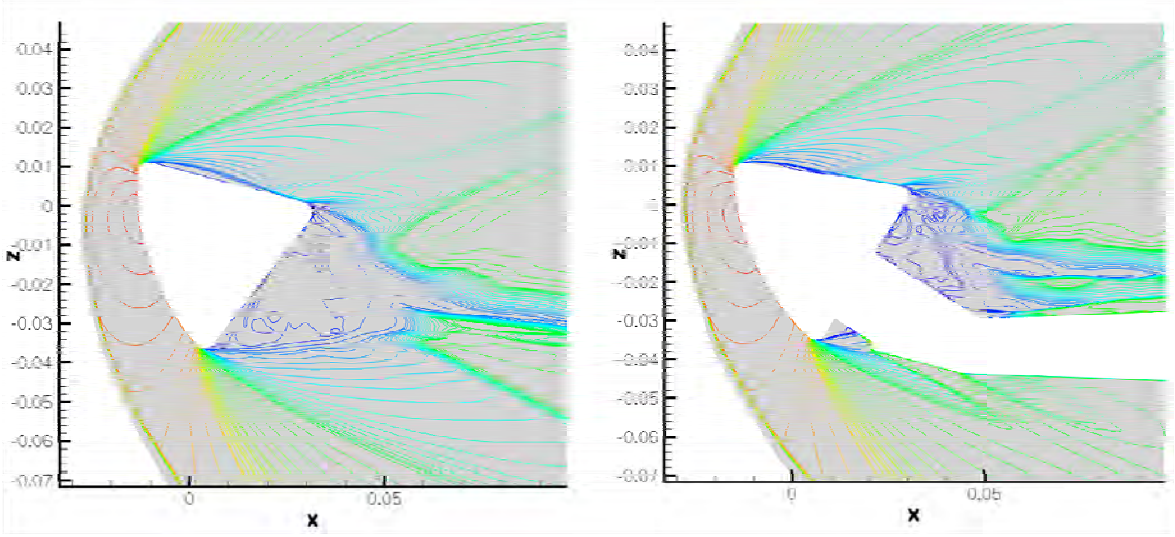

Figure 6-11: AS-202 in TST27 (Without Sting) Mach 2 AoA 19 Symmetry Plane Computed with LORE: Effect of Sting/Blade vs. No Sting/Blade on 8M Cells Mesh.

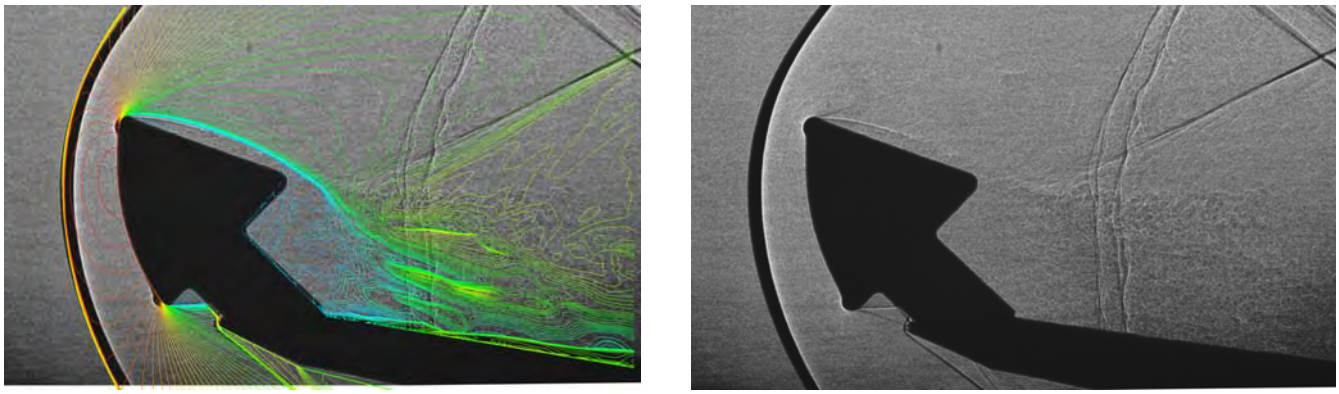

Figure 6-12: Mach 2, Angle of Attack 14 deg, Pt = 27Bar, T0 = 285 K.

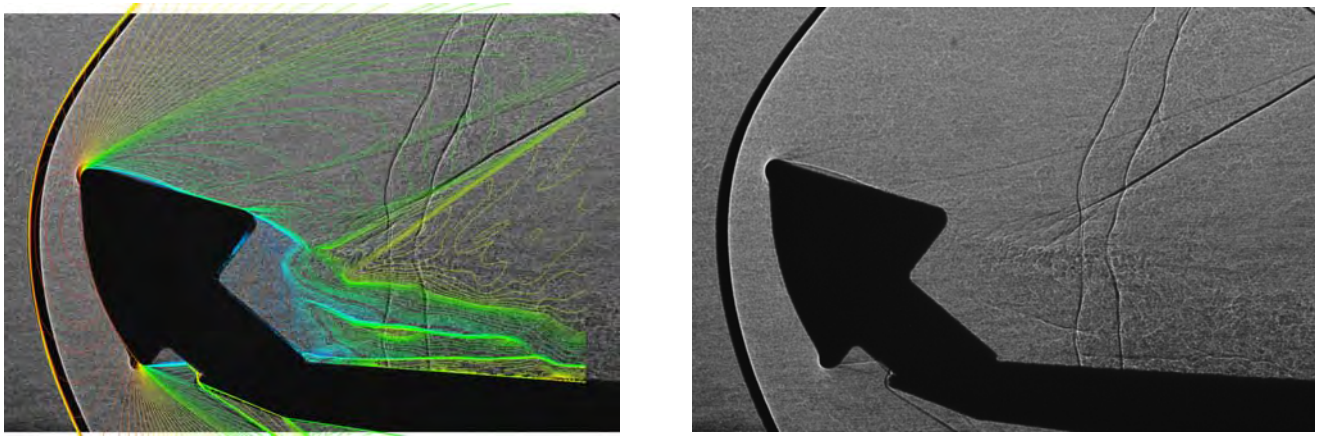

Figure 6-13: Mach 2, Angle of Attack 19 deg, Pt = 27Bar, T0 = 285 K.

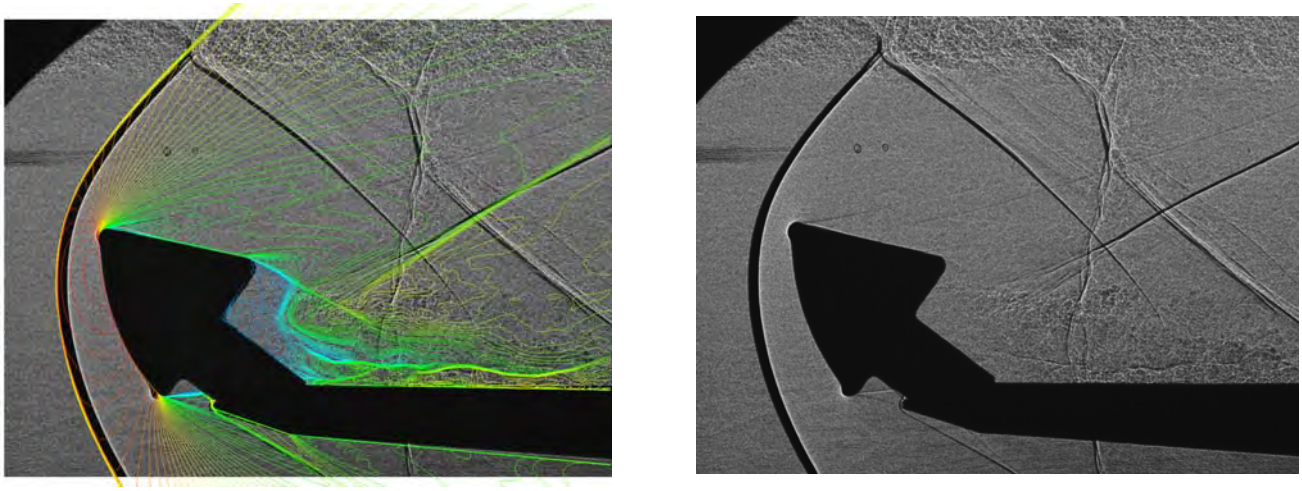

Figure 6-14: Mach 2, Angle of Attack 22 deg, Pt = 27Bar, T0 = 285 K.

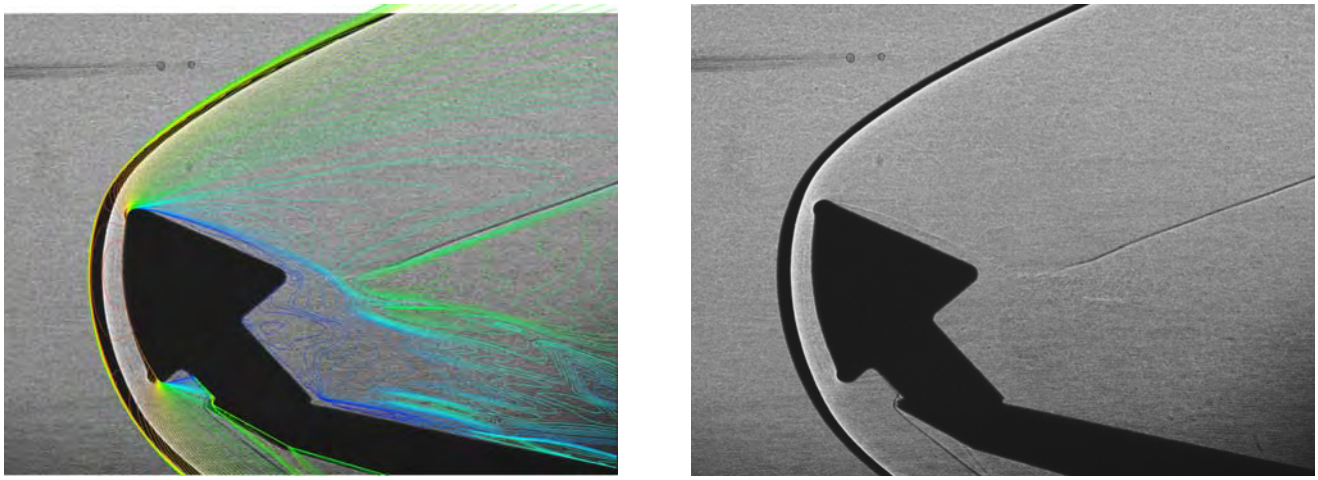

Figure 6-15: Mach 4, Angle of Attack 10 deg, Pt = 12Bar, T0 = 285 K.

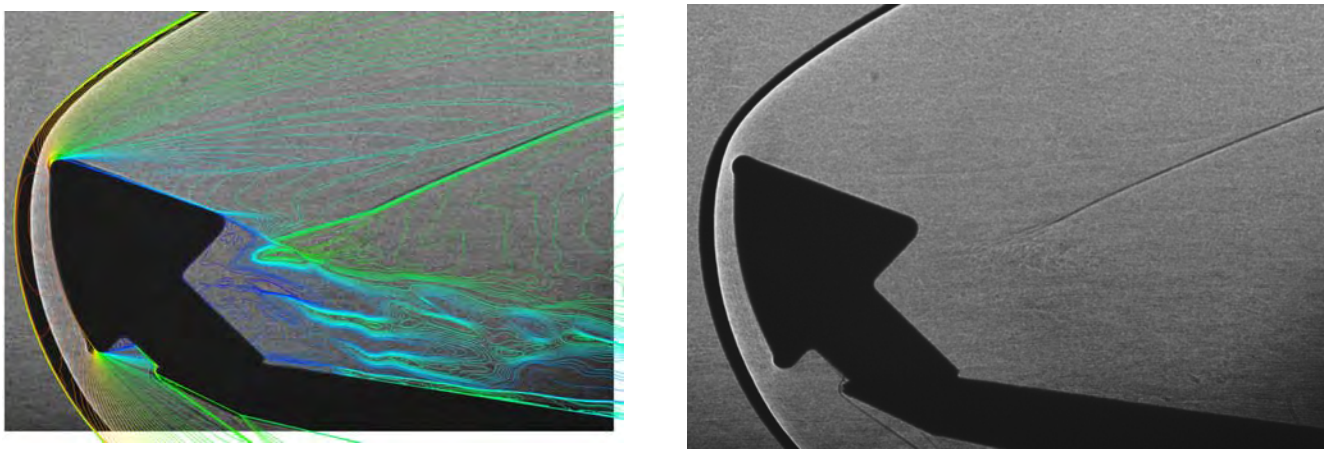

Figure 6-16: Mach 4, Angle of Attack 14 deg, Pt = 12Bar, T0 = 285 K.

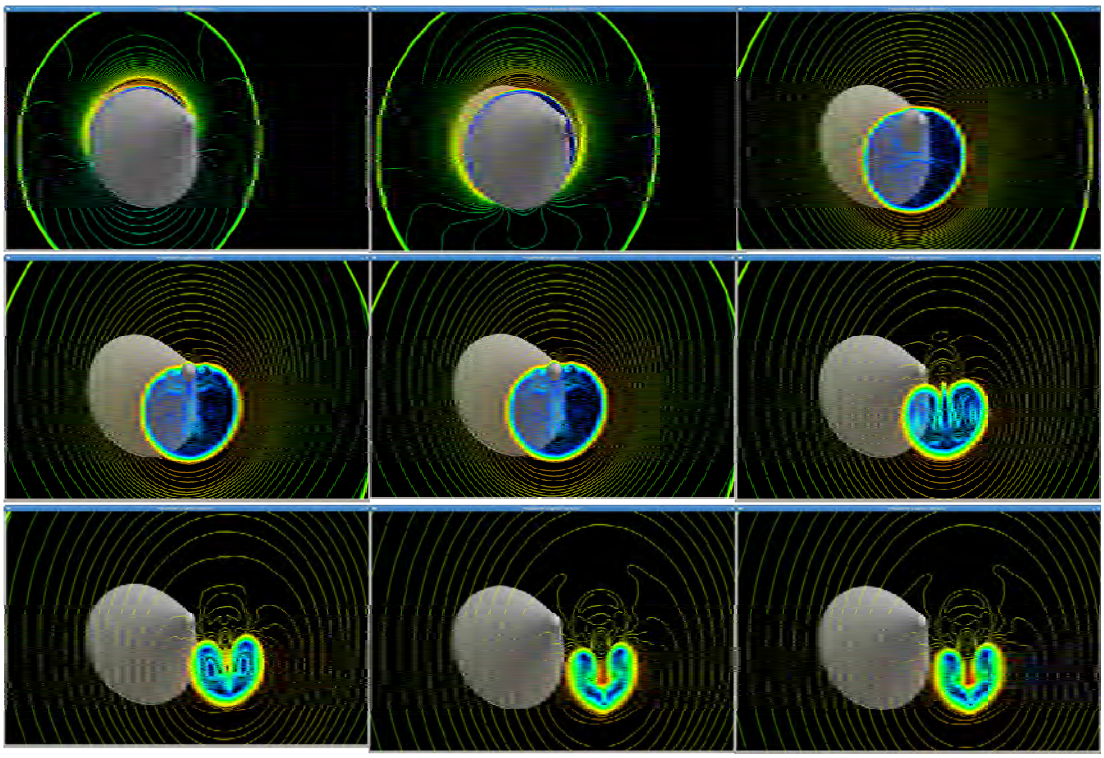

Figure 6-17: AS-202 in TST27 (Without Blade) Mach 2 AoA 19 Mach Contour X-Cut Planes Computed with LORE, 8M Cells Mesh.

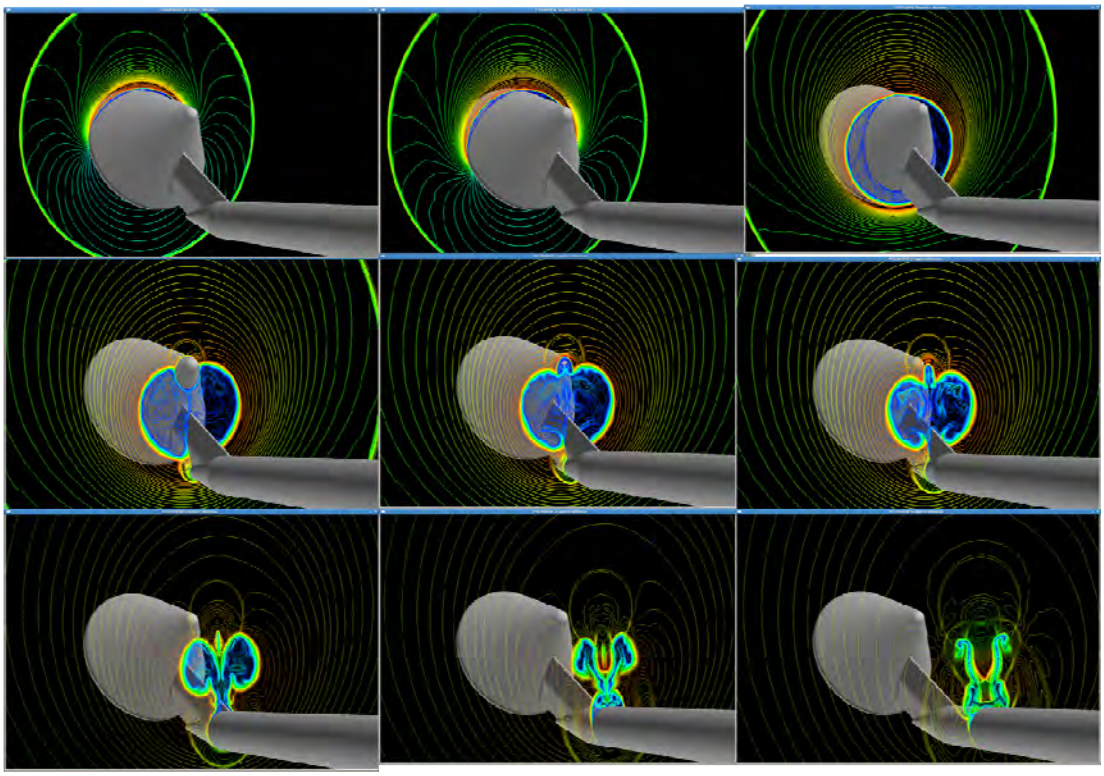

Figure 6-18: AS-202 in TST27 (With Blade) Mach 2 AoA 19 Mach Contour X-Cut Planes Computed with LORE: Effect of Sting/Blade on 8M Cells Mesh.

The Mach 4 results at angles of attack 10° and 14° (depicted in Figure 6-15 and Figure 6-16, respectively) also illustrate excellent agreement between experiment and CFD results. The flow on the upper side is attached at an angle of attack of 14 degrees, whereas it was separated at Mach 2. At an angle of attack of 10° the flow on the upper side separates at the beginning of the cone without re-attaching.

The wind tunnel tests also indicate a lack of sensitivity of the separation length to the free flow Reynolds numbers within the range reached in the TST27. Therefore it can be reliably assumed that the flow remains laminar for the tested conditions. This is confirmed by the good agreement between the CFD results and the tests, since all calculations considered laminar flow conditions only.

As a conclusion, the CFD methods used have demonstrated their ability to reliably predict the flow pattern including the separation behavior identified in the shadowgraphy images from the related wind tunnel tests. The qualitative trend found by Kruse [4] (Figure 6-8) of decreasing separation tendency with increasing Mach number could be fully confirmed by CFD as well as the wind tunnel tests at TU Delft.

6.4.2 AS-202 Flight Test Results and Related CFD Calculations

In this section the comparison between CFD results obtained with different codes to measured afterbody heat fluxes during the AS-202 full-scale flight test is performed. A general discussion of the flow phenomena in the afterbody region is useful in order to understand the different flow conditions seen at the various calorimeter positions. Due to the cross-flow induced by the angle of attack two lobes corresponding to the off-axis trailing vortices are formed, and these twin-lobes extend much further aft in regions away from the pitch plane as these vortices separate in the wake. There are two large subsonic counter-rotating vortices on the leeside, and two more closely spaced smaller vortices below these past the rear apex. This is well reflected in the calculated skin friction stream lines at the AS-202 rear side shown in Figure 6-19 and also clearly evident for the calculated Mach 2 wind tunnel case (Figure 6-17). The large kidney-shaped areas of separated flow associated with this vortex pattern at the upper side of the base are clearly recognizable from the skin friction patterns. A smaller separation region extends from the upper side of the apex. This general separation pattern is well predicted by DPLR, LORE and TAU, with slight variations on the exact position of the separation lines, the LORE result being somewhat closer to the DPLR results than TAU (see Figure 6-20 and Figure 6-21).

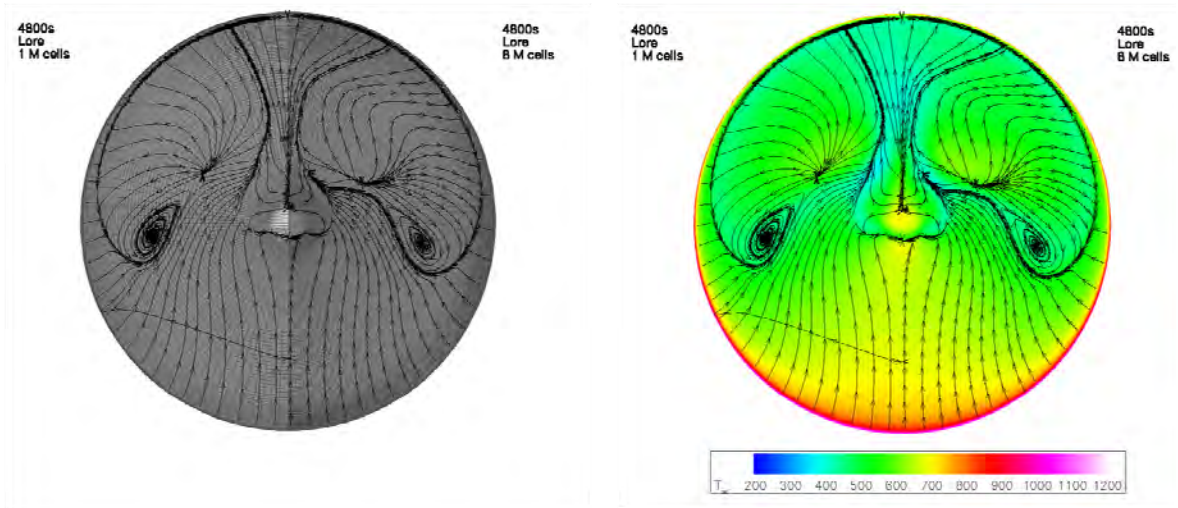

Figure 6-19: Surface Temperatures and Skin Friction Stream Lines on the Back of the AS-202 at 4800 s: Influence of Grid Refinement by Doubling the Mesh in 3 Directions.

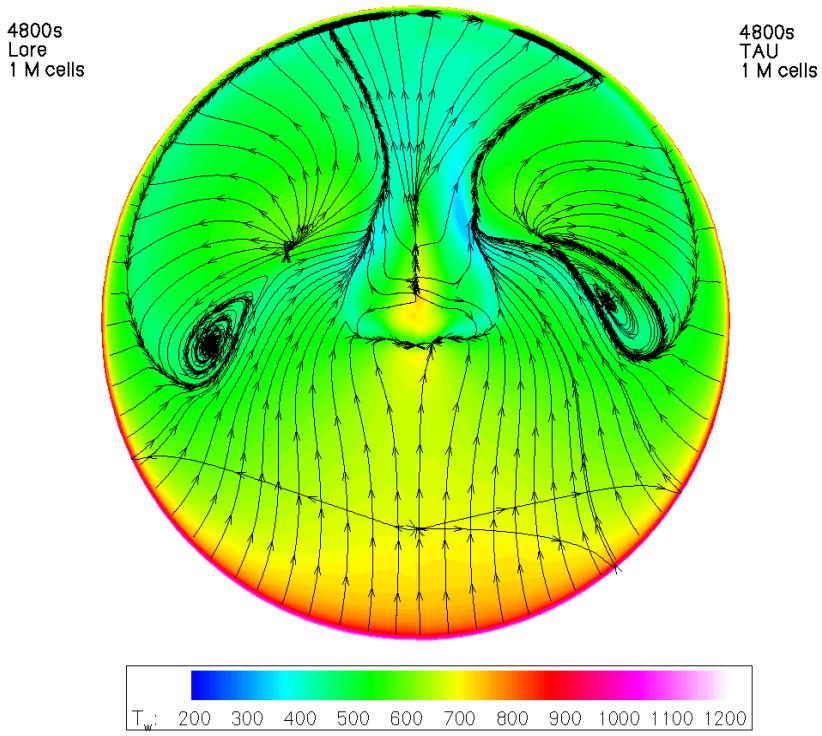

Figure 6-20: Surface Temperatures and Skin Friction Stream Lines on the Back of the AS-202 at 4800 s: Comparison LORE – TAU.

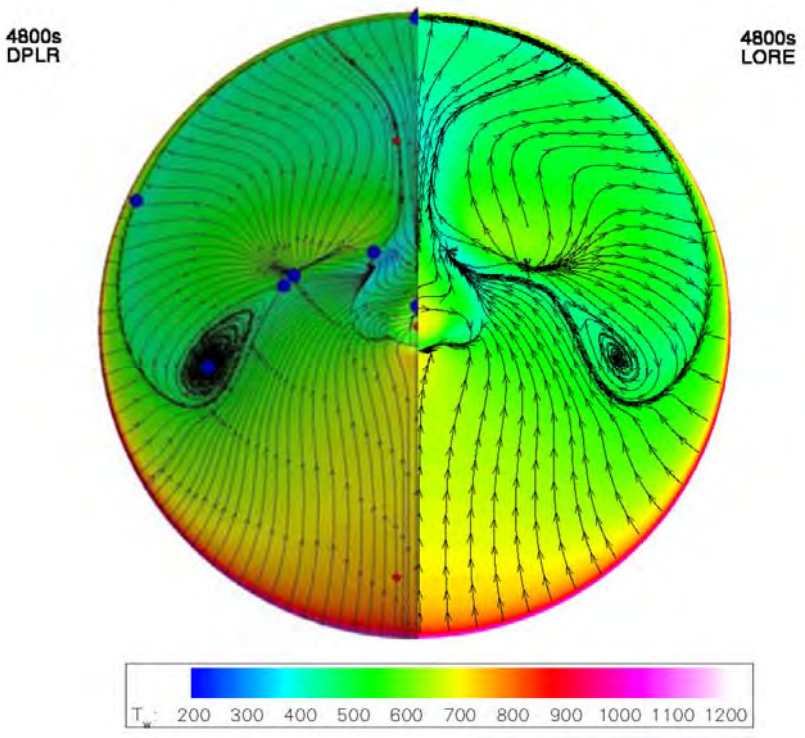

Figure 6-21: Surface Temperatures and Skin Friction Stream Lines on the Back of the AS-202 at 4800 s: Comparison LORE – DPLR.

The comparison between the computed afterbody heat transfer (assuming radiative equilibrium wall conditions with an emissivity of 0.85) in these flow areas and the experimental data for each of the 19 functional calorimeters "a – s" on the AS-202 Command Module is shown in Figure 6-22 (a) – (s). The agreement between the computations and the data is generally within the assumed experimental uncertainty for 15 of the 19 calorimeters. The calorimeters will be discussed in four separate groups: those on the shoulder in attached flow ("*h*" and "*i*") those on the windward (attached) side of the afterbody ("*a-d*", "*f*", and "*g*"), those in the separated flow region ("*e*", "*m*", and "*o-s*") and those near the separation line ("*j*", "*k*", "*l*", and "*n*").

On each plot in Figure 6-22, the flight data, which were scanned from Ref. 1, are shown as crosses. At some locations, particularly during the second heat pulse, there were multiple signal spikes. For example, notice the sharp heating spikes in the flight data on Figure 6-22 (l) at around t = 4460 and t = 4900 s. These spikes were determined by Lee [1] to correspond to the times of RCS firings, and thus are considered to be spurious. The data points that were estimated by the present authors to be spurious are shown on the plots as open circles. The best fit to the data for each case was then obtained using a Fourier-function-based least-squares fitting procedure neglecting the spurious data points. Dashed lines indicate the assumed ±20% uncertainty in the data [4]. For the purposes of this work the uncertainty was assumed to remain constant throughout the entry. Examination of Figure 6-22 indicates that the assumed uncertainty encompasses the majority of the data scatter, with the exception of some of the calorimeters in the separated flow region, which have more scatter during the skip maneuver (t = 4600 to 4800 s). Finally, the CFD results at the trajectory points are shown as red diamonds for the DPLR analyses, as blue triangles for the LORE calculations (blue open triangles are used for a single calculation using a diffusion limited approach for modeling the wall catalycity) and as green diamonds for the TAU code results (unstructured grid results are shown as green open circle).

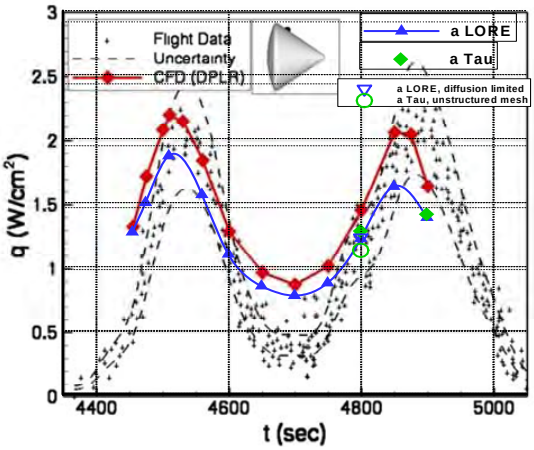

Calorimeter (a)

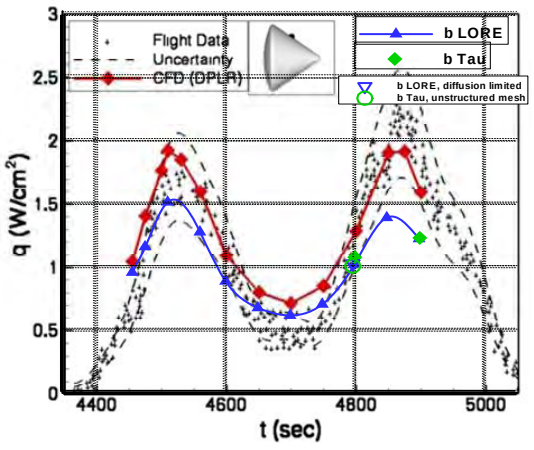

Calorimeter (b)

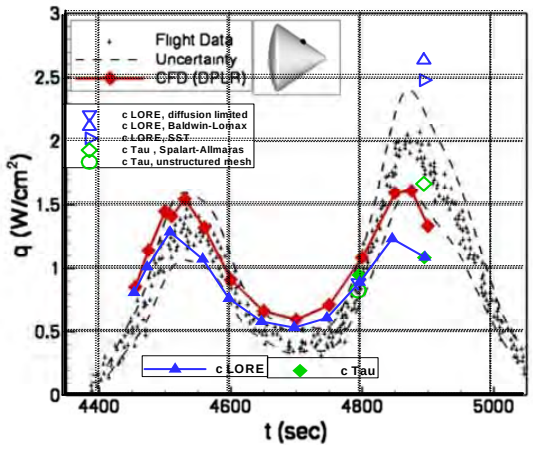

Calorimeter (c)

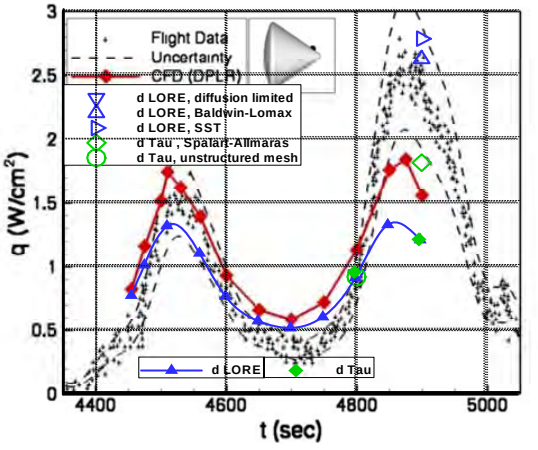

Calorimeter (d)

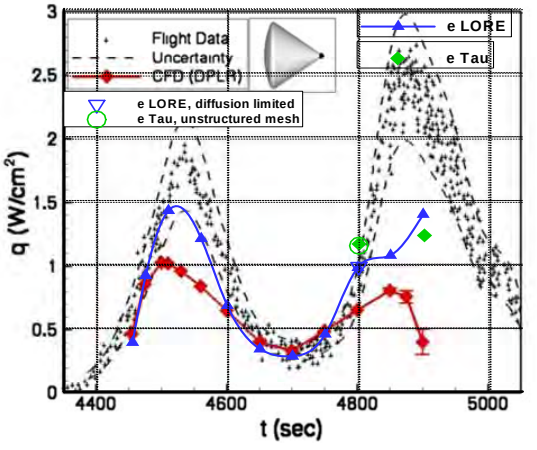

Calorimeter (e)

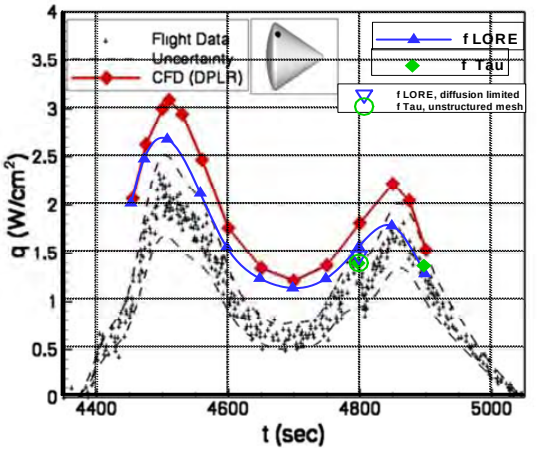

Calorimeter (f)

Figure 6-22: Comparison of Computed and Experimental Heat Transfer for AS-202.

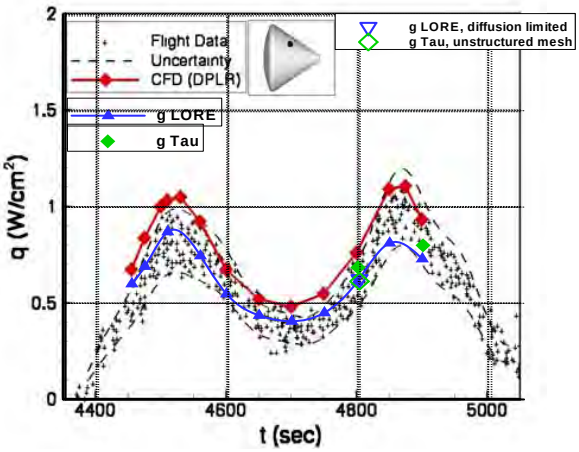

Calorimeter (g)

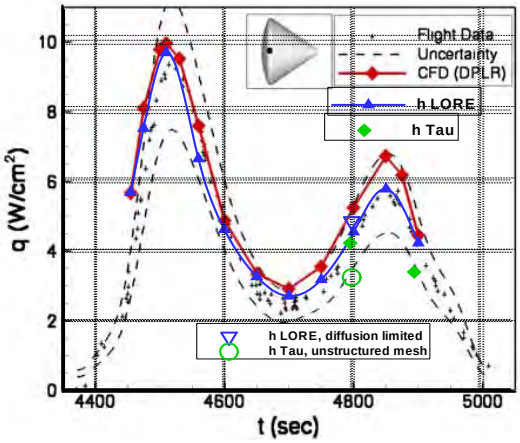

Calorimeter (h)

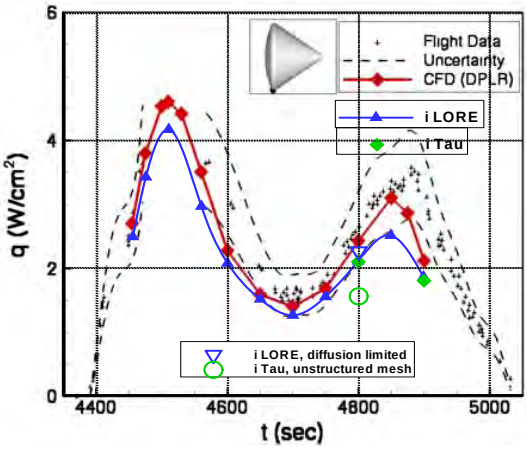

Calorimeter (i)

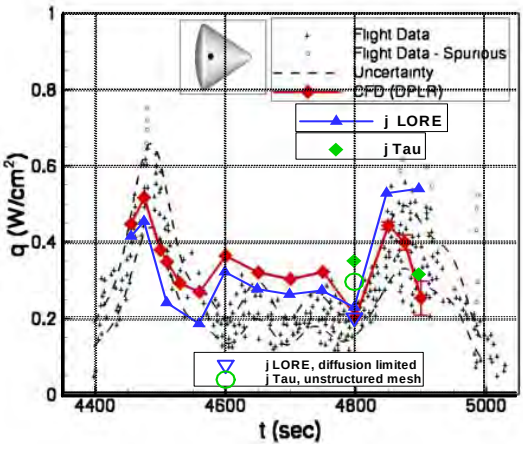

Calorimeter (j)

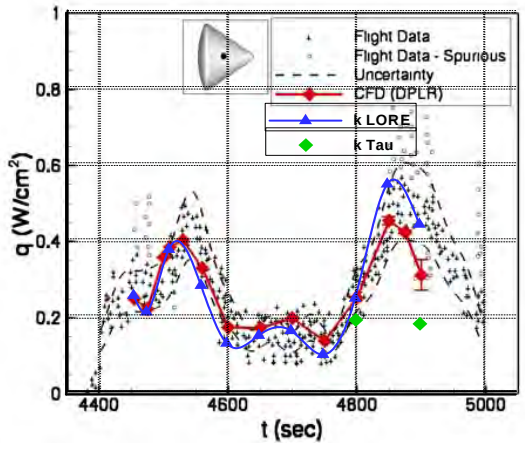

Calorimeter (k)

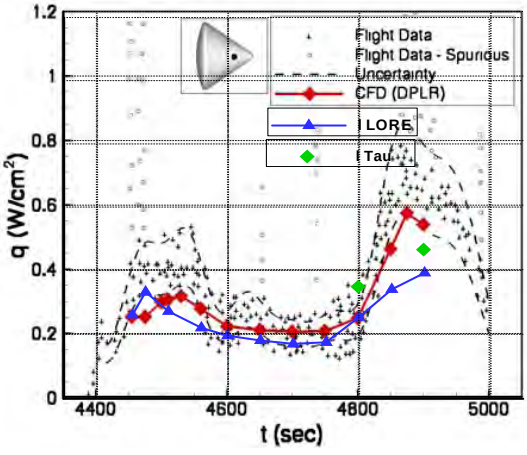

Calorimeter (l)

Figure 6-22: Comparison of Computed and Experimental Heat Transfer for AS-202 (cont'd).

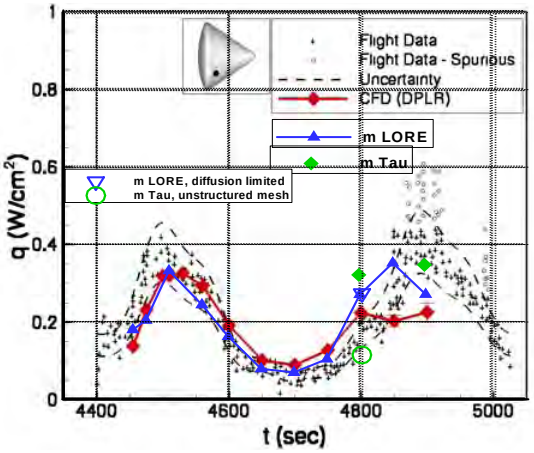

Calorimeter (m)

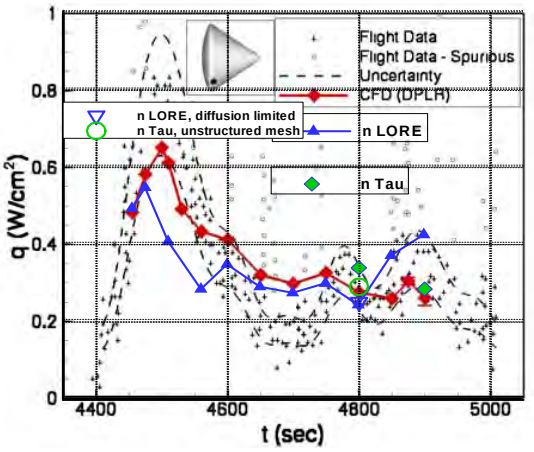

Calorimeter (n)

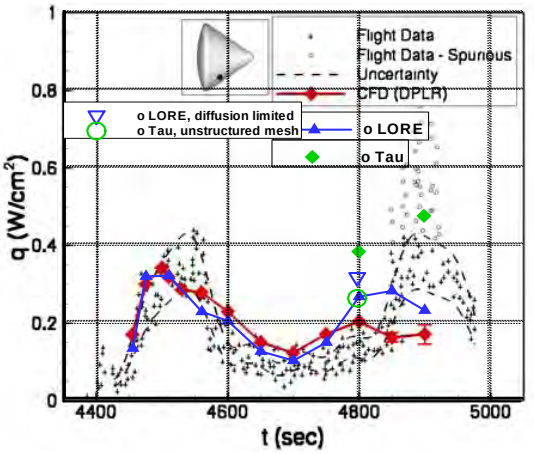

Calorimeter (o)

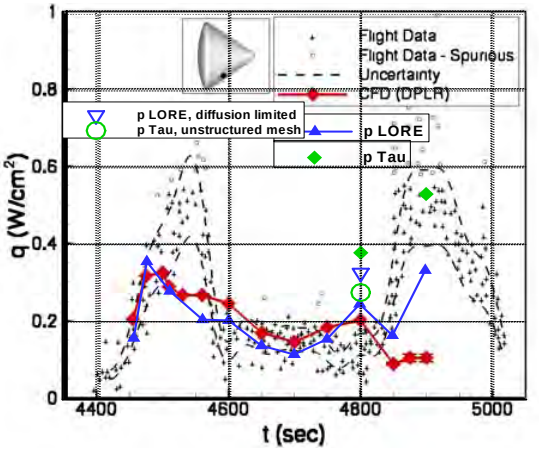

Calorimeter (p)

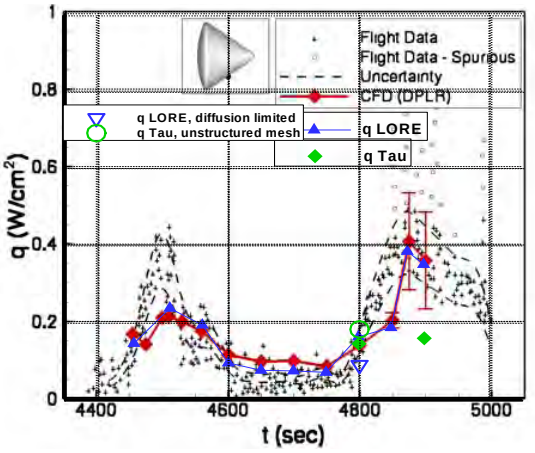

Calorimeter (q)

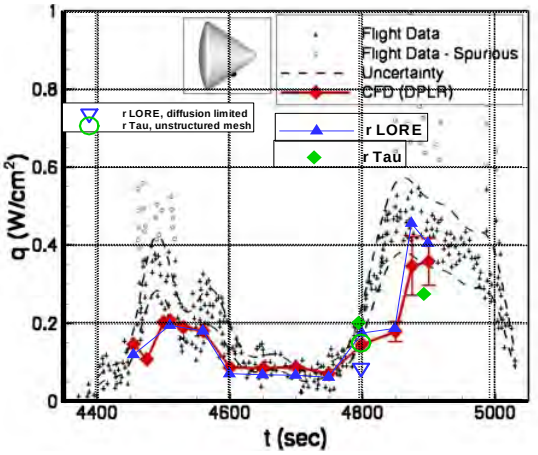

Calorimeter (r)

Figure 6-22: Comparison of Computed and Experimental Heat Transfer for AS-202 (cont'd).

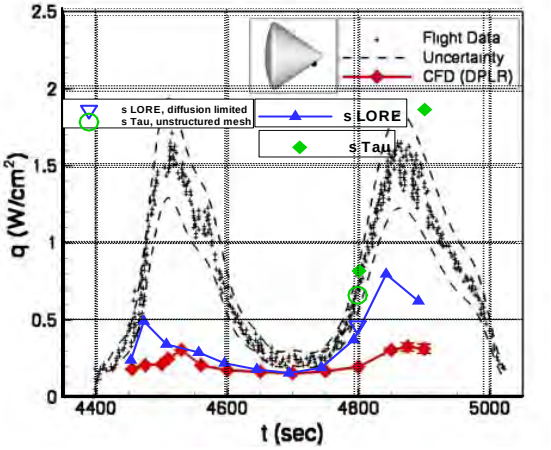

Calorimeter (s)

Figure 6-22: Comparison of Computed and Experimental Heat Transfer for AS-202 (cont'd).

These results are now evaluated separately for the calorimeter positions in the shoulder region, the attached flow region at the afterbody, the separated flow region and separation line region on the afterbody. As reference, the findings concerning the DPLR results are taken from Ref. [4].

6.4.2.1 I – Shoulder Region (Sensors "h", "i")

Two calorimeters were placed on the shoulder just before the maximum diameter point. Calorimeter "h" was placed midway between the windward and leeward centerline (θ = 178.5°), and "i" was placed on the leeward centerline (θ = 270°). Figure 6-22 (h) shows the comparison between the computed heating levels and the flight data for calorimeter "h".

DPLR Results – Good agreement between the CFD and flight data. Peak heat flux predicted by the CFD is about 10 W/cm^2 at t = 4510 s, or about 6% higher than the flight data (9.4 W/cm^2). Agreement is generally within 20% over the entire trajectory, with the largest discrepancy occurring near the minimum between the two heat pulses (t ~ 4700 s). Data for calorimeter "i" on the lee centerline is shown in Figure 6-22 (i): Once again the agreement is within the assumed ±20% uncertainty throughout most of the flight.

LORE Results –The LORE results are slightly below the DPLR results but also within the uncertainty range of the flight data for position "h". For position "i", the LORE results still are mostly within the uncertainty range falling below just after 4800 s. Considering the large gradients in the shoulder region the CFD results compare surprisingly well to the measurements. The result of the single additional calculation using a diffusion limited approach to model wall catalycity (4800 s) is nearly identical to the related result assuming super-catalytic walls. This is true for practically all sensor positions considered.

TAU Code Results – TAU Code calculations were performed for two trajectory points t = 4800 s and t = 4900 s. While the structured Level 1 (1Mio cells) meshes identical to the LORE meshes were used for both points in time, for the 4800 s case a hybrid/unstructured mesh was also employed to allow for comparisons of TAU solutions from structured and hybrid meshes.

The structured TAU results are practically identical to the LORE results for t = 4800 s, however, for t = 4900 s the TAU solution only matches calorimeter "i", and is at the lower end of the uncertainty band for calorimeter "h". The unstructured TAU solution at 4800 s is about 10% below the structured results for both sensor positions.

6.4.2.2 II – Attached Flow Region (Sensors "a", "b", "c", "d", "f", "g")

Six calorimeters were placed on the conical afterbody on the windward side in a region where the flow remained attached throughout the entry. Calorimeters "a" through "d" were placed on or near the windward centerline, as shown in Figure 6-4. Calorimeter "g" was placed approximately midway between the shoulder and rear apex, at $\theta = 143°$. The comparisons between the computed and experimental heat flux for these calorimeters are shown in Figure 6-22 (a) – (d), (f) and (g).

DPLR Results – From the figures we see generally good agreement during the first heat pulse. Heating levels near the peak heating point (t = 4510 s) are predicted to within 10% at all locations. Computed heating levels during the early portion of the second heat pulse also agree well with flight data, although the CFD results for calorimeters "c" and "d" at the final two trajectory points (t = 4850 and t = 4900 s) are lower than the flight data. The difference between the computation and flight data appears to increase with distance from the shoulder (the CFD results for calorimeter "c" are about 23% below the flight data at t = 4900 s, while those for calorimeter "d" under predict flight data by 30%). This may indicate that the flowfield is transitioning to turbulence on the attached afterbody during the second heat pulse – the computed heating at these calorimeters over predicts the flight heating near the trough between the heat pulses, with the amount of over prediction near t = 4700 s ranging from over 100% at calorimeter "a" to about 26% at calorimeter "g". There are several possible reasons for the CFD to predict higher heating than was measured in flight during this time period. During the period between about 4600 and 4800 seconds the spacecraft was undergoing a skip maneuver that resulted in a local maximum altitude at about 4700 seconds. During this skip phase local areas of non-continuum flow may have been present on the afterbody, which could result in an over prediction in heating. Also, during the high altitude skip phase of the entry, the uncertainty in vehicle orientation was much larger than average. In fact, between 4650 and 4750 seconds the uncertainty in angle of attack was approximately ±2 deg., as opposed to ±0.5 deg. during the remainder of the entry. It is possible that the low dynamic pressure during this portion of the trajectory could have prevented the vehicle from maintaining its trim orientation, resulting in a slightly smaller than expected angle of attack. If the angle of attack were small enough the flow could separate on the lee side of the afterbody, significantly reducing the predicted heating.

Calorimeter "f" (Figure 6-22 (f)) was placed near the rear of the shoulder at $\theta = 138°$. For this calorimeter, the CFD predictions are uniformly 33 – 50 % higher than the data. Given the level of agreement seen for the other five calorimeters in this region, as well as that seen for the two calorimeters on the shoulder, the reasons for this disagreement are not clear.

LORE Results – Apart from t = 4900 s, the LORE results are well within the uncertainty range for all sensor positions with the exception of the trough area discussed above (albeit the LORE results are somewhat nearer to the flight data in this area than the DPLR results). For 4900 s, turbulent calculations using the Baldwin-Lomax as well as the Menter's SST model were also performed. These results come out within the upper region of the uncertainty area for calorimeter "d", but somewhat above upper fringe of the uncertainty area for calorimeter "c". This points to a possible turbulent flow situation in this area, not fully developed (transitional).

TAU Code Results – The laminar TAU-Code results are again close to LORE's. This is true for the structured grid as well as the unstructured grid results. In general, the TAU solutions on structured and unstructured meshes tended to be nearly identical in the attached flow regions, whereas deviations between results from structured and unstructured grids were found primarily in the separated flow regions.

For 4900 s, an additional turbulent calculation using the Spalart-Allmaras model delivered heat fluxes well within and at the lower fringe of the uncertainty range for calorimeters "c" and "d".

In summary, all turbulent CFD calculations presented support the assumption of developing/transitional turbulent flow conditions in the area of the sensors in question. In view of the freestream Reynolds number

all flight conditions considered are assumed to be laminar. Although for point (c) and (d) on the windward side, the flight data are hinting towards a turbulent condition, taking into account that the energy in the flow is less in the second peak as shown with the Fay-Riddell results, which is elaborated later in the paper. Possible reasons for transition could be protuberances, deteriorated walls or the promotion of transition due to cross-flow [10]. An assessment was made to verify the laminarity of the base low with a transition criterion, commonly used in projects, in which the Reynolds number based on the momentum thickness over the Mach edge number, Re_Θ/M_e is below 120. In Figure 6-25 the Re_Θ/M_e is plotted for DPLR and LORE over the base region. A large part of the windward base is well below 120. Note that the computed values in a separated flow should not be taken into account since it is impossible to define the boundary layer edge there.

Turbulent augmentation factors resulting from the laminar solutions for selected sensor positions are contained in Table 6-4 for all turbulent solutions at t = 4900 s: Turbulent heat flux results using DPLR (Baldwin-Lomax model) were reported in Ref. 4 for two sensor positions “c” and “d”. Turbulent heat fluxes calculated with LORE (Baldwin-Lomax model and SST model) and with TAU (Spalart-Allmaras model) are given for seven sensor positions “a – d” and “h”. The Baldwin-Lomax model predicts the highest turbulence levels, closely followed by the SST model. As seen for sensor position “c” and “d”, the augmentation factors of the Baldwin-Lomax model compare well between DPLR and LORE. The lower augmentation factors of the Spalart-Allmaras model indicate a not fully developed turbulent flow. The Spalart-Allmaras turbulence model is known to predict fully turbulent flow only gradually after a transitional length. Therefore, the lower turbulent augmentation factors hints at a transitional flow prediction. It can be seen that both the full turbulent values resulting form the Baldwin-Lomax, SST and the transitional Spalart-Allmaras model are within the uncertainty of the flight data. In summary, the flight uncertainty encompasses all turbulent CFD heating levels, whether transitional or fully turbulent, in the area of the concerned sensors.

Table 6-4: AS-202 Turbulent Augmentation Factor Turbulence Modes/Codes for 4900 s.

Calorimeter Code/Model	a	b	c	d	g	*h*
TAU/lam	1.22	1.07	1.21	1.24	3.36	1.79
TAU/SA	1.46	1.67	1.8	1.52	3.45	2.16
Factor SA	**1.20**	**1.46**	**1.55**	**1.49**	**1.34**	**1.03**
LORE lam	1.23	1.07	1.21	1.39	4.18	1.86
BL	3.16	2.96	2.64	2.61	1.91	8.91
Factor BL	**2.29**	**2.41**	**2.48**	**2.15**	**2.62**	**2.13**
LORE SST	2.31	2.68	2.49	2.82	1.27	5.55
Factor SST	**1.67**	**2.18**	**2.33**	**2.33**	**1.67**	**2.18**
DPLR lam			1.8	2.4		
DPLR BL			3.2	3.2		
Factor BL			**2.46**	**2**		

6.4.2.3 III – Separated Flow Region (Sensors "m", "o", "p", "q", "r", "e", "s")

Seven calorimeters were placed in a region for which the flow remained separated during the entire heating portion of the entry.

DPLR Results – Computational results for five of these, calorimeters "m" and "o-r" are in generally good agreement with the flight data (see Figure 6-22 (m) and (o) – (r)). At each of these locations the peak heat flux during each pulse was between 0.2 – 0.4 W/cm^2. Agreement between the simulation and flight data was generally within 15% during the first heat pulse and the trough between the pulses. In contrast, the CFD prediction was generally lower than the flight data during the second heat pulse, which could be a consequence of turbulent transition. Note that the computed flow in the separation region became unsteady after t = 4850 s. Therefore the computational results for 4850, 4875, and 4900 seconds include "error" bars, which attempt to bound the unsteadiness of the computed heat transfer.

The results for calorimeter "p" require further discussion. This calorimeter is located in close proximity to "o" (see Figure 6-22), and the computational results predict very similar heat fluxes for each. In contrast, the flight data indicate that the peak heating levels at calorimeter "p" were significantly higher than those at "o". As a result the CFD under predicts the heating at calorimeter "p" by about 45% at t = 4530 s, while the prediction at calorimeter "o" is well within the data scatter. This apparent discrepancy can be explained by examination of the after body layout in Ref. [1]. While calorimeter "o" is mounted on a smooth area of the heat shield, calorimeter "p" was placed immediately in front of one of the rendezvous windows. Given this, it seems likely that the window created a local flow disturbance that affected the heat flux measured by calorimeter "p".

Calorimeter "e" was placed at the rear apex of the aeroshell. As seen in Figure 6-22 (e), the computations agree well with the flight data early in the first heat pulse and during the trough, but the computations significantly under-predict the peak heating levels. At t = 4530 seconds the CFD result is about 45% lower than the flight data indicate. The disagreement during the second heat pulse can possibly be due to turbulent transition, but the differences in the first pulse are more difficult to understand. One possibility is that the local geometry of the apex is not accurately modeled in the current simulations.

By far the poorest agreement between the flight data and the CFD occurs at calorimeter "s" Figure 6-22 (s), which is near the rear apex on the leeward side near the centerline. At this location the flight data indicates heating levels nearly as high as those at the apex (calorimeter "e"), and slightly higher than those observed at calorimeter "d", which was at the same x-location but near the windward centerline. The computations predict very low heating levels at this location, consistent with those in the rest of the separated flow region. The reasons for this disagreement are not clear. Physically, the apex should create a separated flow region immediately behind it that would result in significantly lower heat transfer at calorimeter "*s*" than either "*e*" or "*d*". This relation is consistent with all CFD predictions although the absolute values are far off. This difference in absolute values can be only explained by a different local flow structure in the CFD solutions.

LORE Results – The LORE calculation are generally significantly closer to the flight data for the second heat pulse than the DPLR results, albeit both LORE and DPLR also remain in some cases below the uncertainty band of the flight data.

TAU Code Results – The TAU results capture the second heat pulse at 4900 for sensors "o" (within 10% above the uncertainty limit) and "p" (nominally). On the other hand the heat flux at *t* = 4800 s is over-predicted by TAU. At sensors "q" and "r" the TAU results match the flight data at 4800 s but are significantly lower at 4900 s, near the lower limits of the "unsteadiness" error bars applied to the DPLR results. It must be underlined however, that in this low heatflux region, **absolute** heatflux density deviations in the order of just 1 W/cm^2 are of concern. Such low variations are considerably more challenging to model,

considering the relative error bands (heat flux levels in the attached flow regions are one or two order above the heat fluxes typical for the separated regions). Interestingly, for the apex region "s", the best agreement between CFD and flight data is obtained wit the TAU code. This can be explained by the somewhat different separation line pattern predicted by TAU in that area.

When comparing the results of the three different codes it should be noted, that there are geometric differences between the apex as modeled and the flight vehicle that could result in different fluxes. There is also the possibility of a non-laminar heat flux condition in this region, which could lead to significantly higher fluxes. This could be attributed to a deteriorated wall or transition promotion due to cross-flow.

6.4.2.4 IV – Separation Line Region (Sensors "j", "k", "l", " n")

Four calorimeters ("j, k, l, n") were placed in locations that were very near the separation line. Because the separation point is a function of Reynolds number, these calorimeters were in attached flow during a portion of the trajectory, and separated flow during the remainder.

DPLR Results – The agreement between the computations and the flight data for these calorimeters was also generally good throughout the entry, as seen in Figure 6-22 (j) – (l) and (n). The clearest evidence of transition from attached to separated flow can be seen at calorimeter "*j*", where the CFD shows sudden jumps in computed heating between t = 4560 and 4600 s and again between t = 4750 and 4800 s as the flow at this location attaches and then separates again. Similar jumps can be seen in the raw flight data at this location around t = 4600 and 4750 s (see Figure 6-22 (j)), although the levels are 20 – 30% lower than that predicted by the CFD. The computation also shows a jump in heating at calorimeter "*k*" at t = 4700 s that corresponds to a transition from separated to attached flow. However in this case the scatter makes it impossible to determine whether a corresponding event was seen during the flight. Transition from a separated to an attached flow state is not readily visible in the surface heating at the other two calorimeter locations, however the general good agreement between the computations and the flight data indicates that the extent of separation is accurately predicted in the current simulations.

LORE Results – For the sensors near the separation lines LORE/DPLR are alternatively closer to the flight data during certain trajectory phases: this is especially noticeable for the data points towards the end of the trajectory, after t = 4800 s, at sensor positions "j, "l" and "n", were the LORE and DPLR results tend to diverge. This underlines the fact that for those calorimeter positions, minor differences in the determination of the separation line positions between the codes can have a significant impact.

TAU Code Results – TAU results alternate between heat flux values nearer at DPLR or LORE data, depending on the time and sensor position. Again differences in the precise determination of the separations lines can be expected to show a significant impact on the individual results.

In summary, throughout most of the flight trajectory points considered, the afterbody heat fluxes are predicted within the uncertainty range of the flight measurements by all three CFD Codes DPLR, LORE and TAU, in spite of the fact that different wall catalycity models, reaction rate constants, and structured as well as unstructured CFD meshes were employed between the codes, which result in differences among the CFD results. As expected, larger deviations between the codes and flight data occur in separated flow areas.

6.4.3 Evaluation of Semi-Analytical, Approximate Engineering Approaches for the Assessment of Afterbody Heat Fluxes

As an alternative approach, the LORE and TAU CFD results obtained for 4800 s and 4850 s, resp, has been used to approximate the sensor heat fluxes vs. time over the complete trajectory range by scaling the CFD generated heat fluxes for the freestream velocity and density at 4800 s (V = 6210 m/s, ρ = 0.000137 kg/m^3)

with the freestream densities and velocities associated with all other trajectory points of interest via the simple relationship (Fay-Riddell stagnation point analysis):

$$Q(t) / Q(4800s) = [\rho(t) / \rho(4800s)]^{0.5} \times [V(t) / V(4800s)]^{3}$$

This simplified approach is often used in project work to approximately determine the heat flux evolution on re-entry vehicles from just one or two (comparatively expensive) Navier-Stokes CFD solutions over the whole trajectory.

The heat fluxes for sensor positions “a, b, g” and “h” on the windward afterbody side in comparison to the flight data and to the full range of DPLR CFD results is shown in Figure 6-23. The curves in Figure 6-23 basically underline for the current case the validity of this engineering approach in a conservative sense, considering that the maximum absolute heat flux peaks tend to be higher than the flight measurements, albeit the maximum between left and right peak is in some cases interchanged compared to the flight measurements. However, it is evident that the local accuracy here depends heavily on the flow region, sensor “h” showing a significantly better correlation to the flight data (fully within the uncertainty range throughout the trajectory) than the other sensors shown. However, at all sensor positions shown, an area in the middle of the heat flux peaks falls within the uncertainty range of the flight data.

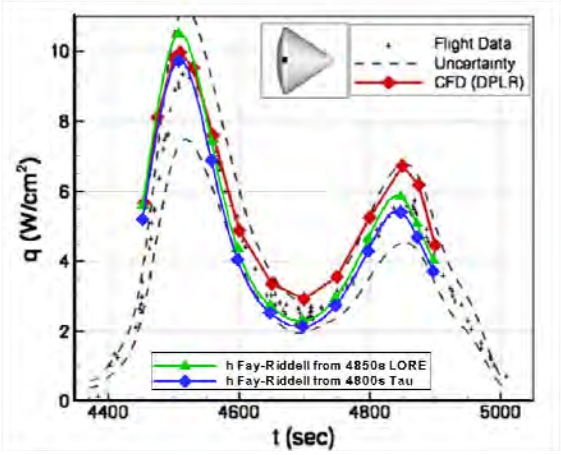

Calorimeter (h)

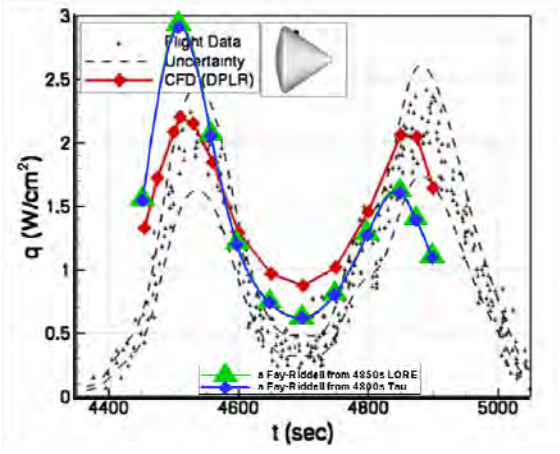

Calorimeter (a)

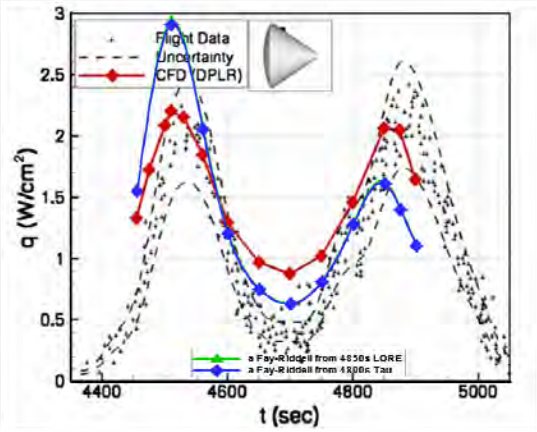

Calorimeter (b)

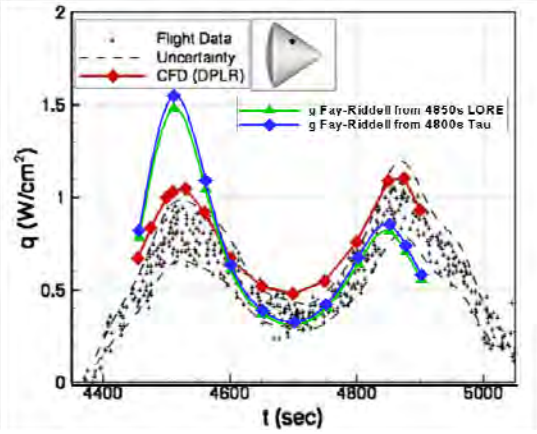

Calorimeter (g)

Figure 6-23: Heat Flux Time History on Windward Side of the AS-202 Base Computed with Fay-Riddell Anchored with One CFD Analysis.

Since the data are basically scaled with respect to the stagnation point heat flux using this engineering approach, the general trend of the heat fluxes on all positions on the surface is implicitly assumed to follow the trend of the stagnation point heat flux which obviously does not work out equally well for all positions at the afterbody surface.

The relation of measured base flow heat fluxes (colored curves) vs. flight time at all calorimeter positions to the stagnation point heat fluxes can be found in Figure 6-24. The stagnation point heat flux density of AS-202 was determined through the Fay-Riddell formula without correction for the angle of attack (black curve in Figure 6-24).

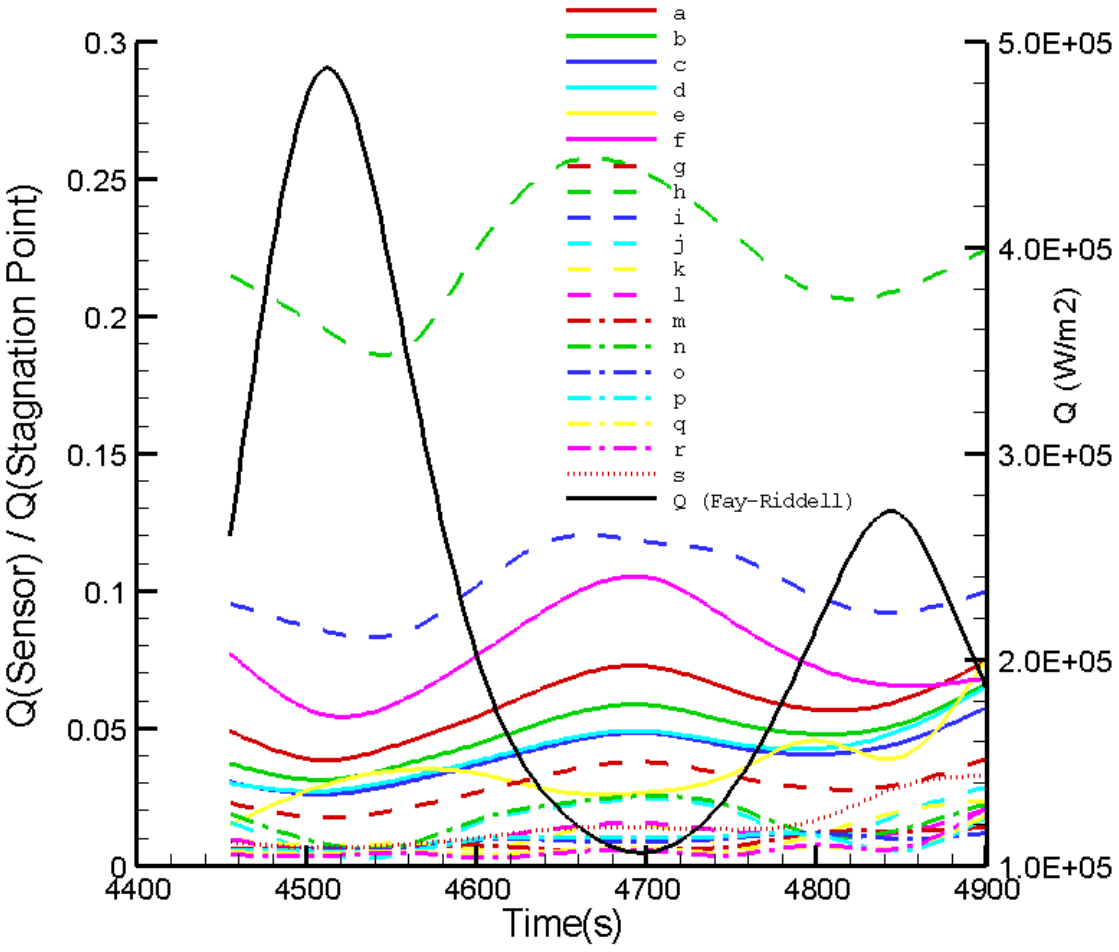

Figure 6-24: Analytical Heat Flux Prediction/Relation of Measured Base Flow Heat Fluxes to Fay-Riddell Stagnation Point Heat Flux.

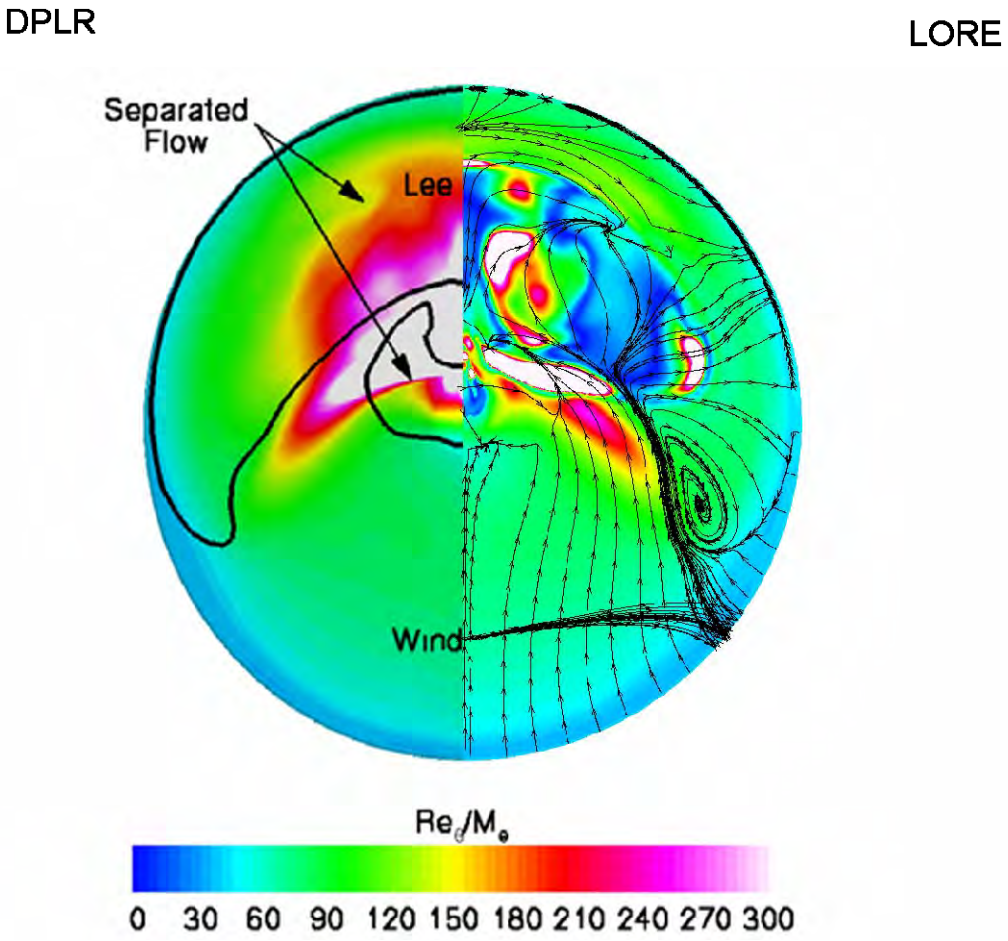

Figure 6-25: Comparison of Computed Transition Parameter on the Conical Afterbody for t = 4900 s.

Now Figure 6-24 shows that the measured heat fluxes at the majority of the 19 calorimeter positions remain at or below 7% of the Fay-Riddell stagnation point heat flux throughout the trajectory. Only 3 calorimeters “h”, “i” and “f”, all positioned at or very close to the shoulder, recorded higher heat flux levels going up to 26% of the Fay-Riddell heat fluxes in the case of “h”

Even if the 20% uncertainty on top of the measured flight data is applied, it can be concluded that the assumption of the base heat fluxes nowhere exceeding ~10% of the Fay-Riddell heat flux represents a conservative engineering estimate for the Apollo shape. Accordingly, just in the shoulder region of the afterbody, application of ~35% of the Fay-Riddell heat fluxes seems to provide a conservative engineering estimate.

6.5 CONCLUSIONS

In order to assess the predictive capability of capsule base flows with hypersonic CFD codes, the AS-202 shape have been investigated in well-controlled laminar supersonic wind tunnel flow conditions. Flight afterbody heating data of the Apollo AS-202, measured during a large portion of its re-entry has been used for the assessment of prediction capabilities in the presence of reacting flows.

To that end, a wind tunnel campaign has been performed in the TST27 facility at the TU Delft. The tests have provided reference data for the appraisal of current high fidelity hypersonic CFD codes used in most

ESA entry projects. During the tests, flow patterns with particular emphasis on shear layer separation at the capsule shoulder were investigated for various combinations of angle of attack and Mach number. The CFD calculations performed showed an excellent agreement to the flow topologies observed during wind tunnel tests, in terms of capturing salient flow features: Bow shock, shoulder region, wake area Shock-shock interactions/flow interferences due to the presence of a wind tunnel blade mounting, local separation and reattachment of the capsule flow and characteristic flow patterns of the leeside/wake flow have been accurately reproduced.

The good predictive capabilities of the CFD codes, LORE, TAU and DPLR, involved in the comparison of AS-202 in-flight afterbody heat flux measurements has been established, taking into account the large flight uncertainties and the very low levels of heat fluxes (<10 W/cm^2). Relative deviations are still found in the calculated afterbody heat flux levels between flight data and CFD as well as between different CFD codes which tend to be largest in areas of separated flow, and sensitive to details of the different numerical schemes. However, in these areas the absolute heat flux levels tend to be comparatively small, i.e., even a small deviation in absolute terms has a greater impact on relative error.

Since the computed heat fluxes agreed well to the AS-202 flight data within the uncertainty for most of the calorimeters, the present design margin of 200% commonly applied to afterbody simulations, could be reduced.

6.6 ACKNOWLEDGMENTS

The authors would like to thank Rafael Molina of the European Space Agency for providing his support, Stan van Gemert, COO, for enabling and managing the computational infrastructure at AOES and the CEO, Paul Pearson, for the support to the AVT making this work possible. Also many thanks to Greg Byshenk and Alessio Terpin, for building an optimized cost-performance cluster environment and Marco van Duijn.

6.7 REFERENCES

[1] Lee, D.B., Bertin, J.J. and Goodrich, W.D., “Heat Transfer Rate and Pressure Measurements Obtained During Apollo Orbital Entries”, NASA TN D-6028, October 1970.

[2] Lee, D.B., “Apollo Experience Report: Aerothermodynamics Evaluation”, NASA TN D-6843, June 1972.

[3] Hillje, E., “Entry Flight Aerodynamics from Apollo Mission AS-202”, NASA TN D-4185, October 1967.

[4] Wright, M.J., Prabhu, D.K. and Martinez, E.R., “Analysis of Afterbody Heating Rates on the Apollo Command Modules, Part 1”, *Journal of Thermophysics and Heat Transfer*, Vol. 20, No. 1, pp. 16-30, 2006.

[5] Walpot, L., “Development and Application of a Hypersonic Flow Solver”, Ph.D. Thesis, T.U. Delft University, May 2002.

[6] Gerhold, T.O., Friedrich, J.E. and Galle, M., “Calculation of Complex Three-Dimensional Configurations Employing the DLR-TAU-Code”, 16th Aerospace Sciences Meeting, Reno, NV, USA, AIAA Paper 97-0167, January 1997.

[7] Walpot, L.M.G., Noeding, P., Tarfeld, F., Molina, R.C., Gülhan, A. and Paulat, J.-C., “Transonic and Supersonic Static Stability Analysis of the CARV Reentry Vehicle”, 14th AIAA/AHI Space Planes and Hypersonic Systems and Technologies Conference, AIAA Paper 2006-8077, 2006.

[8] Gupta, R.N., Yos, J.M., Thompson, R.A. and Lee, K.-P., “A Review of Reaction Rates and Thermodynamic and Transport Properties for an 11-Species Air Model for Chemical and Thermal Nonequilibrium Calculations to 30000K”, NASA-RP-1232, 1990.

[9] Kruse, R., “Transition and Flow Reattachment behind an Apollo-like Body at Mach Numbers to 9”, Technical Note D-4645, NASA, 1968.

[10] Anderson, J.D., “Hypersonic and high temperature gas dynamics”, AIAA, 1988.

[11] Schrijer, F.F.J., and Walpot, L.M.G.F.M., “Experimental Investigation of the Supersonic Wake of a Reentry Capsule”, 48th AIAA Aerospace Sciences Meeting, Orlando, FL, USA, AIAA-2010-1251, January 2010.

Chapter 7 – EXPERIMENTAL INVESTIGATION OF THE SUPERSONIC WAKE OF A RE-ENTRY CAPSULE

Ferry Schrijer
Delft University of Technology
NETHERLANDS

Louis Walpot
Advanced Operations and Engineering
NETHERLANDS

The wake behind an Apollo shaped capsule is investigated in the framework of the 'afterbody heating' topic in the RTO WG043 working group. Measurements are performed by means of schlieren, shadowgraphy and Stereo Particle Image Velocimetry (SPIV) and are used for CFD validation purposes. The model geometry is a scaled version of the AS-202. It was found from the shadowgraph results that the angle of attack where separation occurs decreases with increasing Mach number and is not influenced by the Reynolds number. Furthermore, it was possible to correlate the shear layer transition location using $Re_{2,xt}$, which is the Reynolds number based on post normal shock conditions where the length scale is the flow path from stagnation point to transition point. SPIV measurements were obtained at Mach 2 and 0° and 25° angle of attack. For the 0° model, the wake was completely separated while for the 25° model the wake was partially separated and reattaches half way the model. Overall the PIV data return a quantitative three dimensional description of the velocity field around the capsule.

7.1 INTRODUCTION

Uncertainties in afterbody heating predictions can be related for given re-entry flight conditions to both the thermo-chemistry between the vehicle surface material and the fluid, as well as to the actual flow field established around the vehicle. In the comparative assessment of the heat transfer prediction performance of different CFD models against free flight test data; the absence of reliable information on the flow field structure can form an important source of uncertainty, which can be up to 200%. Moreover, the effects of flow transition to turbulence and of large scale flow unsteadiness require to be ascertained before proceeding with CFD computations, based on the laminar flow regime or the inclusions of turbulence modelling. This work gives experimental velocimetry and schlieren/shadowgraphy results for the flow around an Apollo-like capsule that was tested in a range between Mach 2 and 4. In order to build a high quality experimental data base for CFD comparison stereo particle image velocimetry was used and information is given on the location of shear layer transition. A correlation that allows the prediction of the location of shear layer transition it also presented in this chapter.

7.2 EXPERIMENTAL APPARATUS

7.2.1 Flow Facility and Wind Tunnel Model

The flow facility used in the experiments is the TST27 transonic/supersonic blowdown wind tunnel; see Figure 7-1. It has a 27 × 28 cm^2 test section and features two flexible nozzle walls that allow to continuously vary the Mach number between 0.5 and 4.2. The total pressure in the settling chamber can be varied from 2 bar at Mach 0.5 to 20 bar at Mach 4.2, which results in a unit Reynolds number range from 25 × 10^6 to 150 × 10^6. The maximum run-time of the facility is 300 s. Two 30 cm diameter schlieren windows in the side of the test section are available for optical access. In the current experiments, the wind tunnel was operated in the Mach range between 2 and 4 with a total pressure ranging from 2.7 to 12 bar and a total temperature of 288 K. The capsule geometry used for the definition of the wind tunnel model is a scaled version of the AS-202 outer moldline as defined in Wright et al. [1]. The model has a diameter of 50 mm and is fabricated out of Makrolon, it is side-mounted on a stainless steel sting. Two models are

used for 0 and 25 degrees angle of attack – see Figure 7-2. For angles of attack that deviated from the 0 or 25 degrees (shadowgraphy measurements), the sting was placed under an angle.

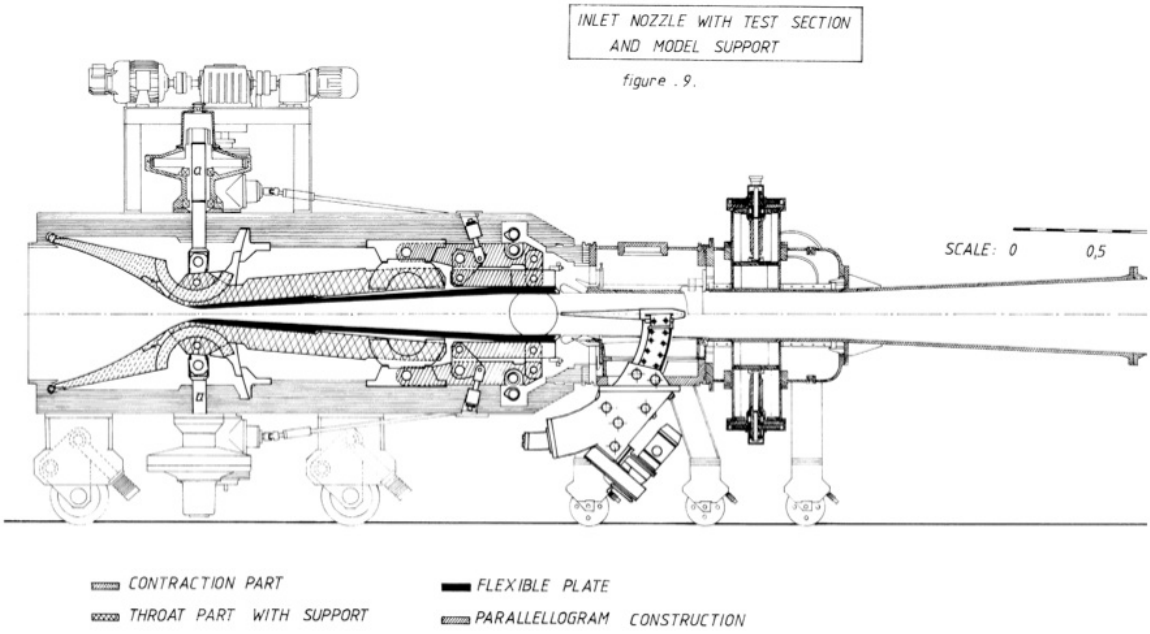

Figure 7-1: Schematic of the TST27 Wind Tunnel.

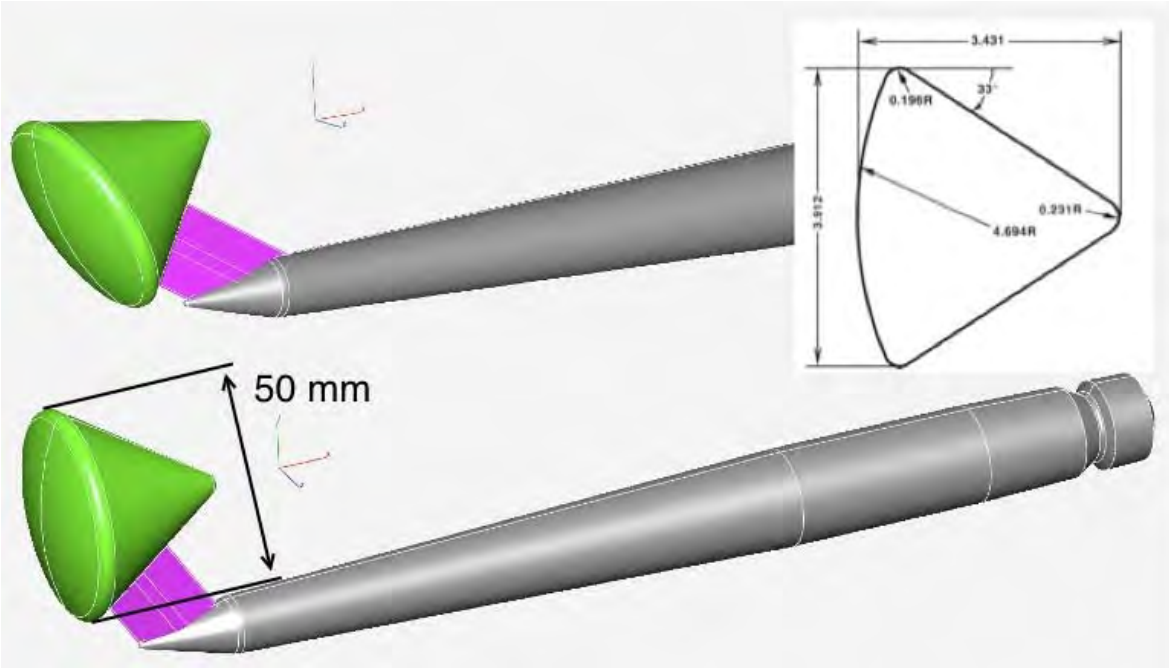

Figure 7-2: Model and Sting Geometry for 0 and 25 Degree Models (Insert: Model Definition by Wright et al. [1]).

7.2.2 Shadowgraphy and Particle Image Velocimetry

The shadowgraphs were obtained using a 3872 × 2592 pixel Nikon D80 camera. The illumination was provided by a Xenon spark light with an emission time of 20 ns, effectively freezing the flow in a single snapshot. The PIV measurements are performed using a high rep rate illumination and imaging system. A Quantronix Darwin Duo Nd-YLF double pulse laser was used as light source at a repetition rate of 500 Hz. The laser was rated at 20 mJ per pulse with a duration of 200 ns. The pulse time separation was set to $\Delta t = 5$ µs which resulted in a particle displacement of approximately 2.5 mm between two illuminations. The light was formed into a sheet and introduced into the wind tunnel by means of a retractable probe as shown in Figure 7-3 (top). The light sheet thickness was approximately 1.5 mm.

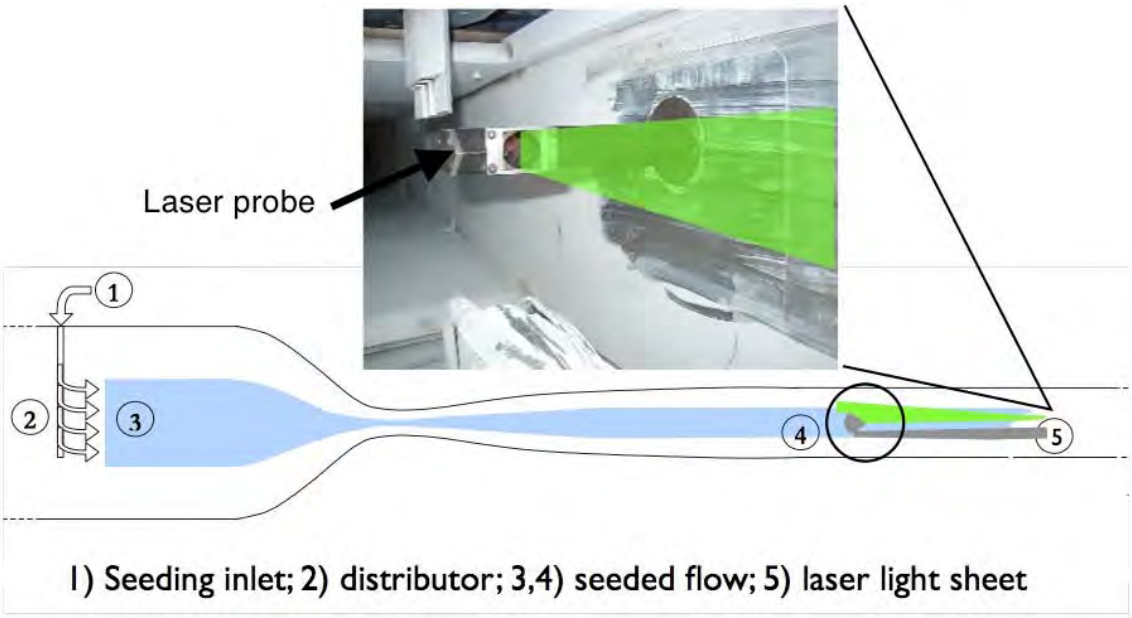

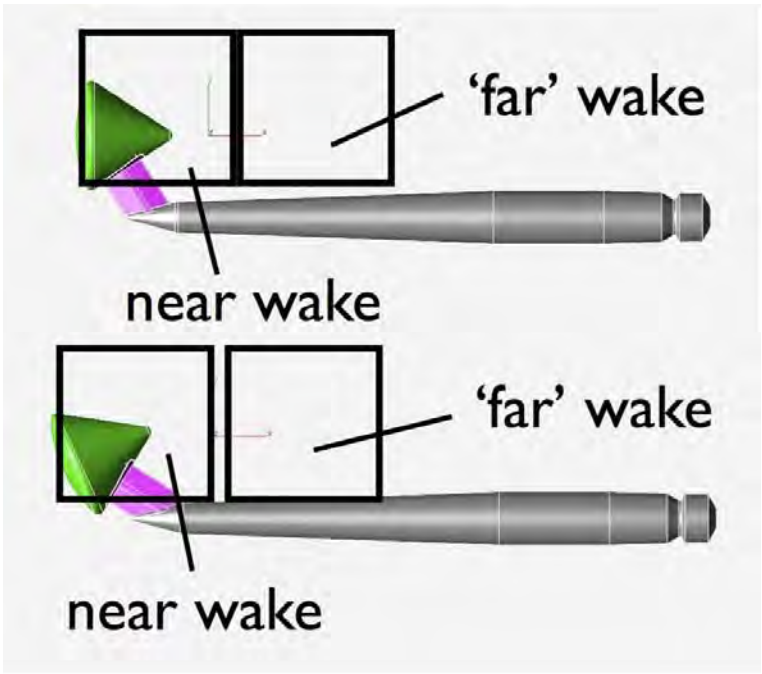

Figure 7-3: Seeding and Illumination System (top), Field of View for the 0° and 25° Models (bottom).

The particle images were recorded by means of two PCO FastCAM cameras which are equipped with a 1024 × 1024 pixel CMOS sensor. A Nikkor lens with a focal length of 60 mm was used at an $f_{\#}$ = 2.8, furthermore the particle images were slightly defocussed in order to prevent peak locking. For each model two fields of view were considered; the wake region and the 'far' wake region, see Figure 7-3 (bottom), each field of view was set to 8 × 8 cm^2. The measurement planes were offset in the z – direction (symmetry plane) and the following planes were measured: z = [0, 4, 7, 10, 13, 16, 19, 22, 25, 28, 31, 34] mm. For each plane 500 recordings were used to obtain the velocity data. PIV measurements were done using a stereo setup, which enabled to measure all three velocity components in the plane [2]. The PIV image interrogation window size was set to 32 × 32 pixels with an overlap factor of 75%. This corresponds to a measured vector pitch of 0.7 mm.

7.3 SHADOWGRAPHY RESULTS

7.3.1 Shear Layer Separation

Shear layer separation at the capsule shoulder was investigated for various combinations of angle of attack, Mach and Reynolds number. First it was determined whether the flow was attached or separated from the windward side of the capsule. In Figure 7-4 an example is given for a separated (left) and attached case (right).

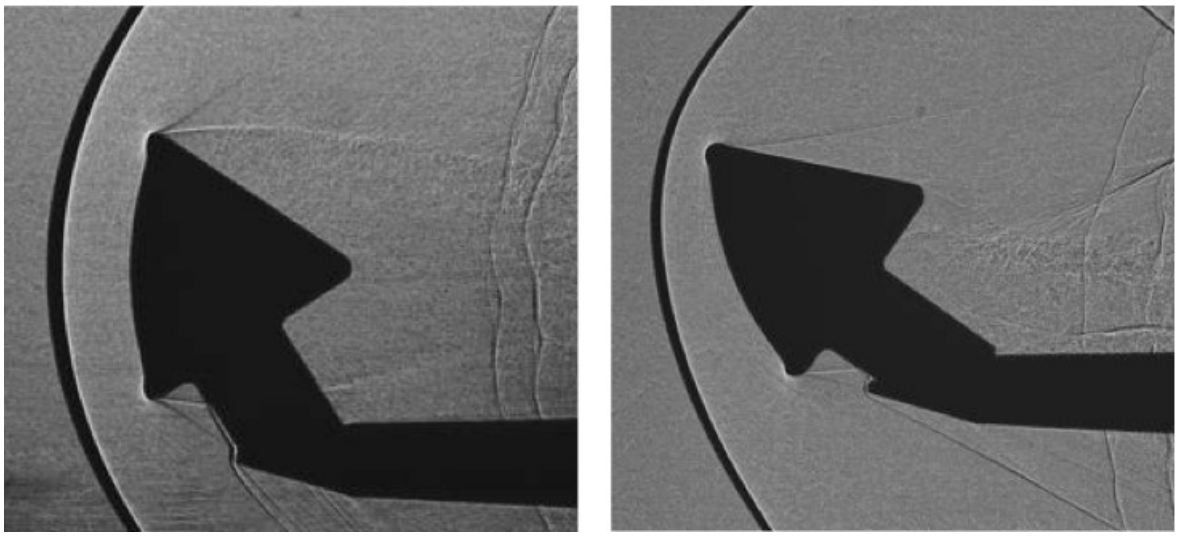

Figure 7-4: Shadowgraph Images for Mach 2, $Re_D = 1.75 \times 10^6$, α = 0° (left) and α = 25° (right).

It was found that in the current range, the Reynolds number has no effect on separation. Furthermore it was found that for increasing Mach numbers, the flow stays attached for smaller angles of attack. Similar results were obtained by Kruse et al. [3]. In Figure 7-5, the measurement points are given in angle of attack and Mach number parameter space. A blue circle denotes the flow conditions for which the shear layer was found to be attached while the separated cases are represented by a red triangle. In the figure also the curve-fit from Kruse et al. is shown that forms the border between an attached and a separated shear layer. As can be seen, the separation angle of attack decreases with increasing Mach number. However the angle of attack values found by Kruse et al. are smaller for Mach 2. This is due to the fact that in those measurements models were used that had sharp shoulders, in that case the separation point is defined and a more or less centred Prandtl-Meyer expansion is formed. In the current experiments, the flow expands more gradually and therefore is likely to separate more easily.

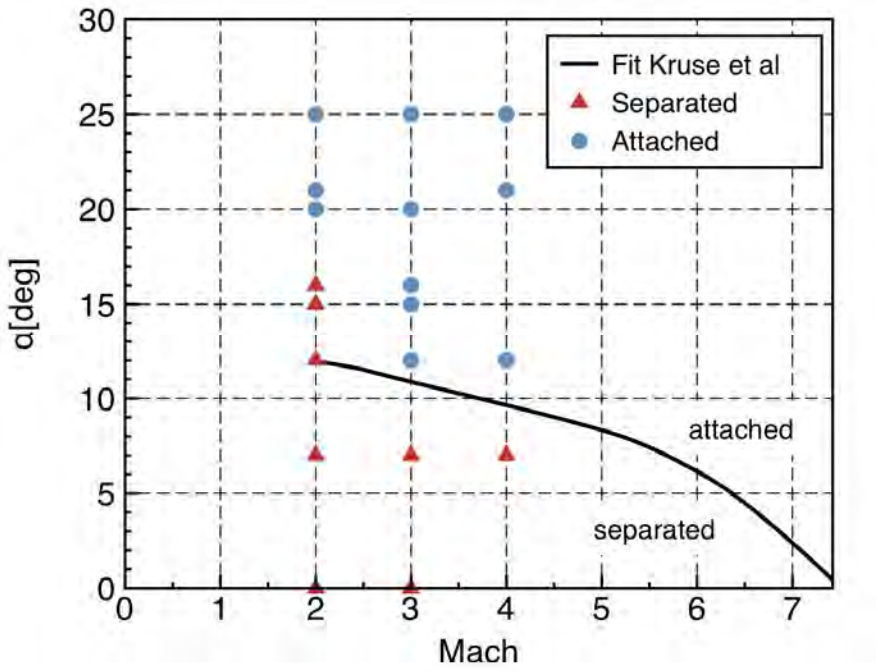

Figure 7-5: Shear Layer Condition as a Function of Mach Number and Angle of Attack.

7.3.2 Shear Layer Transition

The state of the shear layer (laminar or turbulent) is assessed by means of shadowgraph visualization. When the shear layer undergoes the transition from laminar to turbulent, the nature of the flow changes. In Figure 7-6 a zoomed shadowgraph is shown of the shear layer emanating from the capsule shoulder. The shear layer is imaged as a dark-light line. Close near the separation point the line is rather sharp and defined. Moving further downstream, the line becomes less defined and has a more grainy structure. This point has been considered as the shear layer transition location.

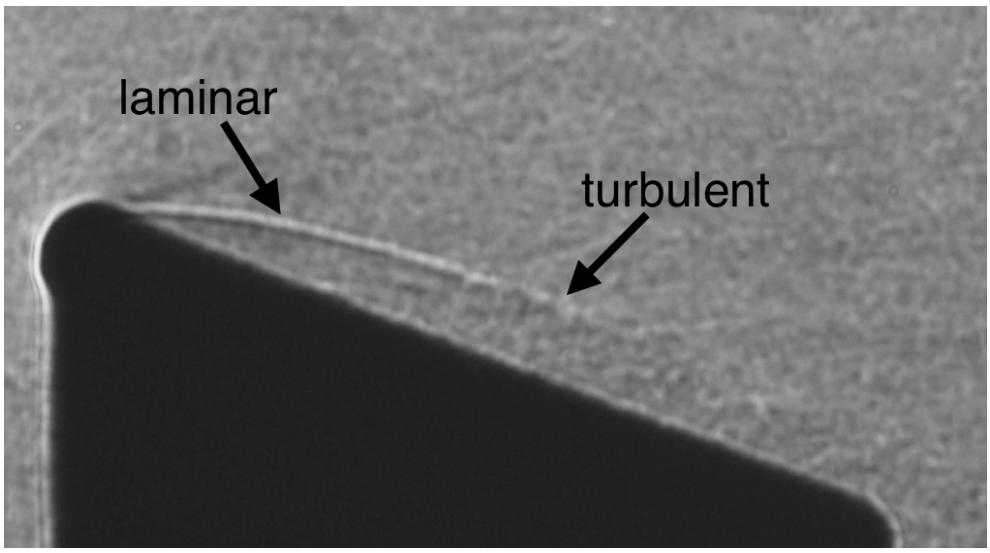

**Figure 7-6: Shadowgraph Indicating Shear Layer Transition;
Mach 2, α = 15° and $Re_D = 1.75 \times 10^6$.**

The shadowgraphs show that the location of the shear layer transition point depends on α, M and Re. It was found that the shear layer transition location can be correlated using a single parameter: $Re_{2,xt}$. This is the Reynolds number based on the flow conditions downstream of the (normal) bow shock, where the distance from the stagnation point to the shear layer transition location is used as the characteristic length scale:

$$Re_{2,x_t} = \frac{\rho_2 u_2 x_t}{\mu_2}$$

The Mach number is accounted for by taking the values downstream of the bow shock, therefore taking into account the shock strength. The angle of attack is taken into account by regarding the length from the stagnation point to the transition point instead of, for example, the length from the shoulder of the model to the transition point (as was done by Kruse et al.). For the current experiments it was found that for all cases: $Re_{2,xt} = 0.8 \times 10^6$, see Table 7-1.

Table 7-1: Shear Layer Transition Location.

Mach	α [deg]	$Re_D \times 10^6$	x_t/D	$Re_{2,xt} \times 10^6$
2	0	1.75	0.75	0.82
2	10	1.74	0.73	0.80
2	15	1.74	0.70	0.78
2	20	1.75	0.67	0.76
2	20	2.36	0.52	0.83
3	0	2.59	0.80	0.78
3	10	1.97	0.95	0.78
4	10	2.88	1.03	0.77

7.4 PARTICLE IMAGE VELOCIMETRY RESULTS

Raw PIV recordings are shown in Figure 7-7; in case of the 0° model there are no particles present in the wake making it impossible to perform a flow investigation by means of PIV in this region. In the shoulder region the flow undergoes large accelerations as it expands. Due to their inertia the tracer particles slip, see [4], which has two effects, it causes the particles to lag with respect to the surrounding flow and the particle streamlines are shifted with respect to the flow streamlines. The particle streamline is always shifted towards regions with lower accelerations. In case of the expanding flow over the shoulder it means that they are shifted outward, preventing particles to enter the wake.

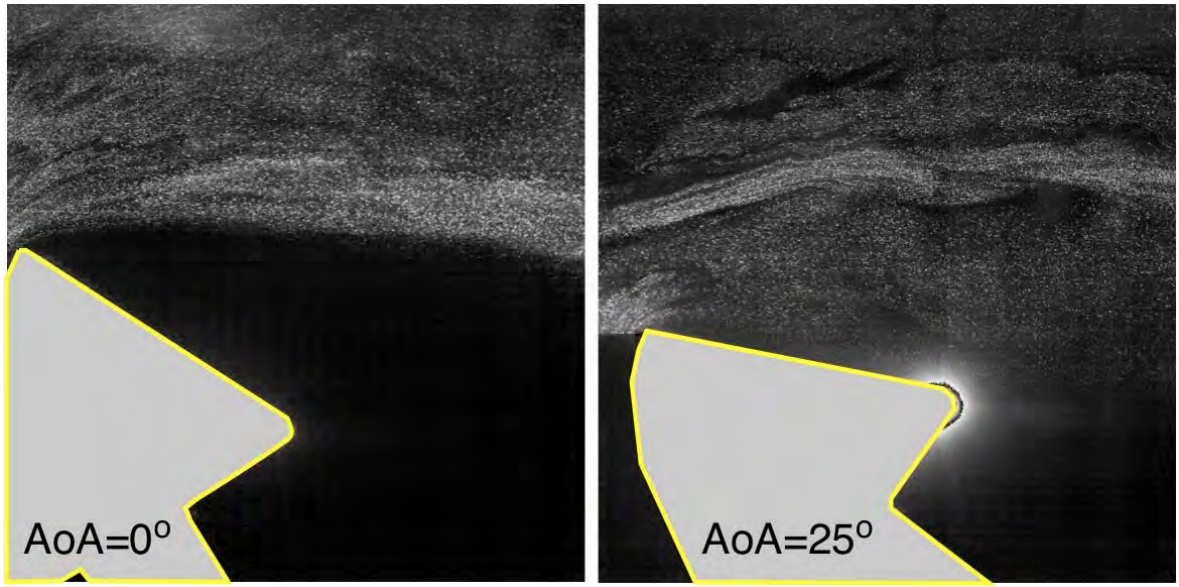

Figure 7-7: PIV Recordings for the 0° and 25° Models at Mach 2.

The extent of particle slip is quantified by the particle time relaxation τ_p, which is the time constant in the simplified particle motion expression [5]:

$$\frac{dU_p}{dt} = \frac{U_f - U_p}{\tau_p},$$

where U_p is the particle velocity and U_f is the flow velocity. PIV measurements were performed in the Hypersonic Test Facility Delft [6] at Mach 7 where the particle slip effect was even more pronounced. For the solid TiO_2 tracer particles used in those experiments, the relaxation time was determined experimentally by means of a shock wave test [7] and the value was $\tau_p = 2.5\ \mu s$. In Figure 7-8 an example PIV recording is given of the flow over the wind tunnel model at 0° at Mach 7. Overlaid is a laminar CFD solution that is used to compute the particle paths for $\tau_p = 2.5\ \mu s$ (red) and $\tau_p = 0\ \mu s$ (yellow) where the latter is equivalent to a streamline. From the local particle concentration, the bow shock is clearly visualized as a bright region (the particle density increases with the thermodynamic density). As can be seen from the image, the location of the bow shock indicated by the increase in particle density does not match the shock location obtained from CFD calculations. This is caused by the particle relaxation; since it takes time before the particles decelerate to the post-shock velocity also the particle concentration will increase further downstream. Near the capsule shoulder the particle concentration decreases again, this is caused by the decrease in thermodynamic density and the effect of particle slip. For the current particles a trajectory is computed starting from a surface streamline. According to the computation, particles are expected above the red line while no particles are expected below. As can be seen from the image, the prediction agrees very well with the measurement, almost no particles are detected below the red particle path. In the experiments performed at Mach 2, DEHS was used as seeding material. For these particles also shock wave tests were performed and a relaxation time of $\tau_p = 2.1\ \mu s$ was obtained [8]. However, as can be seen from Figure 7-7, also this value is still too large.

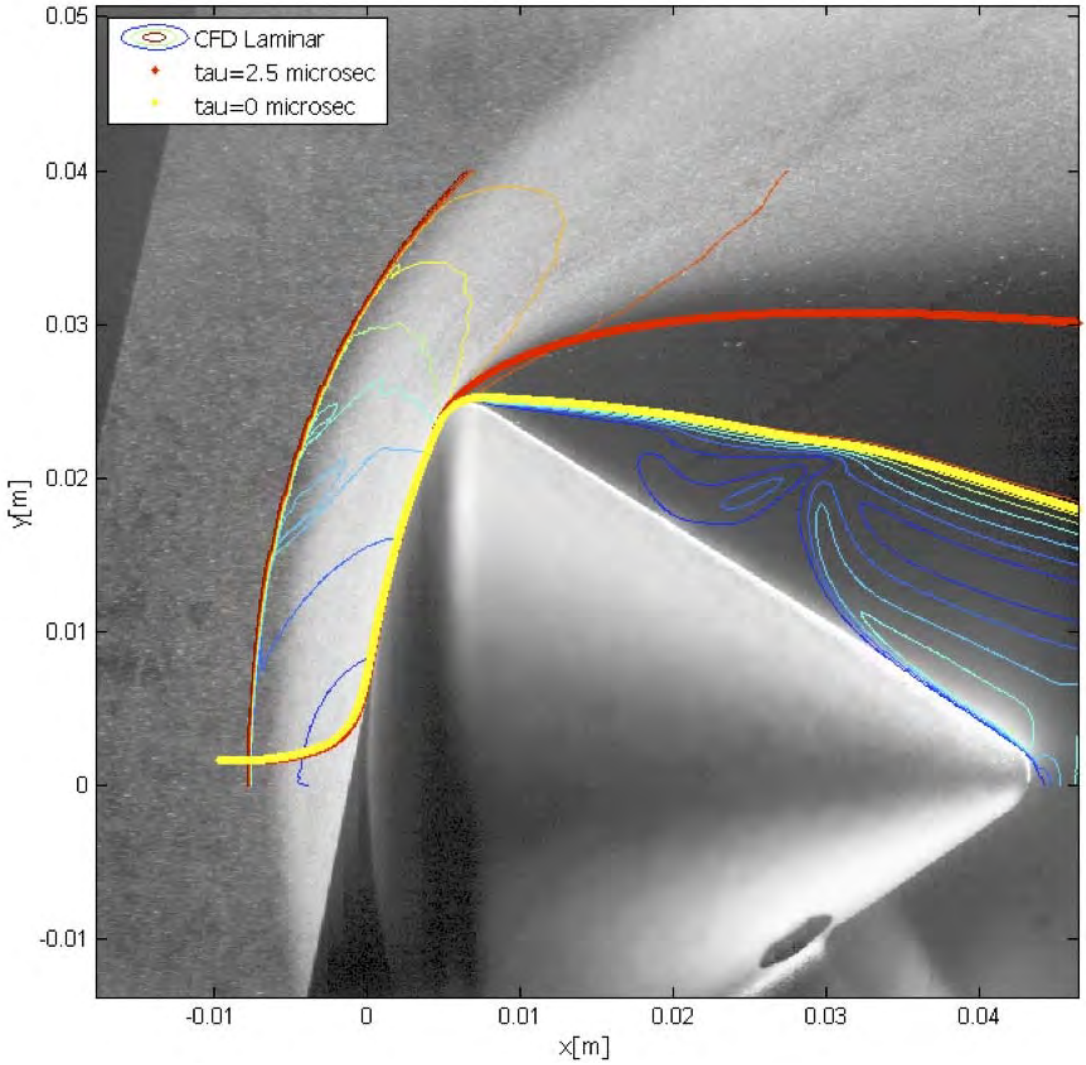

Figure 7-8: PIV Recording at Mach 7 Including Particle Paths Obtained Using a Laminar CFD Computation.

7.4.1 Capsule at 0° Angle of Attack

In Figure 7-9 on the bottom-right a schlieren visualization of the flow around the 0° capsule is shown. The bow shock is clearly visualized as well as the expansion over the model shoulder. As can be observed from the image, the flow over-expands and a lip shock is formed. Downstream of the shoulder the separated shear layer develops and it does not reattach on the model. In the back of the image the bow shock reflection on the wind tunnel window is visible.

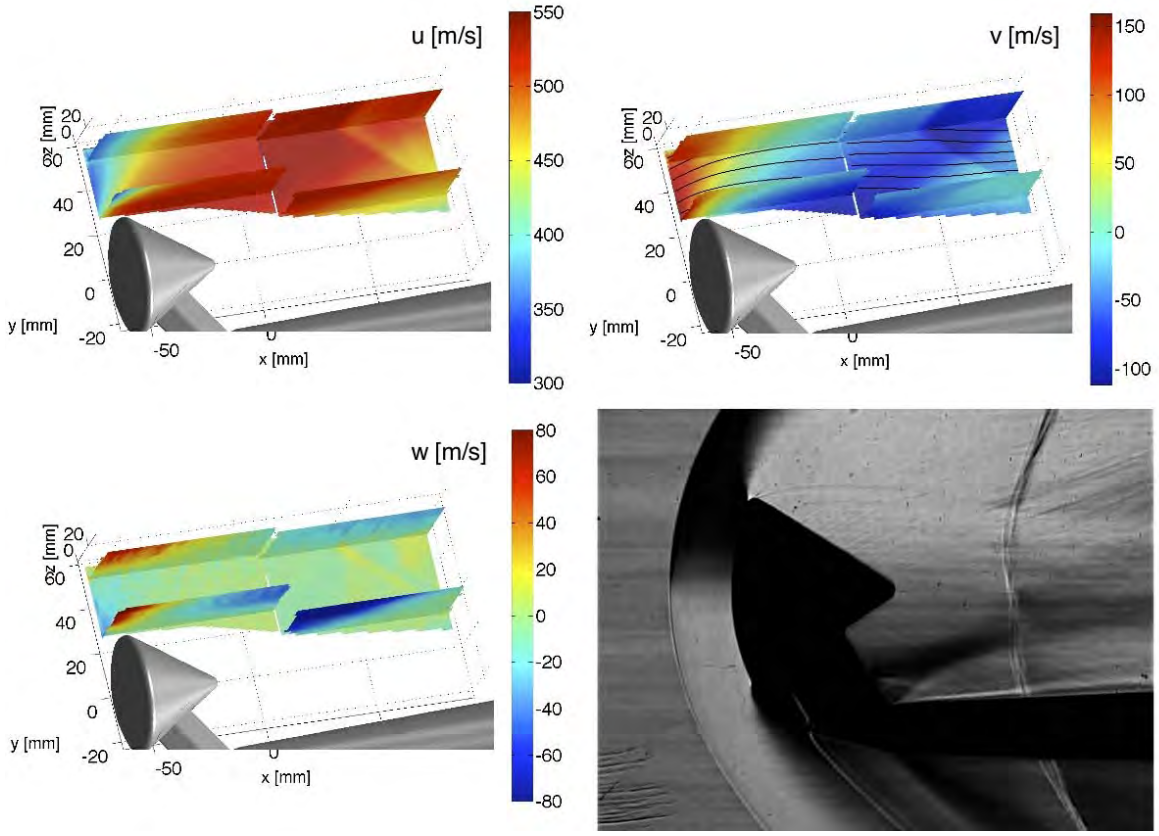

Figure 7-9: SPIV Results and Schlieren Image of the 0° Model at Mach 2 and $Re_D = 1.75 \times 10^6$.

The Stereo PIV (SPIV) results are given in the symmetry plane ($z = 0$ *mm*) and two horizontal cuts. The expansion from the low velocity region downstream of the bow shock over the model shoulder is clearly visualized. When the *u*, *v* and *w* velocity components at the front of the model are regarded with respect to *z*, the three dimensionality of the flow is apparent; in the front the w component increases with z and the u component decreases. In the 'far' wake region the reflected bow shock coming from the wind tunnel wall is measured. Also the shock coming from the re-compression in the capsule wake is clearly visualized.

7.4.2 Capsule at 25° Angle of Attack

The PIV and schlieren results for the 25° model are given in Figure 7-10. The overall flow structure looks similar to the 0° case however it can be observed that the shear only partially separates from the upper side of the capsule. At the model shoulder a small shock wave is present where separation occurs. Further downstream, approximately halfway the model, a stronger shock is formed where the shear layer reattaches. Downstream of the capsule a strong shock is present where the wake is re-compressed. The shock emanating from the reattaching shear layer is also captured by the PIV measurements (the *u* component decreases and *v* component increases). Furthermore the velocity field gives a good overview of the three-dimensional flow field directly behind the capsule. The 'far' field clearly shows the three dimensional pattern of reattachment shock that emanates from the wake behind the capsule.

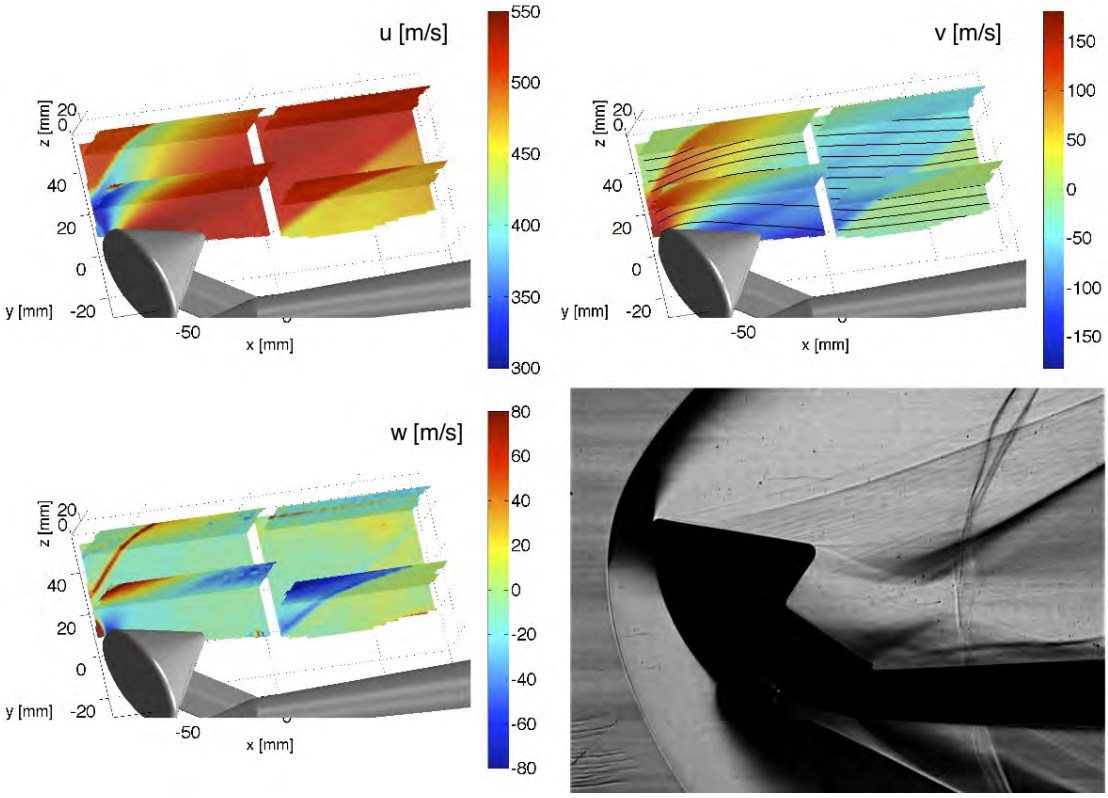

Figure 7-10: SPIV Results and Schlieren Image of the 25° Model at Mach 2 and $Re_D = 1.75 \times 10^6$.

7.5 CONCLUSIONS

The flow over an Apollo type capsule is investigated with the emphasis on the separated shear layer and wake region in the framework of the working group RTO WG043. The model geometry is a scaled version of the AS-202. The state of the shear layer (separated or attached) was observed using shadowgraphy and it was found that the angle of attack for which the shear layer separates decreases with increasing Mach number, furthermore it was observed that the Reynolds number has no appreciable effect on this. The location where the shear layer undergoes transition from laminar to turbulent was obtained from the shadowgraphs. It was found that the Reynolds number based on the transition location (from stagnation point to transition point) and post normal shock flow conditions was constant: $Re_{2,xt} = 0.8 \times 10^6$. Stereo PIV measurements are performed to measure the three-dimensional flow field around the capsule at Mach 2 for 0° and 25° angles of attack. Two 8 × 8 cm^2 fields of view are considered ('near' and 'far' wake) and the planes are offset at 11 *z*-locations. The full three-dimensional average velocity field is constructed by combining the measurement planes. Furthermore schlieren visualizations are performed as a complementary measurement technique. The results for the 0° capsule give a good overview of the three-dimensional flow structure. The shear layer emanating for the capsule shoulder was separated. Recompression of the wake occurs downstream of the capsule and the recompression shock is captured in the velocity field. For the 25° capsule, the shear layer appeared to be only partially separated and shear layer reattachment occurs approximately halfway the capsule. This was found in both the schlieren visualization and the PIV results, however in case of the PIV results the three-dimensional structure of the separation shock is captured.

7.6 REFERENCES

[1] Wright, M., Prabhu, D. and Martinez, E., "Analysis of Apollo Command Module Afterbody Heating Part I: AS-202", *Journal of Thermophysics and Heat Transfer*, Vol. 20, No. 1, 2006.

[2] Prasad, A., "Stereoscopic particle image velocimetry", *Experiments in Fluids*, Vol. 29, pp. 103-116, 2000.

[3] Kruse, R., "Transition and flow reattachment behind an Apollo-like body at Mach numbers to 9", Technical Note D-4645, NASA, 1968.

[4] Schrijer, F. and Scarano, F., "Particle slip compensation in steady compressible flows", 7th International Symposium on Particle Image Velocimetry, Rome, Italy, 2007.

[5] Melling, A., "Tracer particles and seeding for particle image velocimetry", *Meas. Sci. Technol.*, Vol. 8, pp. 1406-1416, 1997.

[6] Schrijer, F. and Bannink, W., "Description and Flow Assessment of the Delft Hypersonic Ludwieg Tube", *Journal of Spacecraft and Rockets*, Vol. 47, No. 1, 2010.

[7] Schrijer, F., Scarano, F. and van Oudheusden, B., "Application of PIV in a Mach 7 double-ramp flow", *Experiments in Fluids*, Vol. 41, pp. 353-363, 2006.

[8] Ragni, D., Schrijer, F., van Oudheusden, B. and Scarano, F., "Assessment of particle tracers time response by the shock wave test and PIV", 6th International Symposium on PIV, 2009.

Chapter 8 – CONCLUSIONS AND OUTLOOK FOR FUTURE ACTIVITIES

John D. Schmisseur
United States Air Force Office of Scientific Research
USA

8.1 LESSONS LEARNED REGARDING THE PLANNED USE OF FLIGHT RESEARCH DATA

As noted in Chapter 1, the unforeseen delays and flight failures occurring in both the HIFiRE and HyBoLT programs required AVT-136 to alter the planned program of work from one building towards an assessment of computational capabilities utilizing flight research data to one focused on simulation validation utilizing benchmark ground test experimental data. While the potential risk associated with planning a Task Group effort on anticipated flight research data was considered during the organization of AVT-136, the group felt the potential benefit associated with access to the flight data warranted acceptance of the increased risk. In retrospect, several key observations associated with the planned utilization of flight research data can be drawn from the experiences of AVT-136.

Planned efforts based on data to be collected in the future face an increased risk of failure due to data unavailability. This most obvious lesson learned from the Task Group experience warrants little further discussion. It should be noted, however, that the research and analysis done in preparation for utilization of the flight data should still be highly useful if the flight data does eventually become available. From this perspective then, there was no "wasted" effort in preparation to analyse the flight data, just delayed return in the research investment.

Existing flight data may not be well-aligned with planned research objectives. Considerable thought within AVT-136 was given to the availability of the existing high-quality flight research data collected by DLR under the SHEFEX I flight experiment. SHEFEX – Sharp Edge Flight Experiment – collected data on the flight performance of a faceted vehicle manufactured from flat sections of thermal protection system material. While the experiment is considered a tremendous success for DLR and a validation of the faceted vehicle concept, the faceted surface made the SHEFEX vehicle poorly suited for exploration of the aerothermodynamic phenomena identified as the scientific objectives of the AVT-136 effort.

Planned flight research data is not well-aligned with the full range of scientific challenges associated with hypersonics. The HIFiRE 1 and HyBoLT experiments were designed to provide flight data on boundary layer transition. Additionally, HIFiRE 1 will provide data on shock/boundary layer interactions. While these data are well-aligned with two of the six topic areas emphasized by AVT-136, only the ESA EXPERT program (which was not part of the planned scope of AVT-136) appears to address some of the gas-surface interaction, rarefied flow and base flow issues that are critical to the development of future hypersonic capabilities. It is clear that there is a significant need for additional flight research opportunities that address a broader range of critical phenomena, especially those associated with increased flow enthalpies.

8.2 PERSPECTIVE ON THE VALUE OF INTERNATIONAL ACTIVITIES

As noted both in Chapter 1 and in Section 6.4 below, 33 conference presentations highlighting contributions to AVT-136 were made by leading researchers in the six scientific topic areas addressed by the Task Group. Such contributions were not funded by AVT-136 and were essentially donated to the Task Group from the existing research programs of the contributing authors. The willingness to contribute research resources to

international working groups organized under RTO has been a persistent characteristic of the hypersonics research community extending back through WG10 and WG18. The members of AVT-136 have given careful consideration to this phenomenon and have concluded the following:

> *Individual researchers are willing to volunteer their time and resources for international collaborative activities because they consider it an honor. A critical aspect of ensuring that participation is considered an honor is to promote the presentation of contributions to the international effort in special conference sessions and issues of archival journals.*

In other words, researchers are eager to contribute their efforts to an international collaborative effort if they have an opportunity to be recognized for their contribution within the open research community. AVT-136 strongly recommends that the Applied Vehicle Technology Panel consider this observation when determining the scope of future working group activities.

Additionally, a consistent theme echoed by the membership of AVT-136 is that international collaboration opportunities provided by RTO Task Groups play a critical role in fostering communication and coordination within the international research community. Despite the advantages of modern internet-based communication, the physical and circadian differences separating the North American and European research communities still deters frequent collaboration. The integrated experiences of the membership of AVT-136 clearly indicate that the RTO-organized efforts such as WG18, WG10 and AVT-136 have played a critical role in the establishment and sustainment of cooperative efforts within the international research community which transcend the limited duration of the Task Groups.

8.3 RECOMMENDATIONS FOR FUTURE AVT EFFORTS IN AEROTHERMODYNAMICS

AVT-136 enjoyed enthusiastic support from the research communities and organizations of the participating countries during the four-year duration of the Task Group. A possible contributing factor to this success is the fact that Task Group meetings were conducted at major research sites in both North America and Europe, resulting in increased opportunities for researchers to become entrained in the program. Another plausible argument is that the six scientific topics addressed by the group facilitated engagement by a broad spectrum of the research community. Regardless of the motivation for such broad support, it is clear that international interest and support for collaborative efforts in hypersonics remains strong. Thus, the members of AVT-136 strongly recommend the continuation of international collaborative efforts in aerothermodynamics under the auspices of the Applied Vehicle Technology Panel.

A description of research topics for potential follow-on efforts to AVT-136 is provided below. One issue that became clear during the course of AVT-136 is that there are dramatic differences in the research communities that contributed to the six topic areas addressed by the Task Group. As a result of the differences in technical challenges, availability of funding, and acceptance of benchmark problems and processes, the unification of multiple research thrusts under a common Task Group may not have been the optimal approach. Inspired by this observation, the potential future efforts described below have a more focused scope of research than that of AVT-136. The intent behind this recommendation is to enhance the efficiency and effectiveness of future efforts. It should be noted that the list below is just a partial list of a broad range of potential activities.

Validation of Numerical Simulations of Shock Wave / Boundary Layer Interactions – Work in this area has historically been strongly supported by members of the RTO community and there is continued significant interest in the topic. Significant advancements in the state-of-the-art have been driven by the assessments of WG18, WG10 and now AVT-136, so it is apparent that the Task Group model works well in this research area. It is recommended that a new Task Group focused on Shock/Wave Boundary Layer Interactions be organized by the Applied Vehicle Technology Panel.

Assessment of Research Capabilities and Needs in Boundary Layer Laminar-Turbulent Transition – In recent years, and especially under AVT-136, this topic area has suffered from a lack of research contributions to Task Group efforts. This deficit appears tied to a dearth of research funding for potential contributors. There is clear international interest in the area and several strong bilateral collaborations resulted from the relationships between researchers fostered as part of the Task Group experience. It is recommended that this topic area be explored in the future as a *Specialists' Meeting* rather than as a Task Group. This approach may elicit a stronger response from the research community and allow the development of a perspective which may be instrumental in the development of future research funding.

Assessment of Predictive Capabilities for Turbulent Heat Transfer – Despite the relatively benign appearance of the topic, design of efficient hypersonic systems is predicated on the prediction of turbulent heat transfer over a variety of surfaces, including those influenced by roughness, material degradation, ablation and catalytic heating. Unfortunately, capabilities to predict such phenomena even on smooth flat surfaces for high Mach numbers are still exceptionally limited. There is significant interest in this topic within the funding agencies of the United States and it is anticipated that there would be significant potential contributions to this topic if it were the focus of a Task Group.

Standard Practices for Catalytic Heating Experiments and Simulations – Interest in this research area produced numerous contributions to the AVT-136 effort. While the AVT-136 effort provided an important assessment of this area, the potential exists to guide further developments in this community through the establishment of widely-accepted benchmark problems and data sets. Such an objective could be accomplished with an initial Specialist's Meeting which could characterize specific research needs and set the stage for an eventual Task Group on the subject.

8.4 CONFERENCE PAPERS PRESENTED IN ASSOCIATION WITH AVT-136

The following papers were presented at the Sixth European Symposium on Aerothermodynamics for Space Vehicles, November 2008, Versailles, France.

S20: RTO-WG043 / Code Validation

- D. Knight, Assessment of Aerothermodynamic Flight Prediction Tools for Shock Interactions.
- D. Gaitonde, Evaluation of CFD for 2-D and 3-D high-speed flow predictions.
- A. Panaras, High-speed Unsteady Flows around Concave Axisymmetric Bodies: Flow Instabilities and their Control.
- S. Schneider, Influence of Freestream Noise on Hypersonic Transition.
- I. Nompelis, Numerical Simulations of Hypersonic Double-Cone Flows with Real Gas Effects.
- S. Borrelli, RTG-043: Sub-Group "Nose and Leading Edges".
- M. Barnhardt, Analysis of the Reentry-F Experiment Using Detached Eddy Simulation.
- J. Olejniczak, An Overview of Radiation Modeling Work for Shock Heated Gas for RTO AVT-136.
- F. Schrijer, Experimental Capsule Afterbody Flow Investigation.

S24: RTO-WG043 / Gas-Surface Interaction I

- M. MacLean, Assessment of Aerothermal Heating Augmentation Attributed to Surface Catalysis in High Enthalpy Shock Tunnel Flows.
- M. Balat-Pichelin, Catalycity of Zirconia and of ZrB2-Based Ultra-High Temperature Ceramics.

- G. Herdrich, Investigation of Catalysis and Reaction Schemes: Ground-based Experiments, Modeling and Extrapolation to Flight.
- M. Cacciatore, Catalytic Activity of Silica Surfaces in Dissociated Oxygen/Nitrogen from AB Initio Calculations.
- A. Schettino, Design and Rebuilding of New Experimental Tests on a Double Cone at Mach 9.

S28: RTO-WG043 / Gas Surface Interaction II

- M. Fertig, SiC Oxidation and Catalysis Modelling for Re-Entry Heating Predictions.
- R. Sayós, Theoretical Dynamics Study of Several Atomic and Molecular Oxygen Processes over a Silica Surface.
- A. Lani, A Residual Distribution Method for Hypersonic Flows in Thermo-Chemical Non-Equilibrium.
- L.M.G.F.M. Walpot, Numerical and Experimental AS-202 Base Flow Investigation.

The following papers were presented at the 48th AIAA Aerospace Sciences Meeting, January, 2010, Orlando, FL, USA.

Session: Overview of AVT-136: Flight Experiment Assessment via Ground Test and CFD

- AIAA-2010-1465 **Shock Interactions Investigations Associated with AVT- 136 (Invited)**
  D. Knight, Rutgers University, Piscataway, NJ, USA; and J. Longo, German Aerospace Center (DLR), Germany.
- AIAA-2010-1466 **Summary of Hypersonic Transition Research Coordinated Through NATO RTO AVT- 136 (Invited)**
  S. Schneider, Purdue University, West Lafayette, IN, USA.
- AIAA-2010-1467 **Experimental Methodologies and Assessments to derive Catalysis relevant Parameters (Invited)**
  G. Herdrich, University of Stuttgart, Stuttgart, Germany.
- AIAA-2010-1468 **Base Flow Investigation of the Apollo Command Module in the Frame of AVT- 136 (Invited)**
  L. Walpot, Advanced Operations and Engineering Services Group, Leiden, Netherlands; P. Noeding, EADS Astrium, Bremen, Germany; F. Schrijer, Delft University of Technology, Delft, Netherlands; and M. Wright, NASA Ames Research Center, Moffett Field, CA, USA.

Session: Shock Interaction Studies Under RTO AVT-136

- AIAA-2010-1281 **A Review of Experimental Studies with the Double Cone Configuration in the LENS Hypervelocity Tunnels and Comparisons with Navier-Stokes and DSMC Computations (Invited)**
  M. Holden, J. Harvey, T. Wadhams, and M. MacLean, CUBRC, Buffalo, NY, USA.
- AIAA-2010-1282 **Numerical Investigation of Double-Cone and Cylinder Experiments in High Enthalpy Flows Using the DLR TAU Code (Invited)**
  B. Reimann, German Aerospace Center (DLR), Braunschweig, Germany; and V. Hannemann, German Aerospace Center (DLR), Göttingen, Germany.
- AIAA-2010-1283 **Numerical Investigation of Double-Cone Flow Experiments with High-Enthalpy Effects (Invited)**
  I. Nompelis and G. Candler, University of Minnesota, Minneapolis, MN, USA.

- AIAA-2010-1284 **An Assessment of CFD for Surface Load Prediction in High-Speed Flows (Invited)**
  D. Gaitonde, U.S. Air Force Research Laboratory, Wright-Patterson AFB, OH, USA.
- AIAA-2010-1285 **Chemically Reacting Flows Around a Double Cone, Including Ablation Effects (Invited)**
  D. Drikakis, Cranfield University, Cranfield, Great Britain.

Session: Contributions to RTO AVT-136

- AIAA-2010-1246 **A Review of Transition Studies on Full-Scale Flight Vehicles at Duplicated Flight Conditions in the LENS Tunnels and Comparisons with Prediction Methods and Flight Measurement (Invited)**
  T. Wadhams, M. MacLean and M. Holden, CUBRC, Buffalo, NY, USA; S. Barry, NASA Langley Research Center, Hampton, VA, USA.
- AIAA-2010-1247 **Modeling Approaches for Gas-Surface Interactions (Invited)**
  G. Herdrich, University of Stuttgart, Stuttgart, Germany.
- AIAA-2010-1248 **Catalysis Phenomena Determination in Plasmatron Facility for Flight Experiment Design (Invited)**
  O. Chazot, F. Panerai, and J. Muylaert, von Kármán Institute for Fluid Dynamics, Rhode-Saint-Genèse, Belgium; and J. Thoemel, ESA, Noordwijk, Netherlands.
- AIAA-2010-1249 **Realization of a Gas-Surface Interaction Test Case for Model Validation (Invited)**
  D. Fletcher, University of Vermont, Burlington, VT, USA.
- AIAA-2010-1250 **CFD Analysis of CUBRC Base Flow Experiments (Invited)**
  M. Barnhardt and G. Candler, University of Minnesota, Minneapolis, MN, USA; M. MacLean, CUBRC, Buffalo, NY, USA.
- AIAA-2010-1251 **Experimental Investigation of the Supersonic Wake of a Reentry Capsule**
  F. Schrijer, Delft University of Technology, Delft, Netherlands; L. Walpot, Advanced Operations and Engineering Services Group, Noordwijk, Netherlands.

REPORT DOCUMENTATION PAGE

1. Recipient's Reference	2. Originator's References	3. Further Reference	4. Security Classification of Document
	RTO-TR-AVT-136 AC/323(AVT-136)TP/388	ISBN 978-92-837-0142-2	UNCLASSIFIED/ UNLIMITED

5. Originator

Research and Technology Organisation
North Atlantic Treaty Organisation
BP 25, F-92201 Neuilly-sur-Seine Cedex, France

6. Title

Assessment of Aerothermodynamic Flight Prediction Tools through Ground and Flight Experimentation

7. Presented at/Sponsored by

This Report Documents the Efforts of Task Group AVT-136.

8. Author(s)/Editor(s)	9. Date
Multiple	November 2011
10. Author's/Editor's Address	**11. Pages**
Multiple	194

12. Distribution Statement

There are no restrictions on the distribution of this document. Information about the availability of this and other RTO unclassified publications is given on the back cover.

13. Keywords/Descriptors

Aerothermodynamics	Flight experiments	Reentry systems
Base flows	Ground testing	Reentry thermophysics
Blunt body entry vehicles	Laminar-turbulent transition	Thermal protection systems
Catalytic heating	Radiation transport	Turbulent flow on blunt bodies
Computational fluid dynamics	Rarefied flow	

14. Abstract

AVT-136 was organized to assess and improve the understanding and prediction of aerothermodynamic phenomena and aerothermal loads for space transportation and earth/planetary entry systems through ground and flight experimentation. To achieve this goal, efforts were organized around six scientific topic areas: 1) Nose and Leading Edges; 2) Shock Interactions and Control Surfaces; 3) Shock Layers and Radiation; 4) Boundary Layer Transition; 5) Gas-Surface Interactions; and 6) Base and Afterbody Flows. Although it was recognized from the onset of AVT-136 activities that reliance on flight research data yet to be collected posed significant risk to the achievement of Task Group objectives, the group concluded the significant benefit to be derived from comparison of computational simulations with flight data warranted pursuit of such a program of work. Unfortunately, program delays and failures in the flight programs contributing to the AVT-136 effort prevented access to flight research data. Despite this setback, most of the scientific topic areas developed by the Task Group made significant progress in the assessment of current capabilities. Additionally, the activities of AVT-136 generated substantial interest within the international scientific research community and the work of the Task Group was prominently featured in a total of six invited sessions dedicated to AVT-136 in the Sixth European Symposium on Aerothermodynamics for Space Vehicles and the 48th (2010) AIAA Aerospace Sciences Meeting.

NORTH ATLANTIC TREATY ORGANISATION

RESEARCH AND TECHNOLOGY ORGANISATION

BP 25
F-92201 NEUILLY-SUR-SEINE CEDEX • FRANCE
Télécopie 0(1)55.61.22.99 • E-mail mailbox@rta.nato.int

DIFFUSION DES PUBLICATIONS

RTO NON CLASSIFIEES

Les publications de l'AGARD et de la RTO peuvent parfois être obtenues auprès des centres nationaux de distribution indiqués ci-dessous. Si vous souhaitez recevoir toutes les publications de la RTO, ou simplement celles qui concernent certains Panels, vous pouvez demander d'être inclus soit à titre personnel, soit au nom de votre organisation, sur la liste d'envoi.

Les publications de la RTO et de l'AGARD sont également en vente auprès des agences de vente indiquées ci-dessous.

Les demandes de documents RTO ou AGARD doivent comporter la dénomination « RTO » ou « AGARD » selon le cas, suivi du numéro de série. Des informations analogues, telles que le titre est la date de publication sont souhaitables.

Si vous souhaitez recevoir une notification électronique de la disponibilité des rapports de la RTO au fur et à mesure de leur publication, vous pouvez consulter notre site Web (www.rto.nato.int) et vous abonner à ce service.

CENTRES DE DIFFUSION NATIONAUX

ALLEMAGNE
Streitkräfteamt / Abteilung III
Fachinformationszentrum der Bundeswehr (FIZBw)
Gorch-Fock-Straße 7, D-53229 Bonn

BELGIQUE
Royal High Institute for Defence – KHID/IRSD/RHID
Management of Scientific & Technological Research for Defence, National RTO Coordinator
Royal Military Academy – Campus Renaissance
Renaissancelaan 30, 1000 Bruxelles

CANADA
DSIGRD2 – Bibliothécaire des ressources du savoir
R et D pour la défense Canada
Ministère de la Défense nationale
305, rue Rideau, 9e étage
Ottawa, Ontario K1A 0K2

DANEMARK
Danish Acquisition and Logistics Organization (DALO)
Lautrupbjerg 1-5, 2750 Ballerup

ESPAGNE
SDG TECIN / DGAM
C/ Arturo Soria 289
Madrid 28033

ESTONIE
Estonian Ministry of Defence
Estonian National Coordinator for NATO RTO
Sakala 1, Tallinn 15094

ETATS-UNIS
NASA Center for AeroSpace Information (CASI)
7115 Standard Drive
Hanover, MD 21076-1320

FRANCE
O.N.E.R.A. (ISP)
29, Avenue de la Division Leclerc
BP 72, 92322 Châtillon Cedex

GRECE (Correspondant)
Defence Industry & Research General Directorate, Research Directorate
Fakinos Base Camp, S.T.G. 1020
Holargos, Athens

HONGRIE
Hungarian Ministry of Defence
Development and Logistics Agency
P.O.B. 25, H-1885 Budapest

ITALIE
General Secretariat of Defence and National Armaments Directorate
5th Department – Technological Research
Via XX Settembre 123, 00187 Roma

LUXEMBOURG
Voir Belgique

NORVEGE
Norwegian Defence Research Establishment, Attn: Biblioteket
P.O. Box 25
NO-2007 Kjeller

PAYS-BAS
Royal Netherlands Military Academy Library
P.O. Box 90.002
4800 PA Breda

POLOGNE
Centralna Biblioteka Wojskowa
ul. Ostrobramska 109
04-041 Warszawa

PORTUGAL
Estado Maior da Força Aérea
SDFA – Centro de Documentação
Alfragide, P-2720 Amadora

REPUBLIQUE TCHEQUE
LOM PRAHA s. p.
o. z. VTÚLaPVO
Mladoboleslavská 944
PO Box 18
197 21 Praha 9

ROUMANIE
Romanian National Distribution Centre
Armaments Department
9-11, Drumul Taberei Street
Sector 6
061353, Bucharest

ROYAUME-UNI
Dstl Knowledge and Information Services
Building 247
Porton Down
Salisbury SP4 0JQ

SLOVAQUIE
Akadémia ozbrojených síl gen.
M.R. Štefánika, Distribučné a informačné stredisko RTO
Demänová 393, Liptovský Mikuláš 6
031 06

SLOVENIE
Ministry of Defence
Central Registry for EU and NATO
Vojkova 55
1000 Ljubljana

TURQUIE
Milli Savunma Bakanlığı (MSB)
ARGE ve Teknoloji Dairesi Başkanlığı
06650 Bakanliklar
Ankara

AGENCES DE VENTE

NASA Center for AeroSpace Information (CASI)
7115 Standard Drive
Hanover, MD 21076-1320
ETATS-UNIS

The British Library Document Supply Centre
Boston Spa, Wetherby
West Yorkshire LS23 7BQ
ROYAUME-UNI

Canada Institute for Scientific and Technical Information (CISTI)
National Research Council Acquisitions
Montreal Road, Building M-55
Ottawa K1A 0S2, CANADA

Les demandes de documents RTO ou AGARD doivent comporter la dénomination « RTO » ou « AGARD » selon le cas, suivie du numéro de série (par exemple AGARD-AG-315). Des informations analogues, telles que le titre et la date de publication sont souhaitables. Des références bibliographiques complètes ainsi que des résumés des publications RTO et AGARD figurent dans les journaux suivants :

Scientific and Technical Aerospace Reports (STAR)
STAR peut être consulté en ligne au localisateur de ressources uniformes (URL) suivant: http://ntrs.nasa.gov/search.jsp
STAR est édité par CASI dans le cadre du programme NASA d'information scientifique et technique (STI)
NASA Langley Research Center, STI Program Office, MS 157A
Hampton, Virginia 23681-0001
ETATS-UNIS

Government Reports Announcements & Index (GRA&I)
publié par le National Technical Information Service
Springfield
Virginia 2216
ETATS-UNIS
(accessible également en mode interactif dans la base de données bibliographiques en ligne du NTIS, et sur CD-ROM)

NORTH ATLANTIC TREATY ORGANISATION

RESEARCH AND TECHNOLOGY ORGANISATION

BP 25

F-92201 NEUILLY-SUR-SEINE CEDEX • FRANCE
Télécopie 0(1)55.61.22.99 • E-mail mailbox@rta.nato.int

DISTRIBUTION OF UNCLASSIFIED RTO PUBLICATIONS

AGARD & RTO publications are sometimes available from the National Distribution Centres listed below. If you wish to receive all RTO reports, or just those relating to one or more specific RTO Panels, they may be willing to include you (or your Organisation) in their distribution.

RTO and AGARD reports may also be purchased from the Sales Agencies listed below.

Requests for RTO or AGARD documents should include the word 'RTO' or 'AGARD', as appropriate, followed by the serial number. Collateral information such as title and publication date is desirable.

If you wish to receive electronic notification of RTO reports as they are published, please visit our website (www.rto.nato.int) from where you can register for this service.

NATIONAL DISTRIBUTION CENTRES

BELGIUM
Royal High Institute for Defence – KHID/IRSD/RHID
Management of Scientific & Technological Research for Defence, National RTO Coordinator
Royal Military Academy – Campus Renaissance
Renaissancelaan 30
1000 Brussels

CANADA
DRDKIM2 – Knowledge Resources Librarian
Defence R&D Canada
Department of National Defence
305 Rideau Street, 9th Floor
Ottawa, Ontario K1A 0K2

CZECH REPUBLIC
LOM PRAHA s. p.
o. z. VTÚLaPVO
Mladoboleslavská 944
PO Box 18
197 21 Praha 9

DENMARK
Danish Acquisition and Logistics Organization (DALO)
Lautrupbjerg 1-5
2750 Ballerup

ESTONIA
Estonian Ministry of Defence
Estonian National Coordinator for NATO RTO
Sakala 1, Tallinn 15094

FRANCE
O.N.E.R.A. (ISP)
29, Avenue de la Division Leclerc
BP 72, 92322 Châtillon Cedex

GERMANY
Streitkräfteamt / Abteilung III
Fachinformationszentrum der Bundeswehr (FIZBw)
Gorch-Fock-Straße 7
D-53229 Bonn

GREECE (Point of Contact)
Defence Industry & Research General Directorate, Research Directorate
Fakinos Base Camp, S.T.G. 1020
Holargos, Athens

HUNGARY
Hungarian Ministry of Defence
Development and Logistics Agency
P.O.B. 25, H-1885 Budapest

ITALY
General Secretariat of Defence and National Armaments Directorate
5th Department – Technological Research
Via XX Settembre 123, 00187 Roma

LUXEMBOURG
See Belgium

NETHERLANDS
Royal Netherlands Military Academy Library
P.O. Box 90.002
4800 PA Breda

NORWAY
Norwegian Defence Research Establishment, Attn: Biblioteket
P.O. Box 25
NO-2007 Kjeller

POLAND
Centralna Biblioteka Wojskowa
ul. Ostrobramska 109
04-041 Warszawa

PORTUGAL
Estado Maior da Força Aérea
SDFA – Centro de Documentação
Alfragide, P-2720 Amadora

ROMANIA
Romanian National Distribution Centre
Armaments Department
9-11, Drumul Taberei Street
Sector 6, 061353, Bucharest

SLOVAKIA
Akadémia ozbrojených síl gen.
M.R. Štefánika, Distribučné a informačné stredisko RTO
Demänová 393, Liptovský Mikuláš 6
031 06

SLOVENIA
Ministry of Defence
Central Registry for EU & NATO
Vojkova 55
1000 Ljubljana

SPAIN
SDG TECIN / DGAM
C/ Arturo Soria 289
Madrid 28033

TURKEY
Milli Savunma Bakanlığı (MSB)
ARGE ve Teknoloji Dairesi Başkanlığı
06650 Bakanliklar – Ankara

UNITED KINGDOM
Dstl Knowledge and Information Services
Building 247
Porton Down
Salisbury SP4 0JQ

UNITED STATES
NASA Center for AeroSpace Information (CASI)
7115 Standard Drive
Hanover, MD 21076-1320

SALES AGENCIES

NASA Center for AeroSpace Information (CASI)
7115 Standard Drive
Hanover, MD 21076-1320
UNITED STATES

The British Library Document Supply Centre
Boston Spa, Wetherby
West Yorkshire LS23 7BQ
UNITED KINGDOM

Canada Institute for Scientific and Technical Information (CISTI)
National Research Council Acquisitions
Montreal Road, Building M-55
Ottawa K1A 0S2, CANADA

Requests for RTO or AGARD documents should include the word 'RTO' or 'AGARD', as appropriate, followed by the serial number (for example AGARD-AG-315). Collateral information such as title and publication date is desirable. Full bibliographical references and abstracts of RTO and AGARD publications are given in the following journals:

Scientific and Technical Aerospace Reports (STAR)
STAR is available on-line at the following uniform resource locator: http://ntrs.nasa.gov/search.jsp
STAR is published by CASI for the NASA Scientific and Technical Information (STI) Program
NASA Langley Research Center, STI Program Office, MS 157A
Hampton, Virginia 23681-0001
UNITED STATES

Government Reports Announcements & Index (GRA&I)
published by the National Technical Information Service
Springfield
Virginia 2216
UNITED STATES
(also available online in the NTIS Bibliographic Database or on CD-ROM)

ISBN 978-92-837-0142-2